An investigation of buffet over low-observable planforms

Woods, M. I.

Award date:
1999

Awarding institution:
University of Bath

AN INVESTIGATION OF BUFFET OVER LOW-OBSERVABLE PLANFORMS

submitted by M.I.Woods

for the degree of PhD

of the University of Bath

1999

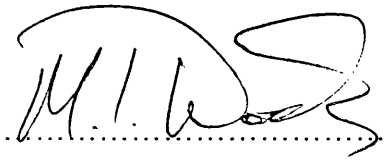

ProQuest LLC
789 East Eisenhower Parkway
P.O. Box 1346
Ann Arbor, MI 48106-1346

SUMMARY

Four generic low-observable planforms constructed using a foam/composite technique have been manufactured and tested in the 2.12 m x 1.51 m wind tunnel at the University of Bath. Models were instrumented with between 137 and 165 Scanivalve pressure tappings in addition to miniature accelerometers. A technique was developed to allow both steady and unsteady pressures, up to a maximum frequency of 500 Hz, to be measured using the Scanivalve tappings. The planforms of the models were specified by British Aerospace (MA&A, Warton) as containing features likely to be encountered on future low observable combat aircraft.

Both steady and unsteady pressure data was acquired over a range of incidences for a total of six configurations. Oilflow visualisation data was acquired in addition to the pressure data. Data was acquired at a range of incidences for each model and later in the test programme, when suitable data storage was available, tests at a variety of speeds were performed. This data was processed to allow the PSDs at each point over the surface to be calculated, and to enable the computation of the RMS pressure fluctuations.

Examination of the pressure data demonstrated that the peak RMS pressure fluctuations were not found under the vortex core as had previously been accepted. Maximum pressure fluctuations were found inboard of the core. This revelation was made possible by the enhanced spatial resolution available using the calibrated Scanivalve technique. It

was found that there were frequencies other than those previously measured by other researchers within the region of high RMS pressures. Specifically, there were points on the surface where two distinct peaks were apparent in the pressure spectra. In addition a third peak was detected directly underneath the primary attachment line of the leading edge vortex. The frequencies of all of these peaks have been shown to vary inversely with the chordwise distance from the leading edge apex. The frequencies were also found to scale linearly with free stream velocity.

Distinct differences were found between models with 40° and 60° of leading edge sweep. The location of the vortex burst had a large influence on the RMS pressure fluctuations over the wing with 60° of sweep. Upstream of the burst there was very little buffet. Conversely, buffet was of similar magnitudes both up and downstream of the vortex burst over the wings with 40° of sweep.

A simple model of conflicting addition and dissipation of pressure fluctuations was proposed to explain the shape of the spanwise RMS pressure distribution. Addition of fluctuations from the shear layer is counteracted by dissipation, with the resulting pressure fluctuations swept outboard. This causes the RMS pressure fluctuations to rise from the primary attachment toward the suction peak with maximum RMS pressure found inboard of the core. This model was applied to one of the planforms under investigation, and allowed the reconstruction of the RMS pressure distribution and the PSDs over the surface of the planform. The utilisation of this model over other configurations may enable the prediction of buffet over arbitrary planforms.

Acknowledgments

A brief note of thanks to the following:

To my supervisor Norman for being insistent.

To EPSRC and the Universities of Bath and Manchester for being generous.

To my parents for being encouraging.

To Dave, Les and Ken for being practical.

To MA&A and SRC for being interested.

To Fraser, Jon, Tony, Mark and Becky for being fun.

And to my wife Jayne just for being...

CONTENTS

NOMENCLATURE

a	Addition Parameter	
c	Wing chord	m
c_0	Wing Root chord	m
$\bar{c}$	Mean chord	m
$\bar{\bar{c}}$	Aerodynamic mean chord	m
c	Complex phase velocity	
C_D	Drag Coefficient	
C_L	Lift Coefficient	
C_{MLE}	Pitching Moment Coefficient about apex	
C_P	Pressure Coefficient	
f	Frequency	Hz
F	Froude number	
g	Acceleration due to gravity	ms^{-2}
h	Fluid depth	m
k	Dissipation Parameter	
K	Vortex Strength	m^2s^{-1}
M_∞	Free stream Mach number	
n	Azimuthal wave number	
n_m	Modified frequency parameter	
p	Pressure	Nm^{-2}
$\bar{p}$	RMS pressure	Nm^{-2}

p_0	Total Pressure	Nm^{-2}
q	Dynamic pressure	Nm^{-2}
q	Swirl Parameter	
s	Wing semispan	m
S	Flow force	$kgms^{-2}$
S	Wing Area	m^2
u	Fluid velocity	ms^{-1}
u'	velocity tangential to vortex	ms^{-1}
v'	velocity normal to vortex	ms^{-1}
U_∞	Free stream velocity	ms^{-1}
U_{RMS}	RMS velocity	ms^{-1}
x	Chordwise distance from apex	m
x_t	Chordwise location of wingtip	m
y	Spanwise distance from Centreline	m
$y_{0.5}$	Vortex half-width	m

α	Incidence	°
α	Axial wave number	
ϕ	Azimuthal co-ordinate	rad
ψ	Stream function	
ρ	Density	kgm^{-3}

ω	Frequency	rad/s
ω_n	Undamped natural Frequency	rad/s
ω_d	Damped Natural Frequency	rad/s
ζ	Proportion of critical damping	

Abbreviations

A/D	Analogue to Digital
BAe	British Aerospace
CFD	Computational Fluid Dynamics
D/A	Digital to Analogue
DDE	Dynamic Data Exchange
FFT	Fast Fourier Transform
HDD	Hard Disk Drive
MAD	Military Aircraft Division
PC	Personal Computer
PSD	Power Spectral Density
RANS	Reynolds Averaged Navier Stokes
RCS	Radar Cross Section
RMS	Root Mean Square

LIST OF FIGURES

CHAPTER 1: INTRODUCTION

1.1 Background

Optimisation criteria for the configuration of a modern military aircraft are very different to those for a civil airliner and result in very different wing planforms, as depicted in Figure 1.1. Civil aircraft are designed predominantly for optimum cruise performance, where aerodynamic characteristics such as high lift to drag ratio are of paramount importance. This principle results in wings with large spans, designed for reduced induced drag, together with moderate sweep to increase the drag rise Mach number. Wing loadings are high (of the order of 6.5 kN/m^2 for a Boeing 777) to reduce profile drag. In contrast, a modern combat aircraft tends to have a low aspect ratio wing with significantly higher sweep. The low aspect ratio wing has several advantages for such an aircraft. The wing root is significantly larger in both chord and thickness increasing structural strength and the shorter wings result in lower wing root bending moments. Wing loadings for the new generation of military aircraft are also generally lower than those for civil aircraft (4.2 kN/m^2 for EF-2000). This, coupled with shorter wings, allow aircraft to manoeuvre more vigourously, typically in the range +9g / -3g for a modern design.

The shorter wings also reduce the inertia of the aircraft in the roll axis, allowing it to be more agile in roll.

Both manned and computerised simulation of air combat (Herbst-1983) have shown that air combat can be divided into 3 distinct regions: Short Range, Medium Range and Long Range. Short range encounters can be defined as those where the aircraft pass each other and reverse headings to obtain firing opportunities, with such contests taking place when aircraft are within approximately 10 miles of their opponents. Previous generation 'rear aspect' missiles resulted in sustained turn rate being of critical importance, with pilots manoeuvering to get behind their opponent and thus facilitate weapons release. An example of an aircraft designed during this era is the F-16, which emerged from the US Air Force's Lightweight Fighter programme in the early 1970s. However, with modern 'all aspect' weaponry combat effectiveness is more sensitive to attainable *unsteady* performance.

In a short range combat encounter aircraft tend to engage in a sequence of head-on passes. After each pass, during which weapons are released, both aircraft attempt to reverse course as quickly as possible to obtain another firing opportunity. In the course of such manoeuvering aircraft often exceed their maximum sustainable turn rate, reducing speed dramatically. Maximum instantaneous turn rates are thus limited by structural limits at moderate and high Mach numbers and by the maximum attainable lift at low speed (See Figure 1.2). The ability to aim the fuselage independently of flight path allows aircraft to utilise gunfire as an effective weapon, with rapid pitching manoeuvres bringing the weapon to bear as the combating aircraft pass. Short range

combat is thus characterised by the conversion of kinetic energy into altitude to move the aircraft to the speed at which maximum instantaneous turn rate is achieved and the use of extreme instantaneous manoeuvres to achieve a firing opportunity, with the sacrifice of further energy. Maximum usable lift, together with a high thrust to weight ratio to replace the energy deficits resulting from the use of extreme manoeuvres are therefore of paramount importance when designing for modern short range combat.

In contrast, medium range engagements are less dynamic and are not characterised by the prolific exchange of velocity and height for high rates of turn. The energy budget is carefully managed with excess power not required for turning utilised either to climb or to accelerate. Manoeuvring is employed to achieve a firing position, to attempt to stay out of the opponent's missile firing envelope and to sustain sufficient energy to attack again or to fight against other opponents in a multiple engagement. Hence, medium range combat is characterised by sustained moderate-g manoeuvres.

Long range combat, at a range greater than approximately 30 miles, involves less manoeuvring by opposing aircraft. Missile range and technology determines the strategies adopted. Since it takes approximately one minute from missile launch to target intercept at a range of 50 miles with a missile speed of Mach 5 (typical for such a missile), it can be seen that the target aircraft can be at an entirely different heading and orientation at missile lock and impact. This makes extreme manoeuvres unlikely in long range combat.

These descriptions of air combat make two major assumptions which are not necessarily true for modern air combat: that opponents detect each other *simultaneously* and begin manoeuvring to bring *identical* weapons to bear. It is the first of these assumptions that the concept of low-observability, or stealth, is designed to challenge.

Obviously, if an opponent can be engaged without counter-detection the initial manoeuvring becomes much simplified; the pilot simply manoeuvres to achieve a firing position and releases the weapon. The technology to achieve such a situation is generally concentrated on the reduction of the radar cross-section (RCS) of the aircraft and, equally importantly, the reduction of radar and infra-red emissions from the aeroplane. The former of these approaches is often apparent from the external shape of a modern aircraft. Figure 1.3 depicts the B-2A Spirit which demonstrates these stealthy characteristics.

The B-2 was designed as a strategic penetration bomber and hence low-observable characteristics were integrated into the design for reasons that differ to those stated above. Stealth was of paramount importance to allow the aircraft to fly undetected into heavily defended airspace before dropping its payload. The first thing to note is that all leading and trailing edges have identical sweep angles (33°), and furthermore all control surface hinge lines, air intakes and exhausts also have the same sweep. This quality is introduced to reduce the number of locations that a radar transmitter / receiver could be positioned and obtain a significant return. Specifically, for a strategic bomber such as the B-2 or an attack aircraft such as the F-117 (Figure 1.5), it is important that the aircraft's target and defences are unaware of the aircraft's approach, thus enabling a

successful mission. This scenario is depicted in Figure 1.4. There is also a characteristic 'double-W' trailing edge. Such discontinuities along the trailing edge of stealth aircraft are also present on the on the F-117A, the only other 'stealth' aircraft currently in service. To reduce radar returns from the engine fan the engines are fed by S-shaped ducts.

However, such external peculiarities form only a part of such an aircraft's efforts to avoid detection. Built into the wing surface is a copper mesh which acts as an antenna, absorbing the radar energy and emitting it as heat. The honeycomb which makes up the primary structure is also radar absorbent and has identical angles to the leading and trailing edge sweeps, similarly to reduce the number of directions from which a significant return can be detected.

Infra-red signatures have also been reduced by thoroughly mixing hot exhaust gases with cooler air and, as has been previously mentioned, electromagnetic emissions from the aircraft's own sensor suite are designed to reduce the chance of detection and are strictly monitored. In addition, electronic defensive aids reportedly (Lambert-1994) include active cancellation of radar returns.

However, the value of stealth properties should not be over-emphasised. Stealth is simply another criteria to optimise alongside other important considerations such as manoeuvrability, thrust, payload and, of course, cost. For an aircraft such as the B-2 where manoeuvrability is not of prime importance for mission success, stealth technology can be given a free rein and non-stealthy items such as fins discarded. The

B-2 was also designed during the 1980s when the cost of such an aircraft was of less concern in light of the on-going cold war. Subsequent events have reduced the number ordered such that the cost is now approximately $2.1 billion per aircraft.

For a future air-superiority or strike aircraft, stealth properties alone will not be sufficient. Stealth is much less important in short range combat when compared to the significant advantage that it can imbue at medium and long range. The aircraft must therefore be able to achieve the extreme manoeuvres required for successful short range encounters described earlier.

However, when a stealthy aircraft manoeuvres to the high angles of attack required for short range combat it is possible that large amounts of flow induced excitation (buffet) would be encountered. Should the frequency distribution of the buffet overlap with one or more structural modes then significant response of the structure (buffeting) may result. This is clearly undesirable and may result in a reduction of the flight envelope and/or in-service repair or replacement modifications. Such problems have been encountered in the past, particularly with reference to the fins of combat aircraft. A specific problem was encountered with the twin-fin F-18, where accelerations experienced at the fin tip were of the order of 500g (Mabey-1991). This problem was solved by a dual approach. Strakes were added to alter the vortex track and the stiffness of the fin structure was increased to separate the frequency of the excitation and the natural frequency of the fin. Both of these approaches are unsatisfactory if a similar problem is encountered on a low-observable aircraft toward the end of the design process. The addition of strakes to a stealthy aircraft has a prohibitive RCS penalty and

the complexity of the internal structure described earlier makes increases in structural strength costly from a weight, and hence performance, perspective.

It is therefore desirable to predict buffet loads during the early design stages of an aircraft such that they can be accounted for from both strength and fatigue viewpoints during the detailed design process. However, initial prediction of buffet loads currently relies on experience of the levels of buffet over aircraft already in service. For example, buffet information for EF-2000 was estimated after consideration of the buffet loads experienced by the Tornado. There is currently no experience of the buffet encountered by a low-observable aircraft and it was felt that a more scientific method of estimating the buffet loads over such an aircraft was required. Such a method was likely to take advantage of the ability of contemporary steady state Computational Fluid Dynamics (CFD) codes to accurately predict vortex strength and track. It was with this aim in mind that the EPSRC research programme GR/J86902, on which this thesis is based was instigated.

1.2 Literature Review

1.2.1 Basic Flow Topology

Figure 1.5 depicts the F-117A 'Nighthawk' aircraft which entered service with the US Airforce in 1981. As can be seen from this diagram, the planform consists of a delta wing with a highly modified trailing edge and sharp leading edges, and hence the

consideration of flows over delta wings is of primary importance when analysing the flow over low observable aircraft.

The unusual flow topology over delta wings has been recognised since the early 1960s when Hall (1961,1966) and Harvey (1962) outlined the basic flow features depicted in Figure 1.6. When set at an angle of attack, the boundary layer from the lower surface of the wing flows outward and separates from the leading edges (provided that they are sufficiently sharp). This separation yields a pair of shear layers which curve and roll up into a pair of vortices situated above the wing. The identities of the discrete shear layers are rapidly lost due to viscous effects (Hall-1961) and the path of a typical fluid particle describes a spiral. The rolled up shear layers spiral inward to form a 'core' which can be defined as the region containing most of the vorticity (Leibovich-1984) or the region where the flow is nearly axisymmetric (Hall-1961). The radius of the core increases in the axial dimension, with the circulation of the vortex increasing approximately linearly with the distance along the axis due to continuous feeding of vorticity into the region of the core. Simultaneously, the axial component of velocity increases to more than double the free stream velocity. This phenomenon is explained by the fact that the pressure gradient in the direction of the spiralling path is negative, although not large, and hence a fluid particle in the core is subject to a continuous accelerating force. The axis of the core is located approximately one core diameter above the lifting surface.

The strength of the leading edge vortex system increases with increasing angle of attack, becoming a dominant flow feature. The pressure distribution over the surface of the wing is significantly affected by the structure, with regions of low pressure created

under the vortex core. These are referred to as 'suction peaks'. This phenomenon is responsible for so called 'vortex' lift, which is dependent on the leading edge sweep and can amount to approximately 30% of total lift (Nelson and Visser-1990).

The adverse pressure gradient in the region of the wing outboard of the leading-edge vortex core causes a secondary separation, depicted in Figure 1.7. The free shear layer which originates at the secondary separation line also rolls up in a manner similar to the leading edge primary vortex, but with vorticity of opposite sign. Secondary separation is a more prominent phenomenon for wings with lower sweep angles (Hoeijmakers-1990). Tertiary separations have also been reported (Del Frate et al.-1990).

The location of the core of the leading edge vortex has been shown to be independent of Reynolds number (Lambourne and Bryer-1962), but compressibility can have a significant effect on the flow topology over delta wings. Erickson et al.-1989 undertook a comprehensive study of the effect of free stream Mach number on the flow over a cropped delta wing with leading edge sweep of 65°. It was discovered that the magnitude of the suction peak reduced, due to a reduction in strength of the leading edge vortex, and the location of the vortex core moved inboard as the Mach number was increased.

Transonic flow was first apparent at a free stream Mach number of 0.60, with pockets of supersonic flow present under the core of the leading edge vortex. Surface flow patterns revealed a cross-flow shock, although this was not strong enough to prompt the boundary layer to separate. As the Mach number was increased beyond 0.80 the shock

caused boundary layer separation, resulting in a large motion of the secondary separation.

1.2.2 The Vortex Burst Phenomenon

A stable vortex with an orderly structure can persist, depending on the sweep angle, up to incidences as high as 25° to 35°. Above this angle of attack, a phenomenon known as *vortex burst* or *vortex breakdown* occurs. Vortex burst can be defined as an abrupt change in the structure of the core of an axisymmetric flow which, before the breakdown, had a large amount of swirl. It is characterised by:

- Retardation of the flow along the axis, taking place within an axial distance of approximately one core diameter.
- Divergence of the stream surfaces near the axis of the flow.
- Stagnation of the flow due to the retardation and appearance of a region of reversed flow on the vortex axis.

During the breakdown the flow field undergoes a dramatic change; the axial velocity profile acquires a wide wake like profile while the tangential velocity distribution becomes flatter with the maximum value placed further outwards in relation to the vortex axis than before the breakdown (See Figure 1.8). This causes loss of lift and reduction in the nose down pitching moment. The evolution of the magnitude of the suction peaks is well documented (Lambourne and Bryer-1962) and the position of the

burst can be estimated by considering the changes in the 'half-width' of the suction peaks (Greenwell and Wood-1992). The rate of change of the half-widths at a given chordwise location with incidence is discontinuous as the burst crosses the location (See Figure 1.9).

The influence of wing geometry and its orientation in reference to the free stream flow on the location of the vortex burst has been investigated by Lambourne and Bryer (1962), Peckham (1961) and many others. The following characteristics are generally agreed:

- For a given configuration the position of the vortex burst depends on the angle of attack. As the incidence is increased the burst appears at the trailing edge of the wing. It then moves toward the apex as the angle of attack is increased further, reaching the apex as the wing stalls (See Figure 1.10). The structure of the leading edge vortex is then replaced by a bluff body type vortex shedding.
- For a given angle of attack, the burst takes place closer to the apex of wings with lower sweep (See Figure 1.10).
- When a wing is yawed the vortex breakdown occurs earlier on the advancing side whereas on the retreating side it is delayed (See Figure 1.11).

Attempts have be made to predict burst location as a function of incidence and sweep (Lambourne and Bryer-1962), the swirl angle based on the perpendicular and axial velocity along the leading edge (Lee and Ho-1990), the circulation of the leading edge vortex (Jumper et al.-1993) and the rate at which vorticity is fed into the leading edge

vortex (Gursul-1995). These are of limited value with measurements of the burst position varying due to the unknown interference of the test rigs and differing turbulence levels of tunnels or simply due to the subjective judgement of an investigator who determines the location of the burst from flow visualisation data. Nelson and Visser (1990) showed that secondary vortices can burst in the same way as the primary leading edge vortices.

Two forms of vortex breakdown have been observed over delta wings, and are generally referred to as 'spiral' and 'bubble' modes (See Figure 1.12). Two further modes have been noted in vortex tubes. Experimentation by Sarpkaya (1971a, 1971b) was concerned with the visualisation of these modes by means of injecting dye into the vortex centre line at varying conditions of swirl and axial velocity.

The spiral mode appears at lower levels of swirl. It is asymmetric and consists of an abrupt deceleration and deformation of the axial filament into a spiral. This spiral persists for a small number of turns before breaking up into turbulence. The bubble mode appears to be an axisymmetric form which is apparent at higher levels of swirl. The core of the vortex decelerates to a standstill with the outer streamlines expanding as if surrounding a solid body. Behind the stagnation point a bubble of recirculating fluid forms, followed by a few spiral turns and transition to turbulence.

The existence of these two modes is the subject of much debate, with opinion divided as to whether the modes are distinctive forms or simply different aspects of the same phenomenon. Leibovich (1984) suggested that the spiral and bubble forms are indeed

different. The measured values of the core expansion ratio (the ratio of the core diameter in the wake to the core diameter in the approach flow) are significantly higher for the bubble form of breakdown. Also, the axial location of the bubble form is located upstream of the position of the spiral mode if conditions are changed to alter the mode.

It seems that the bubble mode only is present under carefully controlled axisymmetric conditions (Escudier-1984). Therefore it seems likely that the spiral mode is a side effect of non-axisymmetric disturbances in the flow. The flow over a delta wing is necessarily non-axisymmetric due to the continual feeding of the vortex sheet from one side.

There are currently no generally accepted theoretical explanations of vortex breakdown over a delta wing. This is, in part, due to the difficulties in obtaining experimental data of both the steady and unsteady velocity and pressure distributions in the region of the vortex burst, enabling predictions of the theories to be judged. The burst phenomenon has been found to be hyper-sensitive to disturbances in the flow, with the insertion of probes of any kind into flow near the burst immediately moving the burst location upstream of the disturbance. Interference to the flow from model mountings have also led to significant variations in the location of the burst (Gursul-1995).

Generally, theoretical studies assume that the flow is inviscid, thus neglecting the effect of Reynolds number on the breakdown. They all agree, however, that the ratio of the swirl to axial velocity plays an important part in vortex breakdown and that adverse pressure gradients promote the breakdown (Hall-1972, Sarpkaya-1974). The degree of

divergence and the upstream conditions also have an effect. Theories can be loosely grouped into two classes, although the two are not mutually exclusive. The former of these classes comprises critical state theories, where breakdown is related to the onset of some critical condition. The second group contains wave propagation and instability theories, which associate the breakdown with amplification and decay of disturbances.

The predominant assumption made in theoretical studies of vortex breakdown has been to ignore asymmetric features; thus theories are more representative of the axisymmetric case present in vortex tube experiments than the flow over a delta wing which is asymmetric due to the continual feeding of the shear layer from the leading edge. Asymmetries are therefore assumed to result from the instability of the basic axisymmetric form to asymmetric disturbances (Benjamin-1962).

The first attempt to describe vortex breakdown as the reaching of a critical state was made by Benjamin (1962,1967) and supplemented by the more rigourous derivation of Fraenkel (1967). Their model was analogous to that of the phenomenon of 'hydraulic jump' in open channel flow.

For a uniform flow of liquid in an open channel there are two possible states, known as subcritical and supercritical, meaning that the Froude number,

$$F = \frac{u}{\sqrt{gh}},$$

is less than or greater than unity, respectively. Here, u is the horizontal velocity, h the fluid depth and g the acceleration due to gravity. A difference between the two states is

in their capability to support infinitesimal standing waves, these being possible only on a subcritical flow.

If an external force is applied to a subcritical flow one of two things can result (See Figure 1.13). If the force is small, a wave train may be created downstream of the disturbance, with the 'wave resistance' equal to the force applied. If the force is larger, the flow may transition to a supercritical state with reduction in 'flow-force', defined as:

$$S = \rho\left(u^2 h + \frac{gh}{2}\right),$$

equal to the force applied. S is therefore greater for a subcritical flow.

Conversely, a supercritical flow can spontaneously 'jump' to a subcritical state (See Figure 1.14). If the transition is mild, where the upstream Froude number is not much greater than unity, waves develop behind the transition so that eventually a steady wave train is established on the subcritical flow. For strong transitions, however, the large excess of flow-force results in a violently unsteady motion leading to 'breaking' of the water's surface; thus the flow becomes very turbulent at the point of transition. An intermediate case between these two extremes is also possible, with a breaking wave occurring slightly upstream of an undular breakdown. Such spontaneous jumps are only possible 'where the situation downstream is capable of bearing the subcritical state of flow that would be developed in the rear of the jump' (Benjamin-1962).

Benjamin assumed that the stream function, ψ, consisted of a stationary axisymmetric perturbation on a steady state, axisymmetric swirling flow,

$$\psi(x,y) = \psi_0(y) + \varepsilon\phi(y)e^{\gamma x}.$$

It was shown that ϕ must be a solution of a second order differential equation for which there is an infinite set of real eigenvalues, γ^2, which allow the solutions for ϕ to satisfy the boundary conditions of the flow. The flow was shown to be supercritical when all eigenvalues are positive and subcritical when at least the first eigenvalue is negative.

It was also shown that there are an indefinitely large number of 'conjugate' pairs of solutions of the stream functions, say ψ_A and ψ_B, which satisfy the conditions prescribed by the original flow, and which coincide at their end points (See Figure 1.15). A similar quantity to flow-force in channel flow was introduced and vortex breakdown was explained in terms of a transition between the state of minimum flow-force (i.e. supercritical) flow and its 'adjacent' subcritical state.

Mager (1972) associated vortex breakdown with the failure of the quasi-cylindrical approximation of vortical flow, where a singularity appears at a point in the flow. The solution upstream of the singularity is double valued, with initial conditions determining the solution branch. Mager postulated the possibility of a 'crossover' from the upper to the lower branch when a singularity was present. This is similar to Benjamin's 'finite jump between adjacent states', and it was shown that the condition for its occurrence coincides with Benjamin's (1962) critical condition. Furthermore, Mager demonstrated

that the upper and lower branches were supercritical and subcritical respectively. Further examination of the 'flow-force' led Mager to conclude that 'finite transitions' and 'crossovers' are equivalent.

Squire (1960) was the first to propose a theory based on wave propagation. He suggested that perturbations could propagate upstream from a downstream disturbance. However, it has been pointed out (Benjamin-1962) that the standing waves considered by Squire can only form to the rear of a disturbance and cannot propagate upstream.

The concept of waves propagating upstream was refined by Randall and Leibovich (1973). They envisaged a downstream disturbance producing axisymmetric waves which then propagate upstream, with the wavelength reducing and the disturbance being amplified due to the flow geometry (a diverging duct). The breakdown was modelled as a 'trapped' solitary wave, its move upstream amplified by the geometry of the flow and at the same time dissipated by viscous effects. The necessity of viscous effects was a shortcoming, since vortex bursts have been noted in flows with extremely low Reynolds numbers. However, later refinements (Leibovich-1985) took into account interactions between axisymmetric and asymmetric modes allowing a further area for energy exchange. Also, although the theory is valid for weak disturbances, the disturbances predicted for vortex breakdown are necessarily large.

Instability theories investigate the amplification or decay of infinitesimally small disturbances superposed on the mean flow under investigation. The theories are based on linear stability analysis applied to the axisymmetric Navier-Stokes equations.

Lessen et al. (1974) and Lessen and Paillet (1974) investigated the stability of an axisymmetric wake to asymmetric disturbances. The wake that they examined was representative of a trailing vortex from an aircraft. Disturbances to the mean velocities and pressure of the form,

$$e^{i(\alpha x + n\phi - \alpha c t)}$$

were examined where α is the axial wave number, n the azimuthal wavenumber of the Fourier disturbance, c is the complex phase velocity and is equal to c_r+ic_i and ϕ the azimuthal co-ordinate.

Expanding the exponent gives,

$$e^{i(\alpha x + n\phi - \alpha c_r t) + \alpha c_i t},$$

Hence the growth rate of the disturbance is αc_i and the frequency of the disturbance is - $2\pi / \alpha c_r$.

It was found that as the swirl parameter, q, was continuously increased from zero, the disturbances died out quickly for all positive azimuthal wavenumbers. However, for negative values of n (i.e. those with helical wave paths opposite in sense to the wake rotation) the amplification rate increases and then decreases (See Figure 1.16) with axial wavenumber. It was found that all wavelengths became damped at levels of q greater than approximately 1.5. This is in contrast to experimental flows (Garg and Leibovich-1979) where vortex burst is apparent even at very high levels of swirl. Lessen and Paillet (1974) also considered the effect of Reynolds number on the stability of the flow and found that viscous effects acted to damp out perturbations. This analysis

was carried out in a different manner by Stewartson (1982) and Leibovich and Stewartson (1983) for the higher azimuthal wave numbers ($|n| \geq 3$) with similar results.

More recently Khorrami (1991) investigated the viscous modes of instability in trailing vortices. The inviscid results of Lessen et al. (1974) were confirmed. However, the growth rates calculated for viscous flows were orders of magnitude smaller than those for inviscid modes, in contradiction of Lessen and Paillet (1974).

Kribus and Leibovich (1994) studied the stability of strongly non-linear waves to three dimensional perturbations. They showed that the most unstable are the perturbations with azimuthal wave number $|n| = 1$, which is consistent with the experimental results of Garg and Leibovich (1979). Additionally, the results showed that the sense of rotation of the streaklines are not always the same, but are dependent on the basic flow (i.e. the initial conditions). This may explain some of the contradictory experimental results obtained using differing experimental apparatus.

Escudier (1988) suggested evidence that the instability is not the direct cause of breakdown. As mentioned earlier, inviscid analysis indicated that all disturbances would be damped for swirl parameters, q, larger than 1.5. However, in practice vortex burst is present even in flows with very high swirl (Garg and Leibovich-1979). Also, instability analysis indicates that the flow is less stable to asymmetric rather than axisymmetric disturbances. In contrast to these predictions, in carefully controlled conditions only the axisymmetric form of breakdown is present. Breakdown appears to be a sudden change, there is no evidence of continual growth of perturbations typical for such a

hydrodynamic instability. In addition, the spiral and bubble modes have been found to interchange under apparently steady conditions. Thus the instability of the spiral form would imply that the asymmetrically unstable flow might somehow stabilise itself to permit the formation of the bubble form. This seems unlikely in practice, unless prompted by transient effects in the flow.

It seems, therefore, that the instability is not the cause of the breakdown. However, the presence of such an instability does result in an important effect of vortex breakdown; the appearance of peaks in the velocity an pressure spectra downstream of the vortex burst. This phenomenon, together with further sources of unsteadiness in vortical flows, will be discussed in Section 1.2.3.

Vortex burst is an extremely complex topic, and has been the subject of much research over the past forty years. However, no generally accepted theory has been proposed that would enable the prediction of the vortex burst location. Additionally, due to the hyper-sensitivity of vortex burst to flow disturbances it has been extremely difficult for experimentalists to acquire accurate results to test the theories adequately. The advent of non-intrusive measurement techniques such as laser doppler anemometry (LDA) and particle image velocimetry (PIV) in recent years has awakened interest in the topic, and it seems likely that the next few years will see advances in both the theoretical and experimental study of the phenomenon.

1.2.3 Unsteadiness in Vortical Flows

A number of investigators including Rao (1990), Wood and Bean (1993) and Mabey (1991) indicate that the occurrence of vortex breakdown has serious implications for advanced, highly manouvrable combat aircraft. For example, Leading Edge eXtensions (LEX) increase the maximum lift coefficient obtainable on the F-18 fighter, thus increasing the survivability of the aircraft (Herbst-1983). The vortex that emanates from the LEX induces a high flow velocity on the suction side in a similar manner to that over a delta wing, enhancing the lift produced. However, fin buffeting occurs for angles of attack where the fins are immersed in the turbulent, energetic wake of the burst LEX vortex. It has been shown that large quasi-periodic structures are present in the breakdown wake, indicated in pressure and velocity spectra as well defined 'peaks'. If the frequency distribution of this aerodynamic excitation overlaps one or structural modes the resulting resonance can cause excessive buffeting, with accelerations experienced of up to 500g (Mabey-1991). This led to a restriction of the flight envelope until the problem was solved; a particularly costly procedure for the manufacturer, who may have to pay compensation, and potentially the pilot who may need to engage in combat in an aircraft with reduced capabilities. The problem was solved by a dual approach. Strakes were added to alter the vortex track and the stiffness of the fin structure was increased to separate the frequency of the excitation and the natural frequency of the fin. As was stated earlier, such approaches are unsatisfactory if a similar problem is encountered on a low-observable aircraft. Investigation of such unsteady loads are therefore of importance.

The quasi-periodic nature of flow caused by vortex breakdown was first noted by Cassidy and Falvey in 1970. However, no spectral analysis of the data was performed. This analysis was first performed by Garg and Leibovich (1979) on Laser Doppler Anemometry (LDA) measurements of velocity fluctuations accompanying vortex breakdown in a 'vortex tube'. Vortex tubes are often used to obtain experimental data regarding axisymmetric columnar vortices. The flow of such a system is simpler than that encountered over a delta wing, and the equipment is generally designed such that the axial and swirl velocities can be altered independently.

Radial traversing showed that locations with the largest peaks in the velocity spectra were located near the edge of the vortex core although both spatial and spectral resolution were poor. Power spectra of both axial and swirl velocities were presented, with maxima in the spectra of similar magnitudes and at the same frequencies for each component. Peaks were found at two distinct frequencies which, within the (admittedly rather poor) frequency resolution of the spectra, were found to be harmonics (See Figure 1.17). The lower of the frequencies was found to compare well with that predicted by instability theory (Lessen et al.-1974, Lessen and Paillet-1974) for an azimuthal wave number of -1.

Spectral analysis of flow velocities have more recently been presented (Hubner and Komerath-1995) for a 59.3° delta wing at an incidence of 25°. Peaks in the spectra were found downstream of vortex breakdown, with the magnitude of the peak increasing and the frequency decreasing as the hot wire probe was traversed downstream. More

intensive testing, involving variations in speed and incidence, was undertaken at a single point. The peak frequency was found to scale linearly with freestream speed and, although the absolute peak spectral intensity increased with increases in incidence and freestream speed, the non-dimensionalised form of the spectral energy decreased with increased freestream speed.

Analysis of the unsteady pressure field over a series of delta wings (Gursul-1994) indicated that the frequency at which excitation was a maximum varied as the inverse of the streamwise distance from the apex at a constant angle of attack. However, the spatial resolution obtained was poor due to the small number of tappings at which pressures were measured (approximately 12 tappings / model). A similar investigation was undertaken (Rediniotis et al.-1993) over a delta wing with 76° sweep, with data acquired at 7 tappings. Peaks in the frequency spectra were experienced, with a single frequency peak noted at low angles of attack and two peaks at high ($\alpha > 70°$) angles of attack. One of the peaks experienced at large incidences was found to be due to alternate shedding of the vortex from the leading edge.

The shear layer that separates from the leading edge contains another potential source of unsteadiness. It had previously been noted (Brown and Roshko-1974) that in free shear layers originating at a splitter plate between two streams of differing velocity, the flowfield contained discrete vortices. Winant and Browand (1974) demonstrated that the growth of such shear layers was the result of a pairing process between two neighbouring vortices. They showed that the mutual influence of one vortex on the other caused them to begin to rotate around each other and merge to form a single

vortex of larger diameter. This process repeated itself until inhibited by the physical constraints of the apparatus. Gad-el-Hak and Blackwelder (1985) discovered a similar phenomenon in the free shear layer of a leading edge vortex. The shear layer was viewed by injecting dye along a slot at the leading edge of a 60° delta wing. A vertical sheet of laser light was then shone perpendicular to the axis of the leading edge vortex. Vortices parallel to the leading edge were found to extend along the entire length of the edge. The trajectories of the vortices followed the general outline of the feeding sheet of the leading edge vortex. Along this course, pairs of vortices rolled around each other and merged in a similar fashion to that described previously (See Figure 1.18). The frequency of shedding of the vortices was proportional to the square root of the Reynolds number of the free stream flow at constant incidence, and was found to decrease with increasing incidence. It has also been reported that these small scale vortical structures form a stationary helix (Washburn and Visser-1994), with some research (Reynolds and Abtahi-1989) indicating that the two forms interchange as free stream turbulence and speed are altered.

1.3 Objectives of Research Programme

Existing design techniques for the preliminary prediction of buffet loads are simplistic at best and are often based on prior project experience, of which there is little for the next generation of military aircraft which have low-observability as an important design parameter. The requirement for such planforms to exhibit 'stealth' characteristics places an additional burden on the predictive capability since these aircraft will be less

amenable to conventional 'fixes' such as strakes and vortex generators due to the RCS penalty of such devices. Structural modifications to increase the stiffness of such aircraft are also more difficult than for a conventional aircraft since the internal structure is also constrained by low-observability criteria.

Recent work at the University of Bath (Wood and Bean-1993) suggested that contemporary time-averaged computational fluid dynamics (CFD) codes could be used to predict vortex track with empirical relationships being utilised to predict the characteristic frequency and amplitude of the unsteady pressure oscillations.

The objectives of the programme were therefore:

- To develop a model manufacture technique with the capability to produce wind-tunnel models instrumented with pressure tappings, dedicated unsteady pressure transducers and accelerometers quickly and at minimum cost.

- To acquire extensive buffet data over a range of planforms containing features likely to be encountered on future low observable combat aircraft. These planforms were defined by British Aerospace (Military Aircraft Division, Warton).

- To derive semi-empirical parameters such that both the frequency and amplitude of buffet over the surface of the wing could be predicted from the time averaged pressures, whether derived experimentally or by utilising a CFD code.

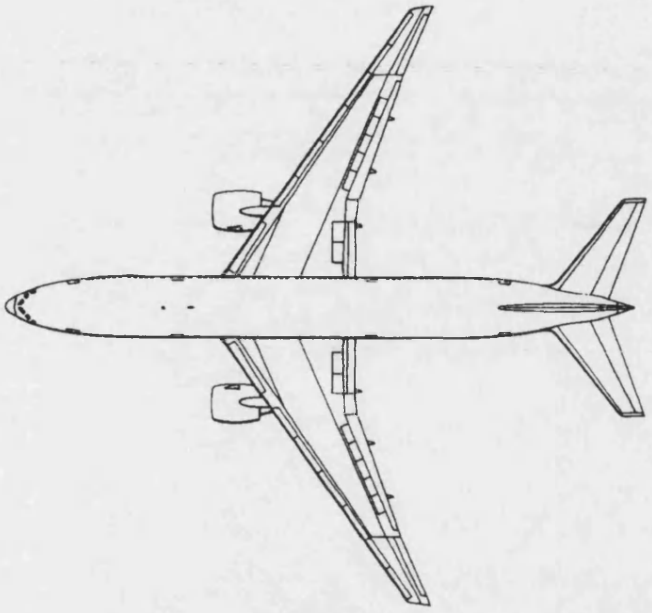

Figure 1.1a:Boeing 777

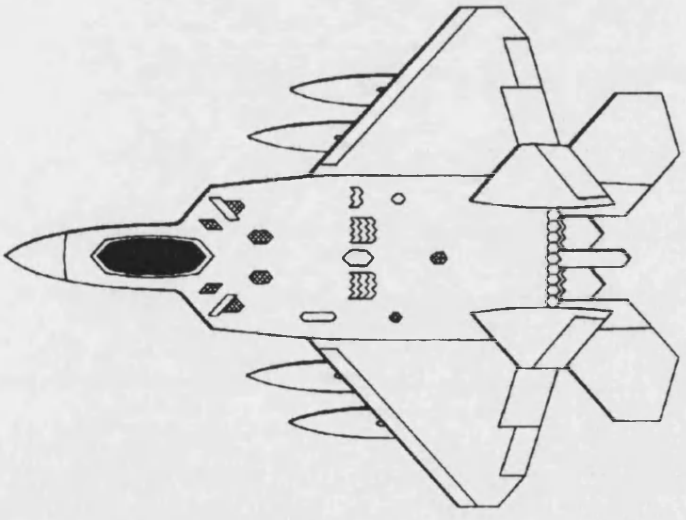

Figure 1.1b: Lockheed- Martin F22A

Figure 1.1 Comparison of Modern Military and Civil Aircraft Planforms

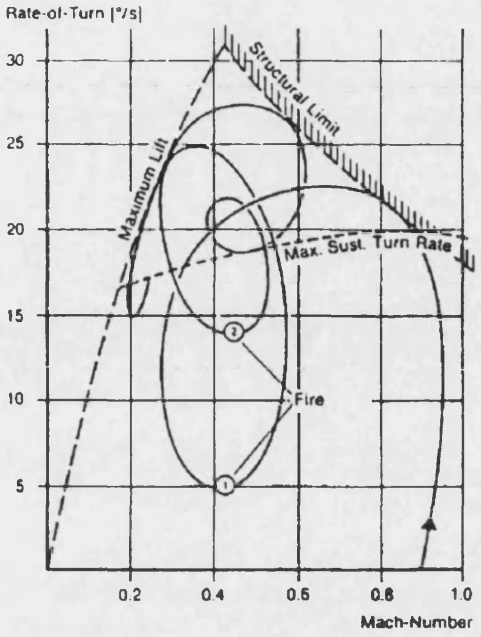

Figure 1.2: Manoeuvring in Short Range Combat
(Herbst-1983)

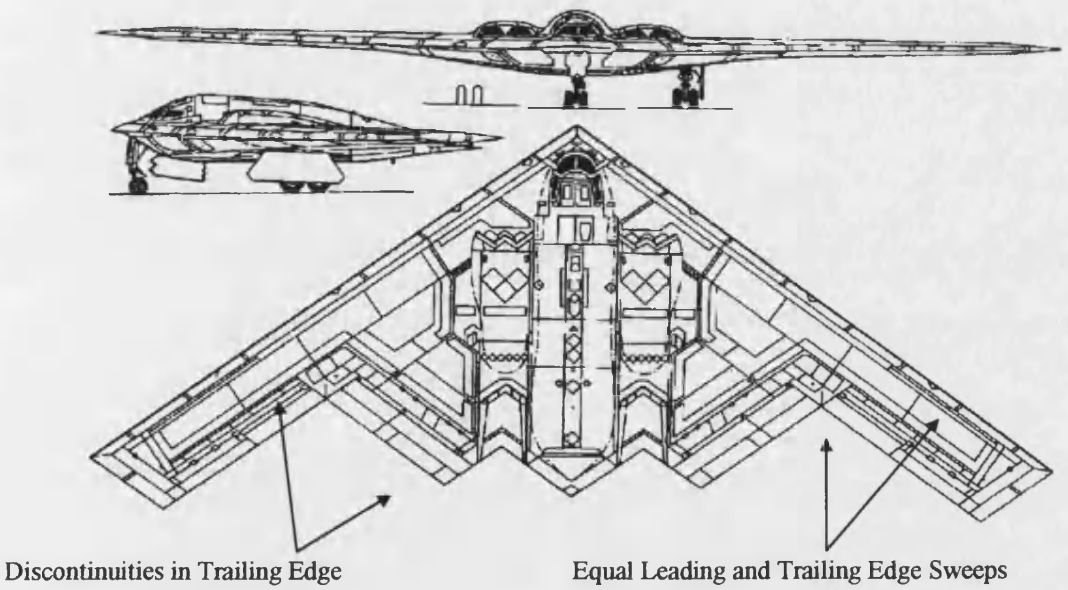

Figure 1.3: The B2A Spirit

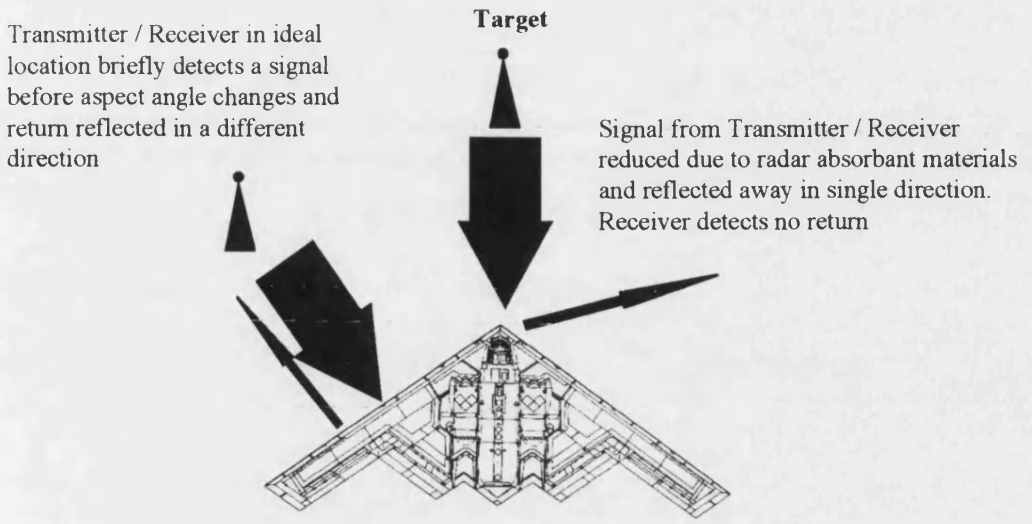

Figure 1.4: Reflection of Radar Signals

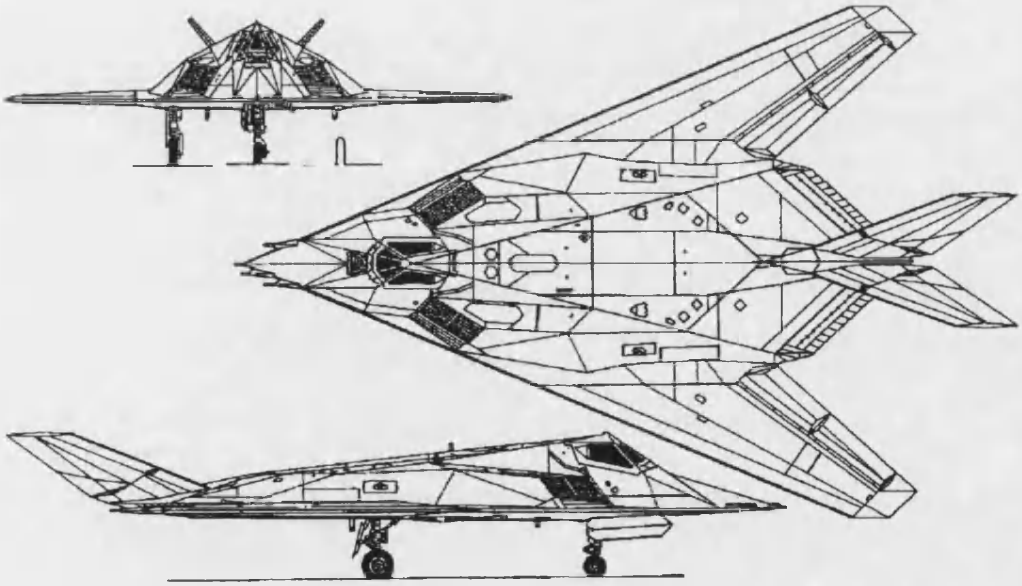

Figure 1.5: The F117A Nighthawk

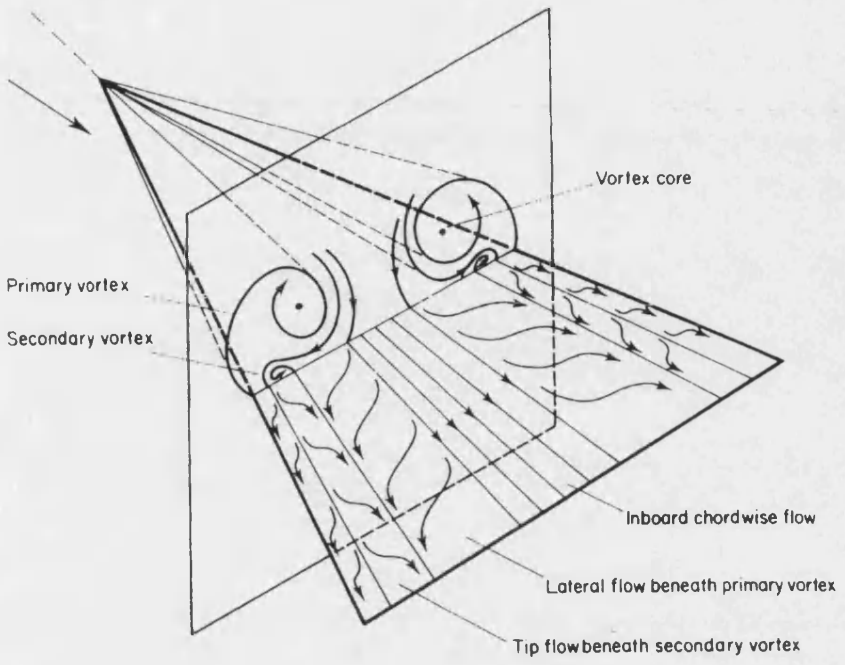

Figure 1.6: Flow Topology Over a Delta Wing
(Houghton and Carpenter-1993)

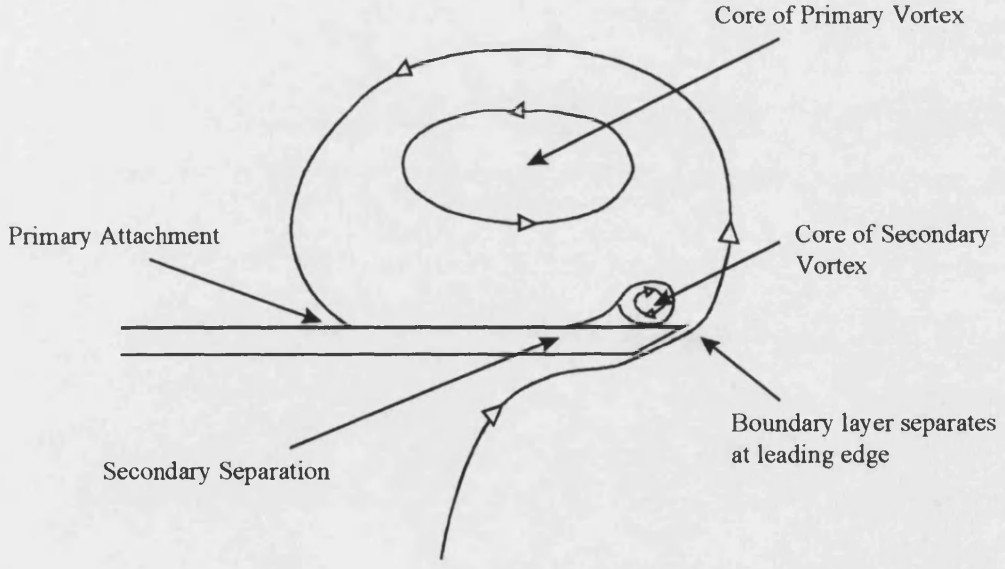

Figure 1.7: Separations and Attachments of a Leading Edge Vortex

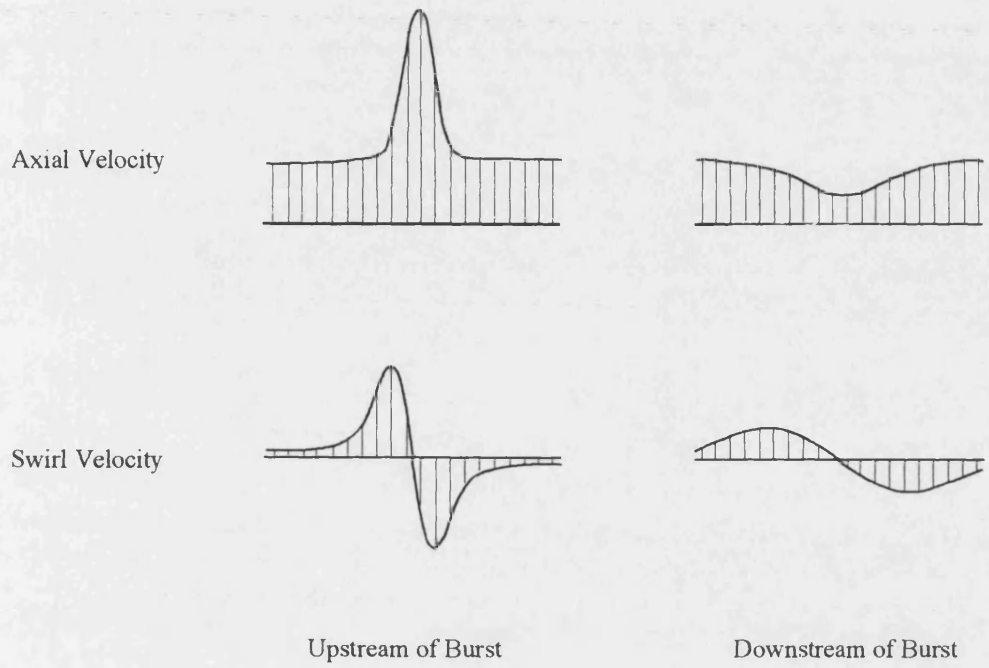

Figure 1.8: Velocity Profile Before and After Vortex Burst

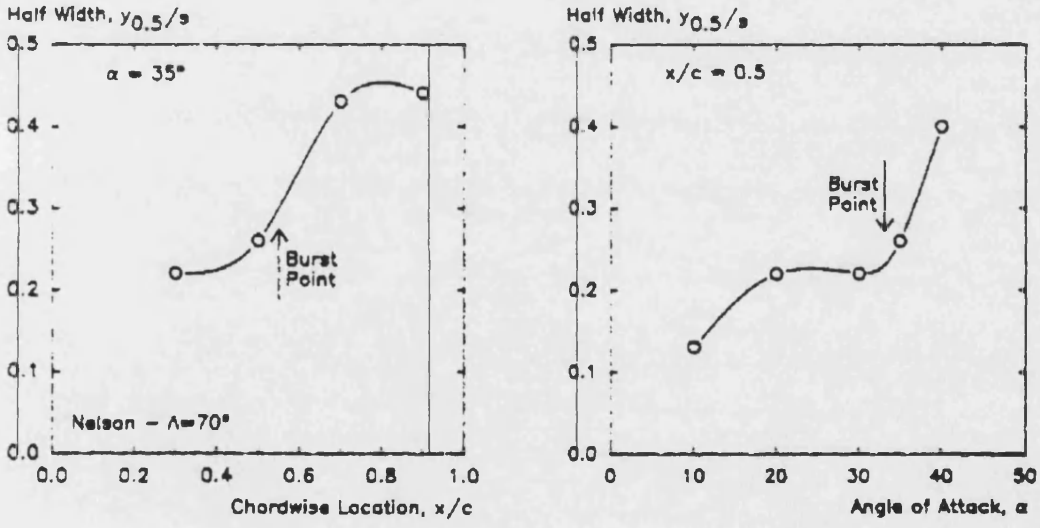

Figure 1.9: Variation of Half Widths of Suction Peaks
(Greenwell and Wood-1992)

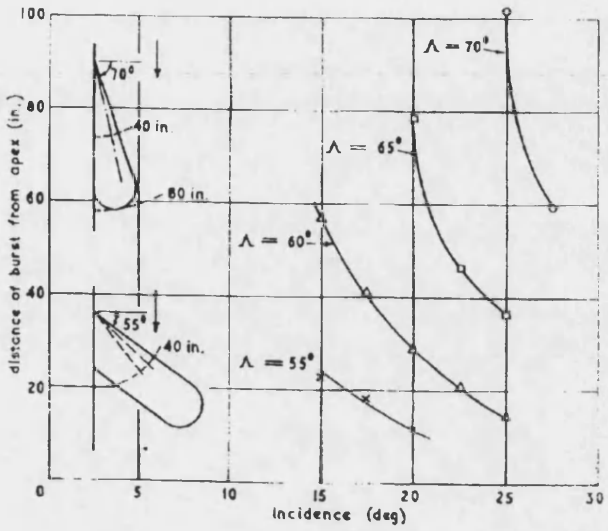

Figure 1.10: Variation of Burst Position with Incidence and Sweep Angle
(Lambourne and Bryer-1962)

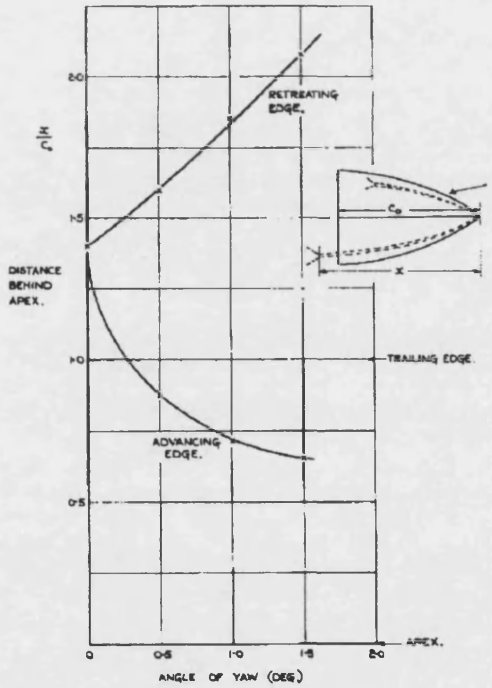

Figure 1.11: Variation of Burst Location with Yaw
(Peckham-1961)

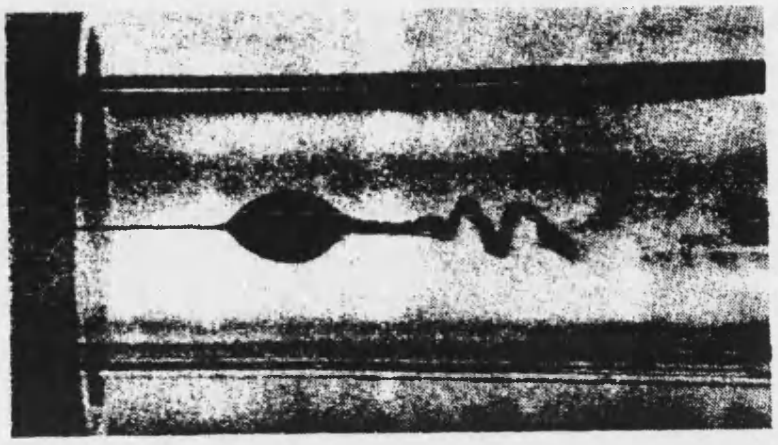

a: Bubble Mode

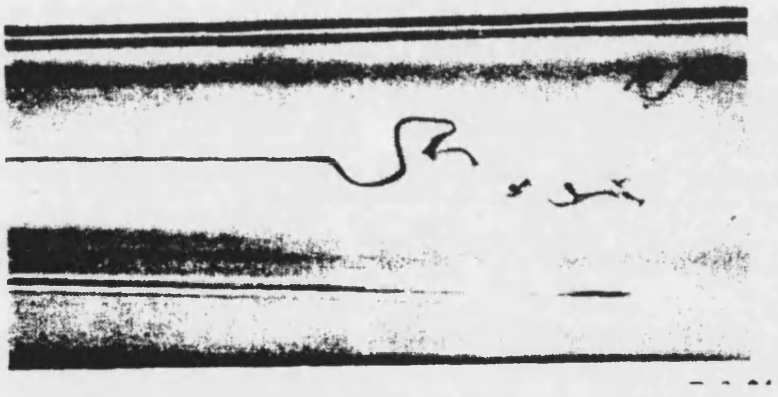

b: Spiral Mode

Figure 1.12: Models of Vortex Breakdown
(Faler and Leibovich-1977)

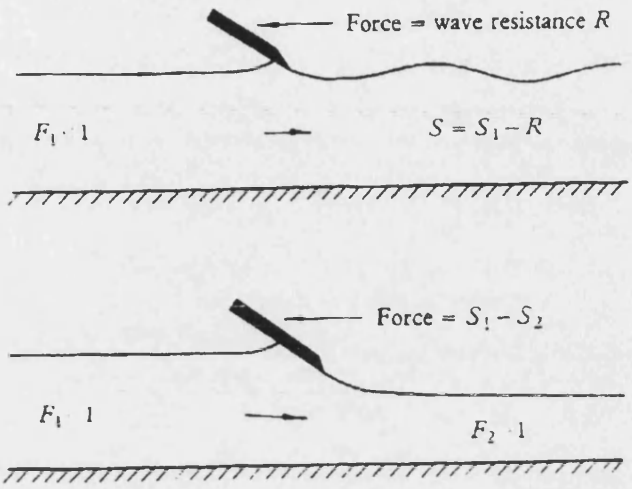

Figure 1.13: Effects of an External Force on a Subcritical Flow
(Benjamin-1962)

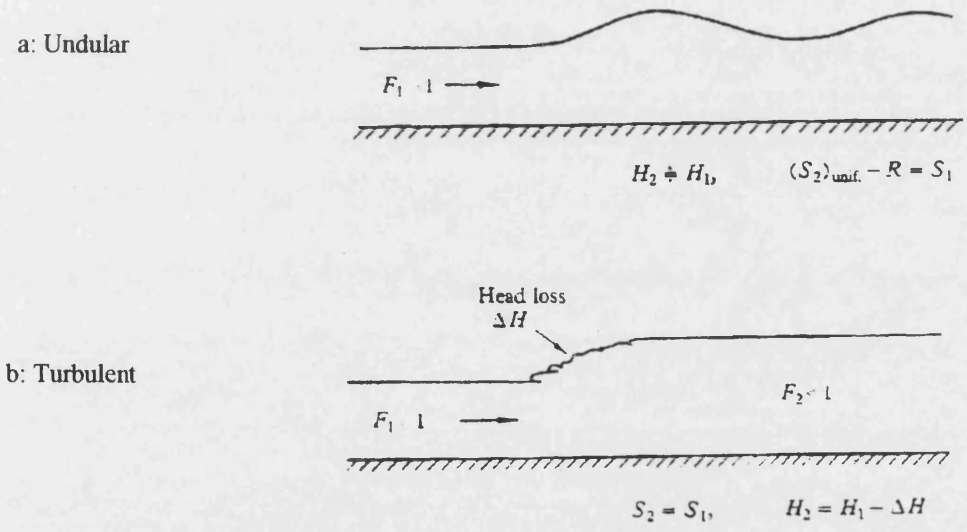

Figure 1.14: Hydraulic Jump
(Benjamin-1962)

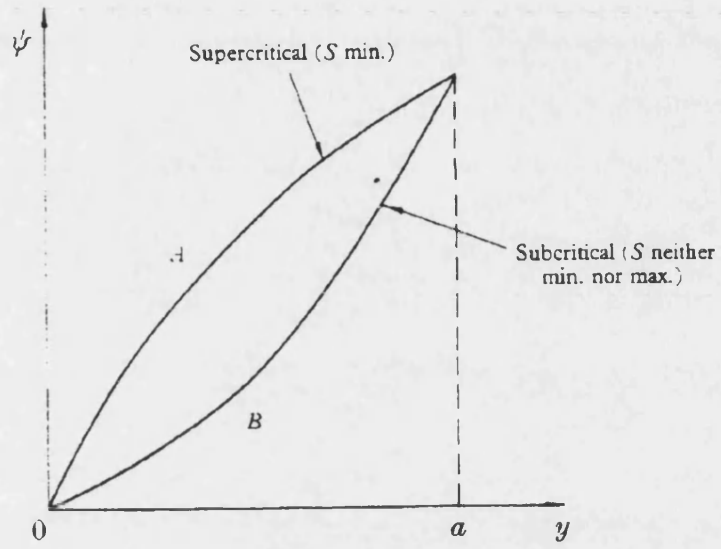

Figure 1.15: Conjugate Solutions

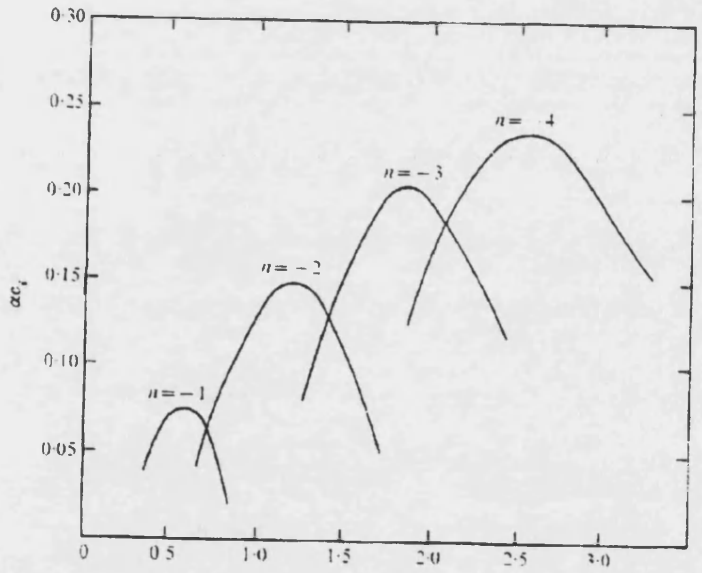

Figure 1.16: Variation of Growth Rate with Axial Wave Number at Constant Swirl (Lessen et al.-1974)

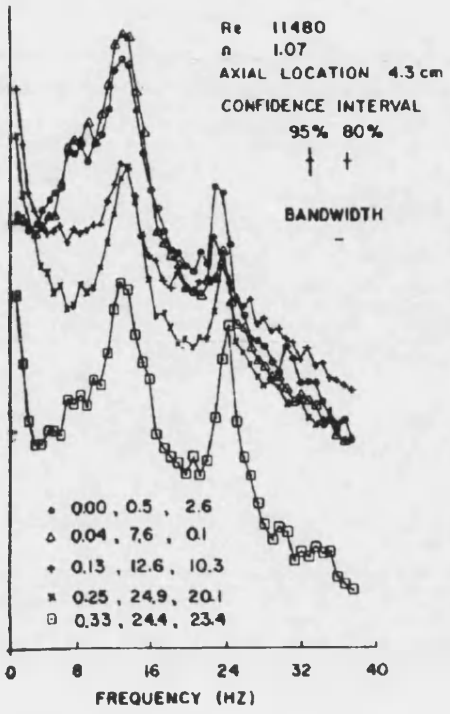

Figure 1.17: Spectral Content of Velocity Fluctuations in a Columnar Vortex (Garg and Leibovich-1979)

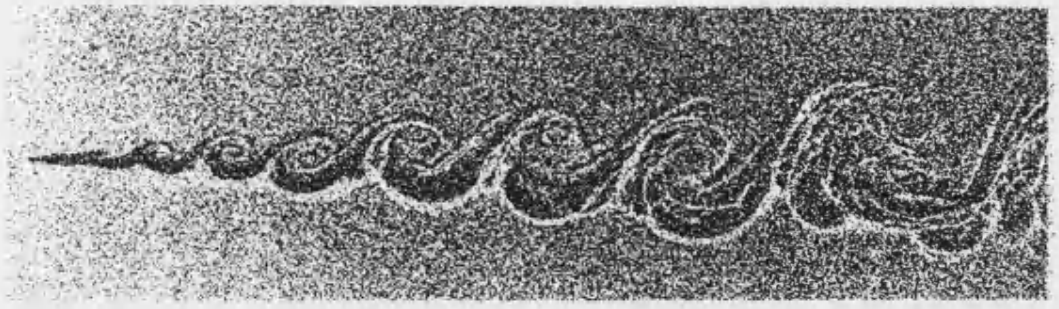

Figure 1.18: Vortex Pairing in a Shear Layer (Brown and Roshko-1974)

CHAPTER 2: EXPERIMENTAL APPARATUS

2.1 Wind Tunnel Facilities

Testing was undertaken in the 'high speed' section of the main wind tunnel facility at the University of Bath. This is a dual purpose closed return facility with a 'high speed' (maximum velocity 45 ms^{-1}) aeronautical working section and a 'low speed' (maximum velocity 12 ms^{-1}) working section and is depicted in Figure 2.1. The pressure drop across the contraction was measured by a digital micromanometer. The variation of the free stream dynamic pressure at the centre line against this pressure drop was measured using a pitot-static tube. Centreline turbulence intensity had previously been measured with a hot wire probe (Greenwell-1993). At typical test conditions the turbulence intensity (U_{RMS}/U_{∞})was of the order of 0.5% and the Reynolds number in the working section was 2.0×10^6 / m.

A six component balance was installed above the wind tunnel. Forces and moments were measured using a load cell system. The balance could be 'locked' mechanically, ensuring that there was minimum motion of the model when unsteady data (buffet/buffeting) were being measured.

Total turntable rotation available in the facility was +200° to -140° and was achieved through a stepper motor, gearbox and drive pinion mounted to the fixed earth frame. This allowed the turntable angle, and hence the incidence of the model, to be changed remotely. A magnetically operated brake was incorporated to eliminate gearbox backlash under wind on conditions.

2.2 Wind Tunnel Models

Four wind tunnel models fitted with extensive instrumentation together with at least one less complex model were required during the duration of the initial two year wind tunnel test phase of the project. The planforms of the models are depicted in Figure 2.2 and were specified by British Aerospace (Military Aircraft Division) Warton as having features likely to be present on future combat aircraft (See Chapter 1 for discussion of 'low-observable' combat aircraft). Models 3 and 4 were each tested in two configurations. The first was as depicted in Figure 2.2, with flow from the top of the diagram. The second was with flow from the opposite direction (i.e. with flow from the bottom of the diagram). These configurations were designated as Models 3* and 4* for Models 3 and 4 in the reverse configurations respectively. The dimensions of the planforms of the four models are depicted in Figures 2.3 to 2.6.

A cross section with constant radius convex lower surfaces and flat upper surfaces was decided upon. The flat upper surface was selected to simplify model manufacture and the lower (curved) surface was chosen to minimise camber and

chamfer effects yet allow sufficient thickness for instrumentation to be installed. The maximum root thickness of each model was set at 50 mm, since this was the thickness of the styrofoam utilised. The thickness to chord ratios of the four manufactured models were therefore different. The thickness to chord ratio of Model 4 was the smallest at 4.9%. Model 1 was the thickest model, with a thickness to chord ratio of 7.2%. It was estimated that such models, if constructed from aluminium using standard methods, would require approximately six months each to manufacture. Hence another construction technique was required.

The method developed utilised simple modelling techniques to construct a model with a light Styrofoam core and composite (glass fibre/epoxy, carbon fibre/epoxy) skins to produce a light, yet extremely strong model. The Styrofoam core was first cut from 50 mm thick sheet. This was then marked with tapping and transducer locations together with routings for the Scanivalve tubing (See Figure 2.7), before being placed, with the marked side face down, on a template of the planform required. The cross-section of the model was then cut; first roughly using a long bladed knife before being sanded to the required size with progressively finer sandpaper. The dimensions of the core were 2 mm less than the dimensions for the completed model to allow for the thickness of skins. Aluminium templates were utilised to ensure dimensional accuracy of the cores. A single skin of glass fibre/epoxy was then applied to the lower (curved) surface to make the model more robust. Vinyl Scanivalve tubes were laid into routes that had been melted into the Styrofoam core (See Figure 2.8). Tubing lengths were kept to a minimum to

maximise the unsteady signal that would be measured by the Scanivalve unit, and yet give sufficient tubing for easy tunnel installation. A tube length of 2.1m was typical.

A glass fibre/epoxy skin was then applied to the upper (flat) surface of the model, thus holding the tubing in position and increasing the rigidity of the model. Successive composite laminates were then added to increase the stiffness of the models. Glass fibre/epoxy skins were used on the upper surface with carbon fibre/epoxy skins utilised on the lower surface to give the models additional strength. The attachment of the models to the balance mechanism needed to be considered early in the design of the rig, since a method needed to be found of transferring load from composite skins to the metal support structure. This was achieved by a combination of two approaches: an aluminium 'root plate' together with four bars embedded into the model. The decision to use this dual scheme was taken to ensure that there was sufficient strength and rigidity at the mounting location when using the unfamiliar construction technique. The four bars can be seen bonded to the foam core in Figure 2.8.

A cross-section of the root of the models is depicted in Figure 2.9. It should be noted that the lower surface carbon fibre skin was wrapped around the root plate. This ensured that not all loads applied to the model were transferred by shear between the composite skin and a metal member, as would have been the case if the skin had not been compressed between the box section and the root plate.

When the required dimensions were achieved by addition and rubbing down of additional skins, the transducers and accelerometers were added to the model. Dimensional accuracy of the planforms was ±2.0 mm although as the construction technique was refined for later models, such as Models 3 and 4, accuracy was better than ±1.0mm. Each wind tunnel model was fitted with six unsteady pressure transducers (Entran model EPE-701-2P) and up to six miniature accelerometers (Entran model EGA-125F-25D). Pressure tappings were then made by drilling perpendicular into the surface of the model into the vinyl Scanivalve tubes (See Figure 2.5) with a 0.6 mm drill. Models had between 137 and 165 Scanivalve tappings.

These techniques enabled a fully instrumented model to be manufactured in approximately two months at greatly reduced cost. The models were extremely lightweight; models without tubing and pressure tappings had masses of approximately 3.0 kg. The majority of this was due to the root plate and the embedded bars. When fully instrumented with tubing, pressure tappings, transducers and accelerometers the models were approximately double the un-instrumented weight. This was largely due to the large number of tubes embedded in the model, together with the additional epoxy resin that was used to affix the tubes securely.

Models were sized such that balance load limits would not be exceeded. The models were deemed sufficiently stiff if they underwent a static defection of less than 1.0% of the model semispan when the maximum expected load (Hodgson and Woods-1994) was applied. Models were then loaded to double the expected static load to

ensure sufficient structural integrity, and were held at this load for a period of over an hour to ensure that there was no slow movement under sustained load.

A splitter plate of diameter 1.25 m with a rounded edge was utilised to act as a symmetry plane and to ensure that the models were outside the influence of the wind-tunnel boundary layers. The models protruded through the splitter plate, and a 5mm layer of grease was used as a seal to ensure that there was no leakage of air between the two sides of the splitter plate. This also had the advantage of isolating the model from any vibration of the splitter plate. This installation is shown schematically in Figure 2.11. A picture of a model installed in the 2.13m x 1.52m wind tunnel at the University of Bath is shown in Figure 2.12.

The outputs from the accelerometers were examined during testing to examine the frequencies of the structural modes of the models. The frequencies at which peaks in the buffeting response for the four models were experienced during testing are depicted in Table 2.1.

Model	1st Structural Frequency	2nd Structural Frequency
1	35Hz	63Hz
2	34Hz	56Hz
3/3*	32Hz	47Hz
4/4*	72Hz	100Hz

Table 2.1: Structural Modes of Installed Models

Although these structural frequencies were in the range at which buffet was expected, no evidence was found of the structural response of the models influencing

the aerodynamic loading. This was likely to be due to the low level of motion of the models during testing. Maximum RMS tip deflections, based on the response of tip mounted accelerometers, were 0.2 mm.

2.3 Instrumentation

Signals from the accelerometers, unsteady pressure transducers, transducers contained within the Scanivalve system and six component balance were acquired and stored by a Personal Computer (PC) based acquisition system utilising the software DT-Vee™ by Data Translation®. The Scanivalve system was also controlled by the computer. The system used is shown schematically in Figure 2.13. The Analogue to Digital (A/D) subsystem used was a DT2839 board by Data Translation®. This is capable of sampling up to 32 channels at rates of up to 416,000 samples/second for each channel. The same board was also capable of Digital to Analogue (D/A) conversion on 2 channels. This board was connected to the accelerometers via DC amplifier cards and a DT739 terminal panel, also supplied by Data Translation®.

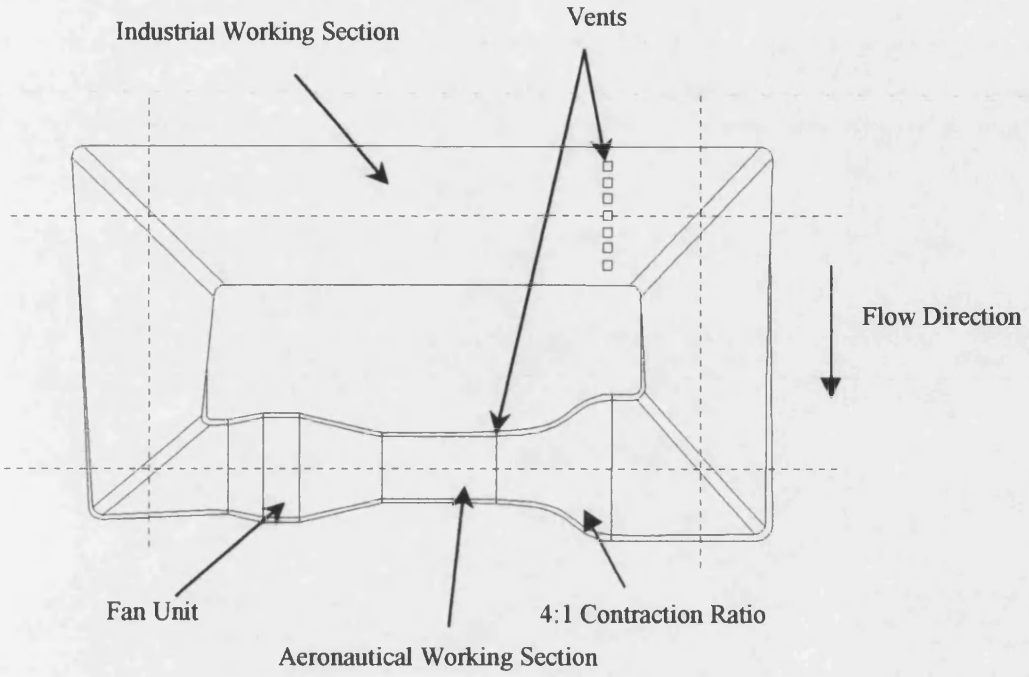

Figure 2.1: University of Bath 2.13m x 1.52m Wind

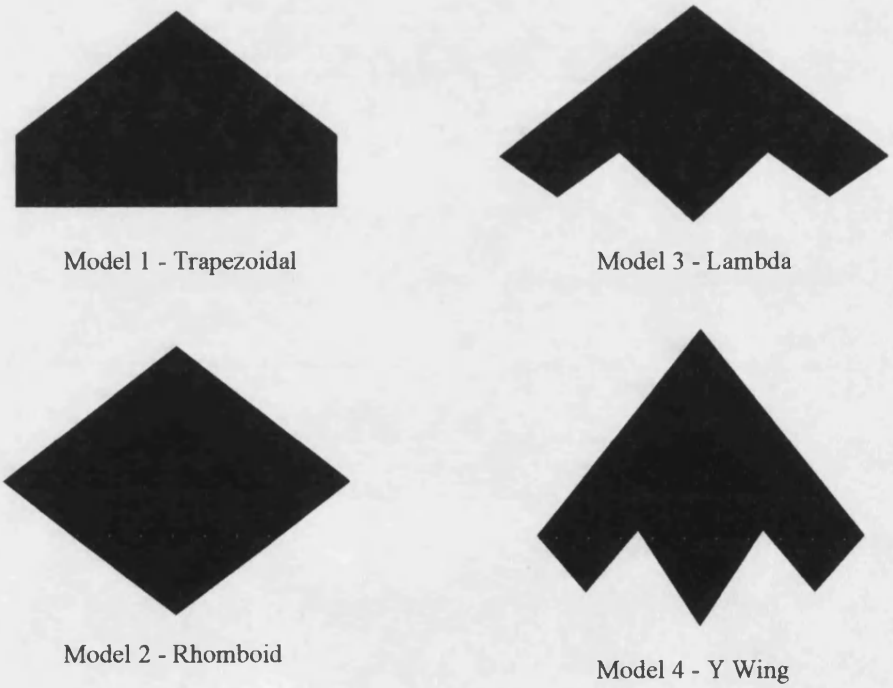

Figure 2.2: Planforms Under Investigation

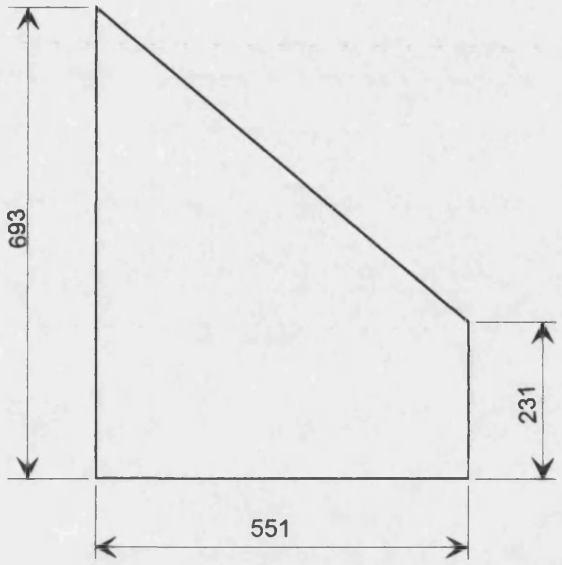

Figure 2.3: Model 1 Planform Dimensions

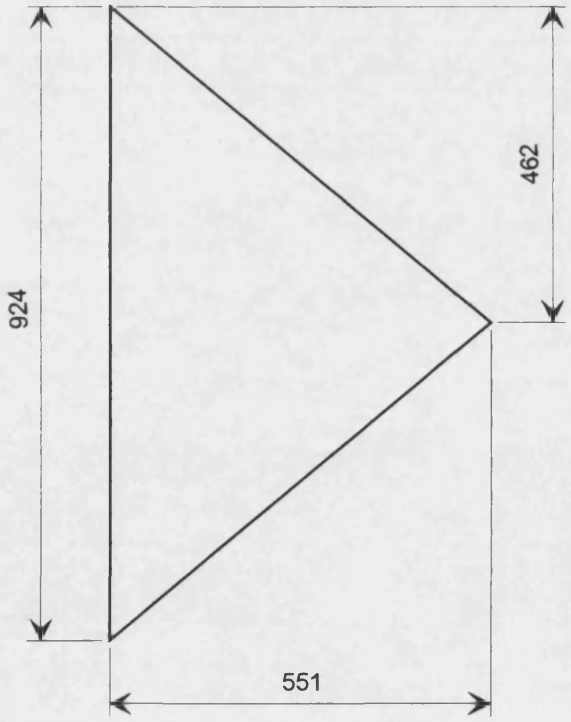

Figure 2.4: Model 2 Planform Dimensions

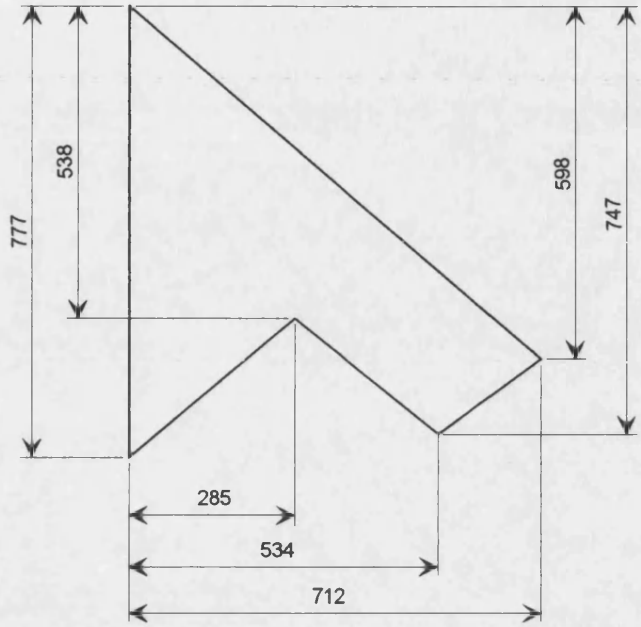

Figure 2.5: Model 3 Planform Dimensions

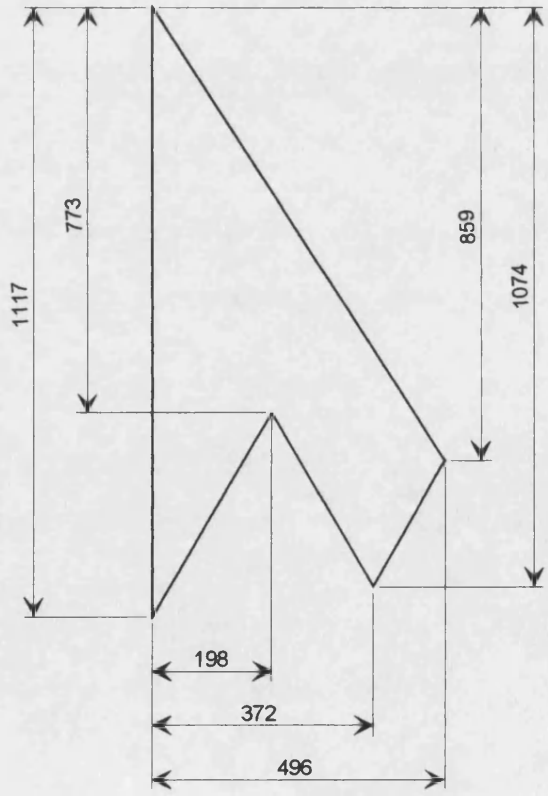

Figure 2.6: Model 4 Planform Dimensions

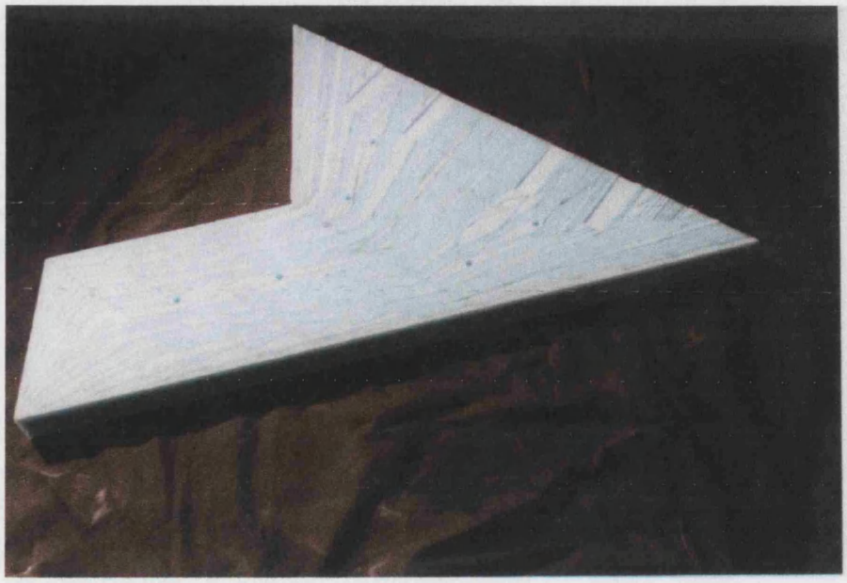

Figure 2.7: Marked Out Foam Core

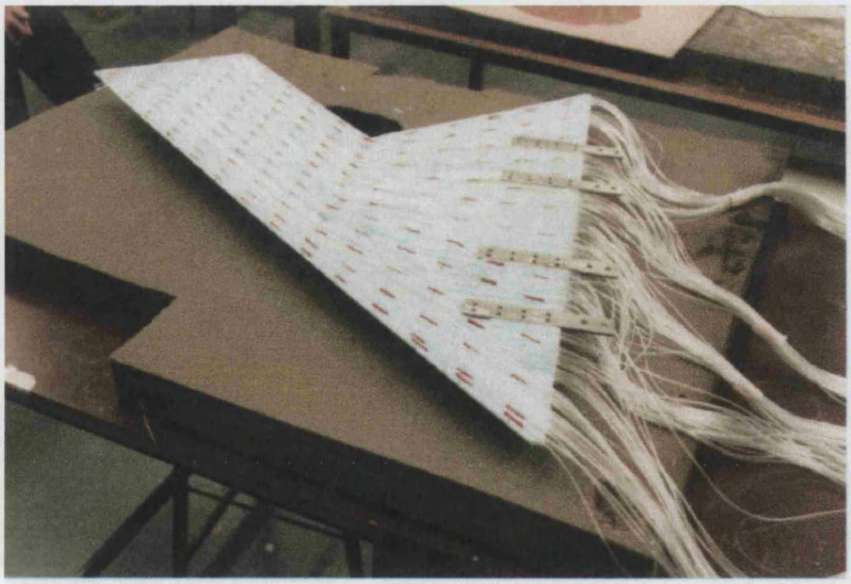

Figure 2.8: Installation of Scanivalve Tubing

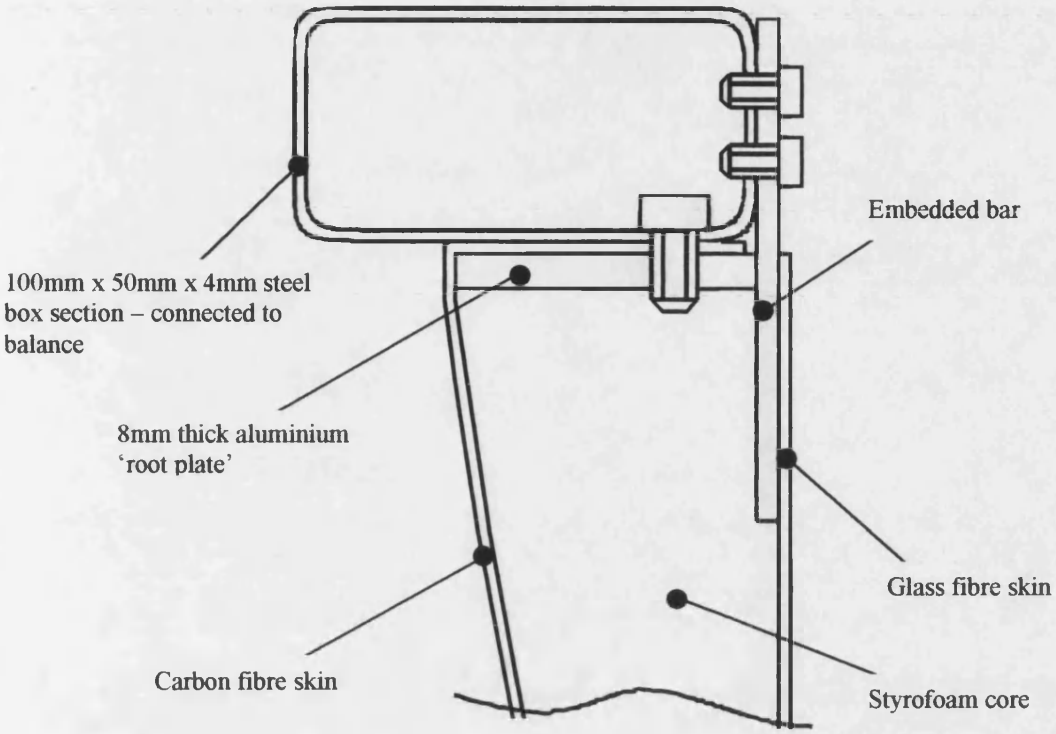

Figure 2.9: Mounting Attachment

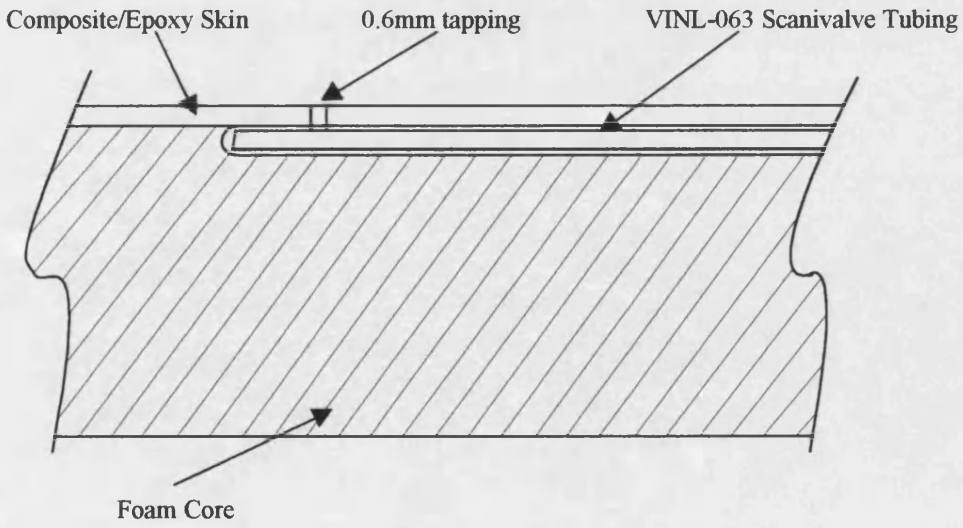

Figure 2.10: Scanivalve Tapping

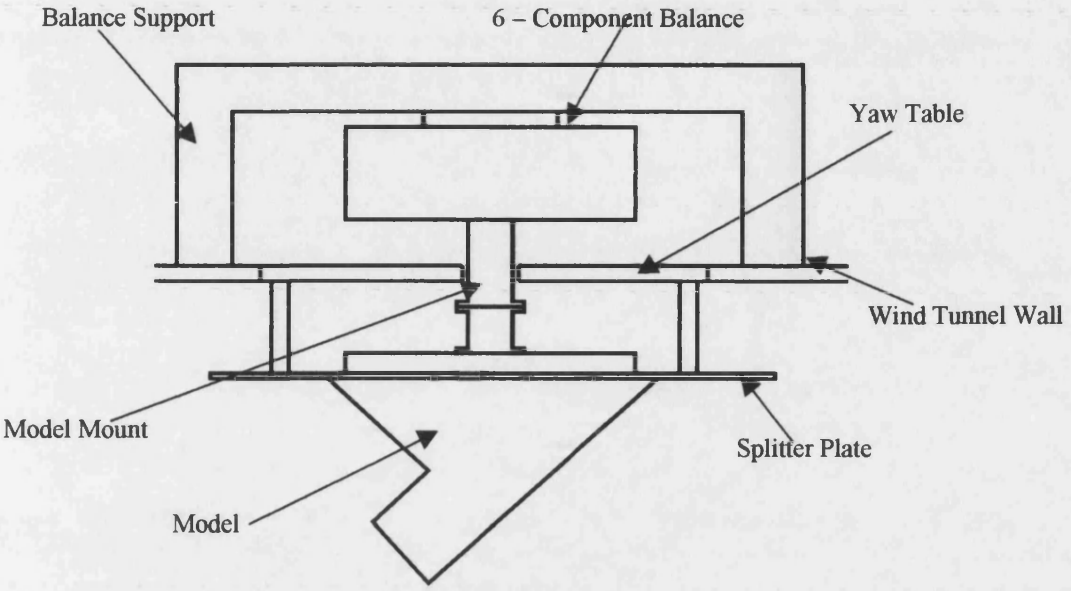

Figure 2.11: Wind Tunnel Installation

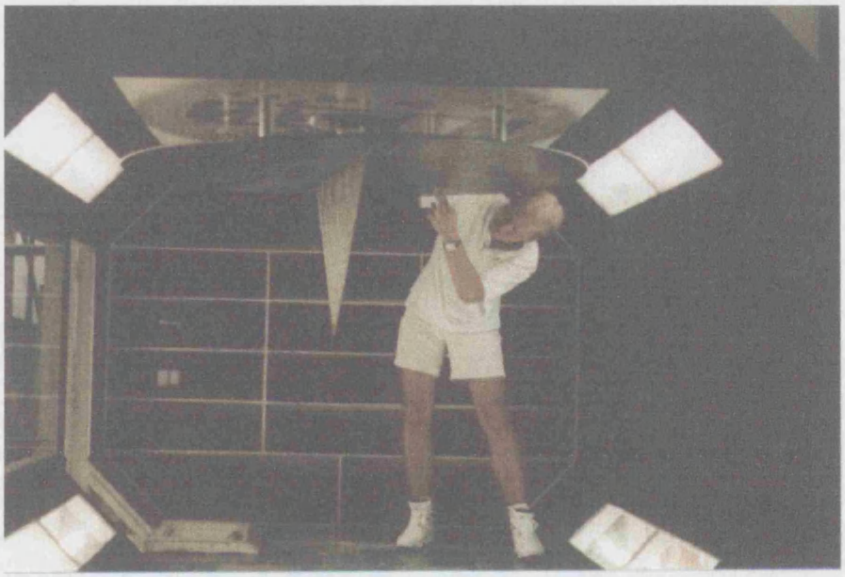

Figure 2.12: Model Installed in Wind Tunnel

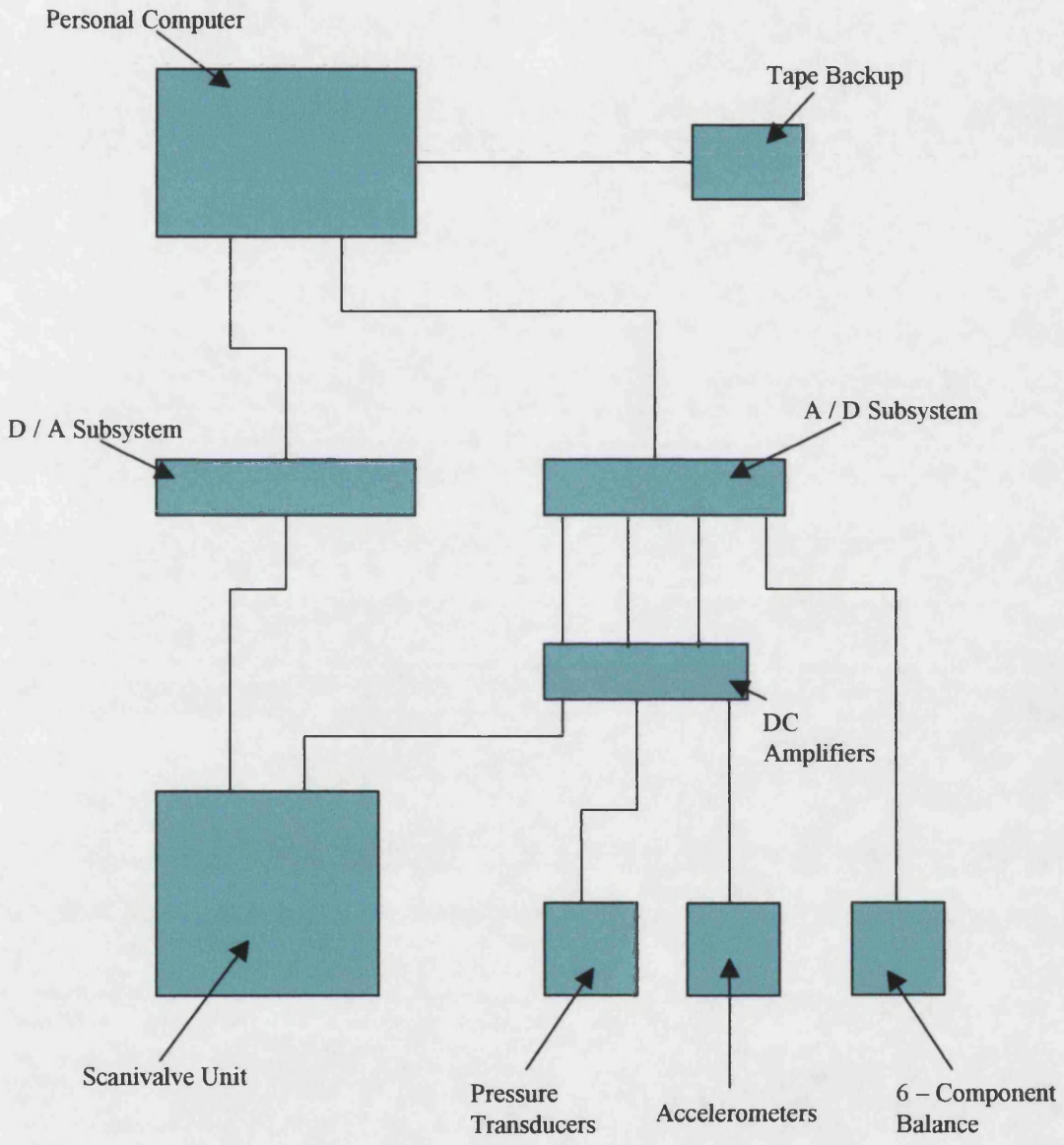

Figure 2.13: Date Acquisition System

CHAPTER 3: EXPERIMENTAL PROCEDURES

3.1 Data Acquisition Techniques

Wind tunnel balance data was acquired utilising the integrated six component balance. The readouts utilised had the facility to output a voltage in addition to their digital displays. This voltage was acquired for each readout by acquiring 500 samples at a rate of 250 samples / second. These readings were then averaged and the equivalent digital readouts calculated. These values were then sent by Dynamic Data Exchange (DDE) to Microsoft Excel and displayed on screen to allow a comparison with the displayed data to be made. The data were sent to specific cells in the spreadsheet dependent on the incidence being tested, whether there was flow over the configuration and whether the model was attached. This allowed force and moment coefficients to be calculated by applying calibration and cross-coupling information supplied with the balance. Graphs of lift, drag and pitching moment were automatically plotted by the spreadsheet during the test procedure.

The flow topology over the planforms was investigated by examining surface flow direction, measured by utilising oil-flow visualisation techniques. This was carried out by spray painting a partially instrumented model, one with no Scanivalve tappings or

pressure transducers, and applying a suspension of titanium dioxide powder in a mixture of paraffin and oleic acid. The model was then set at the incidence to be tested. Surface flows could be deduced by examining streaks formed by shear forces exerted by the airflow. An example of the resulting pattern over Model 4, together with the interpretation of the streak-lines, is depicted in Figure 3.1. The oilflow patterns were recorded on 35 mm film.

Outputs from the accelerometers, transducers built into the models and Scanivalve transducers were amplified through DC amplifier cards before being routed to the PC via the DT739 terminal panel and DT2839 A/D card. Data was stored in DT-Vee specific format on the hard disc drive (HDD) of the PC before being backed up to tape and compact disc. The Scanivalve unit was controlled by the PC. Voltage pulses were generated by the PC and routed by the DT2839 card and DT739 terminal panel to the relevant control inputs on the Scanivalve drive unit.

3.2 Tubing Calibration

To enable unsteady pressures to be measured at a large number of points over the wing a method previously used at the University of Bath to measure unsteady pressures due to wing and control surface oscillations (Pilkington and Wood-1994, Vaughan-1995) needed to be refined such that significantly higher frequencies could be discerned.

Comparisons with surface mounted unsteady pressure transducers were also required to validate the technique.

The method developed utilised a Scanivalve system, generally used for measuring steady pressure data, to acquire unsteady data. This was achieved by calibrating the vinyl tubing linking the tapping to the pressure transducer. To allow unsteady pressure contours to be plotted over the surface of the wing the response function, $r(f)$, of the tubing system connecting the tapping to the pressure transducer within the Scanivalve® unit was required. This would then allow the pressure fluctuations at the tappings to be calculated from the pressure signal measured at the Scanivalve® unit.

Previous work analysing forced oscillations examined frequencies in the range 2Hz to 20Hz. To obtain the response function in this frequency range, a small piston was clamped over the tapping with the piston oscillating at constant frequency. This produced a pressure oscillation at a given frequency and the pressure fluctuations at the input and output were measured. Fast Fourier Transforms (FFTs) of the two signals could then be performed and the response at a single frequency calculated. This was repeated at a suitable number of frequencies resulting in a response function between the input and output of the system throughout the frequency range under examination. This was then repeated for each pressure tapping. This system was not sufficient to calibrate the tubes at frequencies greater than approximately 80 Hz due to inertial loads in the piston. It was also time consuming when a large frequency range was required. Buffet frequencies of up to 500 Hz were expected over the planforms to be considered (Gursul-1994).

A new calibration system was derived and is shown schematically in Figure 3.2. A signal composed of superposed sine waves with frequencies of 2 Hz to 500 Hz at 2 Hz increments, each with the same amplitude and random phase, was constructed. This wave was then converted to an analogue signal and the voltage power amplified to drive the speaker. The pressure fluctuations resulting from this input were measured and the spectral content of the oscillations was calculated. As is clear from Figure 3.3b, this white noise input resulted in pressure fluctuations with little content at low frequencies below approximately 80 Hz and a large spectral content at frequencies above 300 Hz. The response of the speaker could be deduced from these measurements. A new signal was then calculated and generated by the PC, tailored to make the amplitude of the pressure oscillation output by the speaker, $p(f)$, constant in the frequency range considered. The speaker was driven extremely hard at low frequencies, with voltage inputs to the speaker approximately four times those in the initial white noise input at very low frequencies. Similarly, much smaller signals were input in the high frequency range. The spectral contents of the signal input to the speaker and the resultant pressure fluctuations are depicted in Figure 3.3. It is clear from this that the modified speaker input resulted in pressure fluctuations that were of constant amplitude between 20 Hz and 500 Hz. The range of frequencies at which sufficient pressure fluctuations were output for calibration was therefore increased from its previous 80 Hz to 500 Hz range that was possible with the white noise input.

This signal was then utilised to calculate the response functions of the Scanivalve tappings. Data was acquired simultaneously by pressure transducers at the input

(speaker) and output (Scanivalve unit) of the tube. Hence the complex Fourier Transforms of the pressures measured at the tapping and the Scanivalve unit were $p(f)$ and $p^* r$ respectively. Therefore $r(f)$ could be calculated simply by dividing $p^* r$ by $p(f)$. Each Scanivalve tube that was used was cut to the same length, 2.1 m, to minimise the variation in the response functions. However, variations in the internal dimensions of the tubes necessitated that each tapping was calibrated individually. A comparison of $r(f)$ for a small number of tubes is depicted in Figure 3.4. The small peaks apparent in the amplitude ratios at frequencies in the 50-100 Hz region are due to standing waves being set up in the tubes, in a similar manner to those utilised in organ pipes. Increasing the length of the tubes decreases the frequencies at which these peaks occur and reduces the magnitude of the response particularly at these resonant peaks. The shape of the response function is also a function of the material of which the tube is made. Tubes constructed from, for example, steel have higher resonant peaks. The diameter of the tubes also has an impact, with larger diameter tubing resulting in a larger response throughout the frequency range.

A further benefit of the modified calibration input depicted in Figure 3.3, which achieved a constant amplitude input between 20 Hz and 500 Hz is that the effect of the input amplitude, $p(f)$, on the resulting calibration could be examined. The variation in the calibration with changing amplitude is depicted in Figure 3.5. As can be seen from these results the response function, $r(f)$, of the tubing does not vary with changes in the amplitude of the input pressure oscillation for the tubes under examination. Work subsequently undertaken by DERA Bedford (Lynn-1997) has indicated that the response

function of a given tube varies at the resonant peaks that are apparent in some response functions. These peaks are due to standing waves being present in the tubes at certain frequencies. Due to the long length of the tubes utilised during this work such peaks are very small, and hence effects of input pressure oscillation amplitude are not apparent. Hence $r(f)$ is invariant with $p(f)$ for the tubes utilised during this work.

A comparison between the power spectral densities (PSDs) experienced during wind-tunnel testing of a calibrated tube and a surface mounted pressure transducer is shown in Figure 3.6. The pressure transducer was mounted in the wing approximately 5mm from the Scanivalve tapping. This diagram clearly shows that the calibrated Scanivalve tapping, constructed from low cost materials, is capable of acquiring data at frequencies of up to 500Hz that previously required unsteady pressure transducers costing approximately £500.

Toward of the end of the experimental programme, tests were undertaken at Manchester University. A check was made to ensure that the calibrations had not altered since similar tests were undertaken in the Bath tunnel. Changes in the response functions of the tubes might have been experienced due to dirt being trapped in the tappings, despite the care taken to avoid this, or simply due to aging of the model. This might have taken place due to the novel manufacturing techniques employed during model construction, which resulted in no information as to how such models might deteriorate with time. Approximately 13 months elapsed between calibrations. As can be seen from the

response functions plotted in Figure 3.7 no evidence of either of these problems was experienced.

3.3 Data Quality

The stochastic nature of buffet and buffeting signals is well known (Chesneau and Wood-1994) and makes the determination of the optimum data acquisition parameters, such as sample rate and time, of paramount importance to ensure the reliability and repeatability of results without being wasteful in terms of tunnel and analysis time.

To establish optimum times for both buffet and buffeting data, a buffeting profile was first acquired sampling for 20 seconds at a rate of 2048 samples / second. These sample times and rates were based on similar work examining fin buffeting (Chesneau and Wood-1994). This allowed the regions of buffeting onset, peak buffeting and post-peak buffeting to be identified, as shown in Figure 3.8. An incidence in each region was then selected for further study. Both buffet and buffeting repeatability were then assessed at these angles. This was achieved by completing 20 identical tunnel runs at 30 ms^{-1} and acquiring both buffet and buffeting data for 60 seconds. The spread of the Root Mean Square (RMS) of the signals was then plotted against sample time. An example of this is shown in Figure 3.9. It is clear from this result that the standard deviation of RMSs divided by the mean RMS asymptotes at large acquisition times. These tests were repeated for each tunnel entry to ensure consistent repeatability and reliability. Sample

times of 30 seconds and 20 seconds were selected for buffeting and buffet data respectively when testing in the Bath facility. This resulted in standard deviations of RMS values of less than 1.5% of the mean RMS levels for buffeting and less than 2.0% of the mean RMS levels for buffet data throughout the incidence range. Sample times of 45 seconds and 20 seconds were required in the Manchester wind-tunnel for the buffeting and buffet data respectively. These sample times resulted in standard deviations of RMS values of less than 2.0% of the mean RMS levels for both buffet and buffeting data. These deviations are due to the statistical nature of such data, and do not account for uncertainties in the setting of wind-tunnel speed and models incidence. To evaluate these effects entire buffeting profiles were repeated. An example of such a repeat is depicted in Figure 3.10. Repeatability was better than 4.0% for these repeats, which were undertaken on separate days in the wind tunnel test schedule.

Data acquisition rates were set in order to produce sufficient resolution throughout the frequency range under consideration. This, however, needed to be balanced with the additional storage space and processing time required for a corresponding increase in sampling rate. This problem was particularly acute for buffet data due to the large number of tappings under consideration. A sample rate of 2048 samples / second was chosen as the best compromise for both buffet and buffeting data, resulting in approximately 500 megabytes of data being recorded for each of the six configurations tested.

3.4 Data Analysis

The DT-Vee program was used together with Microsoft Excel for the majority of data reduction. Data windowing, FFTs and buffeting RMS calculations were performed using the functions supplied within DT-Vee. The validity of the supplied functions were checked by providing each function with simple signals, such as superposed sine waves. The results output by the DT-Vee functions were then compared with those calculated using other techniques.

Results from the DT-Vee program were sent via a DDE link to Excel where graphs could be plotted to allow quick assessment of the data. Contour plots were produced using the Amtec Tecplot software package.

The raw pressure data needed to be corrected for the effect of the tubing as described in Section 3.2 and this is shown schematically in Figure 3.11. The time history data, in terms of voltage output from the transducer/DC amplifier combination, was scaled to pressure by applying a static pressure calibration. An ensemble averaged FFT was performed within the DT-Vee software to convert the signal to the frequency domain. Hanning windows were applied to the raw data and FFT sizes were selected to achieve spectral resolution of 2Hz. The magnitudes of the FFTs were then sent via DDE link to Microsoft Excel. The response functions, also stored in Microsoft Excel, were applied and the PSDs calculated from the resultant frequency information (Press et al-1986) by running

Visual Basic macros within the spreadsheets. The PSDs were non-dimensionalised with the square of the dynamic pressure and the RMS buffet was calculating the area under the PSDs from 10 to 500Hz (Bendat and Piersol-1971). The validity of the macros and programs utilised was checked by examining an output from a pressure transducer, for which an amplitude ratio of 1.0 was assumed throughout the frequency range. The RMS pressure calculated using this technique was compared with that calculated directly from the transducer output. To check the application of the dynamic calibration within the spreadsheet, which was not checked by this scheme, the calibrated responses were calculated manually for a small number of frequencies and tappings.

To estimate the amplitudes of peaks in the PSDs together with the frequencies at which they were centred a curve fitting routine was written. The amount of spectral information gathered (approximately 25,000 PSDs in total) made it impractical to print each PSD individually and estimate the peaks and centre frequencies manually. It was also felt that automating the estimation of parameters would give a sounder rationale for the selection of each value.

A FORTRAN 77 program was written to estimate parameters that would describe the PSDs. The program had to satisfy certain criteria:

- The model had to be able to distinguish peaks in the spectra
- It had to be able to decide upon the number of peaks
- There had to be sufficient parameters to estimate the magnitude of all peaks

- Additionally, it would be useful to have an estimate of the width of the peak(s)

The program written utilised a non-linear Levenburg-Marquardt least squares method to iterate parameters until a 'best fit' was achieved (Press et al.-1986). This method, together with analysis of the accuracy of the results obtained and a listing of the FORTRAN program utilised, are described in Appendix A. To enable parameters to be fit a model, or 'merit function', to represent the data had to be selected. The merit function selected was that of 2 independent base-excited 2nd order systems superposed with a constant white noise signal. The magnitude of the frequency response of a base excited 2nd order system is described by the function:

$$X = A\sqrt{\frac{1+4\zeta^2\left(\frac{\omega}{\omega_n}\right)^2}{\left(1-\left(\frac{\omega}{\omega_n}\right)^2\right)^2+4\zeta^2\left(\frac{\omega}{\omega_n}\right)^2}}$$

which is plotted in Figure 3.12. A is the amplitude of the input, ζ the proportion of critical damping and ω_n is the undamped natural frequency. These three parameters were fitted for each of the superposed 2nd order systems, and a constant term to represent background white noise was introduced. This resulted in a total of 7 parameters to be fit for each PSD. An example of the comparison between a PSD and the fitted model is shown in Figure 3.13. This form of the merit function was selected after comparing the quality of fit obtained by various differing functions including superposed normal and Poisson distributions. The quality of the curve fit obtained by

using the superposed base excited 2nd order system merit function was far superior to that obtained with any other model.

This model was fitted for all PSDs where the RMS buffet excitation non-dimensionalised with the free stream dynamic pressure was greater than 8%. The parameters were then contour plotted using the Amtec Tecplot package.

3.5 Tests Undertaken

The tests undertaken during the experimental programme are tabulated in Tables 3.1 to 3.6, below. The configuration numbers quoted correspond to those depicted in Figure 2.2.

Configuration	Incidences	Speeds
1	-10° - +40°, 1° increments	30m/s
2	-10° - +40°, 1° increments	30m/s
3	-10° - +40°, 1° increments	25m/s
3*	-10° - +40°, 1° increments	25m/s
4	-10° - +40°, 1° increments	27.5m/s
4*	-10° - +40°, 1° increments	27.5m/s

Table 3.1: Force and Moment Data

Configuration	Incidences	Speeds
1	0°, 1°, 2°, 3°, 5°, 7°, 10°, 13°, 15°, 17°, 20°, 22°, 25°, 27°, 30°	30m/s
2	0°, 5°, 10°, 15°, 20°, 23°, 25°, 30°	30m/s
3	5°, 8°, 10°, 13°, 15°, 17°, 20°, 25°	25m/s
3*	5°, 10°, 15°, 18°, 20°, 25°	25m/s
4	5°, 10°, 15°, 20°, 22°, 25°, 28°, 30°, 32°, 35°	25m/s
4*	5°, 10°, 15°, 20°, 23°, 25°, 26°, 28°, 30°, 35°	25m/s

Table 3.2: Oilflow Visualisation Data

Configuration	Incidences	Speeds
1	-10° - +40°, 1° increments	30m/s
2	-10° - +40°, 1° increments	30m/s
3	-10° - +40°, 1° increments	25m/s
3*	-10° - +40°, 1° increments	25m/s
4	-10° - +40°, 1° increments	27.5, 22.5, 17.5m/s
4*	-10° - +40°, 1° increments	27.5, 22.5, 17.5m/s

Table 3.3: Buffeting Data

Configuration	Incidences	Speeds
1	-10°, -5°, 0°, 2°, 5°, 6°, 9°, 10°, 11°, 13°, 15°, 17°, 20°, 22°, 25°, 27°, 30°, 32°, 35°, 37°, 40°	30m/s
2	0°, 3°, 5°, 8°, 10°, 11°, 12°, 13°, 14°, 15°, 16°, 17°, 18°, 19°, 20°, 22°, 25°, 30°, 35°, 40°	30m/s
3	0°, 1°, 2°, 3°, 4°, 5°, 6°, 7°, 8°, 9°, 10°, 11°, 12°, 13°, 14°, 15°, 16°, 17°, 18°, 19°, 20°, 21°, 22°, 23°, 24°, 25°, 28°, 28°, 30°, 32°, 34°, 36°, 38°, 40°	25m/s
3*	0°, 1°, 2°, 3°, 4°, 5°, 6°, 7°, 8°, 9°, 10°, 11°, 12°, 13°, 14°, 15°, 16°, 17°, 18°, 19°, 20°, 21°, 22°, 23°, 24° ,25°, 26°, 27°, 28°, 30°, 32°, 34°, 35°, 36°, 38°, 40°	25m/s
4	0°, 2°, 4°, 6°, 8°, 10°, 12°, 14°, 15°, 16°, 17°, 18°, 19°, 20°, 21°, 22°, 23°, 24°, 25°, 26°, 27°, 28°, 29°, 30°, 31°, 32°, 33°, 34°, 36°, 38°, 40°	27.5m/s
4*	0°, 2°, 4°, 6°, 8°, 10°, 12°, 14°, 15°, 16°, 17°, 18°, 19°, 20°, 21°, 22°, 23°, 24°, 25°, 26°, 27°, 28°, 29°, 30°, 31°, 32°, 33°, 34°, 35°, 36°, 38°, 40°	27.5m/s

Table 3.4: Mean Pressure Data

Configuration	Incidences	Speeds
1	2°, 6°, 9°, 11°, 13°, 17°, 22°, 23°, 27°, 32°, 37°	30m/s
2	3°, 5°, 8°, 10°, 13°, 14°, 16°, 18°, 20°	30m/s
3	3°, 5°, 8°, 10°, 12°, 13°, 14°, 15°, 17°, 20°, 21°, 25°	25m/s
3*	5°, 8°, 10°, 11°, 13°, 15°, 17°, 18°, 20°, 22°, 25°	25m/s
4	5°, 10°, 12°, 15°, 17°, 20°, 21°, 23°, 24°, 25°, 26°, 27°, 28°, 29°, 30°, 32°, 33°, 34°, 35°, 40°	27.5m/s
4*	5°, 10°, 13°, 15°, 18°, 20°, 23°, 25°, 26°	27.5m/s

Table 3.5: Buffet Data (α Sweeps)

Configuration	Incidences	Speeds
1	No Speed Sweep	N/A
2	No Speed Sweep	N/A
3	8°, 10°, 14°, 17°, 21°	10, 15, 20, 25m/s
3*	8°, 11°, 15°, 17°	10, 15, 20, 25m/s
4	15°, 20°, 25°, 29°, 32°	12.5, 17.5, 22.5, 27.5m/s
4*	15°, 20°, 25°, 28°	12.5, 17.5, 22.5, 27.5m/s

Table 3.6: Buffet Data (Speed Sweeps)

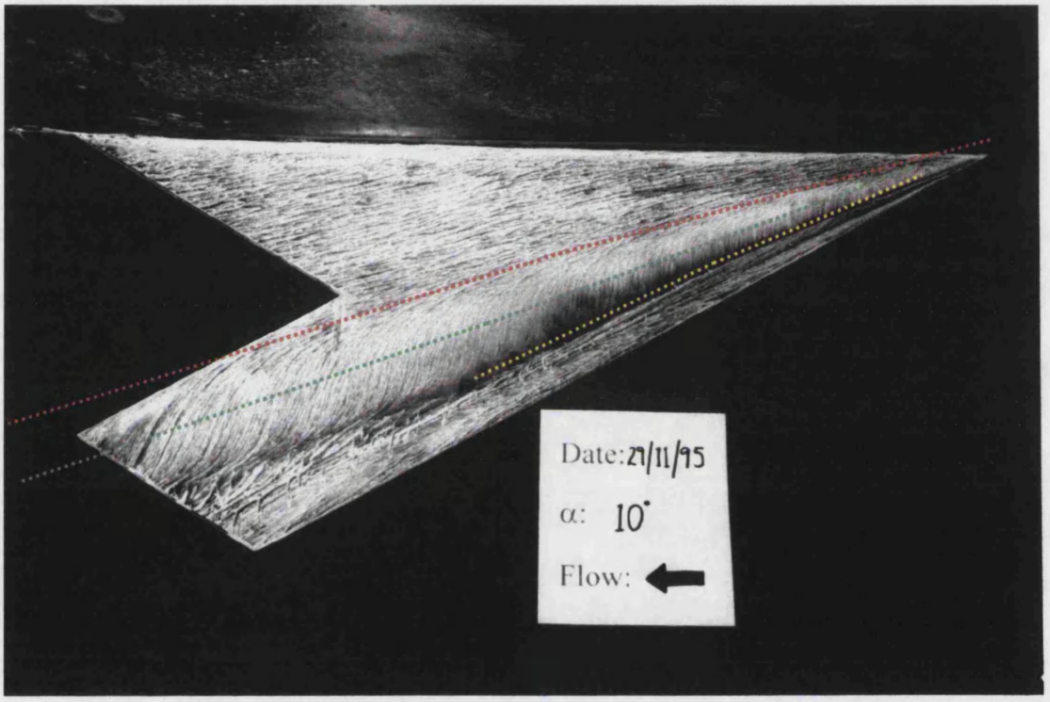

Primary Attachment
Trajectory of Vortex Core
Secondary Separation

Figure 3.1: Oil flow Visualisation

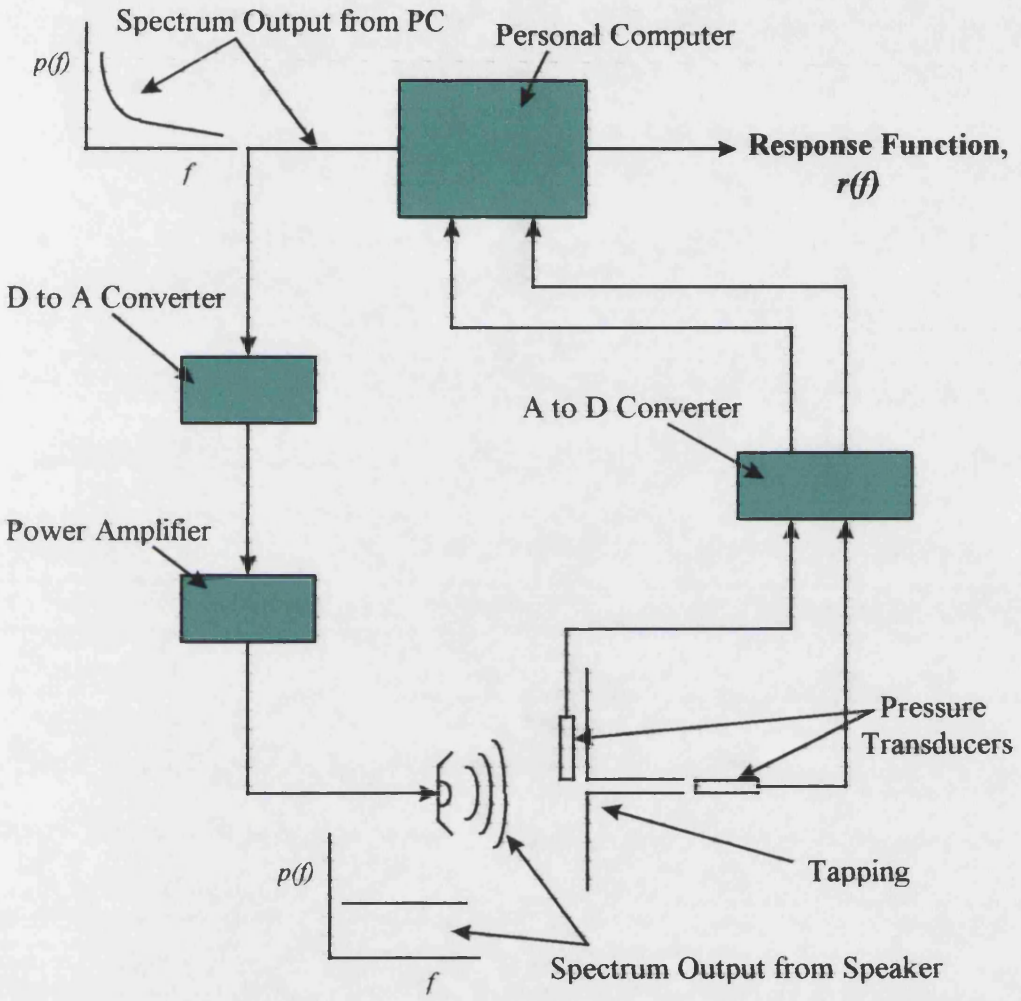

Figure 3.2: Tubing Calibration System

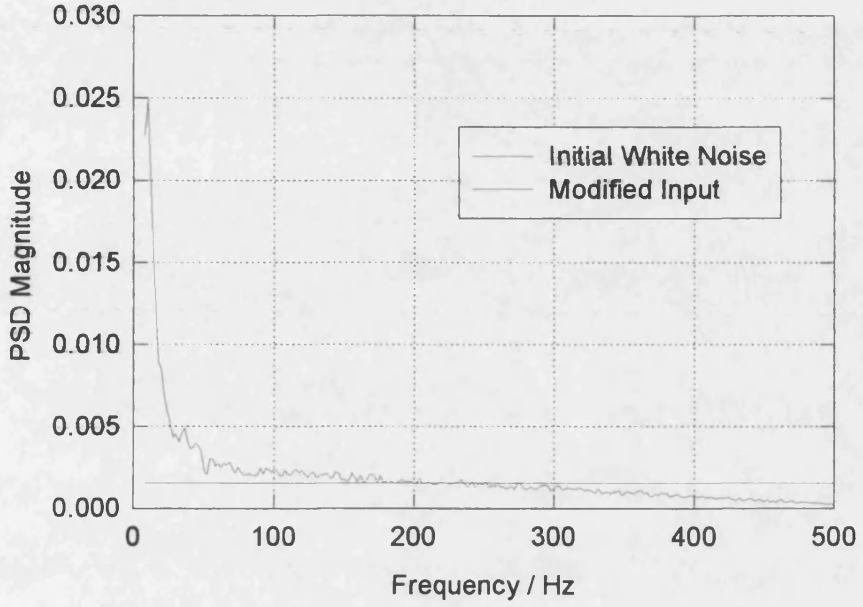

a: Input to Speaker

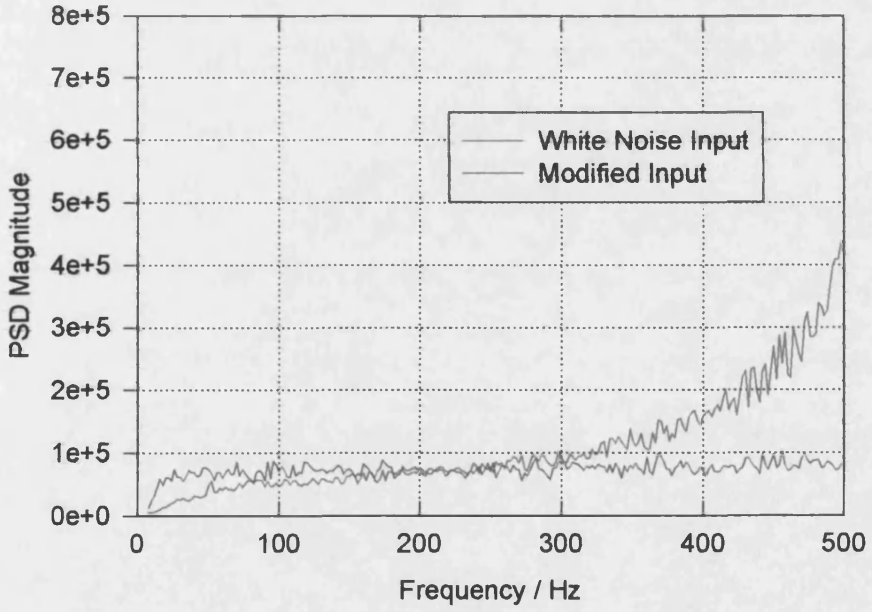

b: Pressure Fluctuations Output from Speaker

Figure 3.3:Tubing Calibration Input and Speaker Response

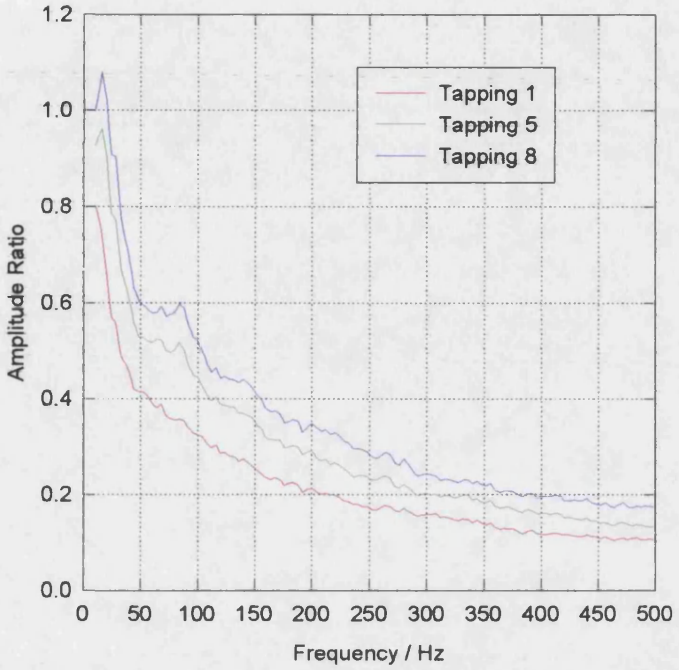

Figure 3.4: Example Amplitude Ratios

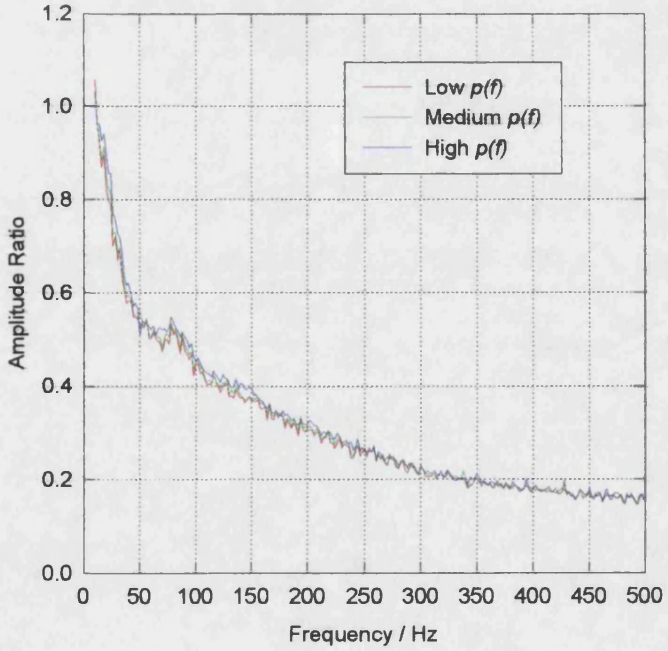

Figure 3.5: Effect of *p(f)* on *r(f)*

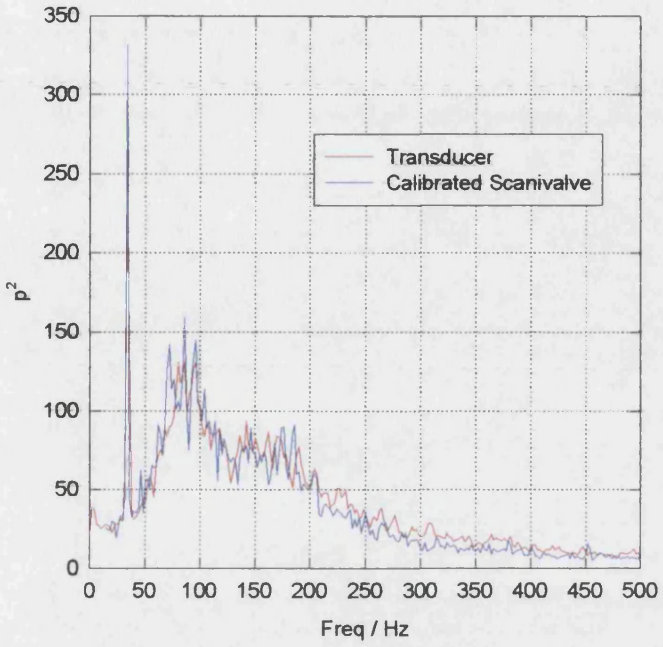

Figure 3.6: Comparison of Pressure Transducer and Calibrated Scanivalve Tapping

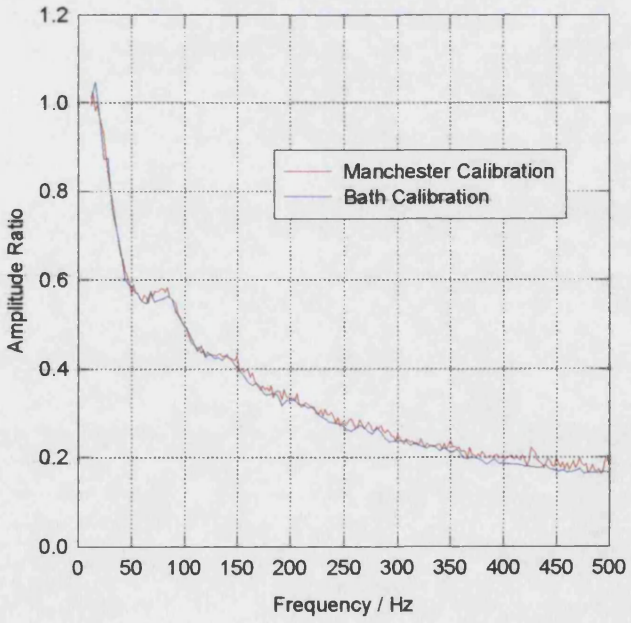

Figure 3.7: Comparison of Bath and Manchester Calibrations

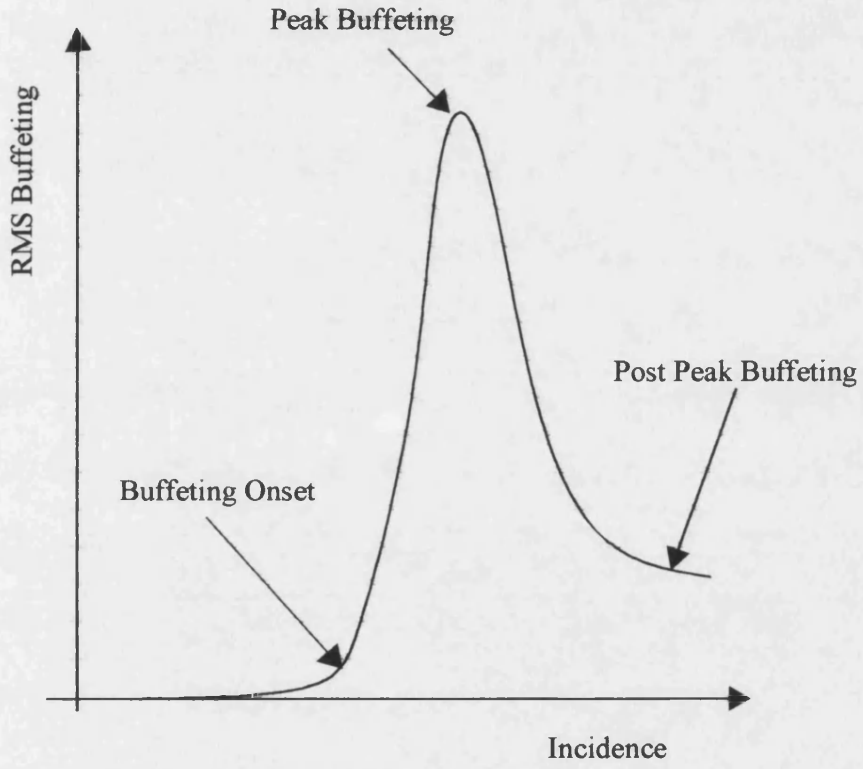

Figure 3.8: Identification of Buffeting Regions

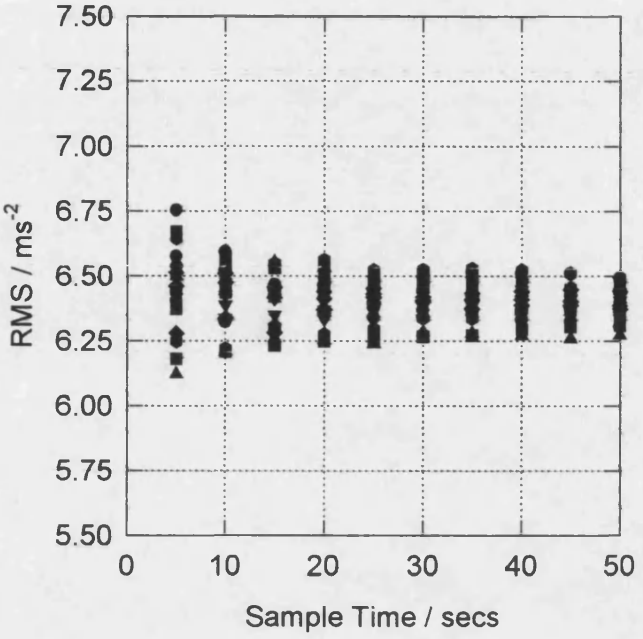

a: Variation of 20 Measured RMSs with Sample Time

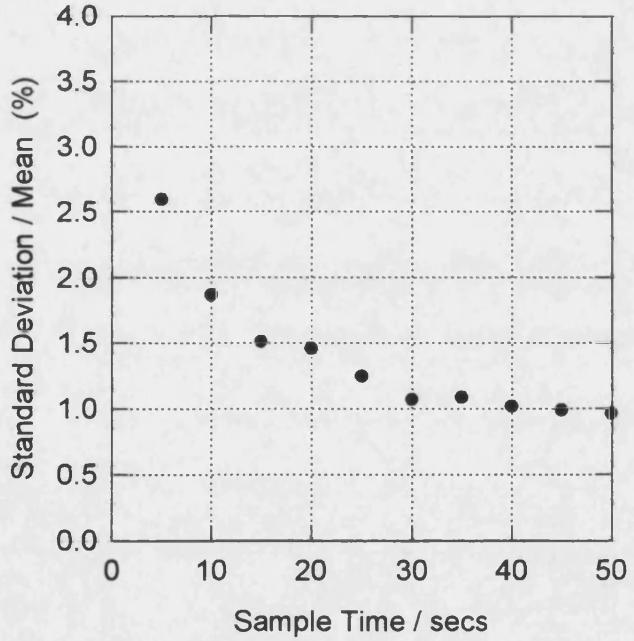

b: Variation of Spread of 20 RMSs with Sample Time

Figure 3.9: Evaluation of Optimum Sample Time

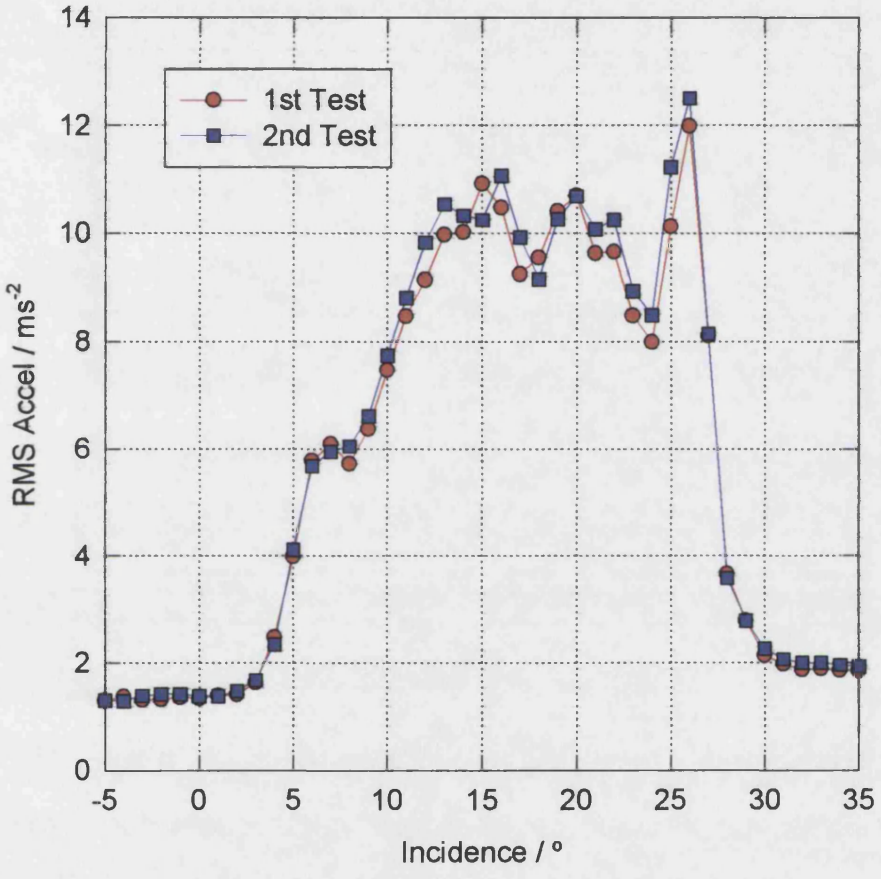

Figure 3.10: Buffeting Profile Repeatability

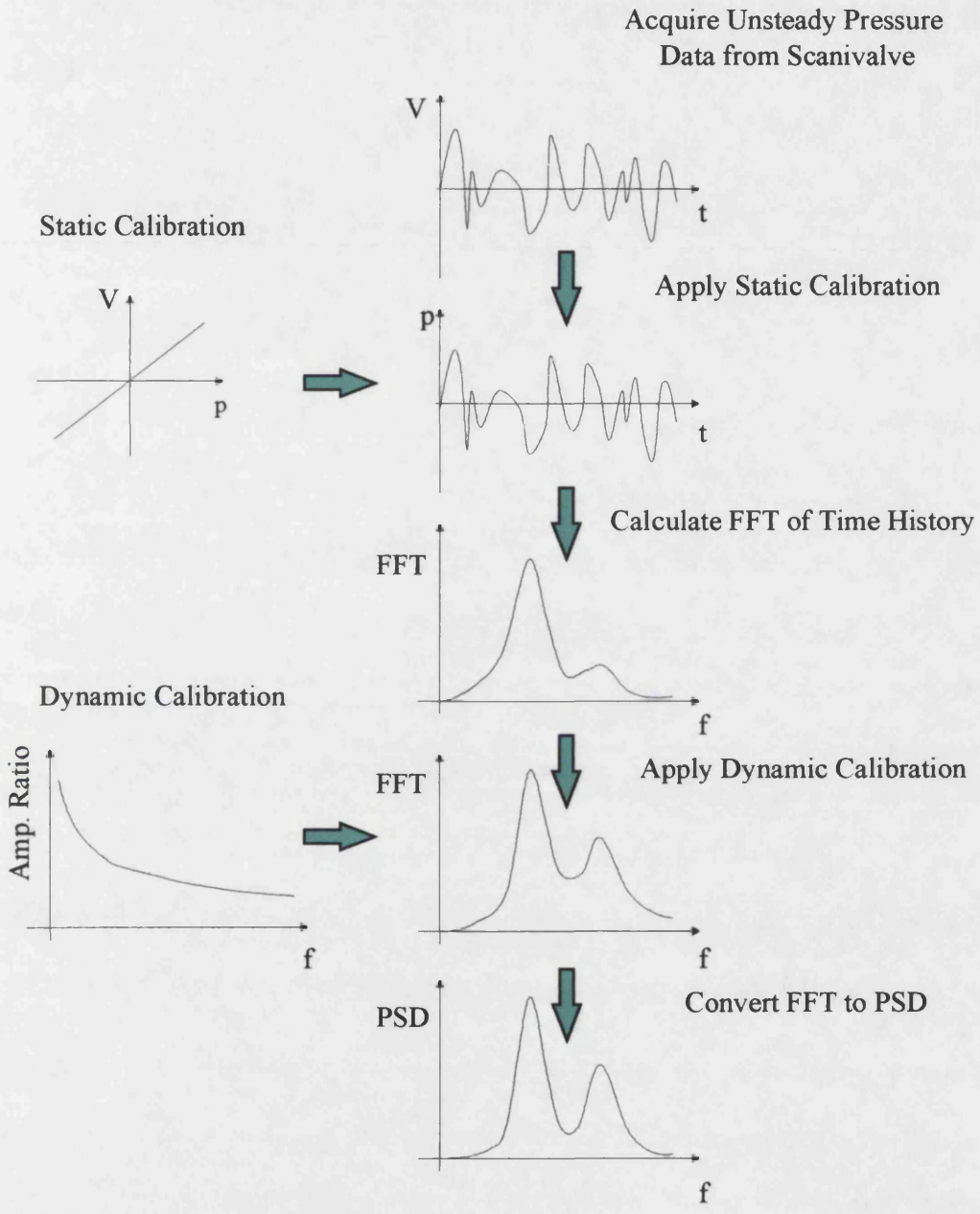

Figure 3.11: Conversion of Acquired Time-Histories to PSDs

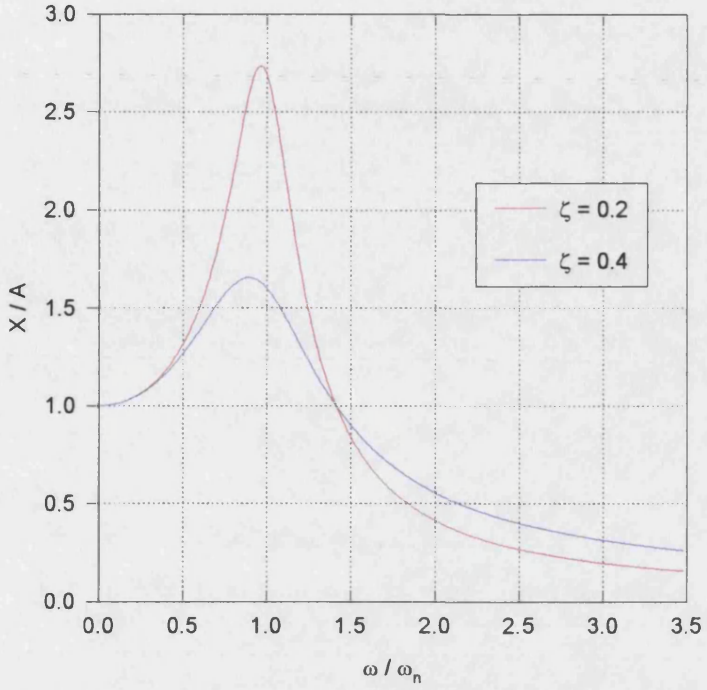

Figure 3.12: Response of a Base Excited 2nd Order System

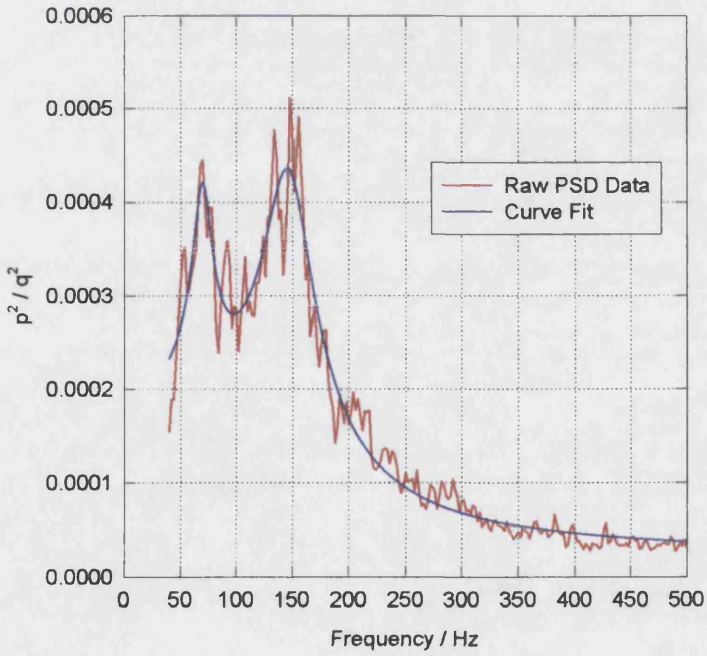

Figure 3.13: Example of Curve Fit

CHAPTER 4. PRESENTATION AND DISCUSSION OF RESULTS

4.1 Force and Moment Data

Force and pitching moment data was acquired for all six configurations to identify the incidences at which the wings stalled and to detect any peculiarities in the forces and moments that might be due to the stealth characteristics of the wings. The configurations tested are shown in Figures 4.1 and 4.2. Note that Models 3 and 4 were each tested in two configurations; a 'forward' configuration where the Models acted as delta wings with modified trailing edges and a 'reverse' configuration where the more complex discontinuous edges were upstream. The reverse configurations are distinguished in the subsequent discussion by the addition of "*" to the Model designation.

The forces and moments acting on Models 1, 2 and 3, each of which has its leading edges swept at 40°, are depicted in Figure 4.3. The negative lift generated for all models at zero incidence is indicative of the negative camber of the models. The lift

curves were approximately linear at incidences up to 10°, as the angle of attack was increased further the lift curve slope reduced until a maximum value of lift was achieved. Maximum lift, with lift coefficients of 0.634, 0.643 and 0.670, was achieved at 19°, 20° and 22° for Models 1, 2 and 3 respectively. Stall was gentle in each case, with the post stall lift dropping to approximately 90% of that at stall for all three models. The variation in the drag experienced by the models as the angle of attack was increased was dominated by the resolved component of the normal force acting on the wing.

The pitching moment, measured about the wing apexes, reduced in a linear manner until an incidence of approximately 10° was reached. The rate at which the pitching moment decreased with incidence then reduced. This increase in pitching moment, relative to the linear decrease experienced at lower incidences, together with the corresponding reduction in lift curve slope previously mentioned is characteristic of the vortex burst phenomenon becoming apparent over the wings (Escudier-1988). Minimum values of pitching moments were reached at angles of attack close to stall for each model. As the angles of attack were further increased there was little change in the pitching moments.

Lift reached a local maximum at an incidence of 22° for Model 3*, as can be seen in Figure 4.4. However, in contrast to Models 1 to 3, where a steady decrease in lift to approximately 90% of the maximum was experienced as the incidence was increased, a drop of 2% in the lift generated was found when the angle of attack was increased

by a further 1° to 23°. As the incidence was increased further the amount of lift generated by the wing increased slowly. The greatest lift, equating to a lift coefficient of 0.732, was experienced at an incidence of 40°, the maximum angle of attack tested.

The forces and moments experienced by Model 4, which had leading and trailing edge sweeps of 60°, are compared to those experienced by Model 3, which had leading and trailing edge sweeps of 40°, in Figure 4.5. At incidences of less than 6°, the lift curve slope for Model 4 was less than that of Model 3. This is as would be expected for attached flow over the models, since the aspect ratio of Model 4 is significantly lower than that of Model 3 (1.93 for Model 4 compared with 3.98 for Model 3). As the incidence was increased beyond 6° the lift curve slope of Model 4 increased. This is typical of wings which have energetic vortices over their upper surface. The almost linear nature of Model 3's lift curve indicates that any vortex that was present over the wing's upper surface made little contribution to the lift.

The effect of the model camber, and its influence on the lower surface flow, can be noted by examining the lift curves at negative incidences in Figure 4.5. If the model had a symmetric cross section, the lift curve at negative incidences would be symmetrical and would pass through the origin. However, since there is negative camber the vortex formed at negative incidence is weaker than that formed at positive incidences. This is apparent as a reduction in the lift curve slope at negative incidences. The difference in lift curve slope at positive and negative incidences is

more marked for Model 4 indicating that a stronger vortex system is present in this case.

Model 4 achieved maximum lift at an incidence of 29°, with the lift curve slope decreasing above incidences of approximately 15°. However, in contrast to all of the models with sweeps of 40°, there was a sharp decrease in lift in the post stall region. As the incidence was increased beyond 29° there was initially a small, but steady, decrease in lift. However, as the angle of attack was increased from 32° to 33° there was a sudden decrease in the lift generated by the wing, with the lift coefficient dropping from 0.974 to 0.776. If the pitching moments generated by Model 4 are examined it can be seen that this dramatic decrease in lift coincided with a sharp increase in the pitching moment about the leading edge, representing a nose up pitching moment. The model was therefore locally unstable in pitch. This would be a potentially dangerous in an aircraft since the marked increase in pitching moment might cause the angle of attack of the aircraft to increase further, thus exacerbating the problem.

The forces and moments generated by Model 4* are compared to those experienced by Model 3* in Figure 4.6, where '*' indicates the 'reverse' flow configuration (see Figure 4.1). As with the comparison of the lift curves of Models 3 and 4, at small incidences the slope of the lift curve for Model 4* was less than that over Model 3*. Again, this would be expected for attached flow over the configuration due to the low aspect ratio of Model 4*. As the incidence is increased, the lift curve slope for Model

4* increased before decreasing at incidences greater than approximately 15°. The lift generated reached a local maximum equivalent to a lift coefficient of 0.775 at an incidence of 27° and varied by less than 2.5% from this value as the incidence was increased further. As for Model 4, the lift curve slope is decreased at negative incidences due to the negative camber of the wing.

4.2 Oil Flow Visualisation

Surface flow visualisation was utilised to identify the main flow features over the upper surfaces of the wings. This was undertaken such that identification of the flow features coincident with steady and unsteady pressure phenomena was possible. The oil flow patterns depicting the surface friction lines over Model 1 as the incidence was increased from 5° to 20° are depicted in Figures 4.7 to 4.11. Free stream flow was from right to left in figures depicting Models 1, 2 and 3, as displayed on the photograph indication card to the right of each model. At an incidence of 5°, depicted in Figure 4.7, a leading edge vortex is apparent over the flat upper surface of the wing. The location of the primary attachment of the vortex is indicated by the dashed red line, and is evident until a chordwise location equal to that of the end of the leading edge. A secondary detachment is discernible close to the leading edge at the wing apex and extends approximately 40% along the leading edge. The primary attachment of the vortex is slightly non-linear, with the sweep of the attachment line increasing slightly toward the trailing edge of the model. As the angle of attack is

increased to 10°, shown in Figure 4.8, the primary attachment of the vortex moved inboard and became apparent downstream of the swept leading edge. The attachment line also became more curved. The secondary detachment became more evident, extending approximately 40% of the distance along the leading edge from the apex with its displacement from the leading edge increased. Increasing the angle of attack to 12°, shown in Figure 4.9, caused the primary attachment to move further inboard. Also, the secondary detachment was only apparent along approximately 30% of the leading edge, reversing the trend observed as the incidence had been increased from 5° to 10°. This may be due to the progression of the vortex burst toward the apex. As described in Chapter 1, downstream of the burst point of a vortex 'half-width' of the suction peak is increased. This results in a reduced adverse pressure gradient as a fluid particle moves outboard, thus inhibiting secondary separation. As the angle of attack is increased further to 15°, depicted in Figure 4.10, this effect becomes more pronounced with a secondary separation being apparent along only approximately 20% of the leading edge. Furthermore, the flow along the outboard sections of the leading edge is reversed, with surface friction streak-lines indicating flow from the wingtip toward the apex. The primary attachment of the leading edge vortex has moved further inboard. The surface friction lines are shown for Model 1 at an incidence of 20° in Figure 4.11. At this angle of attack the vortical structure over the upper surface of the model has almost completely broken down, and a somewhat arbitrary indication of both 'primary attachment' and 'vortex core trajectory' are indicated. The wing is nearing the onset of bluff-body shedding.

The surface friction streaklines over Model 2 are depicted in Figures 4.12 to 4.14. At an incidence of 10°, depicted in Figure 4.12, distinct similarities to the flow over Model 1 were found. A leading edge vortex was apparent over the upper surface of the model, and the primary attachment of the vortex was at a similar sweep to that experienced over Model 1 at the same incidence. The secondary separation of the vortex was apparent along approximately 40% of the leading edge, as for Model 1. As the incidence was increased to 15°, depicted in Figure 4.13, differences in the surface friction lines became apparent. As for Model 1, the primary attachment of the leading edge vortex moved inboard. However, although the secondary detachment extended along approximately 20% of the leading edge, similar to that over Model 1, the flow along the leading edge outboard of the end of the secondary detachment was different for the two models. This is likely to be due to the sweep of the trailing edge of the wing which will modify the flow over the wing, particularly toward the wingtip. At an incidence of 20°, shown in Figure 4.14, the surface flows over Models 1 and 2 were found to be very similar, with reversed flow apparent along the leading edges of both wings.

The results of oilflow visualisation over the upper surface of Model 3 are depicted in Figures 4.15 to 4.18. At an incidence of 10°, shown in Figure 4.15, streaklines characteristic of a leading edge vortex can be discerned. Similarly to Models 1 and 2, both of which also had leading edge sweeps of 40°, the secondary separation extended along approximately 40% of the leading edge. Again, as the incidence was increased to 15°, the primary attachment of the leading edge vortex moved inboard and the

extent of the secondary separation was reduced. Flow at the wingtip was similar to that over Model 2, which also had a swept trailing edge. This is depicted in Figure 4.16. At an incidence of 20°, shown in Figure 4.17, the vortical flow structure was breaking down and clear attachments and detachments were not apparent.

Consideration of the oilflow results depicted for Models 1, 2 and 3 shows that the three generic 40° swept configurations, made by adding a swept trailing edge and a discontinuity along the trailing edge to a baseline configuration, had very similar flow topologies. Leading edge vortices were apparent in each case, and the primary attachment of each configuration progressed in a similar manner. Differences were apparent toward the wingtips, with the configurations with swept trailing edges differing from the baseline model. These differences were apparent in the flow toward outboard of the leading edge vortex system.

The surface flow visualisation patterns over Model 3*, the final model with leading/trailing edge sweep angles of 40° to be tested, are depicted in Figures 4.18 to 4.21. Free stream flow is from left to right in these figures, as indicated on the indication card to the right of each model. Surface flow streaklines resulting from flow over the wing at an incidence of 5° are depicted in Figure 4.18. Three vortex systems can be discerned and complex mixing is apparent in an approximately chordwise line aft of the 'reverse apex', which was the name given to the discontinuity location. The sweeps of the three attachment lines were all very similar. When the angle of attack was increased to 10°, the sweep of all three of the

attachment lines was increased, as shown in Figure 4.19. The mixing of the vortices behind the 'reverse apex' has become asymmetric, with the line along which mixing occurs being at an angle to the symmetry plane. This was in contrast to that observed on a full span flat plate wing with the same planform (Woods and Hodgkin-1994), where the mixing between the two vortices took place along a chordwise line from the reverse apex at all incidences tested. There appeared to be two potential causes of this anomaly. The first is that the differing wing cross sections and thickness distributions may have altered the strengths of the shed vortices sufficiently to cause such an oddity. However, it would seem likely that such an effect would have caused the flow to be symmetric in the case of the models with constant thickness to chord ratio (the semi-span model) rather than in the case of the previously tested flat plate model which had constant thickness, and hence varying thickness to chord ratio, across its span (Lowson and Riley–1995). The influence of testing a semi-span model initially seemed to be a more plausible cause of the asymmetry.

A symmetry plane is utilised to enable the testing of larger scale models in a wind-tunnel. However, semi-span testing has its disadvantages. For example, the addition of the symmetry plane eliminates the possibility of asymmetries in vortex burst location between the port and starboard wings in simple delta wing experiments. In the case under consideration here, the three vortices over the semi-span wing will be 'mirrored' by the symmetry plane. Thus, it was argued, a small increase in the strength of one of the vortices, possibly due to manufacturing defects, might lead to feedback between the stronger vortex and its mirror, eventually leading to an

asymmetry. However, if this were to happen with the full span model an increase in the strength of one of the vortices would not *instantaneously* result in an increase in the strength of the corresponding vortex on the other side. Therefore, the feedback path required for the asymmetry to appear would not be present.

An undergraduate project was supervised to examine the effect of splitter plates on such planforms. The surface flow visualisation over a full span, flat plate model was examined and then a splitter plate was added to the model to remove the feedback path, thus enabling the model to be tested in a semi-span configuration. It was found that no asymmetry was present in either case. The source of this asymmetry is further discussed in Section 4.3.

As the incidence was increased further to 15°, shown in Figure 4.20, the asymmetry became more obvious. The inboard vortex structure had broken down but the two outboard vortices were still apparent. At an incidence of 18°, depicted in Figure 4.21, the two outboard vortices had also broken down and bluff body flow was taking place over the wing.

Surface flow visualisation for Model 4 is shown in Figures 4.22 to 4.28. Flow is from right to left, as indicated on the card to the right of the model. At an incidence of 10°, depicted in Figure 4.22, the distinctive pattern of surface flow due to a leading edge vortex was apparent. The primary attachment line of the vortex extended from the apex toward a point approximately mid-way along the mid-trailing edge. Unusually,

the sweep of the primary attachment line decreased away from the apex. This is due to the discontinuity on the trailing edge forcing the vortex outboard of the reverse apex. The secondary separation was very plain and extended along approximately 60% of the leading edge of the wing. Between the secondary separation and the leading edge were streaklines that seemed to indicate further separations and attachments. These were likely to be due to 'tertiary' vortices (Del Frate et al.-1990).

As the incidence was increased to 15°, shown in Figure 4.23, the secondary separation line became even more distinct and extended from the apex to the trailing edge of the wing. The sweep of the secondary separation line increased quickly downstream of the wingtip in response to the trailing edge sweep. The sweep of the primary attachment line of the leading edge vortex increased, and crossed the trailing edge just outboard of the reverse apex. As at an incidence of 10°, the sweep of the primary attachment line decreased downstream of the apex due to the effect of the trailing edge discontinuity. A new flow feature also became apparent as the incidence was increased from 10° to 15°, a vortical structure emanating from approximately half-way along the mid trailing edge. The rotation of this vortex was in the opposite sense to that of the leading edge vortex. This was due to the influence of the leading edge vortex on the cross-flow component of the free-stream velocity, as shown in Figure 4.24.

At an incidence of 25°, depicted in Figure 4.25, the trailing edge vortex had become more extensive and extended along the entire mid-trailing edge. The primary

attachment of the leading edge vortex had moved inboard of the reverse apex although the core of the vortex was still outboard of this point. The secondary separation extended only along 50% of the leading edge. These trends; the sweep of the primary attachment increasing, the extent if the trailing edge vortex increasing and the core of the leading edge vortex staying outboard of the reverse apex, continued until an incidence of 32° was reached. Surface flow at this incidence is shown in Figure 4.26. The sweep of the primary attachment of the leading edge vortex had increased until it was almost coincident with the symmetry plane. The secondary attachment of the vortex extended along only 30% of the leading edge and the track of the core of the vortex crossed the reverse apex. The trailing edge vortex system had become extensive. However, as the incidence was increased by 1° to an incidence of 33°, a dramatic change in the flow topology over the wing was experienced. The surface flow at this incidence is depicted in Figure 4.27. As is clear from this figure, the flow structure over the wing had broken down as the angle of attack was increased by 1°. This sudden change in flow structure as the incidence was increased from 32° to 33° coincided with the dramatic reduction in lift and the reduction in nose down pitching moment experienced as the angle of attack of the wing was increased from 32° mentioned in Section 4.1. Therefore, the sudden breakdown in flow structure was responsible for these rapid changes in forces and moments.

Oilflows resulting from flow over Model 4* are depicted in Figures 4.28 to 4.31. Free stream flow is from left to right in these figures, as indicated by the card to the right of each model. At an incidence of 10°, depicted in Figure 4.28, the basic flow

structure can be seen to be very similar to that over Model 3* at low angles of attack. Three leading edge vortices have been shed, and complex mixing is apparent in a chordwise direction downstream of the reverse apex. As the incidence of the wing was increased to 15°, shown in Figure 4.29, the line along which this mixing occurred can be seen to deviate outboard of this line. This was in contrast to Model 3*, over which the mixing line moved *inboard* as the angle of attack was increased. As for Model 3*, similar tests over a full-span flat plate model produced no asymmetry (Woods and Hodgkin-1994). The mechanism behind these two asymmetries is discussed in Section 4.3.

As the angle of attack was increased further, the asymmetry became more pronounced until at an incidence of 26°, depicted in Figure 4.30, the middle of the three vortical structures had broken down. A region of recirculation was apparent along the mid-leading edge of the model. Again, this was different to the asymmetry over Model 3*, where the vortex closest to the symmetry plane broke down first and the middle of the three vortices became dominant. This anomaly between the two results may be due to manufacturing inaccuracies. At an incidence of 28°, shown in Figure 4.31, all of the vortices have broken down.

4.3 Steady Pressure Data

A contour plot of the steady pressures, or more accurately the mean pressures, over Model 1 at an incidence of 10° is depicted in Figure 4.32. The white dots on the diagram indicate the locations of tappings, of which there were 143 on this model. The trajectory of the vortex core is also indicated on the figure, and follows the locus of the suction peak. The primary attachment line can be identified by finding the line inboard of the suction peak along which the magnitude of C_p, the pressure coefficient, increases in amplitude. This is the location where the vortex begins to increase the local velocity, thus lowering the local static pressure. The location of the suction peak and primary attachment indicated on Figures 4.8 and 4.32 show good correlation, as would be expected. Such contour plots of the steady pressure data enable the identification of flow features such as these but little quantitative information can be gleaned from such plots.

Figure 4.33 shows how mean pressures at a spanwise slice 0.370 m downstream of the apex varied as the incidence was changed. To ease reference between the planforms the location of the slice was non-dimensionalised by dividing by x_t, the x-location of the wing-tip. For more conventional delta wings the root chord is often used as a reference length, which is obviously equal to the x-location of the wing-tip for such a planform. However, the presence of differing trailing edges necessitates a different reference length.

It is clear from this data that the suction peak, which is coincident with the core of the vortex, moved inboard as the incidence of the wing was increased confirming the results of the oilflow visualisation discussed in Section 4.2. As the incidence was increased the magnitude of the suction peak grew, reaching a minimum pressure coefficient of approximately -1.10 at an incidence of 9°. As the incidence was increased further the suction peak became broader. This phenomenon is consistent with the vortex burst crossing the chordwise location depicted at an incidence between 9° and 11° (Greenwell and Wood-1992). As the incidence is increased further this trend continues, with the suction peak becoming broader until at an incidence of 17° the magnitude of the pressure coefficient under the remnants of the core was only slightly higher than over the rest of the slice.

Figure 4.34 shows how the mean pressures varied over the surface of the wing at an angle of attack of 11°. This clearly shows that the magnitude of the suction peak is larger close to the wing apex, and is reduced as the trailing edge is approached. By measuring the 'half-widths' in Figure 4.33 the data presented in Figure 4.35 can be derived. The half-width is defined as the distance inboard of the suction peak that the pressure coefficient drops to half its peak magnitude (Greenwell and Wood-1992 Examination of this data allows the approximate incidence at which the burst point crossed the chordwise location under consideration to be found, approximately 9° in this case. By considering similar curves for slices at differing chordwise locations the movement of the vortex burst as the incidence was increased could be deduced. It should be noted that although this method gives an indication of the movement of the

vortex burst it relies on the measurement of the width of the vortex, which increases downstream of vortex burst. The vortex 'burst location' measured using this technique is therefore downstream of that which might be measured using, for example, smoke visualisation.

The motion of the vortex burst over Model 1 is depicted in Figure 4.36. From this it can be seen that the burst first appeared over the trailing edge of the wing at an angle of attack of approximately 7° and moved steadily forward until it crossed the station nearest the apex ($x/x_t = 0.4$) at an incidence of about 12°.

A plot of the mean pressures experienced by Model 2 at an incidence of 10° is shown in Figure 4.37. The 137 tappings are represented by white dots. The flow topology over this wing was clearly dominated by a leading edge vortex at this incidence, with the suction peak and primary attachment lines clearly visible. The variation of the mean pressures at a spanwise slice as the incidence was varied is shown in Figure 4.38. As for Model 1, the suction peak and primary attachment moved inboard as the incidence was increased. This pressure distribution, and similar distributions for different chordwise locations were examined to discern the motion of the vortex burst as the angle of attack of the wing was changed in a similar manner to that employed for Model 1. The variation in burst location with incidence is plotted in Figure 4.39. The burst crosses the trailing edge of the wing at an incidence of approximately 9°, in comparison with 7° for Model 1. However, there is sufficient uncertainty in these measurements (±1.5° for Model 1 and ±1.0° for Model 2) that the difference in these

angles may not be significant. The burst then moved forward over the wing as the incidence is increased, crossing the station nearest the apex ($x/x_t = 0.4$) at an angle of attack between 11° and 12°.

The mean pressures measured over Model 3 are depicted in Figure 4.40, with the 165 pressure tappings represented as white dots. Again, the upper surface flow is dominated by a leading edge vortex and the suction peak and primary attachment line can be clearly identified. The variation of the mean pressures at a spanwise slice as the incidence was varied is shown in Figure 4.41. As for Models 1 and 2, the core and primary attachment of the leading edge vortex moved inboard as the incidence is increased. The incidences at which the vortex burst crossed three chordwise locations is depicted in Figure 4.42. Due to the shape of the planform it was impossible to use surface pressure methods to determine whether the burst had crossed points further downstream than $x/x_t = 0.8$. However, it does appear that the burst moves upstream to these locations at higher incidences than for Models 1 and 2 but moves rapidly toward the apex as the incidence is increased. Indeed, the burst appeared to cross all of the chordwise locations at the same incidence!

The trailing edge discontinuity had a profound effect on the pressures downstream of the reverse apex, which are depicted in Figure 4.43. At all incidences shown the suction peak under the leading edge vortex core can be discerned outboard of the trailing edge cut out, corresponding to a spanwise location of $y/s = 0.6$ even at an incidence of 15°. In contrast, the location of the suction peak at $x/x_t = 1.0$ had moved

inboard of this spanwise position at incidences as low as 11° over Model 1 (see Figure 4.34).

The mean pressures measured over Model 4 at an incidence of 10° are depicted in Figure 4.44, with the 165 pressure tappings represented as white dots. Note that the scales of the pressure contours differ to those utilised for Models 1, 2 and 3. The upper surface of the wing was dominated by a leading edge vortex at an incidence of 10°. The variation in the location and strength of the leading edge vortex suction peak is depicted in Figure 4.45. The spanwise slice depicted is taken at a chordwise location upstream of the trailing edge discontinuity. The motion of the vortex burst over the wing, upstream of the trailing edge discontinuity, as the incidence is increased is depicted in Figure 4.46. As for Models 1, 2 and 3 the burst moved toward the apex as the incidence was increased. However, due to the larger sweep of the Model 4 planform, the burst moved over the wing at higher incidences than over the models with 40° swept leading/trailing edges. The burst crossed the chordwise station furthest upstream ($x/x_t = 0.4$) at an incidence of approximately 26° for Model 4, compared to 12° for Model 3.

The effect of the trailing edge discontinuity on the mean flow was more pronounced for Model 4 than for Model 3, where the sweep of the leading and trailing edges was 40°. At an incidence of 15°, depicted in Figure 4.47, a low pressure area became apparent along the mid-trailing edge. Comparison with oilflow data at this incidence, shown earlier in Figure 4.23, revealed that this was due to a trailing edge vortex

structure. The influence of this structure on the mean pressures at a chordwise location approximately halfway along the mid-trailing edge is depicted in Figure 4.48. As is clear from this graph, the trailing edge vortex became the dominant flow feature over this part of the wing as the incidence is increased beyond 15°. Indeed, as the angle of attack was increased to 30°, the peak suction under the trailing edge vortex was 65% greater than that under the leading edge vortex at this chordwise location. This phenomenon therefore had a large effect on the lift generated by the wing, despite its small size. Moreover, since it is very near the trailing edge, its breakdown had a large effect on the pitching moment acting on the wing. Therefore, the abrupt breakdown of this vortex as the incidence was increased from 32° to 33° resulted in a large decrease in lift and a nose up pitching moment.

An example of the mean pressures experienced over Model 3* is depicted in Figure 4.49. As was indicated by oilflow visualisation in Figures 4.18 - 4.21, there were three vortex systems present over the surface. The complex mixing processes apparent from surface friction patterns could not be discerned, although the dominance of the centre of the three vortices could be seen at an incidence of 15°. This was apparent due to reduced suction under the inboard vortex. Similarly, the mean pressures experienced over Model 4* are depicted in Figure 4.50. As for Model 4*, the results of the oilflow visualisation were confirmed with three vortex systems apparent over the upper surface. The dominance of the inboard vortex was confirmed. Suction was reduced under the centre vortex at lower incidences than under the inboard vortex.

The dominance of the vortices can be explained by considering the induced velocities and changes in local incidence caused by the vortices. A spanwise slice through the vortex system is shown in Figure 4.51, if all vortices are assumed to be the same distance above the wing. This will not quite be true, since the apex of the inboard vortex is upstream of that of the outboard pair. The inboard vortex is therefore likely to be slightly further away from the surface than the outboard pair in practice. However, this does not effect the following argument. For ease of reference, the inboard vortex is termed V_1, whilst the two outboard vortices are V_2 and V_3. Image vortices, reflected in the symmetry plane are appended by "*". The distance between the centre of V_1 and V_1* is defined as l_1, that between V_1 and V_2 is l_2 and similarly the distance between V_2 and V_3 is l_3.

As depicted in Figure 4.51, it can be seen that the vortices V_1 and V_1* would act as a simple delta wing if they alone were present. Similarly, V_2 and V_3 would represent a delta wing. The velocities induced by the vortices *outside* of these vortex pairs are indicated in Figure 4.51. For example, V_1 has a superposed velocity vertically upward away from the wing relative to that of an isolated delta-wing. This is due to the upwash from V_2 and V_2*. This upwash is reduced by the downwash from V_3 and V_3* but since these vortices are more remote the net velocity is upward. Similar calculations can be made for each of the three vortices. As is clear from Figure 4.51, the induced velocity, relative to that for two isolated delta wings, is upward for all the vortices. However, there are two important points to note: the velocity induced at V_3 is less than that at either V_1 or V_2 due to its remote location, and the velocities at V_1

and V_2 are more complex. Depending on the locations of the vortices and their relative strengths, the velocity at V_1 may be larger than that at V_2 or vice versa.

The effect of location is most simply shown by considering a group of six vortices representing the wing, each of equal strength. Figure 4.52 depicts such a system, although only four of the vortices are shown for clarity. The remaining two vortices, V_2* and V_3* would be reflected in the symmetry planein a similar manner to V1 and V_1*. If l_1 is large and l_3 is small, shown in Figure 4.52a, the induced velocity at V_2 is larger. Conversely, if l_3 is much larger than l_1, shown in Figure 4.52b, the velocity at V_1 is larger than at V_2.

The relative strengths of the vortices also has an effect. For example, if V_1 is much stronger than V_2 the induced velocity at V_2 will be larger. Obviously, the reverse situation applies as well, but results in the velocity at V_1 being greater.

The induced velocities will increase the local incidence, therefore the vortex at which the induced velocity is highest will increase in strength. This might lead to either V_1 or V_2 becoming dominant, but which vortex grows in strength depends largely upon the geometry of the vortex system. Therefore, the change in sweep between Model 3* and Model 4* is likely to cause the dominant vortex to alter.

4.4 RMS Pressure Data

The data presented in Sections 4.1 to 4.3 concerned the mean flow over the planforms considered. This has been introduced such that the flow topologies, in particular the location and movement of the vortex bursts, could be established. The measurement techniques involved have been established for many years and therefore, despite the development of a valuable model build technique and the unusual nature of the planforms considered, such data are somewhat straightforward to acquire. Until 1994, when the research upon which this thesis is based was initiated, the acquisition of unsteady pressure data was beyond the financial and temporal restrictions present in all but a few special cases. Such studies made use of significant funding to examine unsteady flow characteristics over aircraft which were experiencing excessive buffet (Lee et al. -1994). The techniques described in Chapters 2 and 3 have enabled detailed unsteady pressure measurements to be made over the six configurations and the results of these measurements will be presented, described and discussed in the remaining sections of this chapter.

Contours of the RMS pressures measured over the upper surface of Model 1 at an incidence of 11° are depicted in Figure 4.53. A region of high RMS pressures extended from the wing apex to approximately the mid-point of the trailing edge. The magnitude of the maximum RMS pressure along this line appeared to be approximately constant when such contour plots were examined. To enable the

location of this high RMS region to be related to the mean pressure distribution, the mean and RMS pressures along a spanwise slice at a range of incidences are depicted in Figure 4.54. As is clear from this figure, the vortex core and the region of maximum RMS pressure are not coincident. This is a very significant result since most researchers locate the limited number of miniature pressure transducers generally used for such measurements under the vortex core (Gursul-1994). The maximum RMS pressure is actually present inboard of the core, between the primary attachment and core of the leading edge vortex. Recently, measurements of the vorticity distribution over a delta-wing with 45° of sweep has indicated that spanwise mean vorticity is at a maximum at the attachment location of the leading edge vortex, whilst turbulent kinetic energy reaches a maximum between the attachment and the vortex core (Honkan and Andreopoulos – 1997). This region of maximum turbulent kinetic energy therefore coincides with the area of maximum RMS pressures measured, as would be expected.

Further consideration of Figure 4.54 indicates that the magnitude of the peak RMS pressures varied as the incidence was increased. Furthermore, this magnitude did not seem to be a simple function of the peak suction.

A contour plot of the RMS pressures experienced over Model 2 is depicted in Figure 4.55. As for Model 1 there was a region of high RMS pressure which extended from the apex to approximately the mid-span location of the trailing edge. The magnitude of the pressure fluctuations varied slightly along this line at a given incidence. The

variation in the magnitude and location of the high RMS region as the angle of attack of the model was increased is depicted in Figure 4.56. The region was again found to be located inboard of the core of the leading edge vortex, in its attachment region. A point of moderate RMS pressure can be noted outboard of the suction peak near the leading edge of the model. This phenomenon was also noted at other incidences over this model, but the tapping at which the higher RMS was present varied. However, the tappings at which higher RMS were present were always near the leading edge of the model. It may be that there is a rise in RMS pressure fluctuations under the secondary separation of the model, which is in this region, although there is insufficient data to be sure of such a hypothesis.

A similar contour plot of the RMS pressures experienced over Model 3 are depicted in Figure 4.57. As for Models 1 and 2 there was a region of high RMS pressure which extended from the apex to the reverse apex. Similarly to Model 2, the magnitude of the pressure fluctuations varied slightly throughout this region. The variation in the magnitude and location of the high RMS region as the angle of attack of the model was increased is depicted in Figure 4.58. The region was again found to be located inboard of the core of the leading edge vortex, in its attachment region.

A possible explanation of the spanwise location of the peak in the RMS pressure fluctuations is depicted in Figure 4.59. Moving outboard from the centreline of the models, the RMS pressure fluctuations began to rise at the same spanwise location that the magnitude of the pressure coefficient began to rise, see Figures 4.54, 4.56

and 4.58. This location is the primary attachment line, which coincides with the outer limit of the shear layer. The RMS pressures then rise as the core is approached, reaching a maximum just before the pressure coefficient rises to its maximum magnitude. It therefore seems likely that pressure fluctuations present within the shear layer are convected along with the layer. As the layer impacts the surface the pressure fluctuations are swept outboard, toward the vortex core. Fluctuations are added at a location slightly further outboard, and the sum of these oscillations is again swept outboard. This continues until the inside of the shear layer is reached and no further pressure fluctuations are added. As the fluctuations are swept outboard they will also dissipate due to viscous effects. Thus, the spanwise variation of the amplitude of the RMS pressures will depend on the relative strengths of two effects: the rate of increase of the fluctuations due to addition from the shear layer and the rate of dissipation. This argument will be developed further throughout the remaining sections of this chapter, and forms the basis of the prediction methodology outlined in Chapter 5.

A contour plot depicting the RMS pressure distribution over Model 4 at an incidence of 25° is depicted in Figure 4.60. This shows marked differences to such distributions over Models 1-3, each of which had leading and trailing edge sweeps of 40° compared to the 60° of sweep present over Model 4. The first point to note is that the maximum RMS pressure was present along the mid-trailing edge of the model. This was consistent with the presence of a trailing edge vortex system located in this area. Secondly, the line of high RMS pressure extending from the leading edge apex

toward the trailing edge which was present over Models 1-3 extended only part way from the trailing edge toward the apex. The variation in the magnitude of the RMS pressure peaks as the incidence was increased is depicted in Figure 4.61 for three chordwise locations. The incidences at which the vortex burst crossed the chordwise locations are superposed on the graph. As is clear from this, the rise in the RMS pressure follows the vortex burst, such that there is little buffet upstream of the burst. This has been noted in many previous investigations of velocity and pressure fluctuations over delta wings, see for example Gursul (1994) and Jaworski (1996).

If a comparison of the mean and RMS pressures at a spanwise slice is made, depicted in Figure 4.62, a further difference can be noted. The peak RMS pressure levels were not located inboard of the core of the leading edge vortex, but were found slightly *outboard* of the core. Interestingly, at an incidence of 25°, a double peak in the spanwise RMS pressure distribution was noted. Peaks were apparent just inboard and outboard of the leading edge vortex core location.

There are two distinct ways of resolving this discrepancy. It is possible that the mid-trailing edge vortex is having an influence on the upstream flow. Pressure fluctuations present in the region of the trailing edge vortex may have propagated upstream along streamlines in the leading edge vortex. This would lead to the peaks present outboard of the vortex core. This process is depicted in Figure 4.63. Thus, the peaks outboard of the leading edge vortex core could be due to the propagation of unsteadiness emanating from the interaction between the shear layers of the leading edge vortex

and the trailing edge vortex. Alternatively, they could be the due to upstream propagation of unsteadiness contained within the trailing edge vortex itself.

The inboard peaks would therefore be due to the streamwise propagation of unsteadiness, as for Models 1-3. It seems unlikely that the upstream propagation should be occurring for Model 4 alone. However, the lack of a source of unsteadiness downstream of the measurement locations would not make this apparent from the spanwise RMS distributions for the other models. The presence of fluctuations propagating or decaying both upstream and downstream is predicted by wave propagation models, described in Section 1.2.2. Indeed, Randall and Leibovich (1973) remark that 'the very rapid drop from a supercritical state is consistent with the presence of a large amplitude wave, which is expected to decay exponentially fast both upstream and downstream', where the 'drop from a supercritical state' refers to vortex burst and derives from Benjamin (1967).

Alternatively, and more simply, the outboard peak could be due to the presence of the secondary separation. Motion of this could result in pressure fluctuations that would cause peaks in the RMS pressure distribution. However, if the oil-flow visualisation displayed in Figures 4.23 and 4.25 is considered it can be seen that the peak just outboard of the core cannot be due to this effect at incidences of 20° and 25°.

At an incidence of 15° and a chordwise location $x/x_t = 0.8$ the primary attachment, core and secondary separation are at non-dimensional spanwise locations of 0.50,

0.70 and 0.78 respectively. These locations were measured from the oil-flow visualisation depicted in Figure 4.23. The locations of the primary attachment and the vortex core correlate well with the values found considering the steady pressure distribution in Figure 4.62. In addition, the location of the secondary attachment correlates very well with the location of the maximum RMS pressure.

However, if the RMS pressure data depicted in Figure 4.62 at the higher angles of attack are considered, it can be seen that the RMS pressure peaks move *inboard* as the incidence increases. Examining the oil visualisation data contained in Figure 4.25 shows that the secondary separation has moved outboard, to $y/s \approx 0.95$, at an incidence of 25°. However, there does appear to be an increase, albeit a small one, in the RMS pressure fluctuations in the region of the secondary separation at all three incidences depicted in Figure 4.62. The secondary separation is found at a spanwise location of $y/s \approx 0.85$ at an incidence of 20°. Therefore, in all three cases there is a small rise in the RMS pressure fluctuations under the secondary detachment. Such rises in the RMS pressures in the secondary separation region have been identified over a delta wing with leading edges swept at 60° (Jupp et al. – 1998).

It therefore seems likely that there are *three* effects present to result in the spanwise RMS pressure distributions depicted in Figure 4.62. Firstly, the peak inboard of the vortex core is due to the streamwise propagation of unsteadiness, as for Models 1-3. Secondly, there appears to be a propagation of pressure fluctuations upstream from a downstream source of unsteadiness. The source of this unsteadiness may be the

interaction of the leading and trailing edge vortices or may be due to unsteadiness present within the trailing edge vortex system itself. This source will be discussed further in Section 4.5.3. Finally, there is a rise in RMS pressures under the secondary detachment of the leading edge vortex.

The obvious means of discovering whether simultaneous upstream and downstream propagation is taking place would be to examine auto-correlation results between adjacent tappings. However, this exposes one of the shortcomings of the 'calibrated Scanivalve' technique when compared with the traditional technique employing a large number of pressure transducers. The traditional technique enables correlations between time histories acquired at different tappings to be made, since data is generally acquired at all tappings simultaneously. However, with the calibrated Scanivalve technique developed during this programme of research, data is acquired sequentially at each tapping, making such calculations impossible.

Contour plots of the RMS pressures experienced over Models 3* and 4* are depicted in Figures 4.64 and 4.65 respectively. As for the other models, there are peaks present in these plots which appear to be in the attachment region of the vortices rather than under the vortex cores. However, the situation is confused by the presence of three leading edge vortices in each case. The region in which mixing between vortices took place can be seen to have a moderate level of RMS buffet ($\overline{p}/q$ of approximately 0.10) for each planform. The asymmetry between the inboard and mid-vortices for Model 3* noted in Sections 4.2 and 4.3 is clear in Figure 4.64, with the RMS

pressures associated with the dominant mid-vortex being substantially higher than those under the inboard vortex.

As was previously stated, consideration of contour plots indicated that the peak RMS pressure was approximately constant along the line from the apex to the trailing edge for Models 1-3. To evaluate the variation in RMS pressures along this line more thoroughly, spanwise slices were taken through steady and RMS pressure distributions at varying chordwise locations. An example is depicted in Figure 4.66. As is clear from this graph, the peak values of $\overline{p}/q$ for Model 1 vary between 0.187 and 0.205, a variation of 9.6%. The need to utilise a cubic spline which passed through the measured locations and to gauge the maximum values of the RMS pressure from the peak in the resulting curve may cause the validity of this apparent variation to be questioned.

To examine the variation in peak RMS pressure more thoroughly its value at three chordwise locations is plotted against angle of attack for Model 1 in Figure 4.67. Here, it can be seen that the peak RMS pressure increased as the incidence was increased at the three slices considered. Additionally, the RMS pressures reached a maximum value at an incidence of between 9° and 11° for $x/x_t = 1.0$, between 11° and 13° for $x/x_t = 0.8$ and did not appear to have reached a maximum at an incidence of 13° for $x/x_t = 0.6$. The incidence at which the vortex burst crossed the three chordwise locations is superimposed on Figure 4.67, and it can be see that maximum RMS was experienced when the burst was upstream of the measurement locations.

Similar plots of peak RMS pressure over Models 2 and 3 are shown in Figures 4.68-4.69. In all cases, maximum RMS pressure was reached at a lower incidence at the trailing edge than toward the apex. The incidence at which the vortex burst crossed the chordwise locations is superimposed on these figures, and for all wings the maximum RMS pressure fluctuations were experienced at incidences where the burst was present upstream of the spanwise slice. The magnitude of the RMS buffet is therefore associated with the burst location. This trend confirms previous research undertaken to examine buffet over more highly swept delta wings, although more buffet is experienced upstream of the burst for these novel wings with low leading and trailing edge sweeps of 40°.

Considering the model proposed earlier, which indicated that the RMS pressures were dependent on the rate of addition of fluctuations from the shear layer coupled with the rate of dissipation of the unsteadiness, it can be seen that the relationship between the vortex burst and magnitude of RMS pressures could indicate that there were more fluctuations downstream of the burst, that unsteadiness that was present was dissipated more slowly or a combination of the two effects. This concept is examined further in Chapter 5.

4.5 Power Spectra

4.5.1 Effect of Spanwise Location – Models 1, 2 and 3

Previous work that had examined the power spectra over delta wings (Gursul-1994, Hubner and Komerath-1995) had relied on a small number of pressure transducers distributed over the surface of model to measure pressure fluctuations. Therefore, no work had been done to examine how the frequency content of the pressure fluctuations varied with the spanwise location. As was shown in Section 4.4, the spatial resolution possible with the calibrated scanivalve technique has indicated that peak RMS pressures were not co-located with the core of the vortex, where spectral data has been presented by other researchers. It was therefore of interest to examine the power spectra in this region as well to see if the centre 'characteristic' frequencies also varied in an unexpected way. A typical variation, for Models 1, 2 and 3, in the power spectra across a spanwise 'slice' is depicted in Figure 4.70. The spectra for Model 4 are somewhat different due to the presence of a vortex along the trailing edge of the model. Hence, Model 4 will be considered in a subsequent section. Results for the 'reversed' planforms, Models 3* and 4* will also be considered in a subsequent section. For brevity, results for Model 3 only are displayed in this section, since this was the most complete dataset. Results for Models 1 and 2 followed identical trends.

As is clear from Figure 4.70, there is a distinct variation in the character of the spectra with spanwise location. At the point inboard of the primary attachment, where the RMS buffet is very small, there is little excitation throughout the frequency range examined. The only peak present is at the fan-blade passage frequency. This distinct peak in the spectra is also present in the other power spectra, but has little impact on the calculated value of RMS buffet because it is a sharp peak at a single frequency and hence makes little contribution to the RMS. Care was taken to ensure that the fan blade passage frequency did not coincide with the frequencies of the natural bending and torsion frequencies of the model. This was to ensure that resonance between these pressure fluctuations and the natural modes of the wing did not occur and cause excessive movement of the wing.

When the power spectra in the primary attachment region are examined, where the RMS buffet has risen, a broadband peak centred at a frequency of approximately 110Hz can be discerned. As the region where RMS buffet is at a maximum is approached, there is a distinct change is the power spectra. Now, rather than just the single peak that was present further inboard, there are two peaks in the spectra. The first peak is centred at a frequency of approximately 75Hz whilst the second is centred at a frequency of 150Hz. Within the resolution that can be determined 'by eye' the frequency of the second peak is double that of the first; they are harmonics. Furthermore, when the broadband peak is considered it can be seen that it occurs at a frequency midway between the two harmonic peaks.

If the buffet spectrum outboard of the 'double peak' location is examined it can be seen that a single peak is present, as measured by other researchers (Gursul-1994, Hubner and Komerath-1995). However, the magnitude of the peak is much reduced from that experienced further inboard. Moving further outboard again, it can be seen that, again, there is a single peak at the lower of the frequencies. The magnitude of the peak has decayed further. All of these characteristics are also found in the buffet spectra present over Models 1 and 2.

The demonstration of the presence of three distinct frequencies is a very important result. If predictions of buffet had been based on previous experimental data they would have predicted incorrect centre frequencies, since neither the higher frequency of the 'double peak' spectra or the intermediate frequency in the attachment region would have been predicted. The lower of the frequencies in the 'double peak' spectra is consistent with those found when examining single fin buffeting (Bean-1990) over delta wings.

To support any prediction methodology, it is useful to attempt to explain the origin of the main features of the buffet spectra experienced over the wing. In the previous section, which considered the RMS pressure fluctuations over the models, examination of the relationship between the spanwise distribution of mean and RMS pressures resulted in the conclusion that unsteadiness present in the shear layer was convected outboard. This resulted in a rise in the RMS buffet as the shear layer was

crossed and the core approached, with the simultaneous dissipation of the fluctuations moving the peak RMS pressure inboard of the core.

The presence of peaks at three distinct frequencies was problematic, since none of them appeared to be a 'fundamental' frequency, such that the remaining two peaks were harmonics of this fundamental frequency. Tests of the data acquisition system were undertaken to ensure that these peaks were not due to some conflict whilst acquiring or processing the data. A signal was manufactured which input repeated pulses into the data acquisition system. The interval between the pulses and the width of the pulses were altered to see if these three frequencies, with none appearing to be at a fundamental frequency, could be replicated by a system with a single fundamental frequency via some quirk of the data acquisition system. No such anomaly within the data acquisition system was found.

There therefore seemed to be no simple way of describing a mechanism to produce the double peak spectra. This difficulty was due to, occasionally, the peak at the higher frequency being of higher magnitude than the low frequency peak, as in Figure 4.70. However, if a simple model of the shear layer is utilised, a mechanism to describe the enlarged second peak can be deduced. The system examined is depicted in Figure 4.71. The shear layer is modeled as a two layers of contra-rotating free vortices, which travel from left to right at a constant velocity, U. Interactions between the vortices, such as the tendency of two such vortices to rotate about each other, are

neglected for simplicity. Therefore, the vortices simply travel from left to right, with zero vertical velocity. Since the velocity field due to a free vortex is described by:

$$u' = \frac{K}{2\pi r}, \quad v' = 0$$

where u' and v' are the velocities tangential and normal to the vortex, K is the vortex strength and r is the distance from the centre of the vortex, the velocities induced at a point P, with nomenclature as in Figure 4.72 and the vortex centred at *(x,y)*, are:

$$u_p = v' \sin\alpha$$

$$v_p = v' \cos\alpha$$

but,

$$\sin\alpha = \frac{(y_p - y)}{\sqrt{(x - x_p)^2 + (y - y_p)^2}}$$

$$\cos\alpha = \frac{(x_p - x)}{\sqrt{(x - x_p)^2 + (y - y_p)^2}}$$

and

$$r = \sqrt{(x - x_p)^2 + (y - y_p)^2}$$

Hence,

$$u_p = \frac{K}{2\pi} \frac{(y - y_p)}{(x - x_p) + (y - y_p)}$$

$$v_p = \frac{K}{2\pi} \frac{(x - x_p)}{(x - x_p) + (y - y_p)}$$

Therefore, if the influences of a large number of vortices arranged as in Figure 4.71 are computed, the resultant velocities can be calculated. Since the total pressure, p_0, is constant for free vortices, Bernoulli's equation can then be used to calculate the static pressure at the point, P.

The time histories and associated spectral information calculated using these methods for points A and B in Figure 4.71 are depicted Figures 4.73 and 4.74 respectively. These show that as the shear layer is approached the spectral response at both 2 Hz and 4 Hz rises, with the response at 4 Hz being approximately one-quarter of that at 2 Hz. The frequencies can be scaled to any appropriate values simply by changing the velocity, U, of the shear layer in the model. At point B, situated between the vortices, the response is much different. Since the vortices in each layer are offset from each other, the maximum excitation takes place at 4 Hz, with the magnitude of this excitation being more than three times as great as that at 2 Hz. This is due mainly to oscillation of the vertical velocity, v_p, at this higher frequency since the horizontal velocity, u_p, is fairly constant. This therefore presents a mechanism to explain the presence of a larger peak at the harmonic frequency.

The peak at the intermediate frequency is more problematic, since there seems to be no way of resolving this phenomenon within the same theoretical framework. However, it should be noted that the broad peak at intermediate frequency takes place at locations very close to the primary attachment of the leading edge vortex. The surface flow visualisation over Model 3 at an incidence of 13° is shown in Figure 4.75. If the asymptote denoting the primary attachment the vortex is considered, it can be seen that points along the asymptote will not only be subject to pressure fluctuations from the vortices in the shear layer at that chordwise location. In addition, fluctuations will be convected downstream along the attachment line. Fluctuations at these points closer to the apex are of higher frequency, as will be described in the next sub-section. If these undergo a similar dissipation as seems to be apparent in the spanwise direction, then a broadband peak at an 'intermediate' frequency will result.

4.5.2 Effect of Chordwise Location – Models 1, 2 and 3

Gursul (1994) had shown that the frequencies of the velocity fluctuations over delta wings with leading edge sweeps of 60°, 65° and 70° were approximately inversely proportional to the chordwise distance from the wing apex. The power spectra of the pressure fluctuations over Model 3 at a number of chordwise locations are depicted in Figure 4.76. Tappings within the high RMS excitation, where two peaks in the spectra are apparent, have been selected. This allows the variation of both of the

centre frequencies with chordwise location to be summarised. If the power spectrum at the point nearest to the apex is considered, it can be seen that two peaks are apparent in the spectrum are centred at frequencies of approximately 150Hz and 300Hz. As was indicated when the spanwise variation was considered, these are harmonics within the resolution that can be attained 'by eye'. This tapping is just over 200mm from the apex of the wing. If the other spectra are examined, it can be seen that the frequencies at which the peaks are centred reduces toward the trailing edge of the model. In particular, the tapping 3rd from the apex of the model is just under 400mm from the apex. The frequencies at this tapping are centred at frequencies of approximately 75Hz and 150Hz, again harmonics within the resolution that can be easily attained. These frequencies, at approximately double the distance from the leading edge of model than the first tapping considered, are half those found at the previous tapping. Thus, the indications that the frequencies are inversely proportional to the chordwise distance from the wing apex appear to be correct.

To substantiate this finding, the curve fitting program described in Chapter 3 and Appendix A was utilised to fit parameters to the power spectra. Two of these parameters indicated the frequencies of any peaks present within the spectra. These frequencies are plotted for Model 3 at an incidence of 14° in Figure 4.77. Previous investigations of fin-buffeting at the University of Bath (Bean-1990, Chesneau-1996) had resulted in the use of a non-dimensional frequency parameter such that:

$$n_m = \frac{\bar{f} c \sin \alpha}{U}$$

where f was the centre frequency of the peak buffet and $\bar{\bar{c}}$ the aerodynamic mean chord. Since it seemed likely that the frequency was varying inversely with the distance from the apex, x, this frequency parameter was modified such that:

$$n_m = \frac{fx\sin\alpha}{U}$$

Lines representing constant values of n_m are also displayed on Figure 4.77. It can be clearly seen from this representation that the many of the centre frequencies follow lines of constant frequency parameter. In particular, a large number of tappings display peaks at frequencies corresponding to modified frequencies between 0.27 and 0.33. This corresponds to the lower of the 'double peak' frequencies as depicted in Figures 4.70 and 4.76. Another cluster of peaks is present at modified reduced frequencies of between 0.57 and 0.60 where x<420mm. These peaks correspond to the higher of the 'double peak' frequencies. It should be noted that these high frequency peaks are less common than those at the low frequency are. This indicates the limited number of locations at which the high frequency peaks are present.

As the discontinuity on the trailing edge, generally known as the 'reverse apex' is approached, it can be seen that the peaks clustered at these two reduced modified frequency parameters become less clear, with more scatter in the centre frequencies. The reverse apex is located 538mm in the chordwise direction from the apex. The increase in scatter is due to two effects. Firstly, flow from the pressure surface of the model in the vicinity of the reverse apex will disrupt the leading edge vortex present over the planform. Secondly, the difficulty in discriminating between two peaks, especially when one of the peaks is much smaller, increases as the two frequencies

become closer to each other. Due to the length scales involved, the separation of the frequencies is reduced toward the trailing edge.

4.5.3 Variation Over Planform – Model 4

The power spectra at five tappings are depicted in Figure 4.78. These are arrayed in an approximately spanwise slice and intercept one of the two regions of high RMS pressure present over the planform, the other being present along the mid-trailing edge of the planform. The figure therefore depicts a similar slice to that displayed for Model 3 in Figure 4.70. If these two figures are compared, it can be seen that there are distinct differences between the power spectra. It should be noted when comparing the spectra that the range of the vertical axes if different for the two figures, with the range being two times as great for the Model 4 spectra.

For Model 3, which had leading and trailing edges swept at 40°, it has been shown that there are three distinct frequencies of excitation. Two of these peaks were present at harmonic frequencies within the region of maximum RMS pressures with the third at an intermediate frequency at a location further inboard. The peak at intermediate frequency was present inboard of the high RMS region, underneath the primary attachment of the leading edge vortex. For Model 4, it can be seen that the spectra are dominated by a single peak with approximately constant frequency throughout the slice. Inboard of the region of high RMS pressures, a single broad

peak is present. As the region of high RMS approaches, this peak increases in magnitude before reducing outboard of the high RMS region. However, if the power spectrum at the location of maximum RMS pressure (top right on Figure 4.78) is examined, it can be seen that there is an additional, although comparatively small, peak present at double the frequency of the large peak. This is, in a similar manner to that for Models 1, 2 and 3, at a frequency that is double that of the lower frequency peak. If the steady pressure contour plot depicted in Figure 4.79 is examined, it can be seen that the location of the 'double peak' spectrum is very close to the suction peak, although still slightly inboard of it. The double peak spectrum is the centre of the five tappings. Contour lines as well as flooded areas have been utilised to clarify isobars.

If Figure 4.78 is examined once more, it can be seen that there is a sharp peak in addition to the broadband peaks, at a frequency of 50Hz. It was felt that this peak at 50Hz was unlikely to be electronic interference, which is often present at a frequency of 50Hz. This was because it was encountered at a limited number of tappings for Model 4 only, with the tappings affected varying as the incidence of the model was varied. It should be noted that this sharp peak was not at the fan blade passage frequency, and so was not due to excitation from this source.

The source of this excitation can be deduced by examining Figure 4.80. This depicts the power spectra within and around the other region of high RMS pressure fluctuations; along the mid-trailing edge of the planform. It should be noted that the

magnitude scales on the power spectra are different to those in Figure 4.78, the ranges being double that of the earlier figure. This region of high RMS is present under the vortex that is present along the mid-trailing edge of the model.

Examination of the spectra indicates that the peak in the power spectra at each of the four tappings is at a frequency of 50Hz. The peak is largest at the location nearest to the 'reverse apex', and is greatly reduced when a tapping outside of the mid-trailing edge vortex is examined. However, there is insufficient spatial resolution to be able to determine where, within this region of high RMS pressures, the RMS pressure fluctuations are at a maximum.

This finding is extremely significant for the design of future aircraft, since not only are the RMS pressure fluctuations extremely high in this region, but the fluctuations are concentrated within a very narrow range of frequencies, much lower than that expected. Therefore, if an aircraft panel, or possibly a control surface, in this region had a structural response in this range it would be subject to extreme stresses due to resonance between the structural mode of the panel/control and the buffet acting on the area. Additionally, by examining the power spectra at the tapping outside of this region of high RMS region, it can be seen that this peak in the spectra at a fixed frequency extends outside the mid trailing edge vortex itself. This is also of interest to aircraft designers since it means that, in addition to the local problems caused by resonance between local buffet an panel structural modes, there is an even more

serious problem when the bending and torsion modes of the wing itself are considered.

Examination of the centre frequencies encountered over Models 1, 2 and 3 indicated that the frequencies present were inversely proportional to the distance from the apex of the model. Therefore, the excitation of a *wing* mode at a given flight condition is unlikely to be problematic since excitation of this mode will only be present at a small number of discrete locations over the wing. Thus, a low level of excitation will be present throughout the majority of the flight regime. Although the buffet frequencies will change as the incidence and speed are varied, discussed in a later section, there will often be a small number of locations over the wing where excitation is at the frequency of the wing mode. This will lead to the levels of buffeting varying gently throughout the flight envelope, as incidence and velocity are changed.

However, if a region of constant frequency excitation extends over a large area of the wing then a very different scenario emerges. If this frequency and the wing structural mode now overlap then significant buffeting is likely to occur. Conversely, if the frequencies are not adjacent then very low levels of buffeting are likely. Therefore, a situation can be envisaged where a maneuvering aircraft is encountering minimal buffeting before, suddenly, reaching a point where resonance occurs and a high level of wing buffeting takes place. Therefore, the extent and source of this region of buffet at constant frequency is of supreme importance.

To examine the extent of this region, the curve fitting program was again utilised to derive the frequencies at which excitation took place over the wing. The results are displayed in Figure 4.81. As for the plots for the Model 3 data, lines denoting constant values of n_m based on chordwise distance from the apex are also plotted. It can be seen from this figure that there are two non-dimensional frequencies at which the peaks are centred. The first is at a modified reduced frequency of 0.75, and there is also excitation at higher frequencies. There is a lot of scatter in the centre frequencies of the high frequency peaks, although few are present at frequencies less than those at modified reduced frequencies of 1.50. If the low frequency peak region is examined, it can be see that the centre frequencies follow the line of constant n_m until the trailing edge is approached. Then, at a location between 700 mm and 800 mm from the apex of the model, the frequency of the peaks becomes constant. This continues to the trailing edge of the model. The reverse apex is 773 mm from the wing apex. Therefore, the peak at a constant frequency of 50 Hz is present at locations downstream of the reverse apex. Since there is little excitation inboard of the reverse apex, this excitation at a frequency of 50 Hz must be present outboard of the reverse apex, toward the wing-tip.

Since the frequency distribution of the low frequency peaks are continuous (i.e. the regions of constant n_m and constant frequency intersect at/near the location of the reverse apex) it seems likely that pressure fluctuations in the leading edge vortex shear layer are exciting the trailing edge vortex system. The pressure fluctuations present in the leading edge vortex may be causing the location of the trailing edge

vortex to move at this forcing frequency. This would cause large pressure fluctuations in the region of the trailing edge vortex. It seems unlikely that the pressure fluctuations are due to unsteadiness within the trailing edge vortex system itself. It would be expected, if this were the case, that the excitation would be at a much higher frequency due to the small length scales involved.

4.5.4 Variation Over Planform – Model 3* and 4*

Plots of the variation in the centre frequencies over Models 3* and 4* are displayed in Figures 4.82 and 4.83 respectively. These plots are similar to those displayed earlier to examine the chordwise variation in centre frequencies over Models 1–4. However, since there is more than one apex for these configurations, with each apex at a separate chordwise location, there was more than one 'chordwise distance from apex' that could be selected. Surface flow visualisation (see, for example, Figures 4.19 and 4.29) had shown that there was an approximately chordwise line, to the rear of the reverse apex, along which mixing between the inboard and outboard vortices took place. This therefore constituted a natural 'barrier' in the flow such that points inboard of this area were influenced primarily by the vortex shed from the apex at the centre-line of the model, with points outboard of the apex being affected mainly by the vortex shed from the 'outboard apex'. Therefore, the 'chordwise distance from apex' that is plotted on Figures 4.82 and 4.83 is the distance from the centre-line apex

if the tapping was inboard of the reverse apex. Conversely, if the tapping is outboard of the reverse apex the distance from the outer apex is plotted.

In each of these plots, a discontinuity is present in the distributions of the centre frequencies. Upstream of the discontinuities, which are present at chordwise locations of approximately 190 mm and 210 mm for Models 3* and 4* respectively, the centre frequencies are strongly dependent on the chordwise location. However, downstream of the discontinuities the centre frequencies vary little with chordwise location. This is particularly apparent for Model 4*. It might be expected that these discontinuities might coincide with the chordwise location of the reverse apex for each of these models, since at this point there is no further vorticity shed into the vortex system. However, these discontinuities are well upstream of the reverse apexes, which are located at chordwise distances of 239 mm and 344 mm downstream of the leading edge apex for Models 3* and 4* respectively. It is possible that the frequencies measured are due to interactions between the two vortices that propagate upstream, although this is far from certain and more work on these complex mixing flows is clearly required.

As the trailing edge of Model 3* is approached the centre frequencies begin to vary with chordwise location. In this region the frequencies follow lines of constant n_m. It is interesting to note that the values of constant n_m that result are identical to those depicted for the configuration in the forward configuration (See Figure 4.77).

The presence of more than one vortex generating apex, together with the associated mixing between the resulting vortices, has therefore had an interesting effect on the frequencies at which buffet is centred. Again, this effect is of interest to designers of combat aircraft since it results in large regions with approximately constant centre frequencies which, as previously explained, can have serious impact on the bending and torsional bending modes of the wing. However, the situation is not as serious in these cases since the magnitudes of the buffet are very much smaller.

4.5.5 Impact of Free Stream Velocity

The variation of a typical power spectrum as the free stream velocity was changed is depicted in Figure 4.84. There are two effects of this change in the free stream velocity. Firstly, the centre frequencies change with tests at higher free stream speeds resulting in higher centre frequencies. Secondly, the peak amplitudes decrease as the free stream velocity is increased.

This effect of free stream velocity on peak amplitude was commented upon by Hubner and Komerath (1995) in their investigations of pressure fluctuations at a single point on a delta wing. Their results followed an identical trend to the data presented in Figure 4.84. However, the step of non-dimensionalising the frequency axis of the power spectra was not undertaken.

When the frequency is non-dimensionalised, as shown in Figure 4.85, a much clearer picture emerges. The curves at the three free stream velocities now overlay each other. Therefore, if the power spectra can be predicted at any free stream speed, this can be utilised to predict both the magnitudes of the power spectra and the centre frequencies at any other required speed. This, of course, assumes that there is no significant effect due to changes in Reynolds number or as a result of compressibility effects.

If Figure 4.85 is studied once more, two further points become apparent. Firstly, the curves do not overlay at higher (non-dimensional) frequencies. This is due to noise within the data acquisition system. The signal to noise ratio is much lower at the lower speeds, since the dynamic pressure at 15 m/s is 36% of that at 25 m/s. Therefore, the RMS pressure signals are a similar proportion of those at the higher speed. This noise is then amplified due to the dynamic calibration of the tubing, making it more noticeable at high frequencies due to the low amplitude ratios at these frequencies.

Secondly, the RMS pressures have been calculated by computing the area up to a constant frequency of 500 Hz for all speeds. It can be seen from Figure 4.85, since the RMS pressure is directly related to the area under the curves, that the *calculated* RMS pressures will be higher for the tests undertaken at lower speeds. The use of a constant frequency range will therefore result in an apparent increase in the RMS pressures as the free-stream velocities are decreased. Clearly, since the non-

dimensionalised power spectra overlay each other throughout the region of highest excitation, this is a mis-leading result. It would therefore be sensible to calculate RMS pressures by calculating the area under the curve up to a maximum non-dimensional frequency.

However, this approach would have associated problems. Calculating the RMS to a constant value of n_m would also involve changing the maximum frequency to which the RMS was calculated over the planform. The maximum (dimensional) frequency is inversely proportional to the distance from the apex of the model at constant n_m, and there is always a maximum frequency that can be examined in any dynamic testing, whether due to hardware limitations such as the speed of the A/D card or due to the technique utilised, as in this case. Therefore, if the entire available frequency range is used at the point nearest to the apex, the maximum frequency will be reduced at points away from the leading edge. Indeed, if Model 3 is used as an example a frequency range of 0-500 Hz at the most forward point would equate to a bandwidth of 0-25 Hz near the trailing edge of the model. Therefore, it seems more reasonable to simply state the non-dimensional frequency range that was examined.

4.5.6 Effect of Incidence

The effect of model incidence on buffet has been examined extensively for the fin buffeting case by researchers such as Chesneau (1996) and Bean (1992). These

investigations have confirmed the validity of the modified reduced frequency parameter n_m, mentioned in earlier sections, where

$$n_m = \frac{f\bar{c}\sin\alpha}{U}$$

This parameter has been further modified such that differing locations over the wing may be considered resulting in

$$n_m = \frac{fx\sin\alpha}{U}$$

Therefore, if the non-dimensional frequency is constant over a planform at a range of incidences, the frequency not only reduces toward the trailing edge but also decreases as the incidence is increased. The centre frequencies for Model 4 are plotted in Figure 4.86 at a range of incidences. Lines of constant n_m at these incidences are also plotted. As expected, the frequencies decrease as the incidence is increased, but remain at constant modified reduced frequency, n_m. In addition, the number of locations at which distinct frequencies are discerned increases as the incidence is increased, with the region reaching closer to the leading edge as the incidence is increased. This is in agreement with other results (Gursul – 1994). Results have been shown only for Model 4 since the range of incidences where buffet is experienced for the 40° swept models is much less. For example, the vortex burst is present over the Model 3 only at incidences between 12° and 15°.

Model 1 - Trapezoidal

Model 3 - Lambda

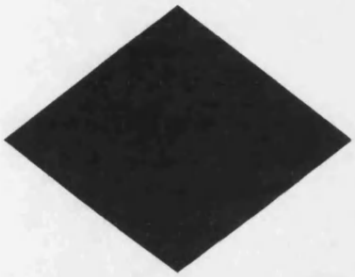

Model 2 - Rhomboid

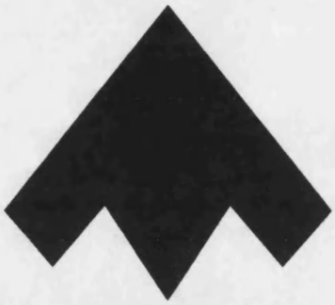

Model 4 - Y Wing

Notes: 1) Flow from top of page
2) '*' indicates reverse flow condition, i.e. Model 3* indicates Model 3 in the reverse configuration, with flow from the bottom of the page

Figure 4.1: Planforms of Models

Figure 4.2: Cross - Sections of Models

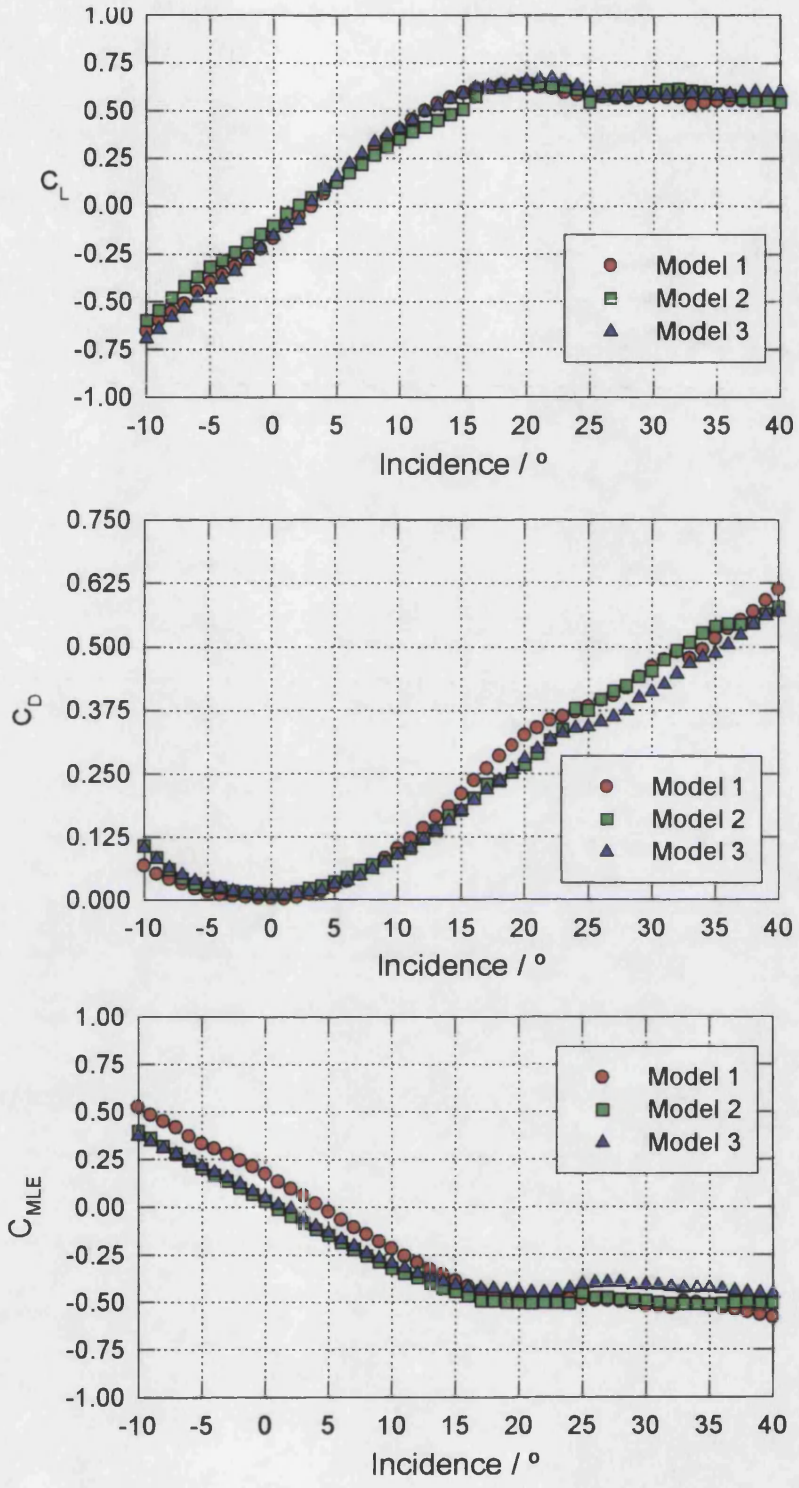

Figure 4.3: Forces and Moments for Models 1, 2 and 3

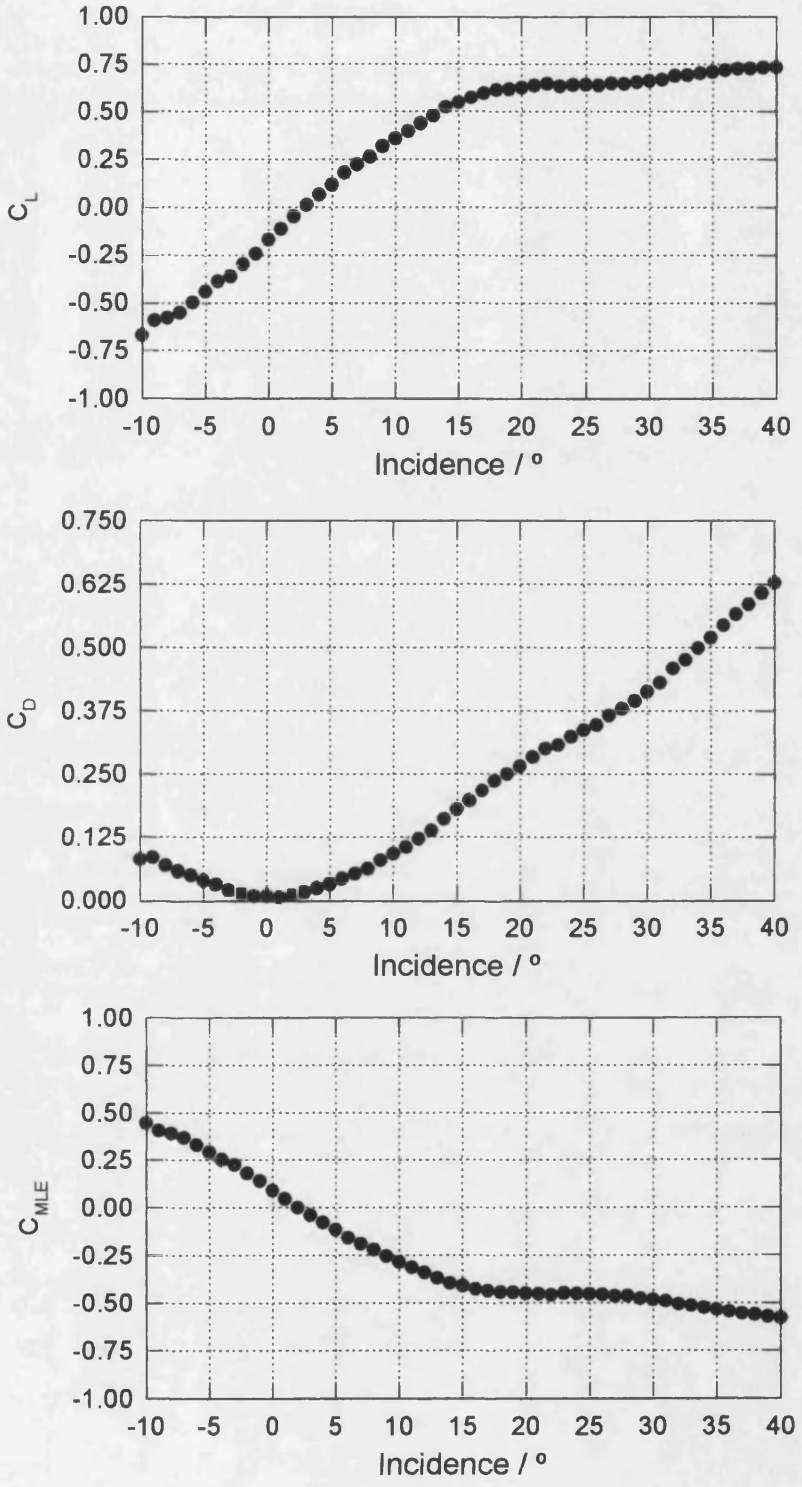

Figure 4.4: Forces and Moments for Model 3*

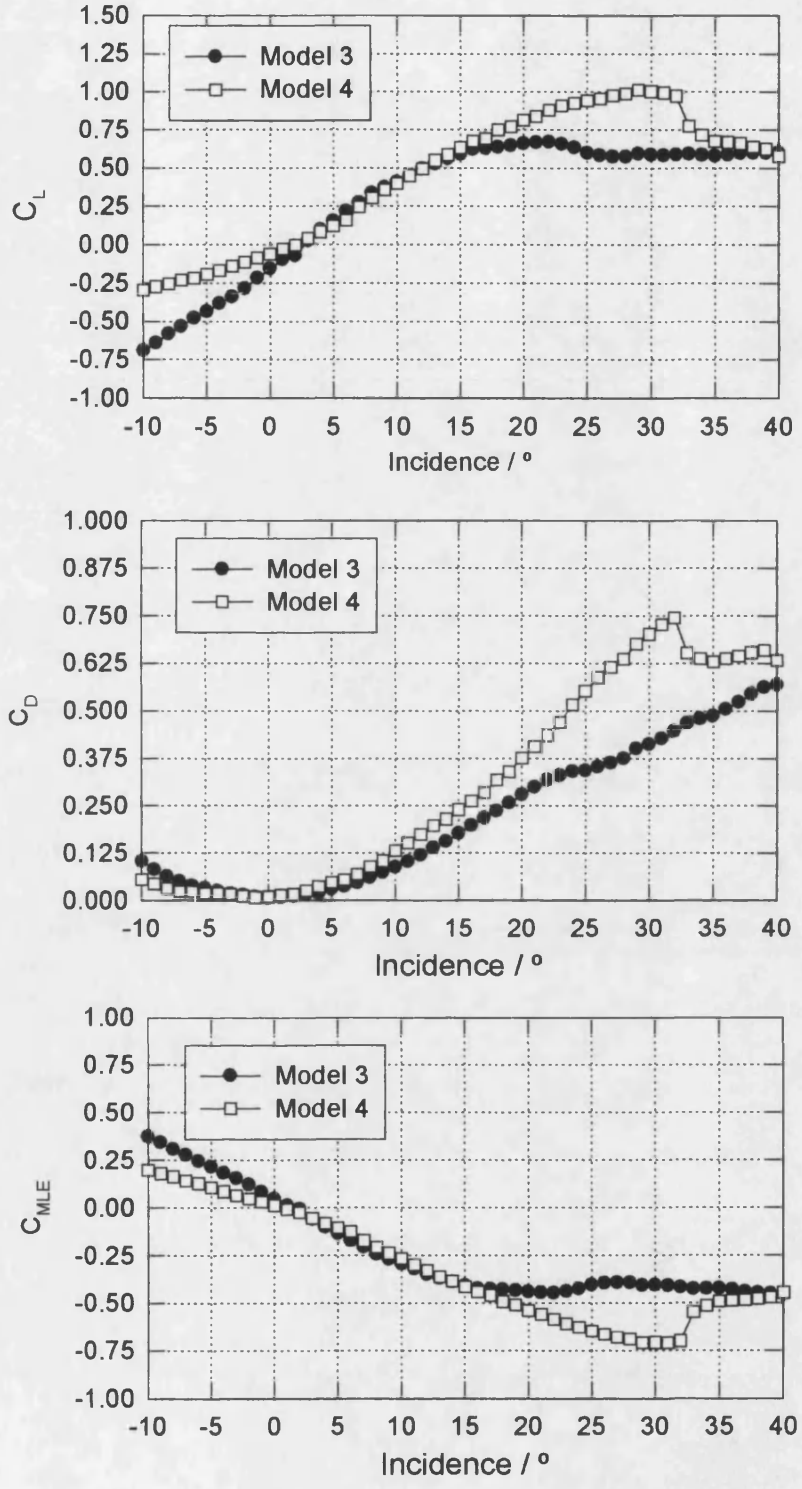

Figure 4.5: Comparison of Forces and Moments for Models 3 and 4

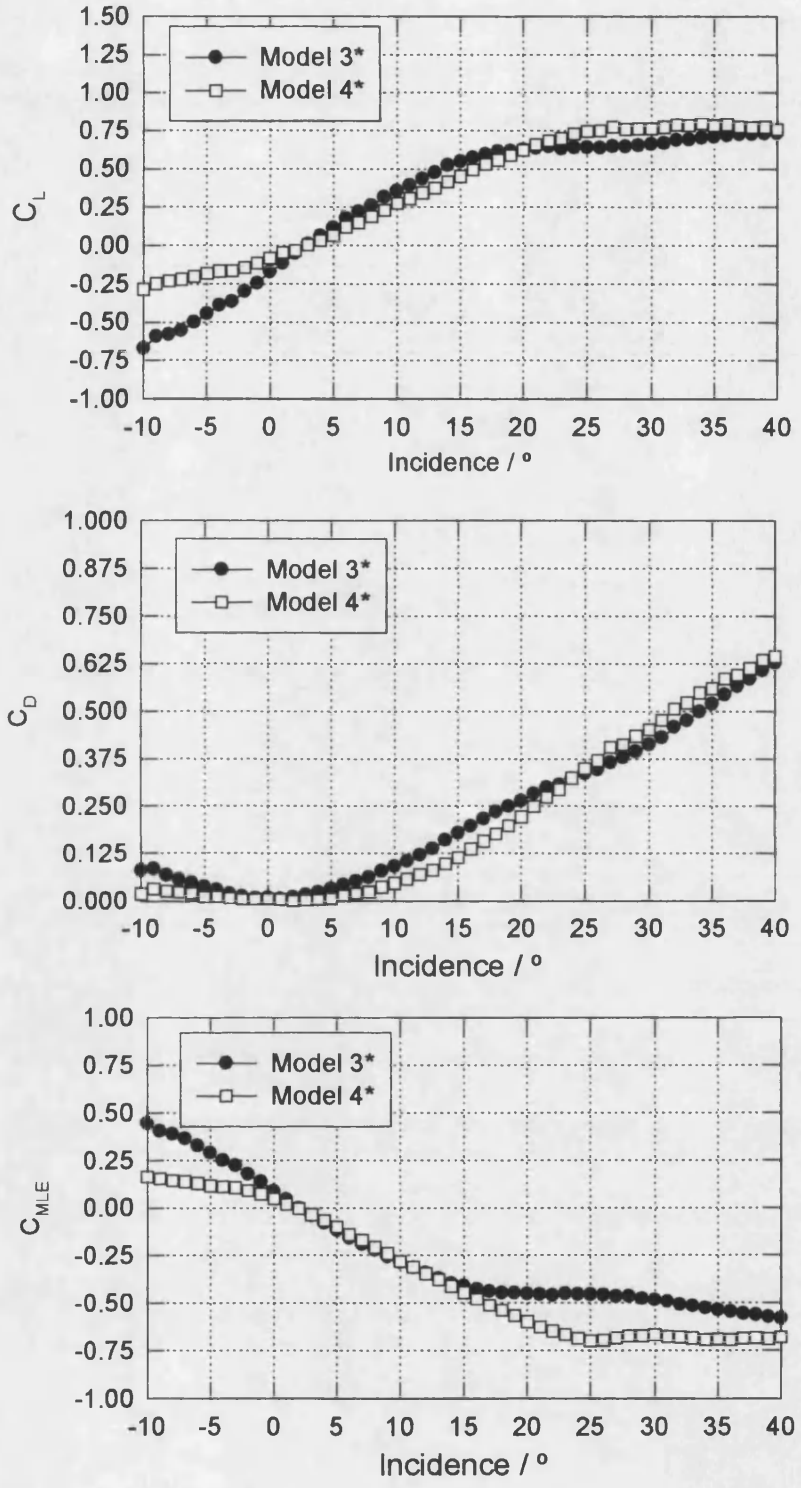

Figure 4.6: Comparison of Forces and Moments Acting on Models 3* and 4*

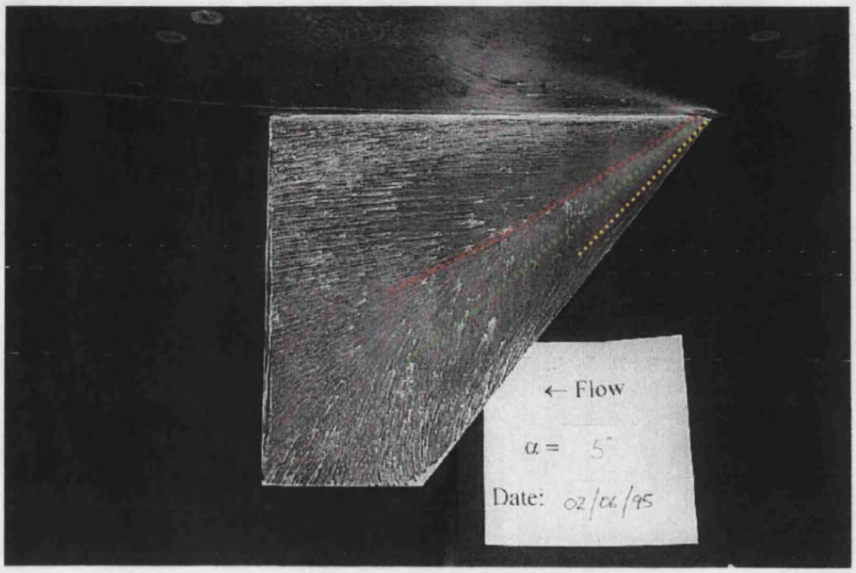

Primary Attachment
Trajectory of Vortex Core
Secondary Separation

Figure 4.7: Oilflow Visualisation Over Model 1 - α = 5 Degrees

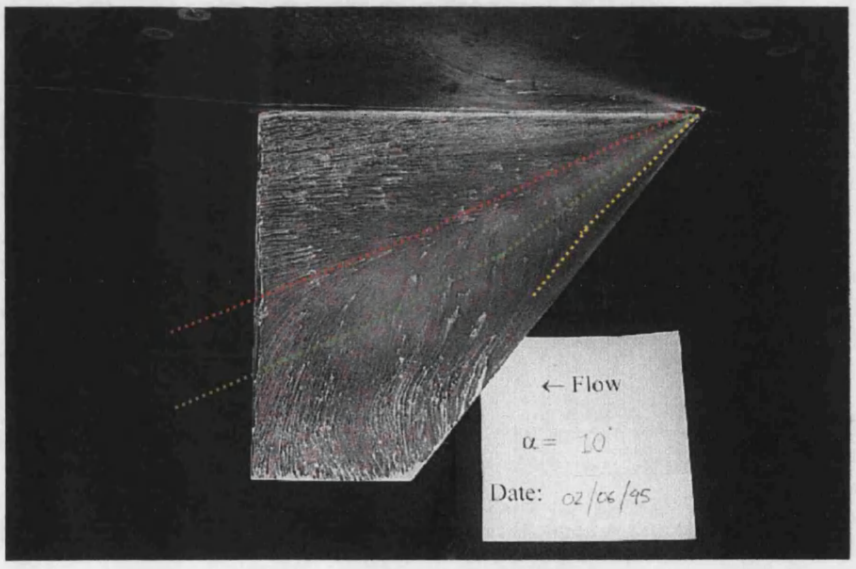

Primary Attachment
Trajectory of Vortex Core
Secondary Separation

Figure 4.8: Oilflow Visualisation Over Model 1 - α = 10 Degrees

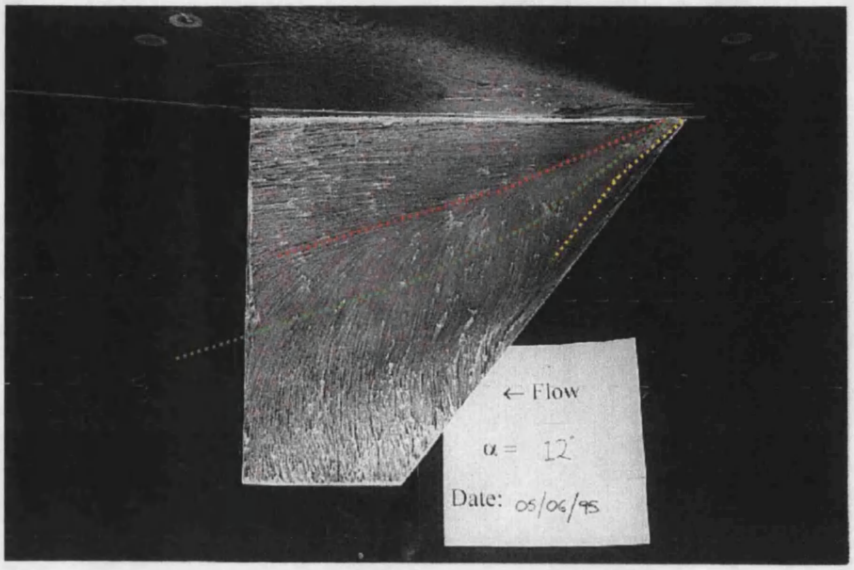

Primary Attachment
Trajectory of Vortex Core
Secondary Separation

Figure 4.9: Oilflow Visualisation Over Model 1 - α = 12 Degrees

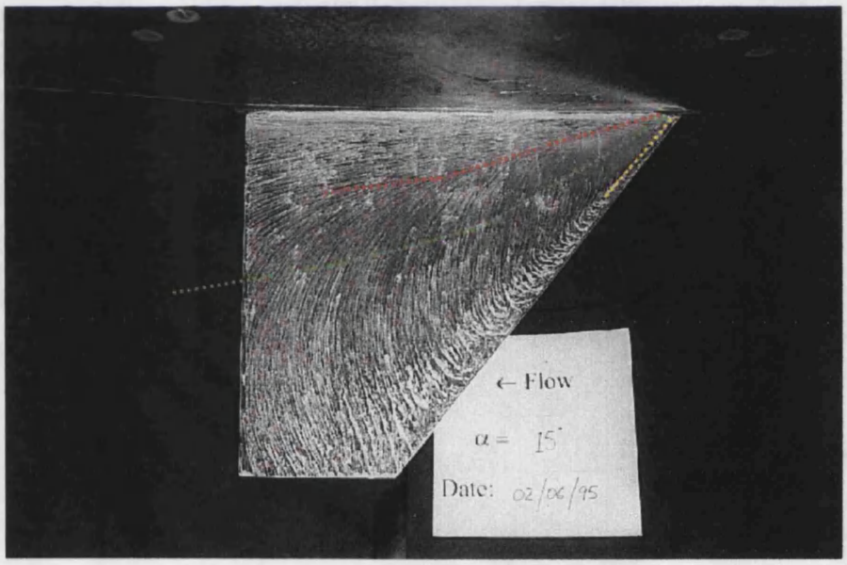

Primary Attachment
Trajectory of Vortex Core
Secondary Separation

Figure 4.10: Oilflow Visualisation Over Model 1 - α = 15 Degrees

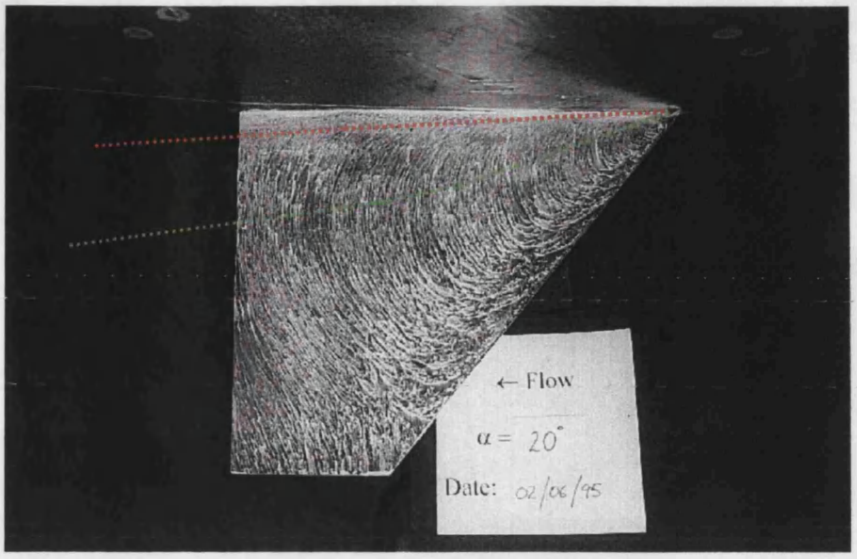

Primary Attachment
Trajectory of Vortex Core
Secondary Separation

Figure 4.11: Oilflow Visualisation Over Model 1 - α = 20 Degrees

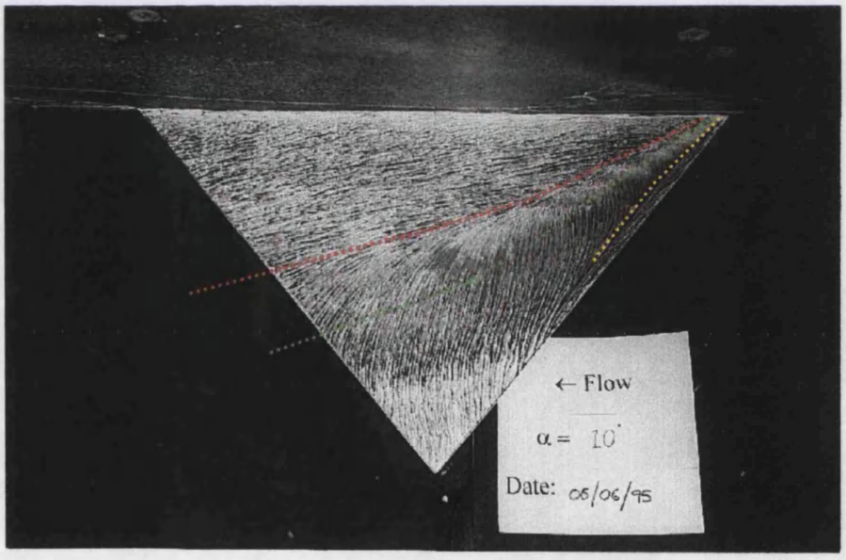

Primary Attachment
Trajectory of Vortex Core
Secondary Separation

Figure 4.12: Oilflow Visualisation Over Model 2 - α = 10 Degrees

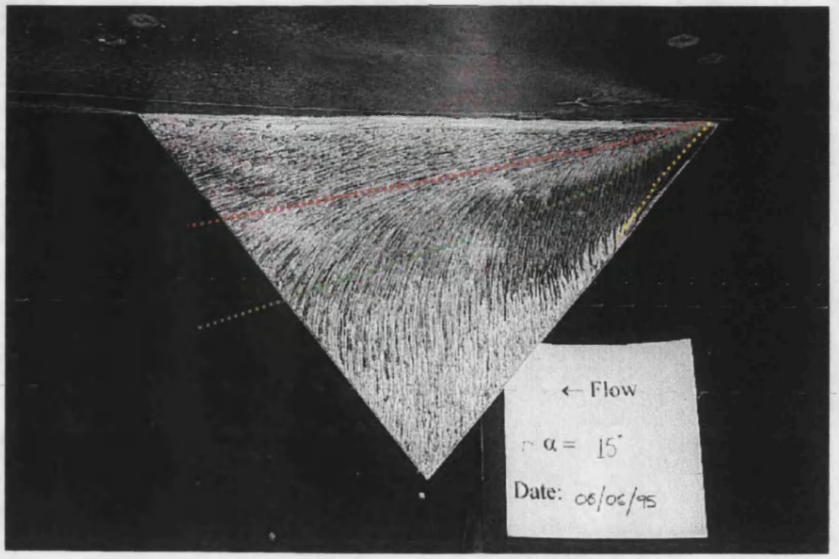

Primary Attachment
Trajectory of Vortex Core
Secondary Separation

Figure 4.13: Oilflow Visualisation Over Model 2 - α = 15 Degrees

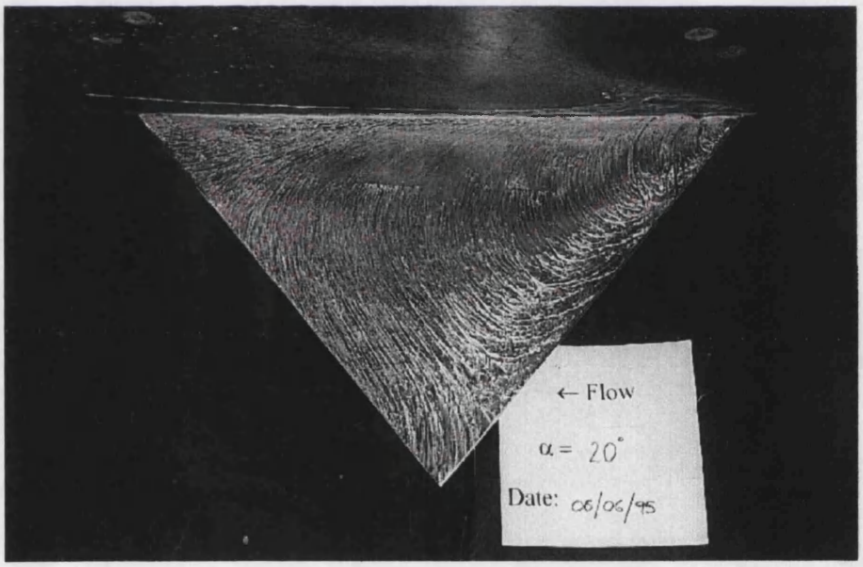

Primary Attachment
Trajectory of Vortex Core
Secondary Separation

Figure 4.14: Oilflow Visualisation Over Model 2 - α = 20 Degrees

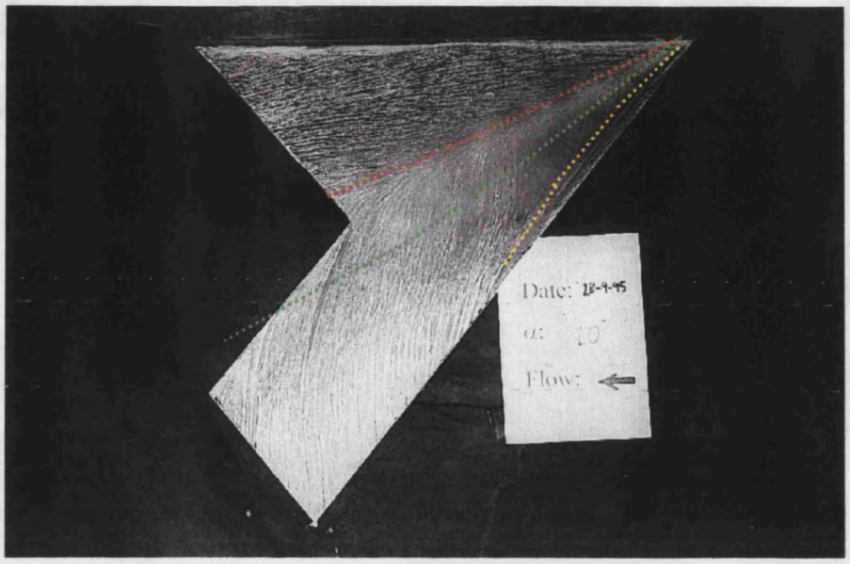

Primary Attachment
Trajectory of Vortex Core
Secondary Separation

Figure 4.15: Oilflow Visualisation Over Model 3 - α = 10 Degrees

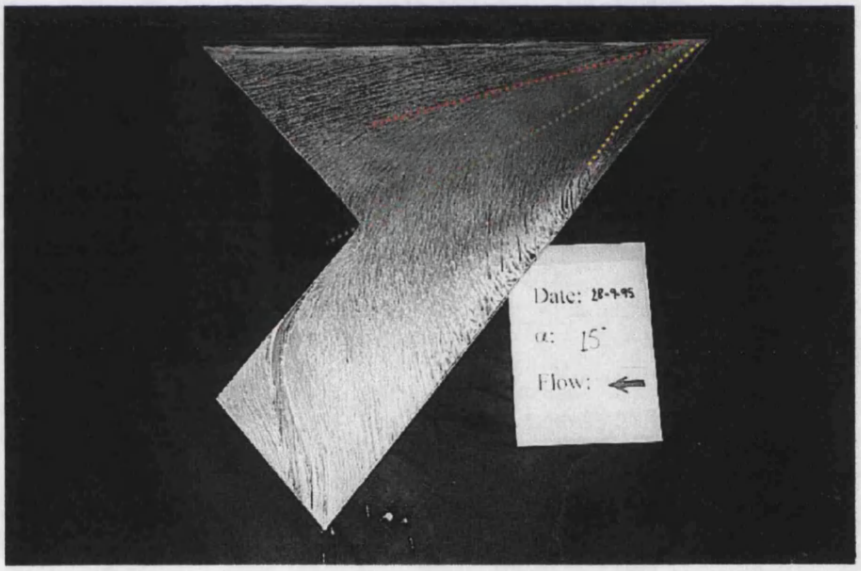

Primary Attachment
Trajectory of Vortex Core
Secondary Separation

Figure 4.16: Oilflow Visualisation Over Model 3 - α = 15 Degrees

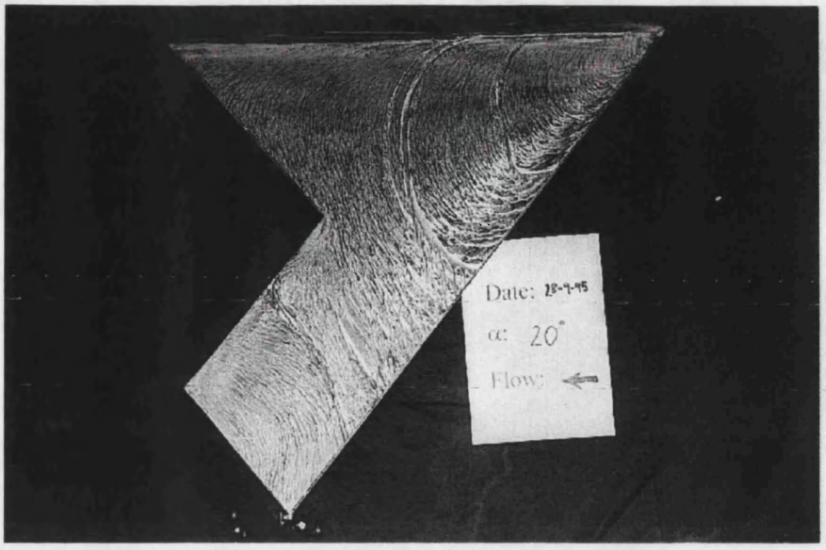

Primary Attachment
Trajectory of Vortex Core
Secondary Separation

Figure 4.17: Oilflow Visualisation Over Model 3 - α = 20 Degrees

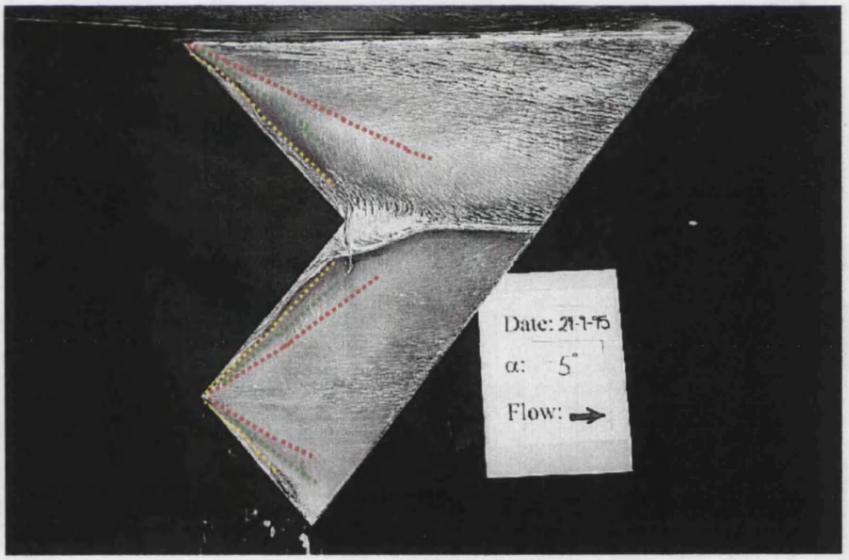

Primary Attachments
Trajectory of Vortex Cores
Secondary Separations

Figure 4.18: Oilflow Visualisation Over Model 3* - α = 5 Degrees

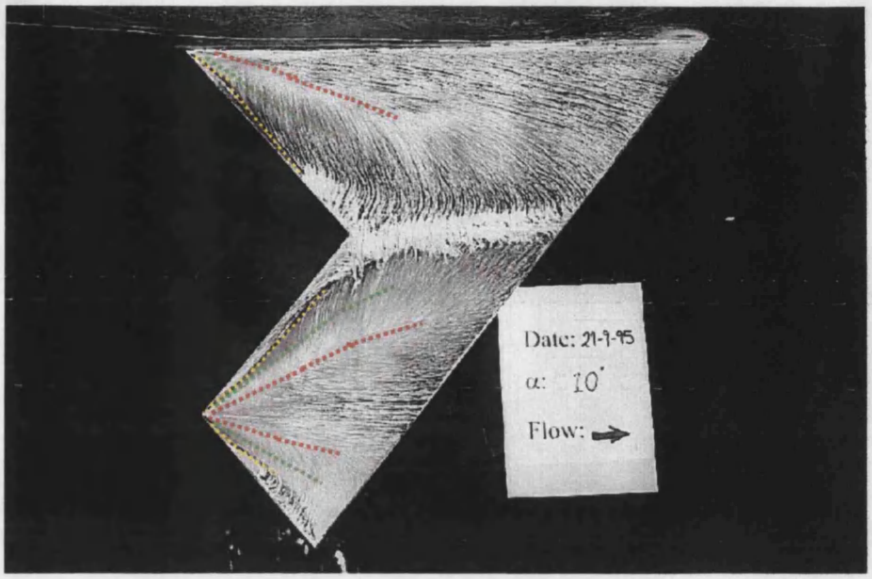

Primary Attachments
Trajectory of Vortex Cores
Secondary Separations

Figure 4.19: Oilflow Visualisation Over Model 3* - α = 10 Degrees

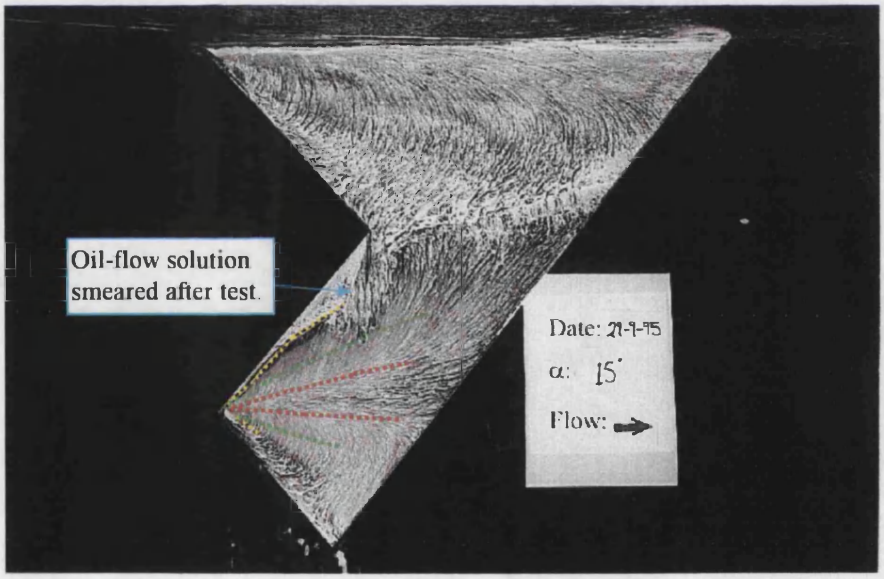

Primary Attachments
Trajectory of Vortex Cores
Secondary Separations

Figure 4.20: Oilflow Visualisation Over Model 3* - α = 15 Degrees

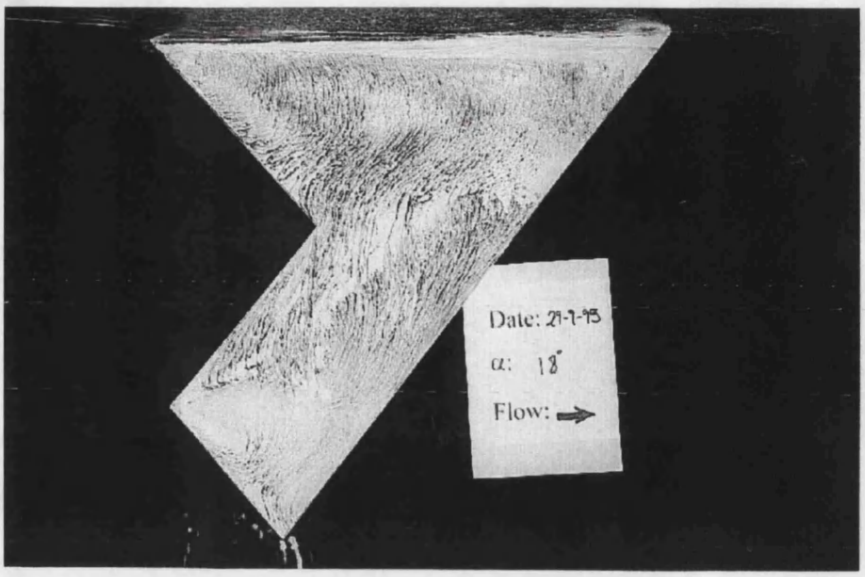

Primary Attachments
Trajectory of Vortex Cores
Secondary Separations

Figure 4.21: Oilflow Visualisation Over Model 3* - α = 18 Degrees

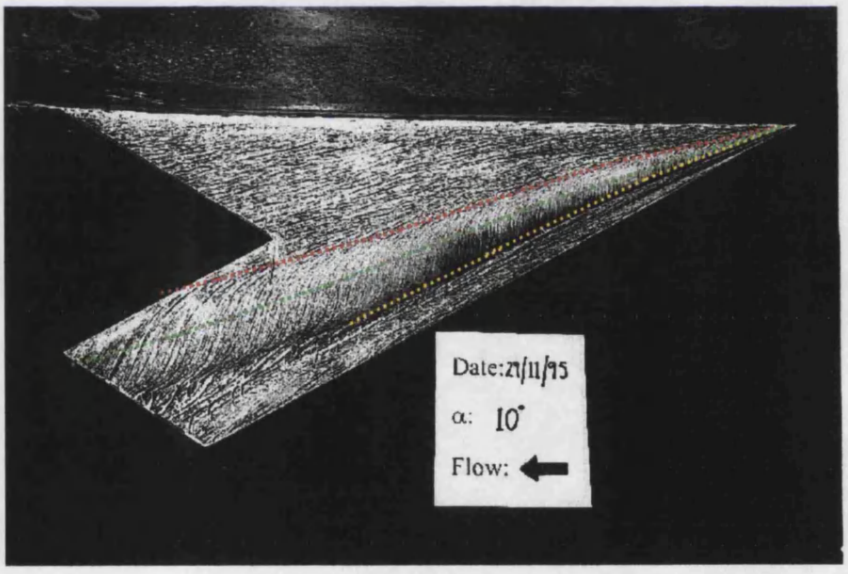

Primary Attachments
Trajectory of Vortex Cores
Secondary Separations

Figure 4.22: Oilflow Visualisation Over Model 4 - α = 10 Degrees

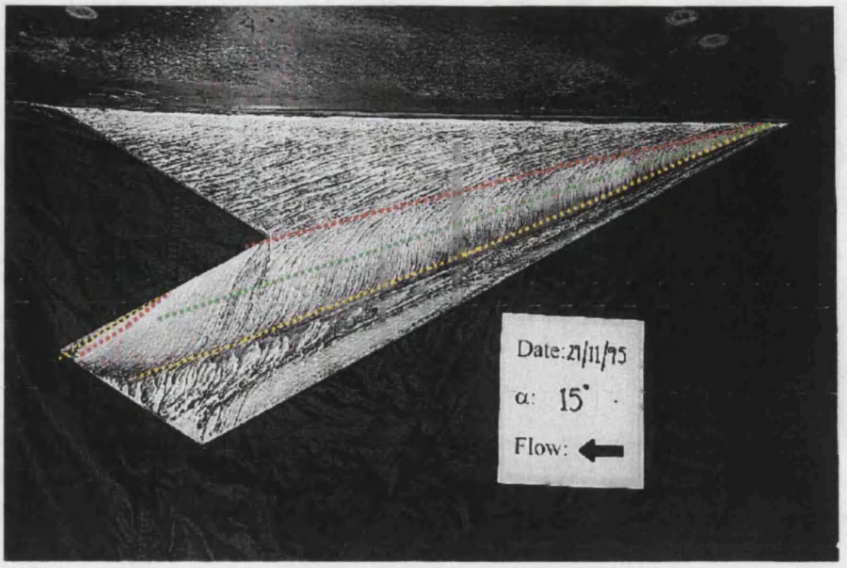

Primary Attachments
Trajectory of Vortex Cores
Secondary Separations

Figure 4.23: Oilflow Visualisation Over Model 4 - α = 15 Degrees

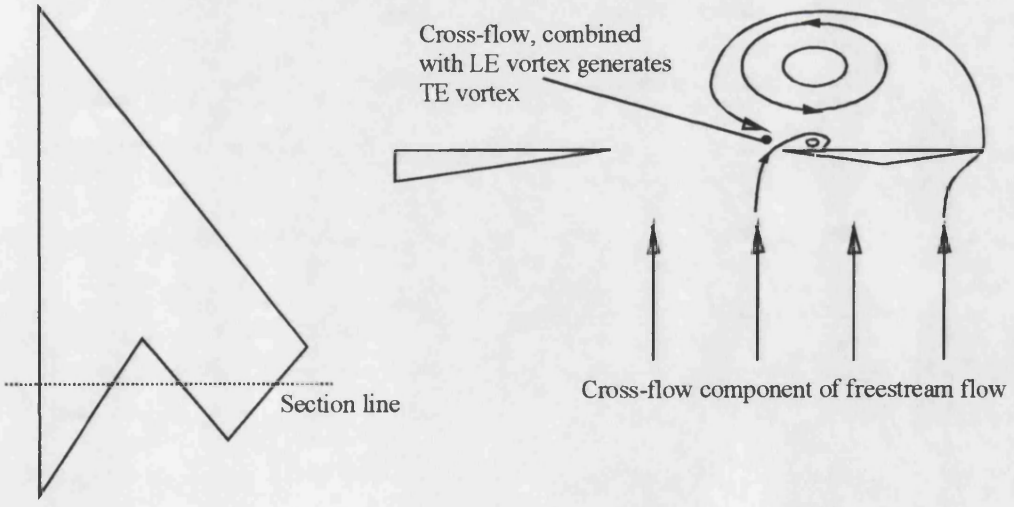

Figure 4.24: Generation of Trailing Edge Vortex

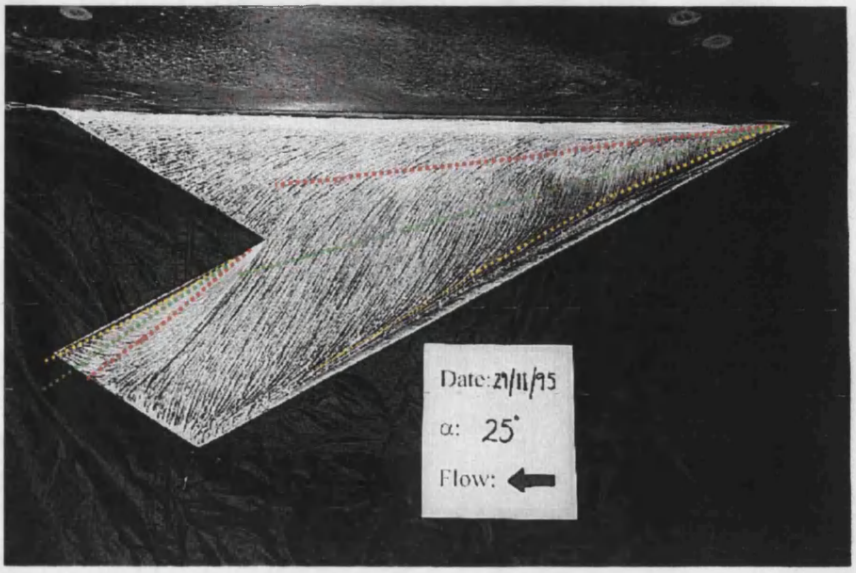

Primary Attachments
Trajectory of Vortex Cores
Secondary Separations

Figure 4.25: Oilflow Visualisation Over Model 4 - α = 25 Degrees

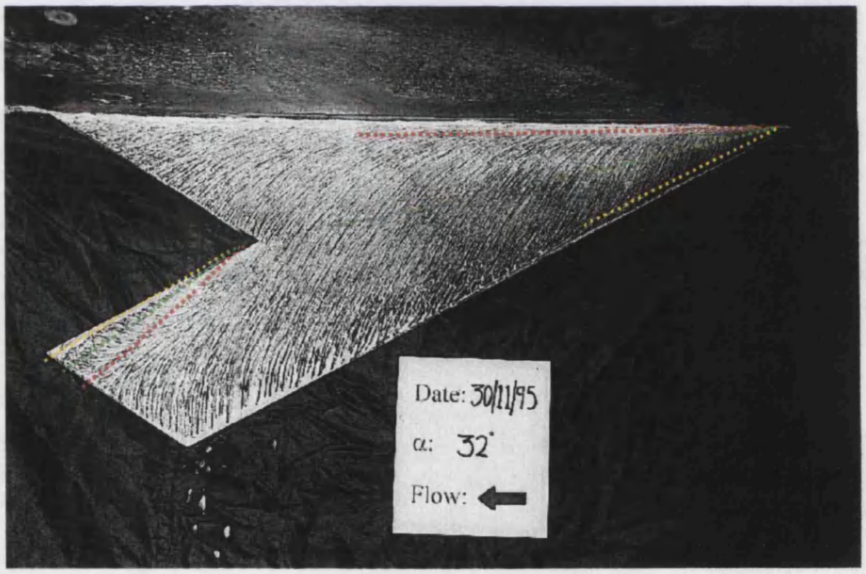

Primary Attachments
Trajectory of Vortex Cores
Secondary Separations

Figure 4.26: Oilflow Visualisation Over Model 4 - α = 32 Degrees

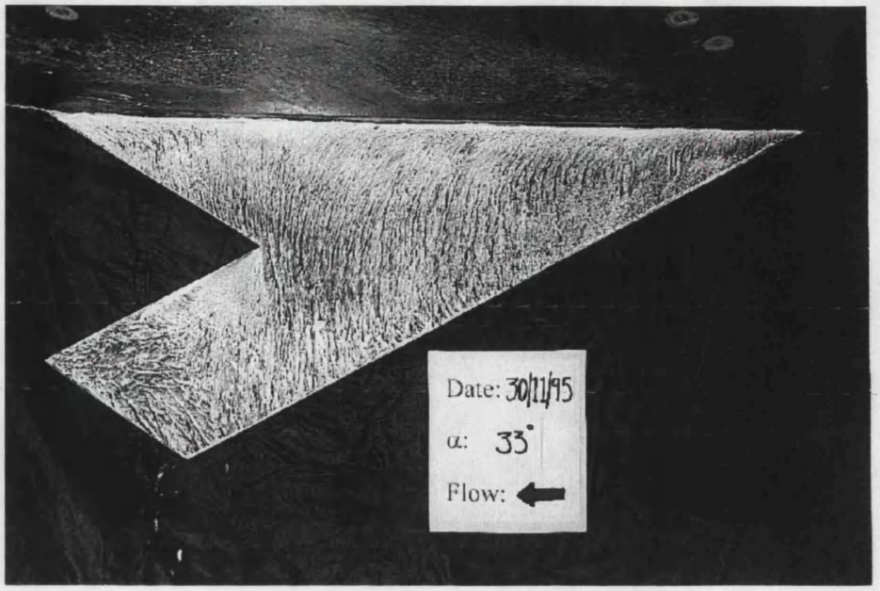

Primary Attachments
Trajectory of Vortex Cores
Secondary Separations

Figure 4.27: Oilflow Visualisation Over Model 4 - α = 33 Degrees

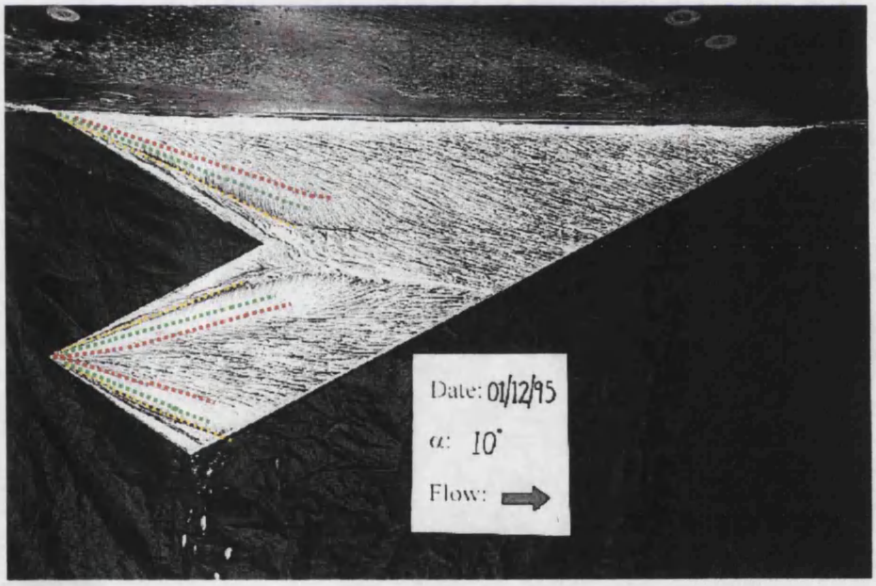

Primary Attachments
Trajectory of Vortex Cores
Secondary Separations

Figure 4.28: Oilflow Visualisation Over Model 4* - α = 10 Degrees

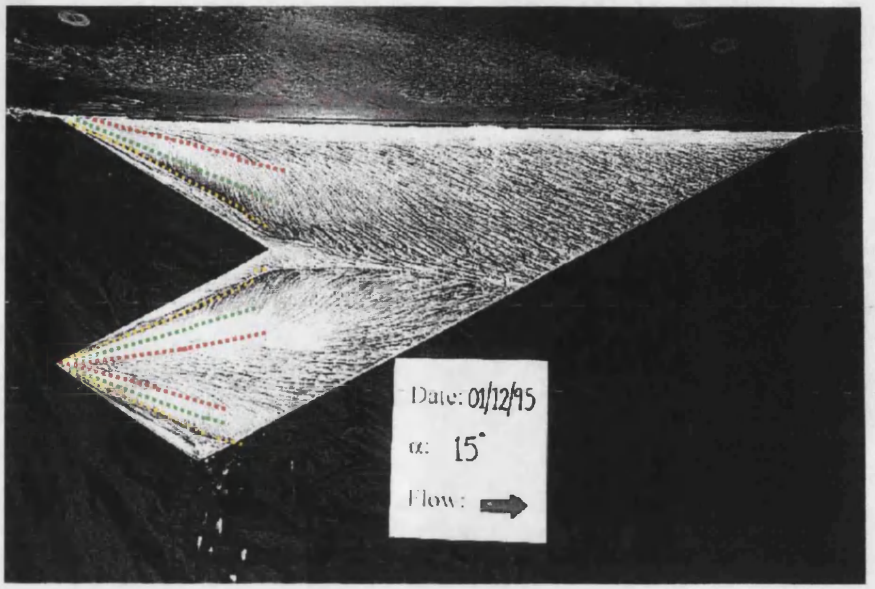

Primary Attachments
Trajectory of Vortex Cores
Secondary Separations

Figure 4.29: Oilflow Visualisation Over Model 4* - α = 15 Degrees

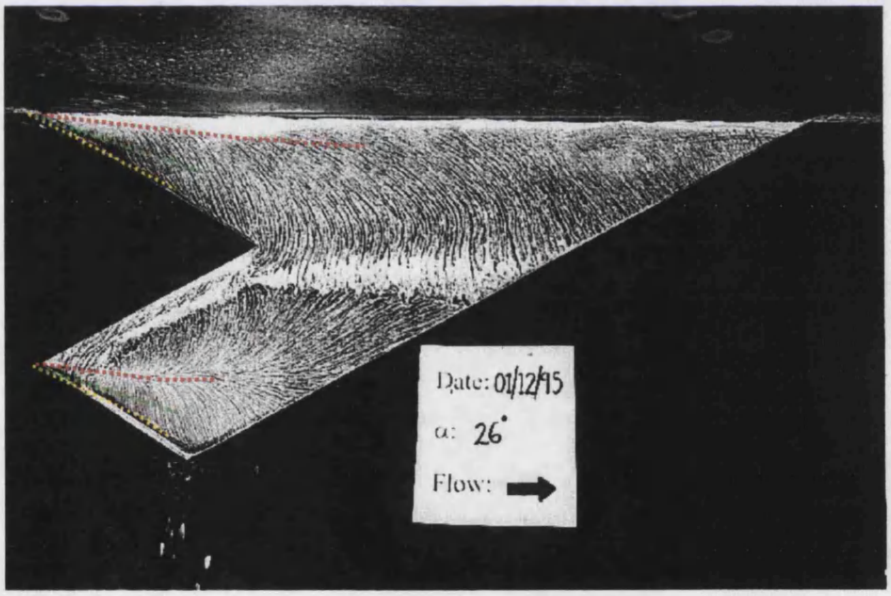

Primary Attachments
Trajectory of Vortex Cores
Secondary Separations

Figure 4.30: Oilflow Visualisation Over Model 4* - α = 26 Degrees

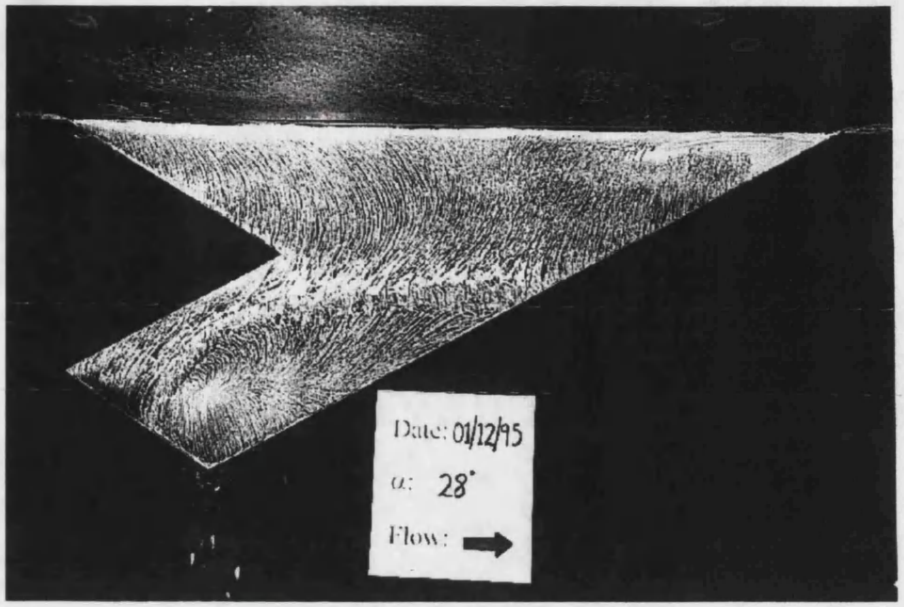

Primary Attachments
Trajectory of Vortex Cores
Secondary Separations

Figure 4.31: Oilflow Visualisation Over Model 4* - α = 28 Degrees

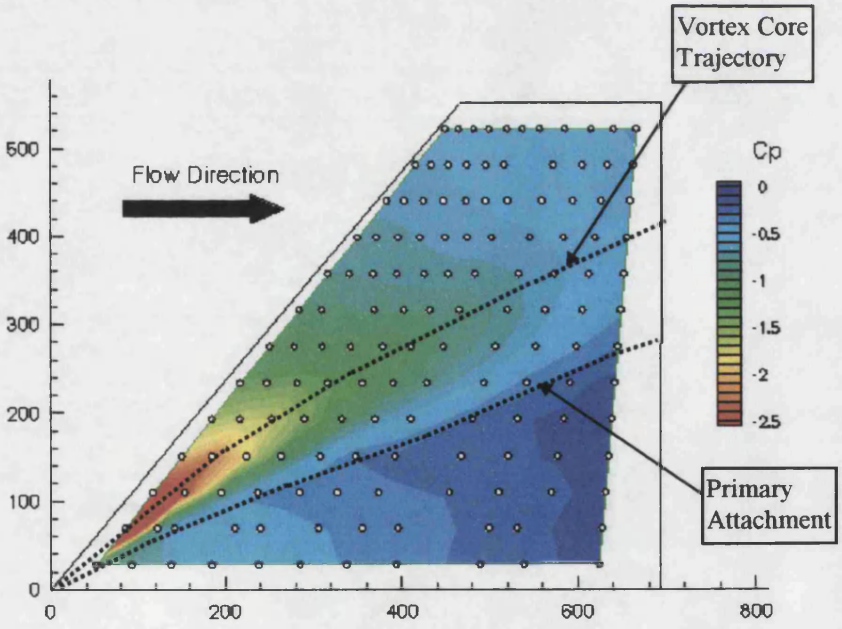

Figure 4.32: Steady Pressures - Model 1, α = 10 Degrees

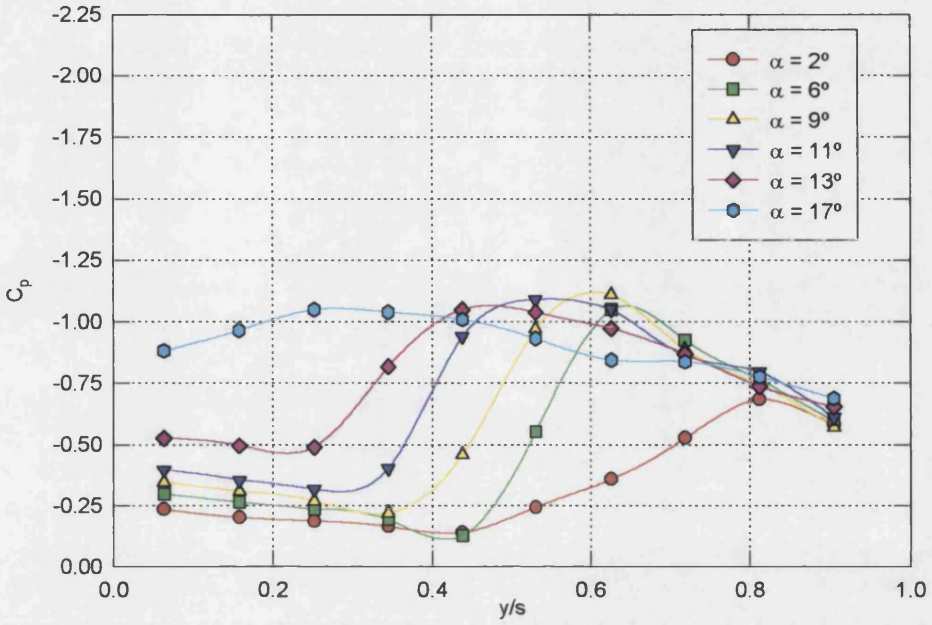

Figure 4.33: Variation of Steady Pressures with Incidence, Model 1, $x/x_t = 0.8$

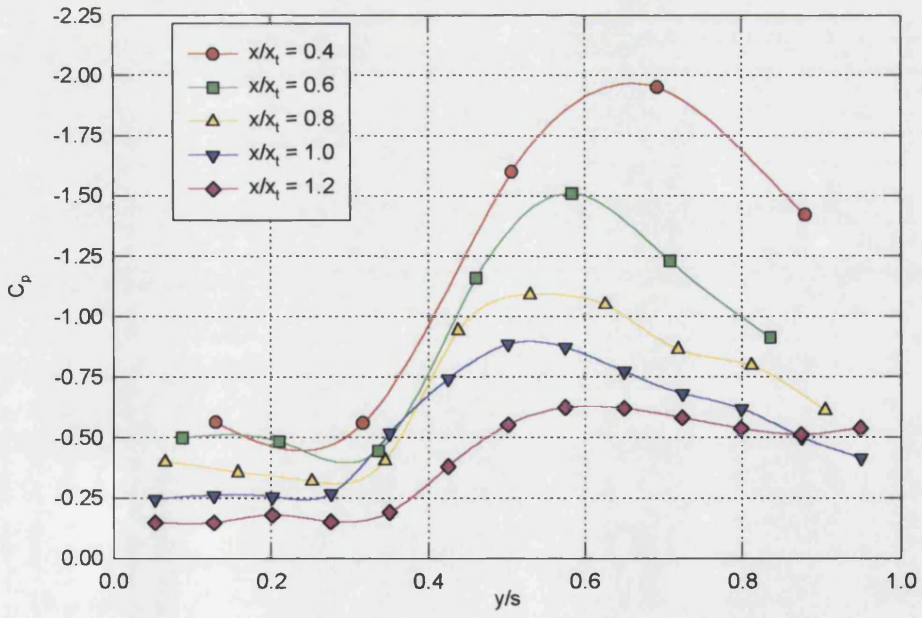

Figure 4.34: Variation of Steady Pressures with Location of Spanwise Slice, Model 1, $\alpha = 11$ Degrees

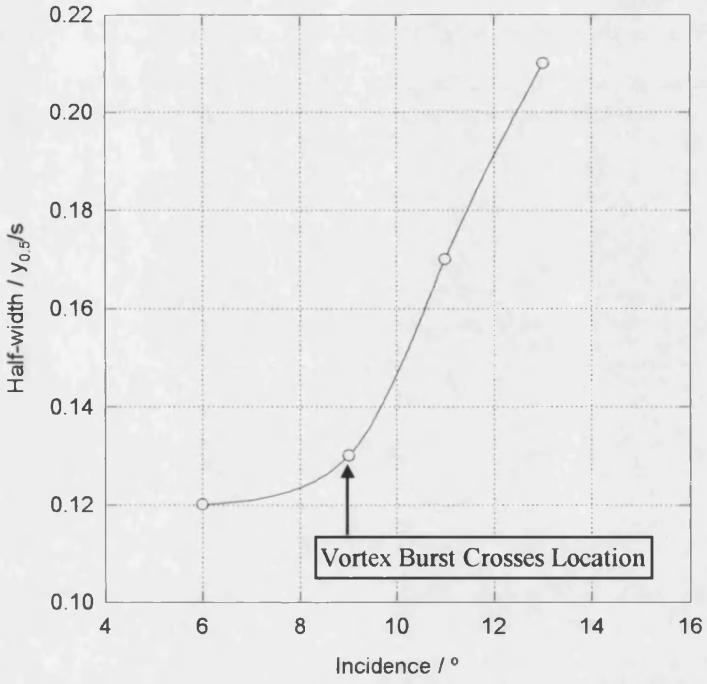

Figure 4.35: Variation of 'Half-Width' with Incidence, Model 1, $x/x_t = 0.8$

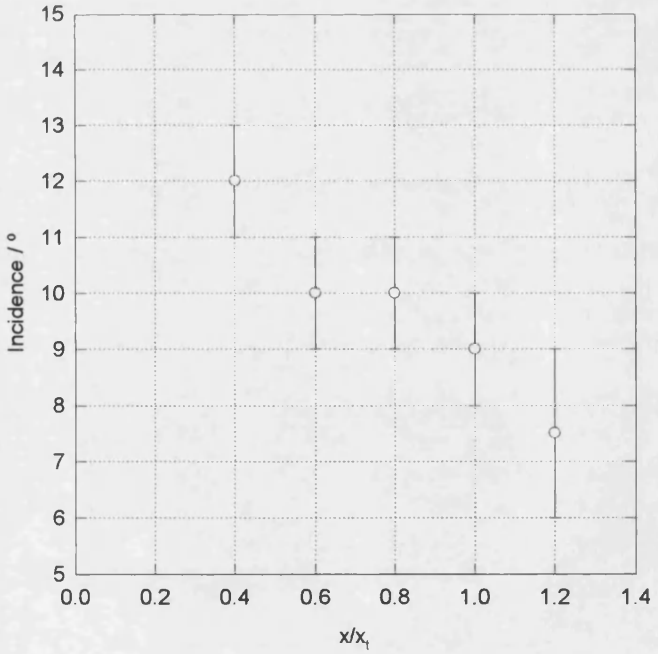

Figure 4.36: Incidence at which Vortex Burst Crosses Chordwise Location, Model 1

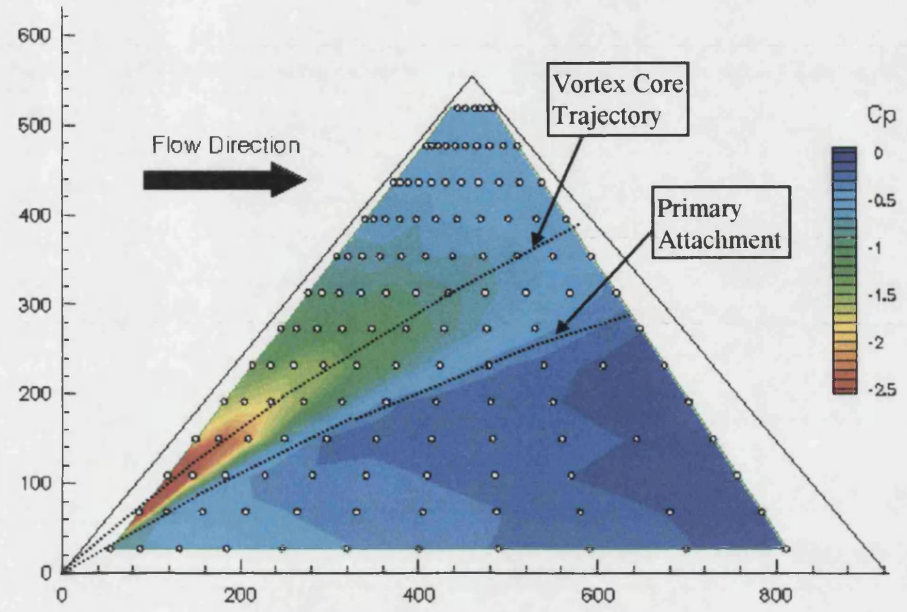

Figure 4.37: Mean Pressures - Model 2, $\alpha = 10°$

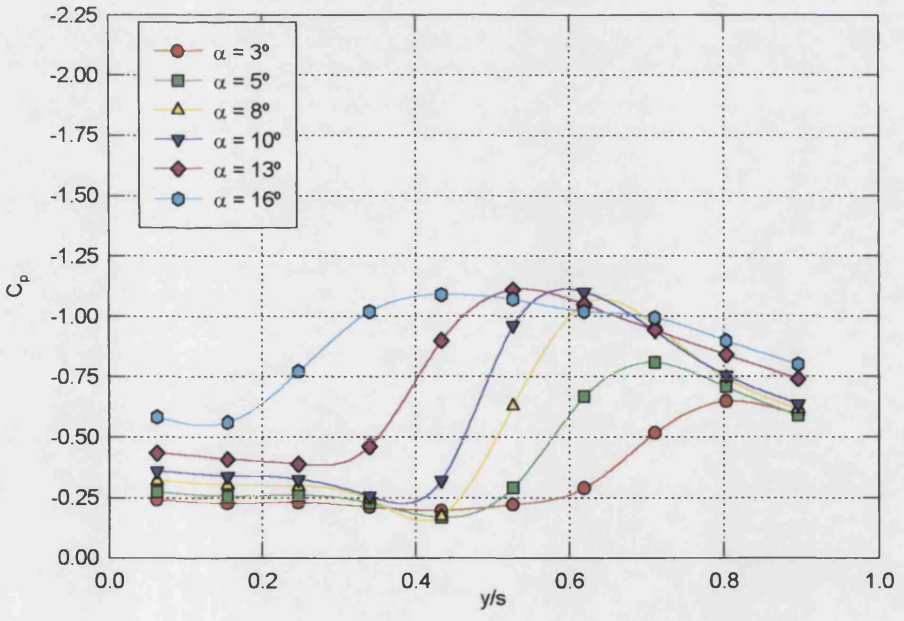

Figure 4.38: Variation of Steady Pressures with Incidence,
Model 2, $x/x_t = 0.8$

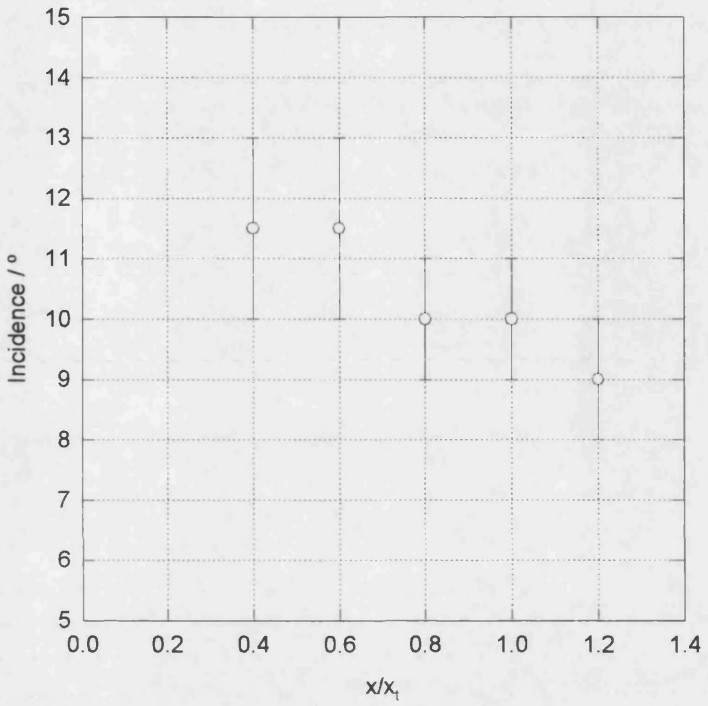

Figure 4.39: Incidence at which Vortex Burst Crosses Chordwise Location, Model 2

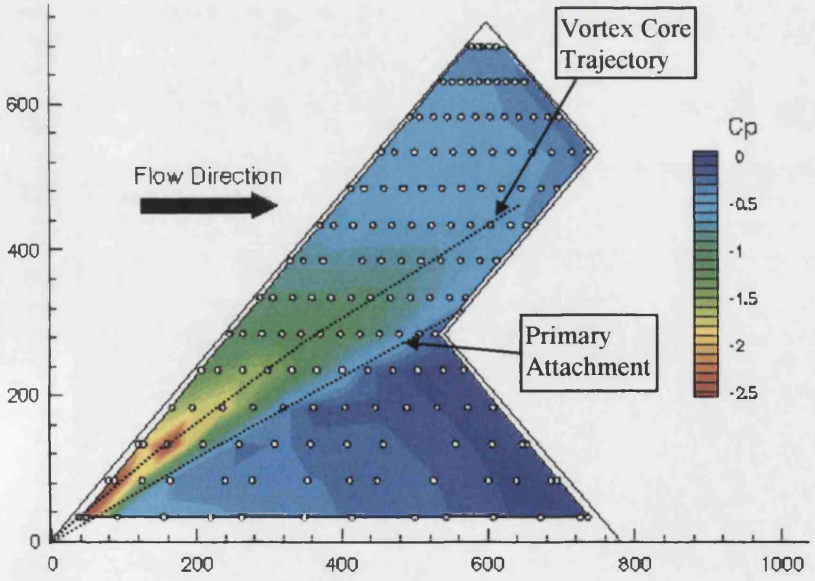

Figure 4.40: Mean Pressures - Model 3, $\alpha = 10°$

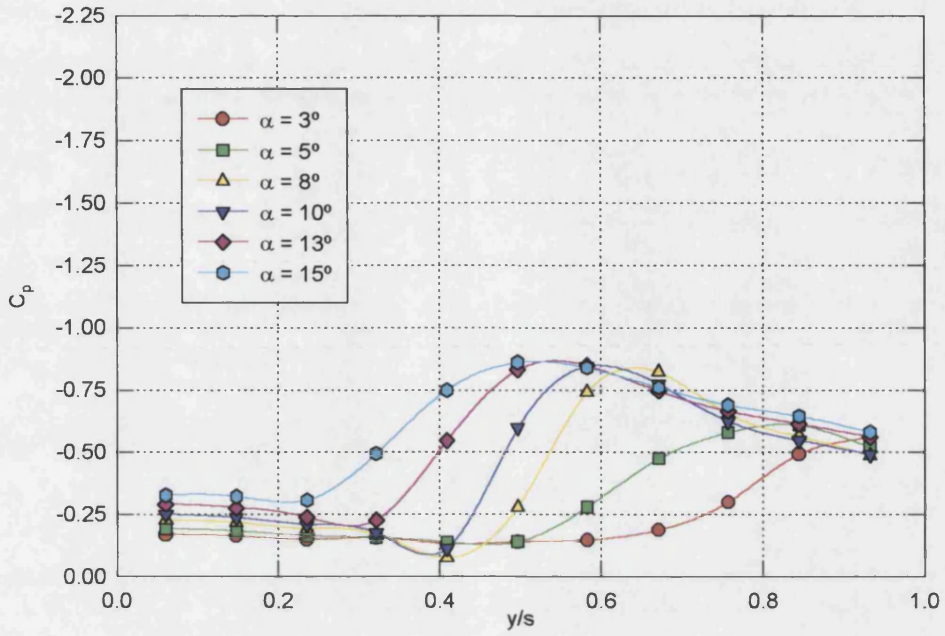

Figure 4.41: Variation of Steady Pressures with Incidence, Model 3, $x/x_t = 0.8$

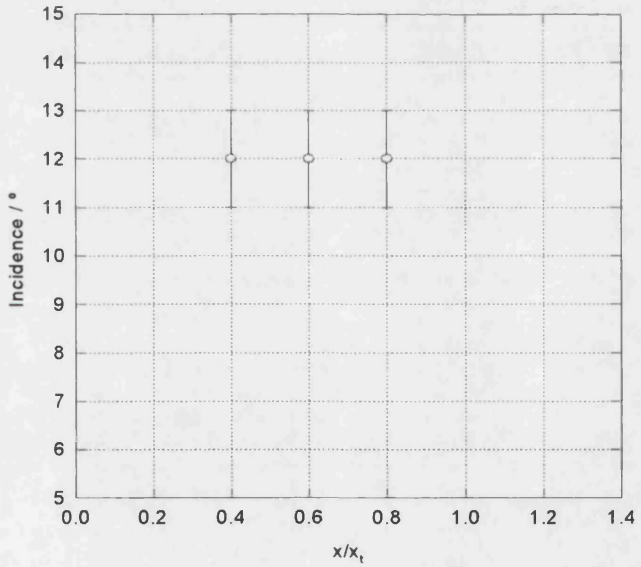

Figure 4.42: Incidence at which Vortex Burst Crosses Chordwise Location, Model 3

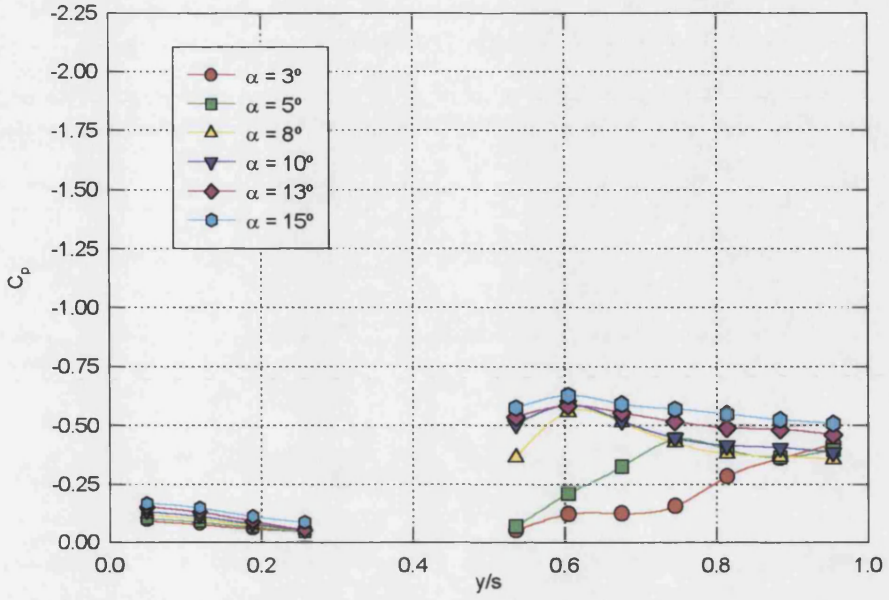

Figure 4.43: Variation of Steady Pressures Downstream of Reverse Apex with Incidence, Model 3, $x/x_t = 1.0$

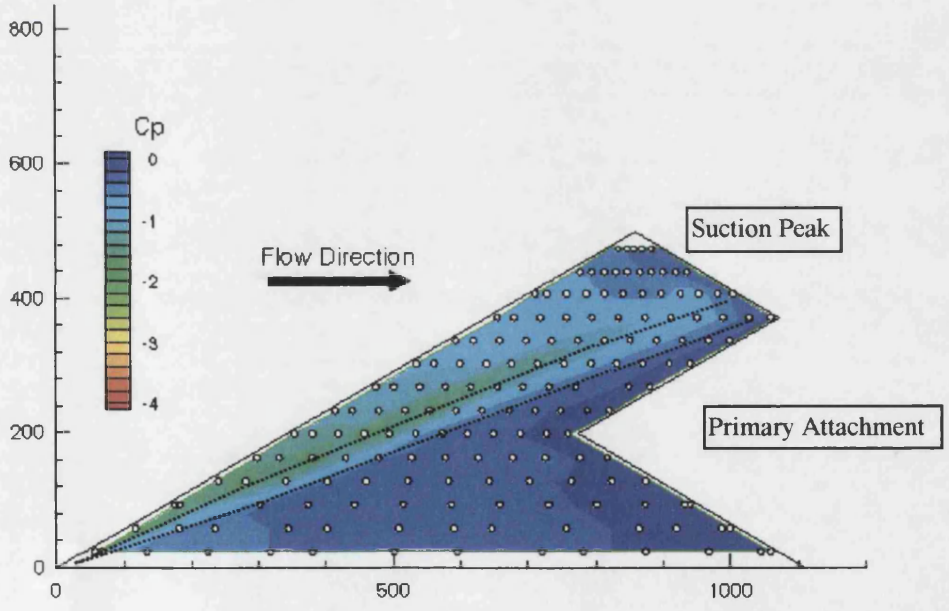

Figure 4.44: Mean Pressures - Model 4, $\alpha = 10°$

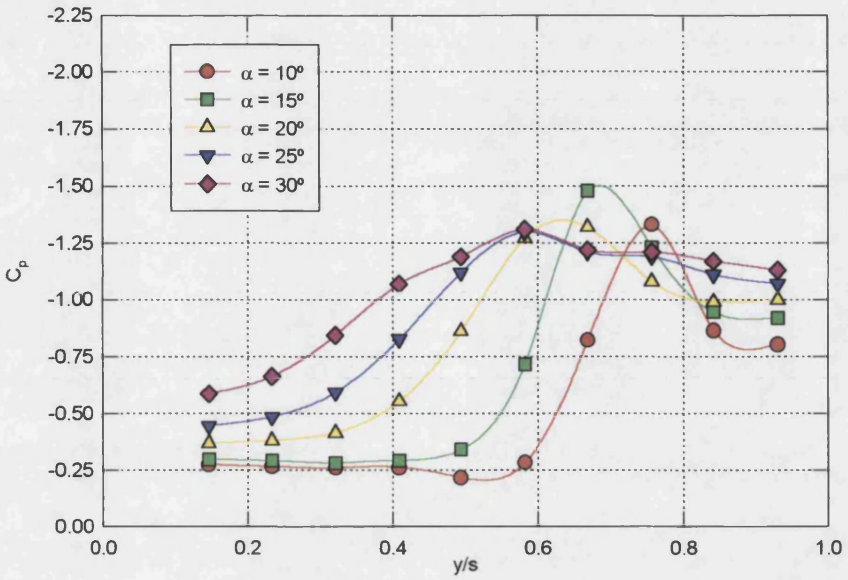

Figure 4.45: Variation of Steady Pressure with Incidence, Model 4, $x/x_t = 0.8$

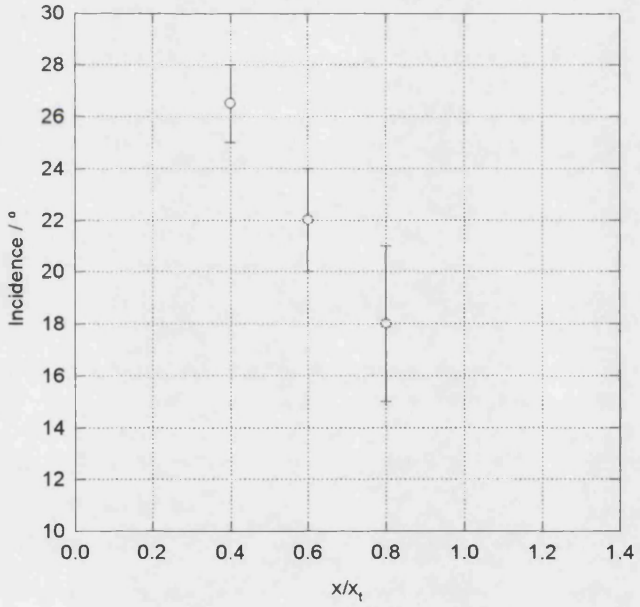

Figure 4.46: Incidence at which Vortex Burst Crosses Chordwise Location, Model 4

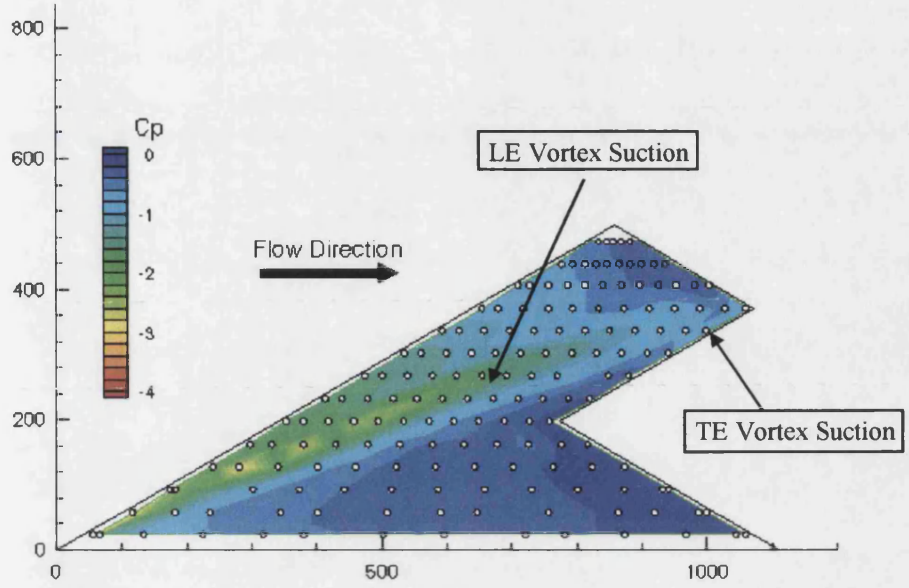

Figure 4.47: Mean Pressures - Model 4, $\alpha = 15°$

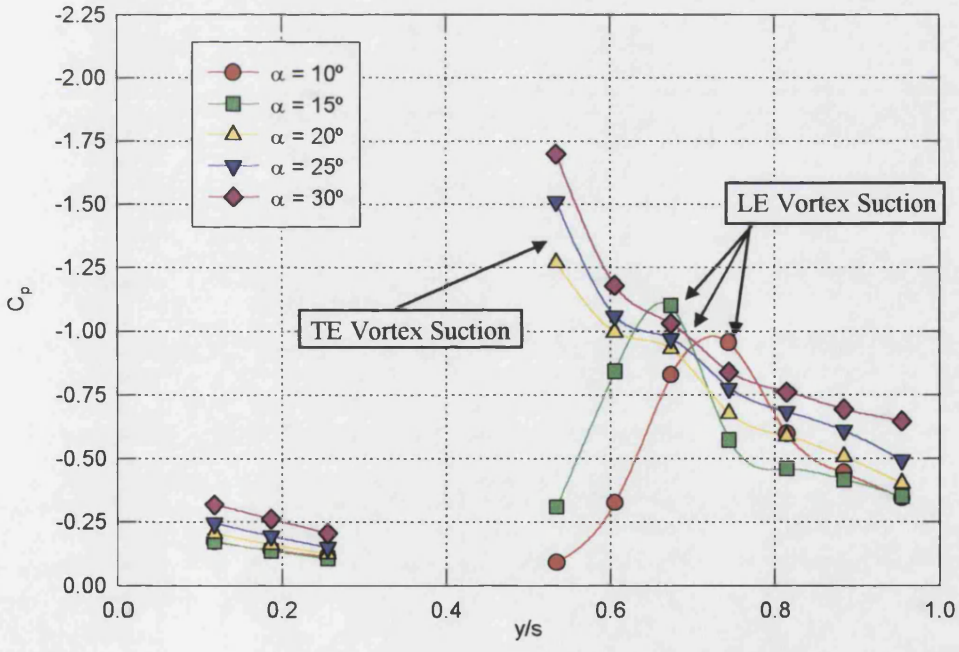

Figure 4.48: Variation of Steady Pressure with Incidence, Model 4, $x/x_t = 1.0$

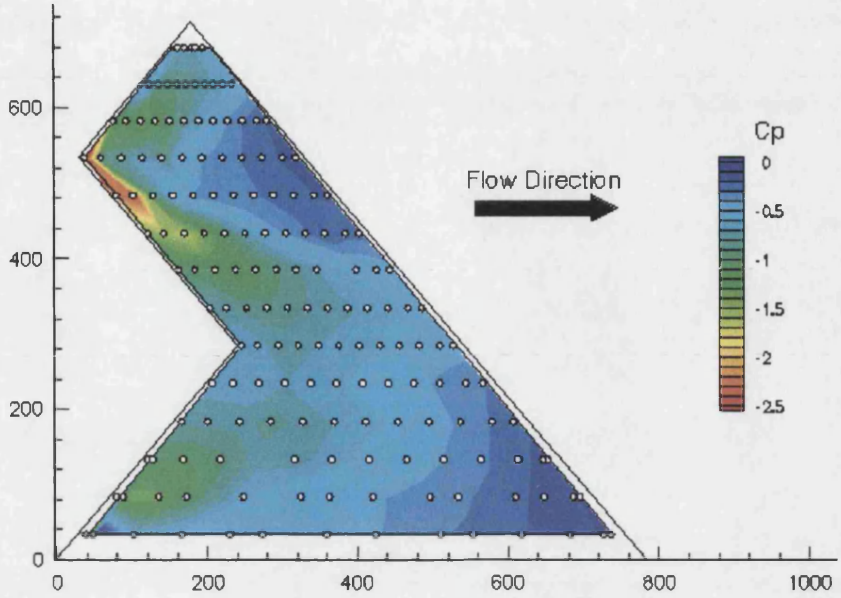

Figure 4.49: Mean Pressures - Model 3*, $\alpha = 13°$

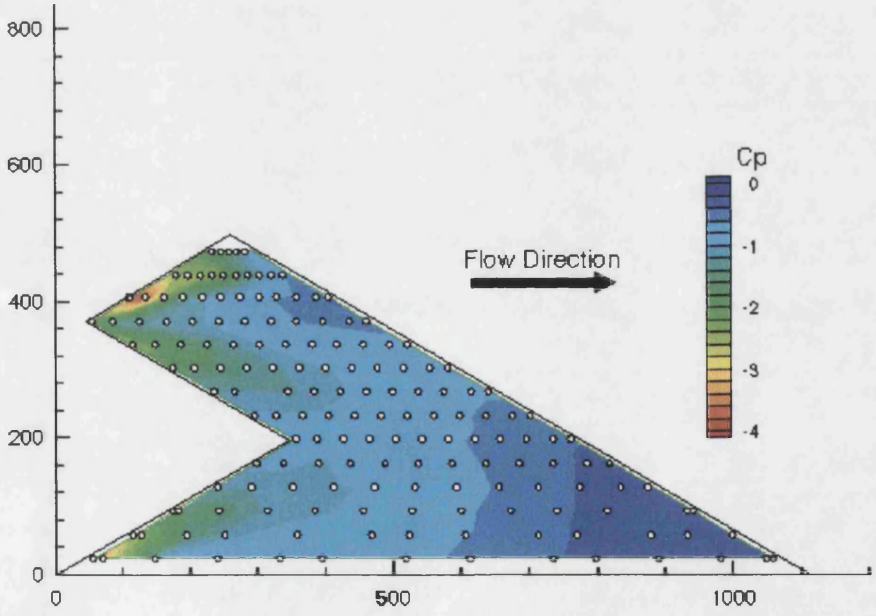

Figure 4.50: Mean Pressures - Model 4*, $\alpha = 25°$

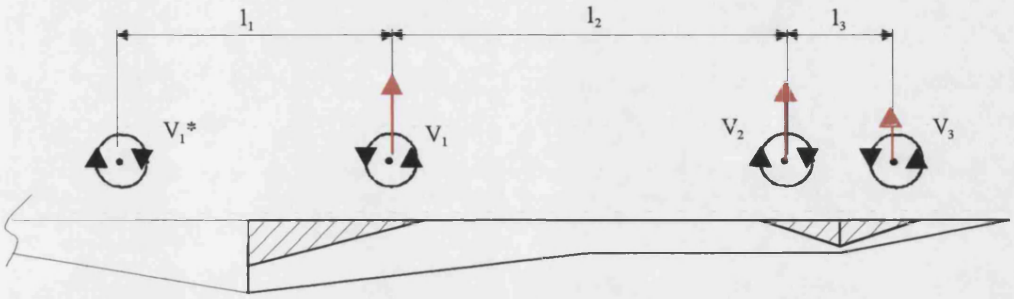

Figure 4.51: Induced Velocities due to Vortex Interactions

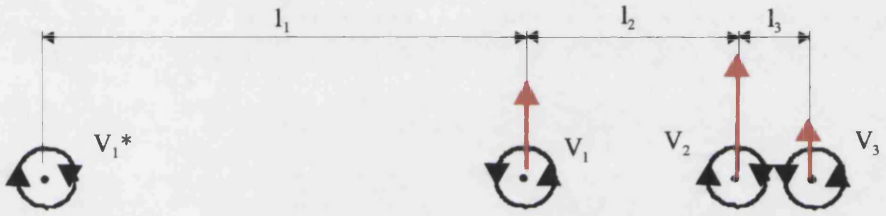

a) Geometry 1

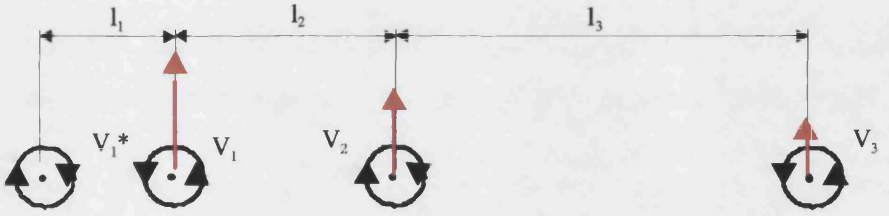

b) Geometry 2

Figure 4.52: Effect of Geometry on Induced Velocities

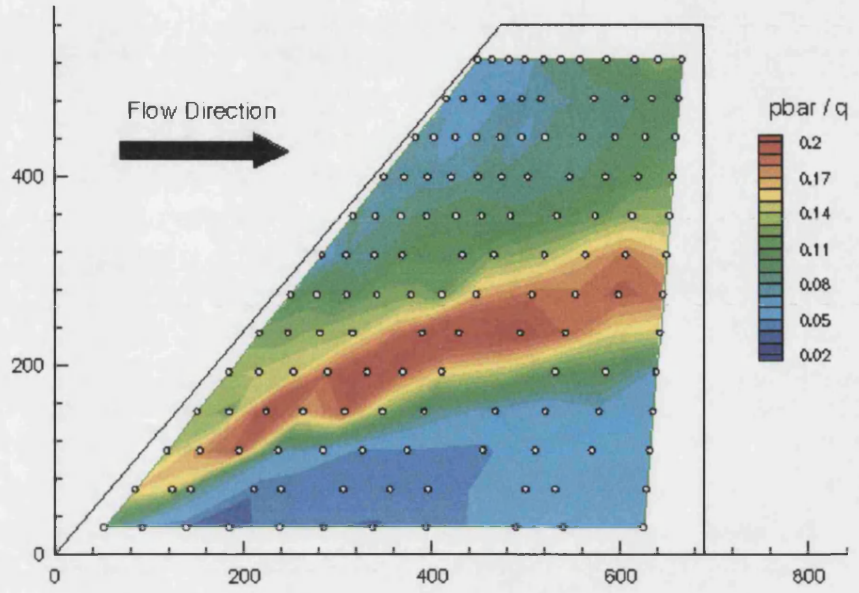

Figure 4.53: RMS Pressures, Model 1, $\alpha = 11°$

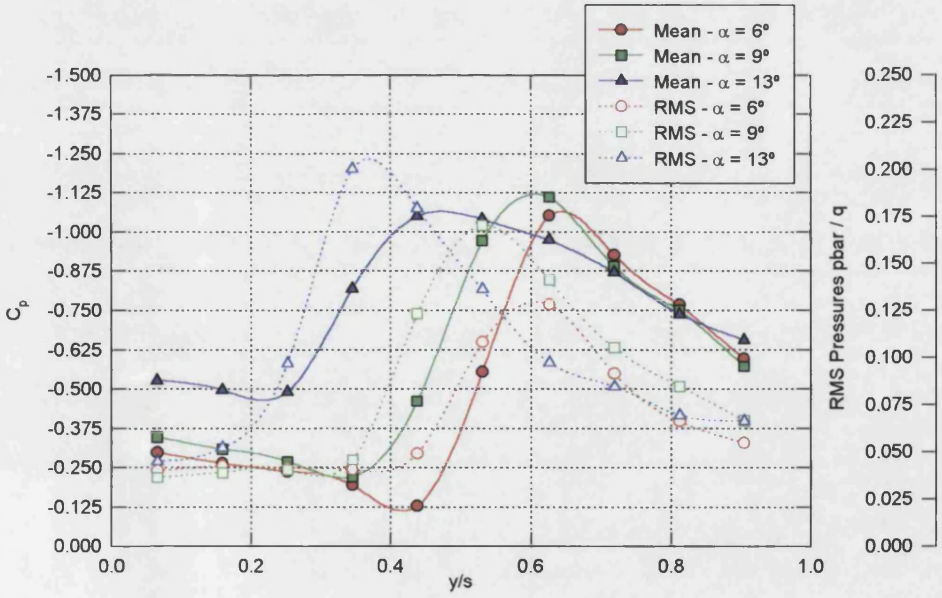

Figure 4.54: Variation of Steady and RMS Pressures, Model 1, $x/x_t = 0.8$

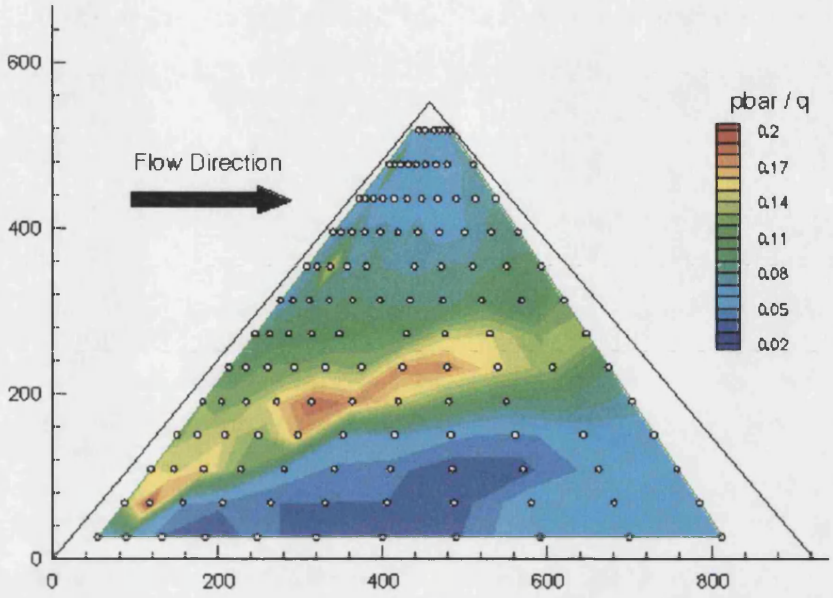

Figure 4.55: RMS Pressures, Model 2, $\alpha = 13°$

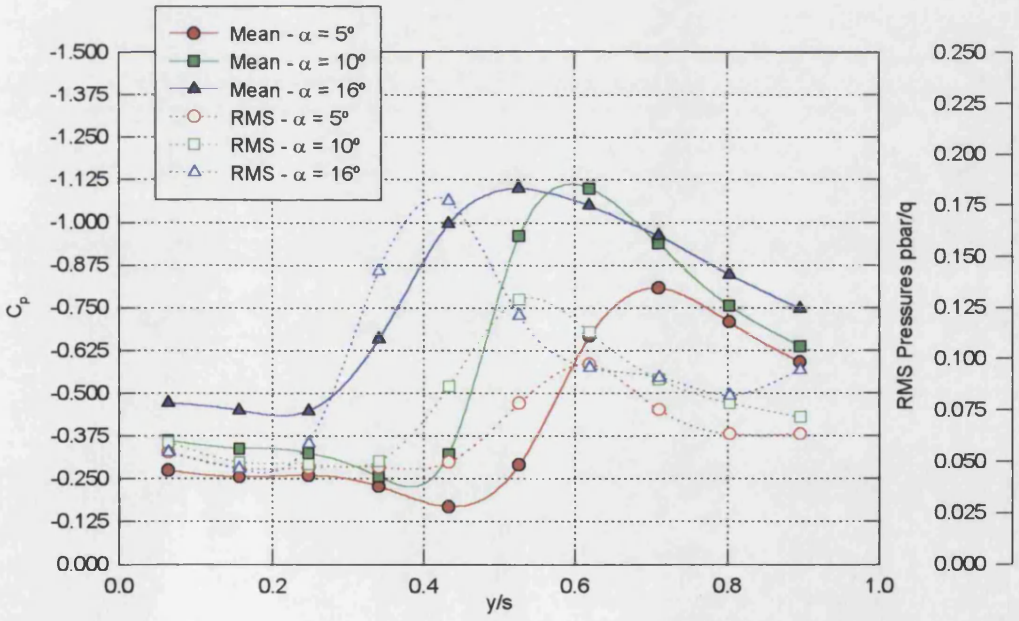

Figure 4.56: Variation of Steady and RMS Pressures, Model 2, $x/x_t = 0.8$

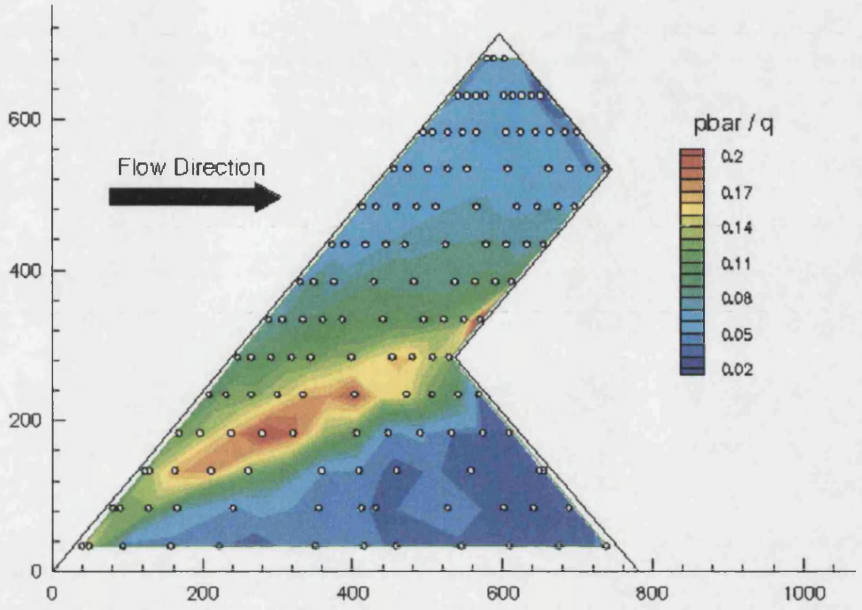

Figure 4.57: RMS Pressures, Model 3, $\alpha = 13°$

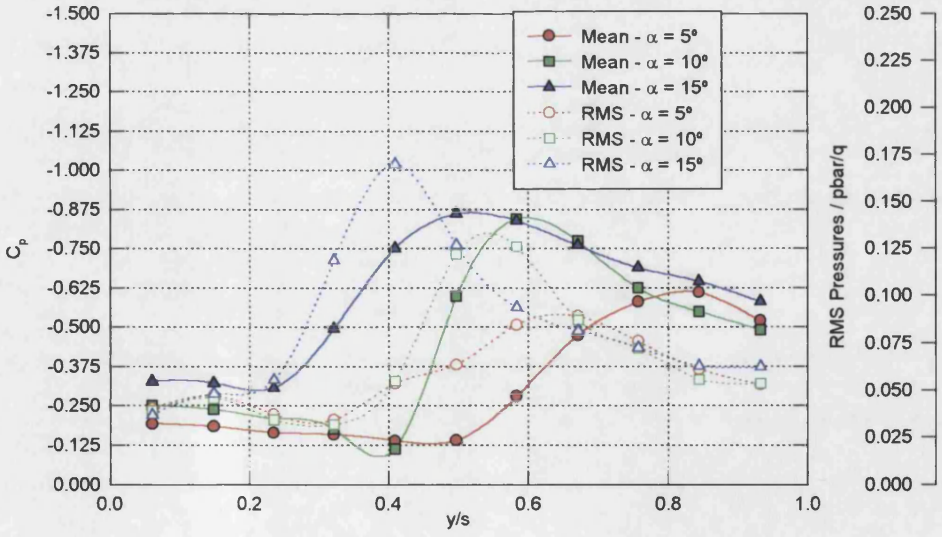

Figure 4.58: Variation of Steady and RMS Pressures, Model 3, $x/x_t = 0.8$

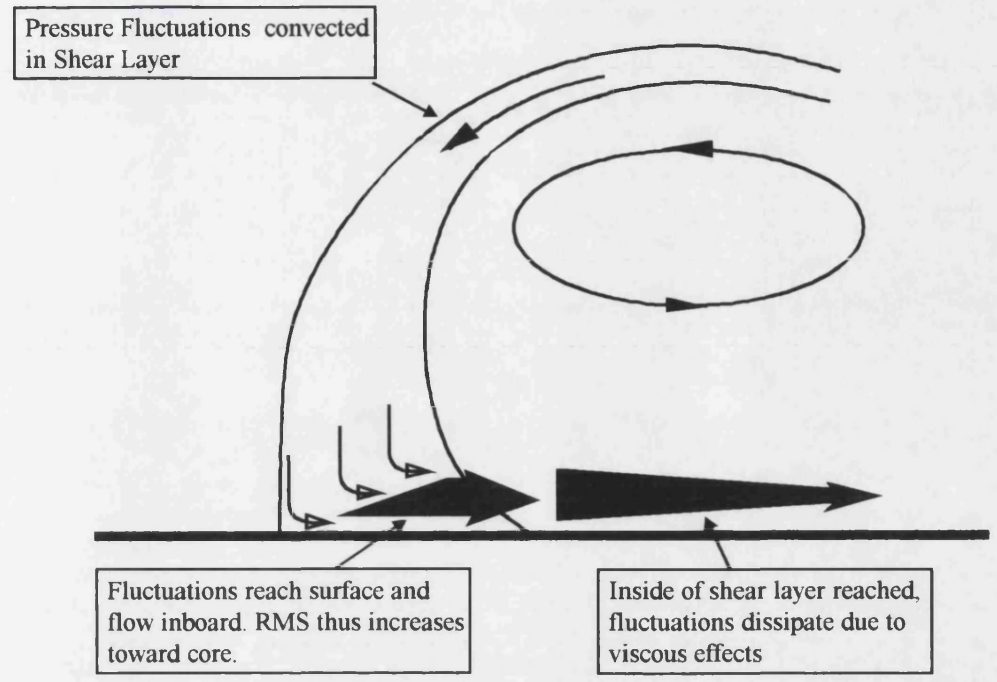

Figure 4.59: Increase of RMS Pressure Across Shear Layer

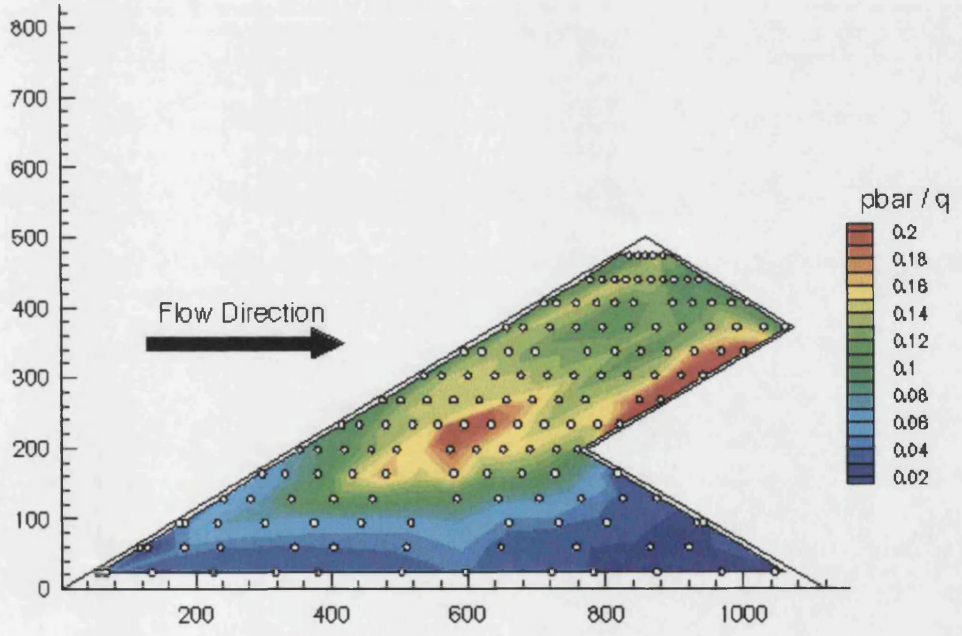

Figure 4.60: RMS Pressures, Model 4, $\alpha = 25°$

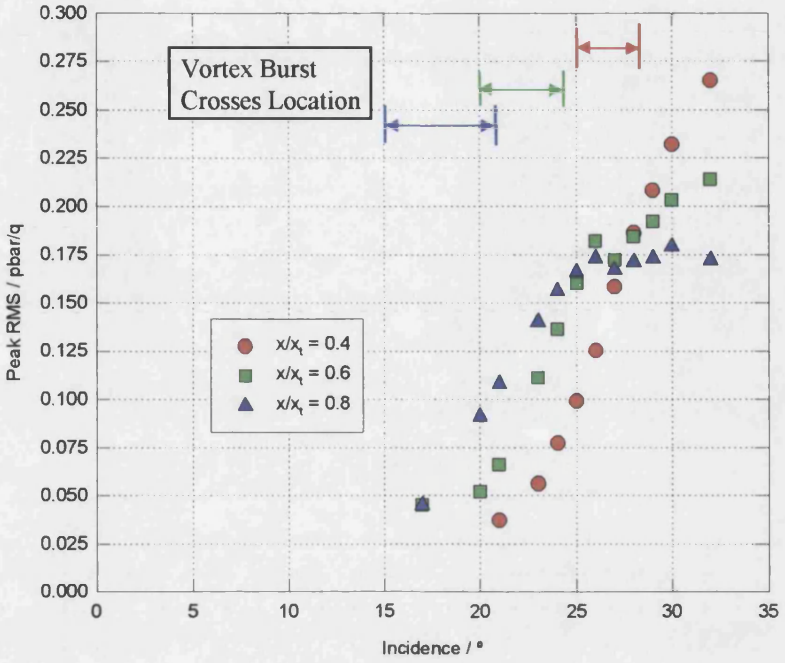

Figure 4.61: Variation of Peak RMS Pressures with Incidence, Model 4

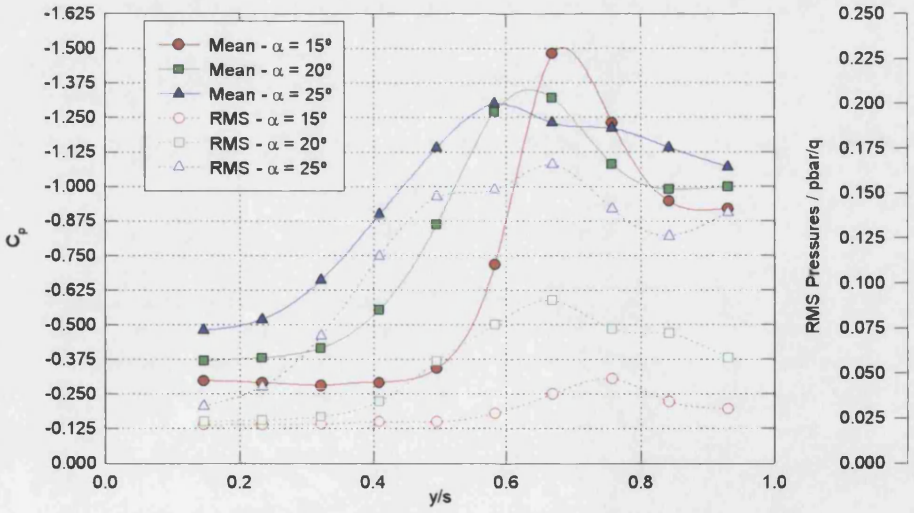

Figure 4.62: Variation of Steady and RMS Pressures, Model 4, $x/x_t = 0.8$

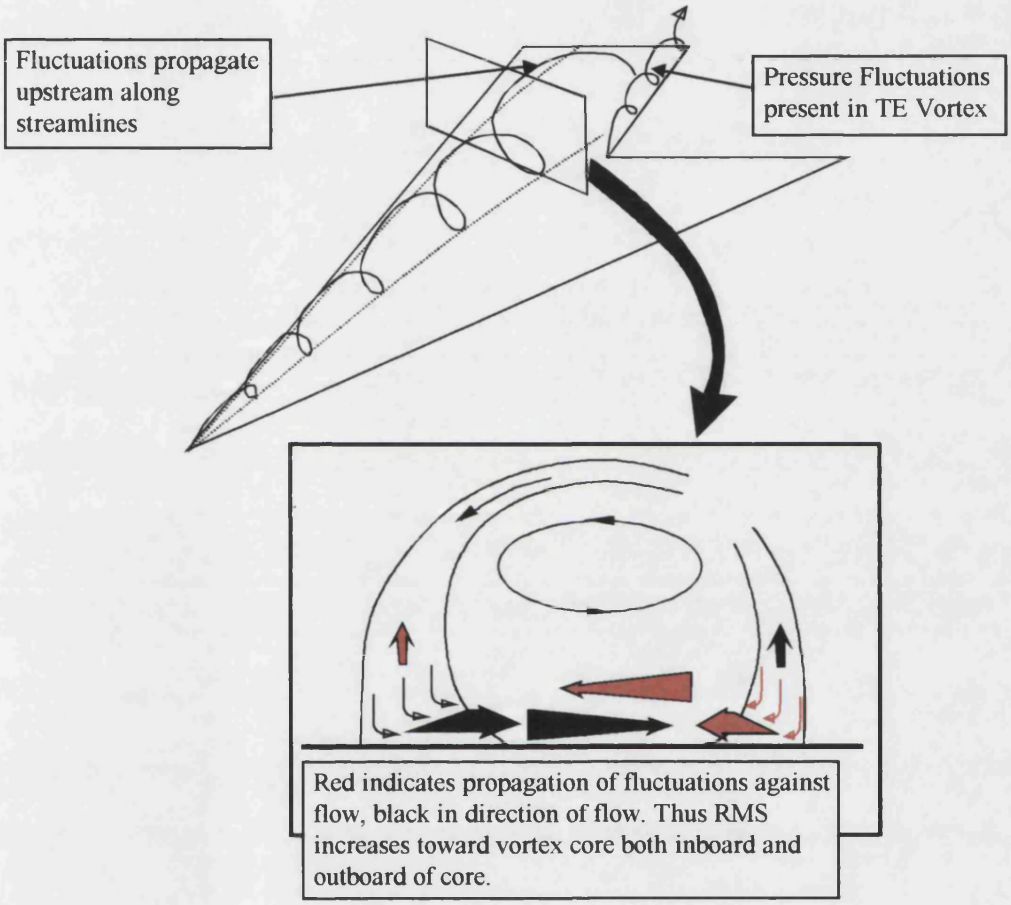

Figure 4.63: Propagation of Pressure Fluctuations

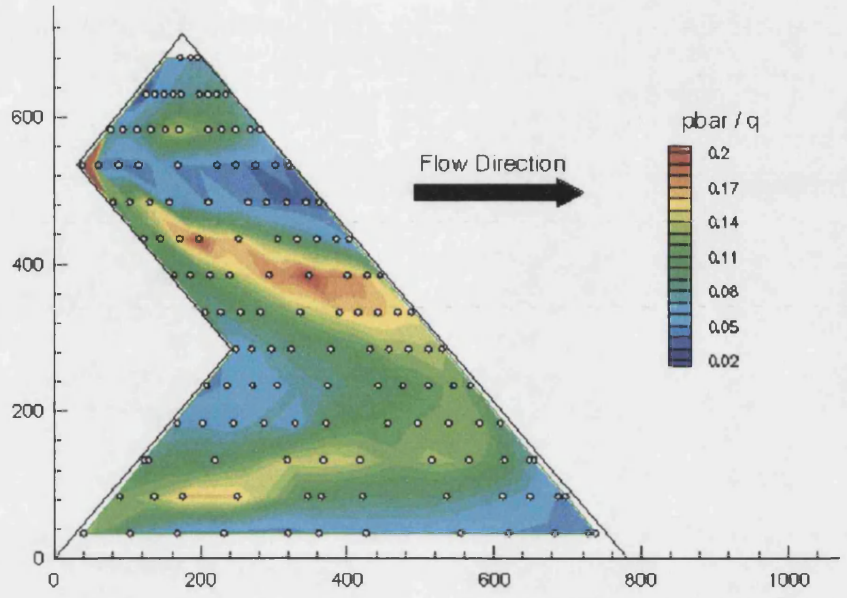

Figure 4.64: RMS Pressures, Model 3*, $\alpha = 13°$

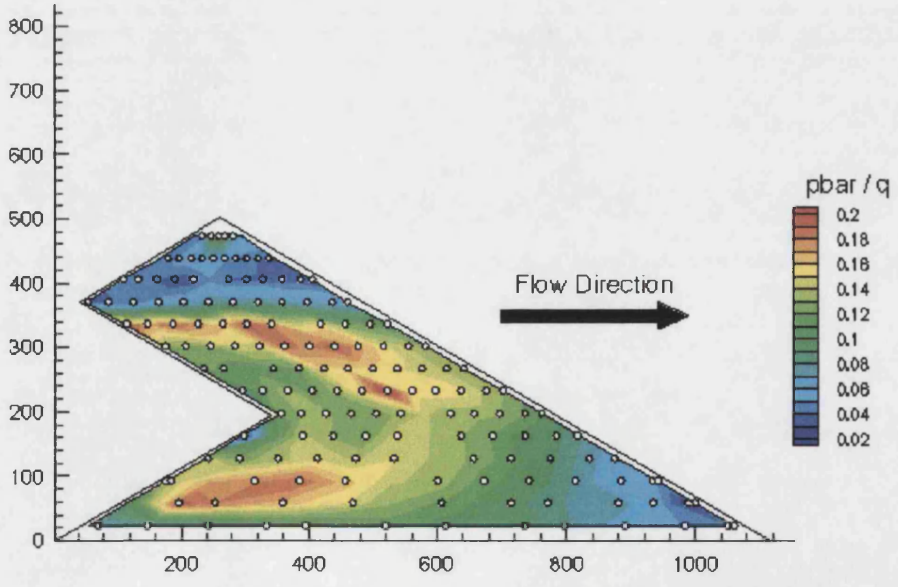

Figure 4.65: RMS Pressures, Model 4*, $\alpha = 25°$

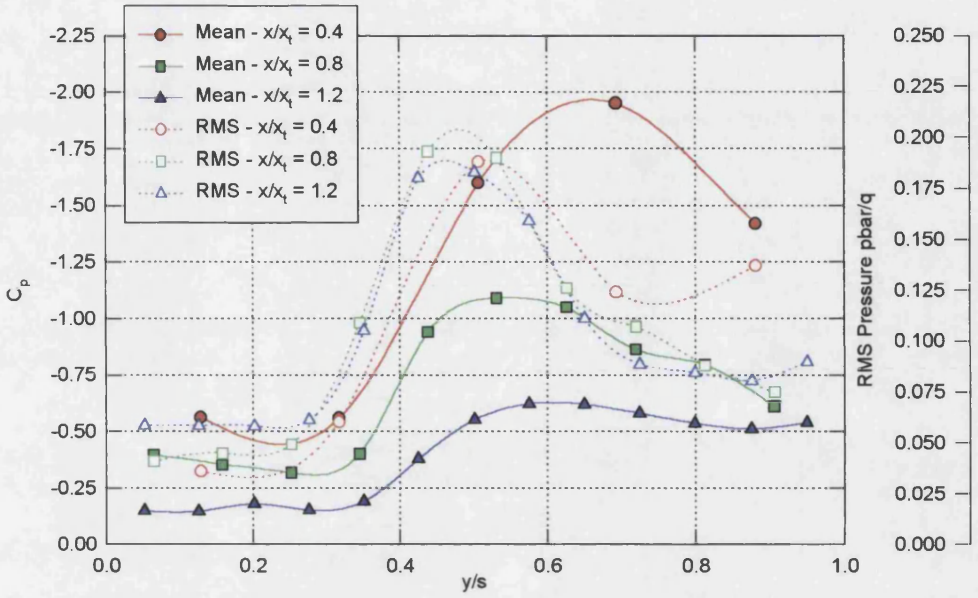

Figure 4.66: Variation of Steady and RMS Pressures, Model 1, $\alpha = 11°$

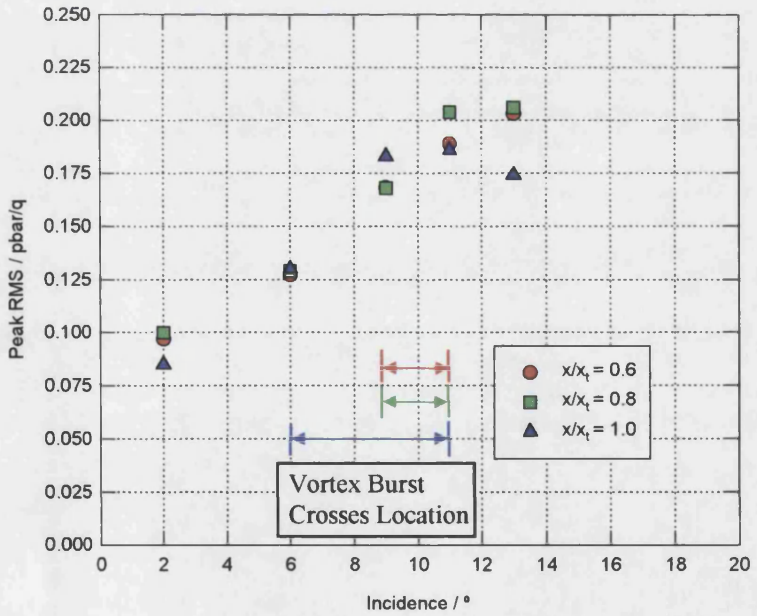

Figure 4.67: Variation of Peak RMS Pressures with Incidence, Model 1

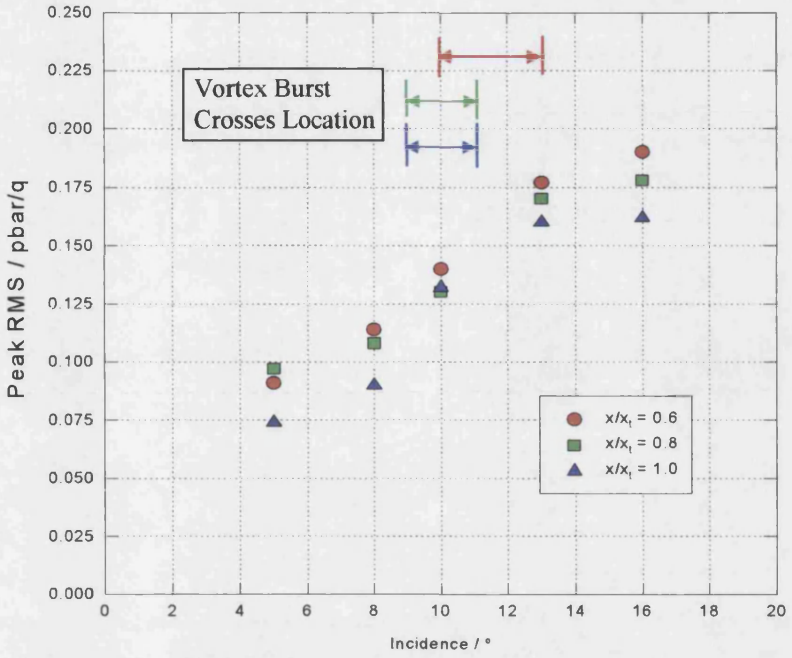

Figure 4.68: Variation of Peak RMS Pressures with Incidence, Model 2

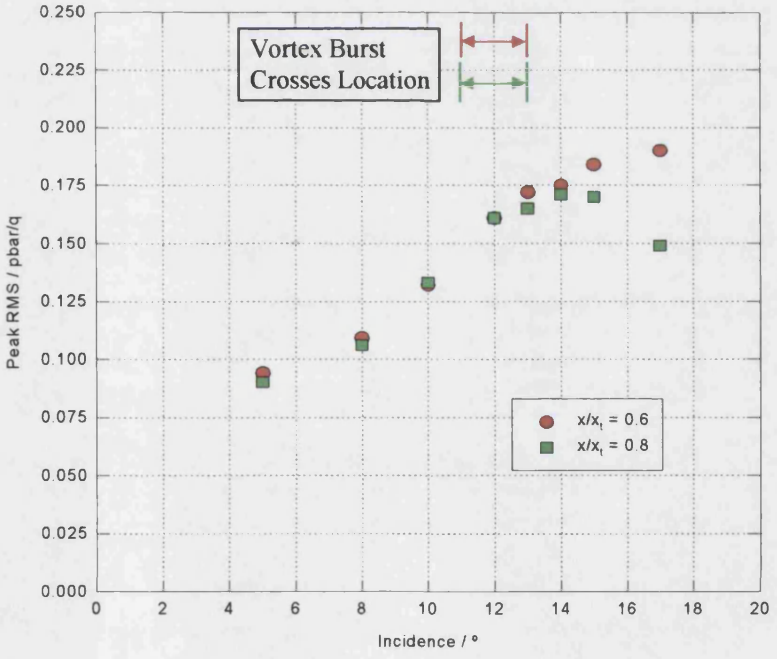

Figure 4.69: Variation of Peak RMS Pressures with Incidence, Model 3

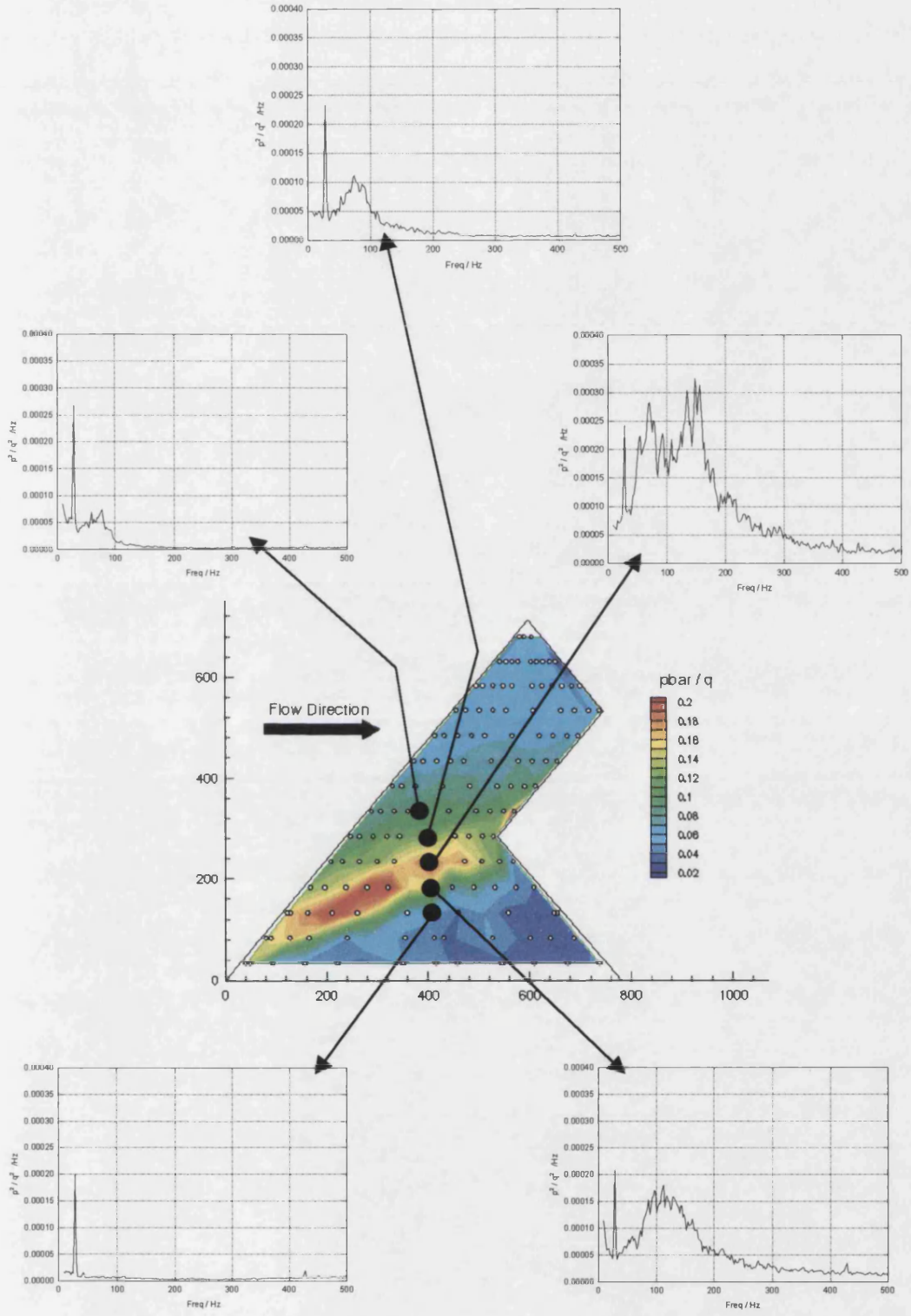

Figure 4.70: Spanwise Variation of Power Spectra, Model 3, α=14°

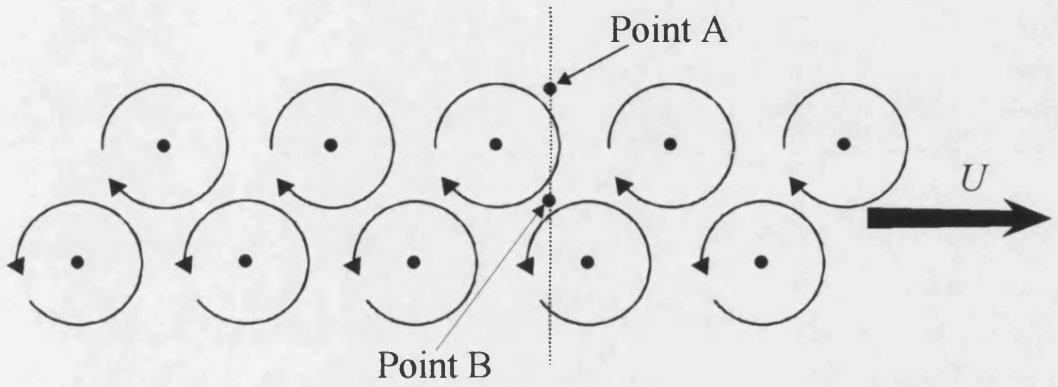

Figure 4.71: Free Vortex Representation of Shear Layer

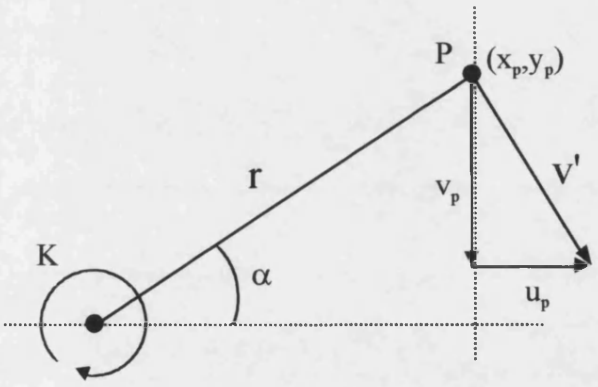

Figure 4.72: Definition of Velocities and Angles

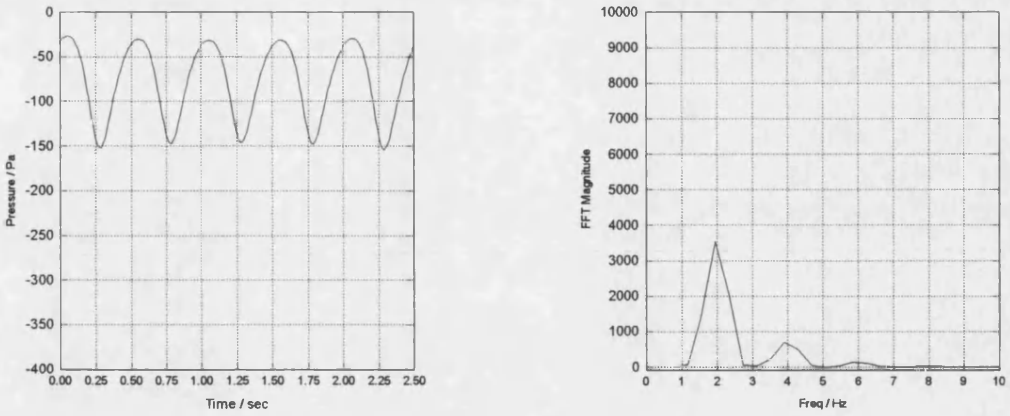

a) Time History b) Frequency Content

Figure 4.73: Pressure Time History and Frequency Content at Point A

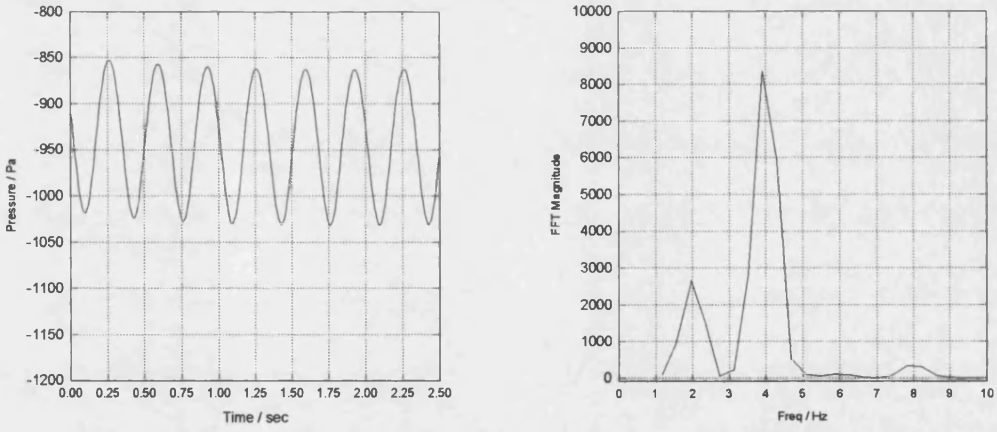

a) Time History b) Frequency Content

Figure 4.74: Pressure Time History and Frequency Content at Point B

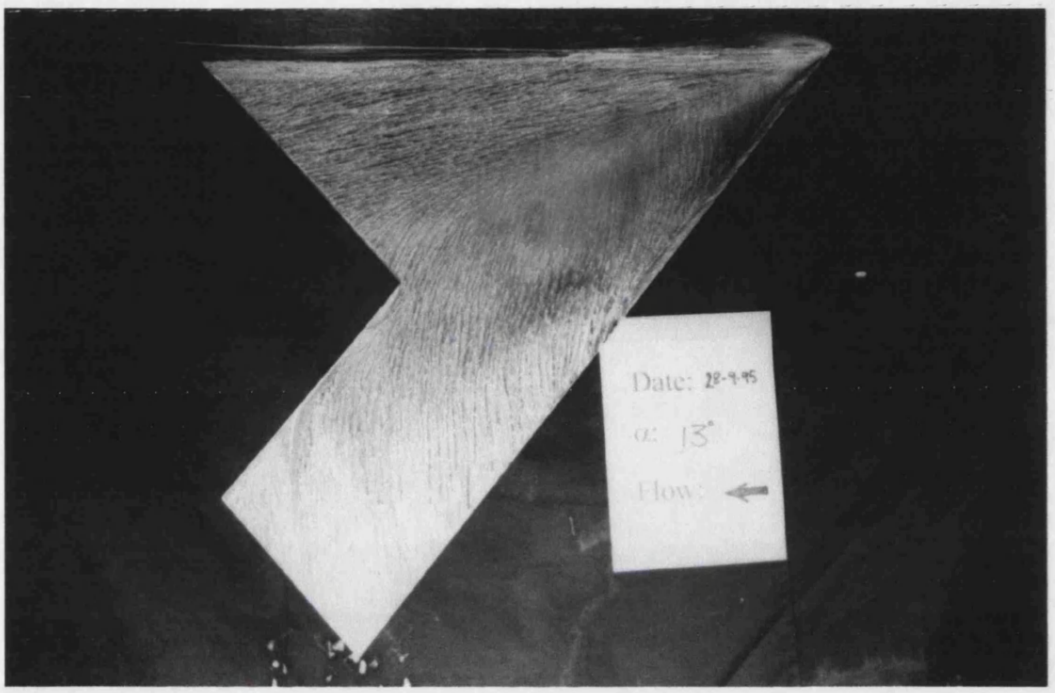

Figure 4.75: Surface Flow Visualisation over Model 3, α=13°

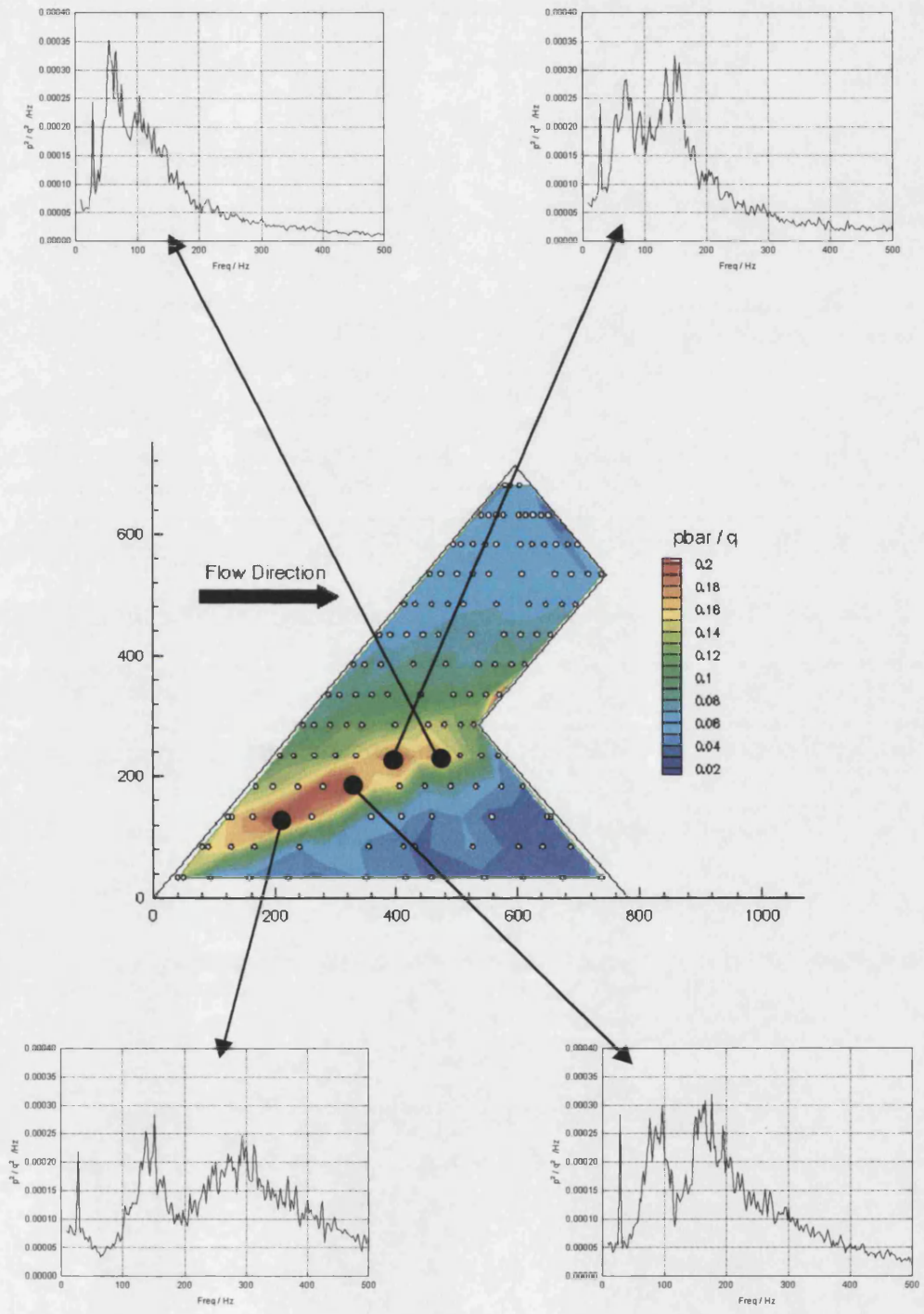

Figure 4.76: Chordwise Variation of Power Spectra, Model 3, α=14°

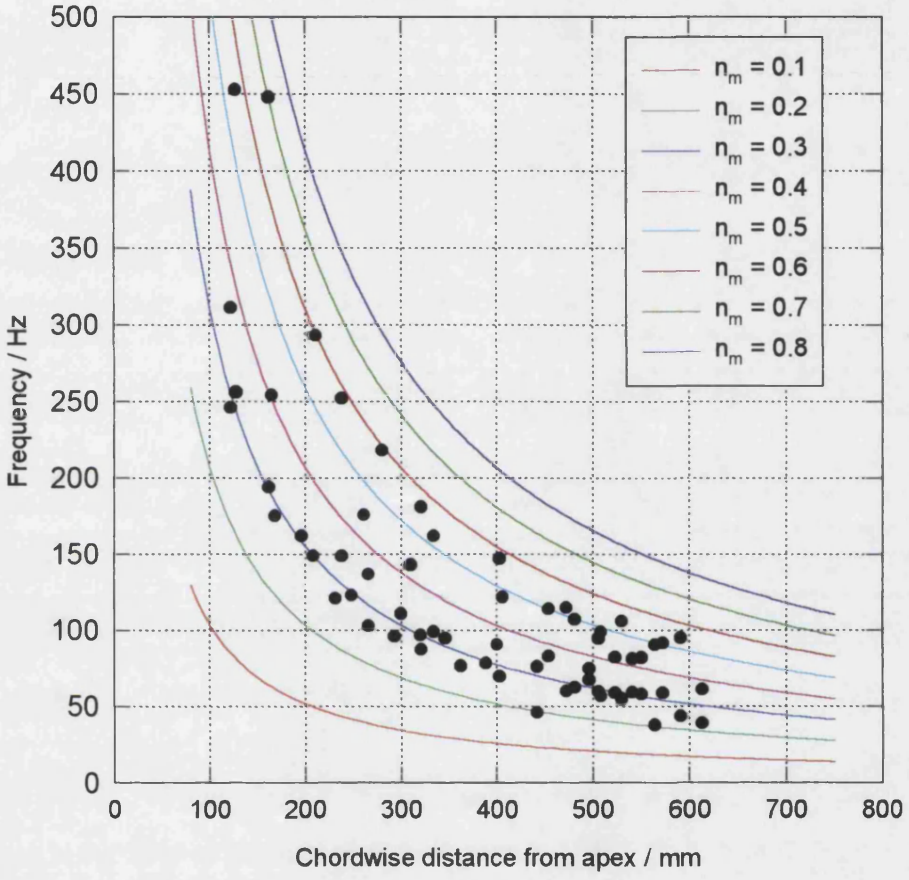

Figure 4.77: Variation of Centre Frequencies with Chordwise Location, Model 3, $\alpha = 14°$

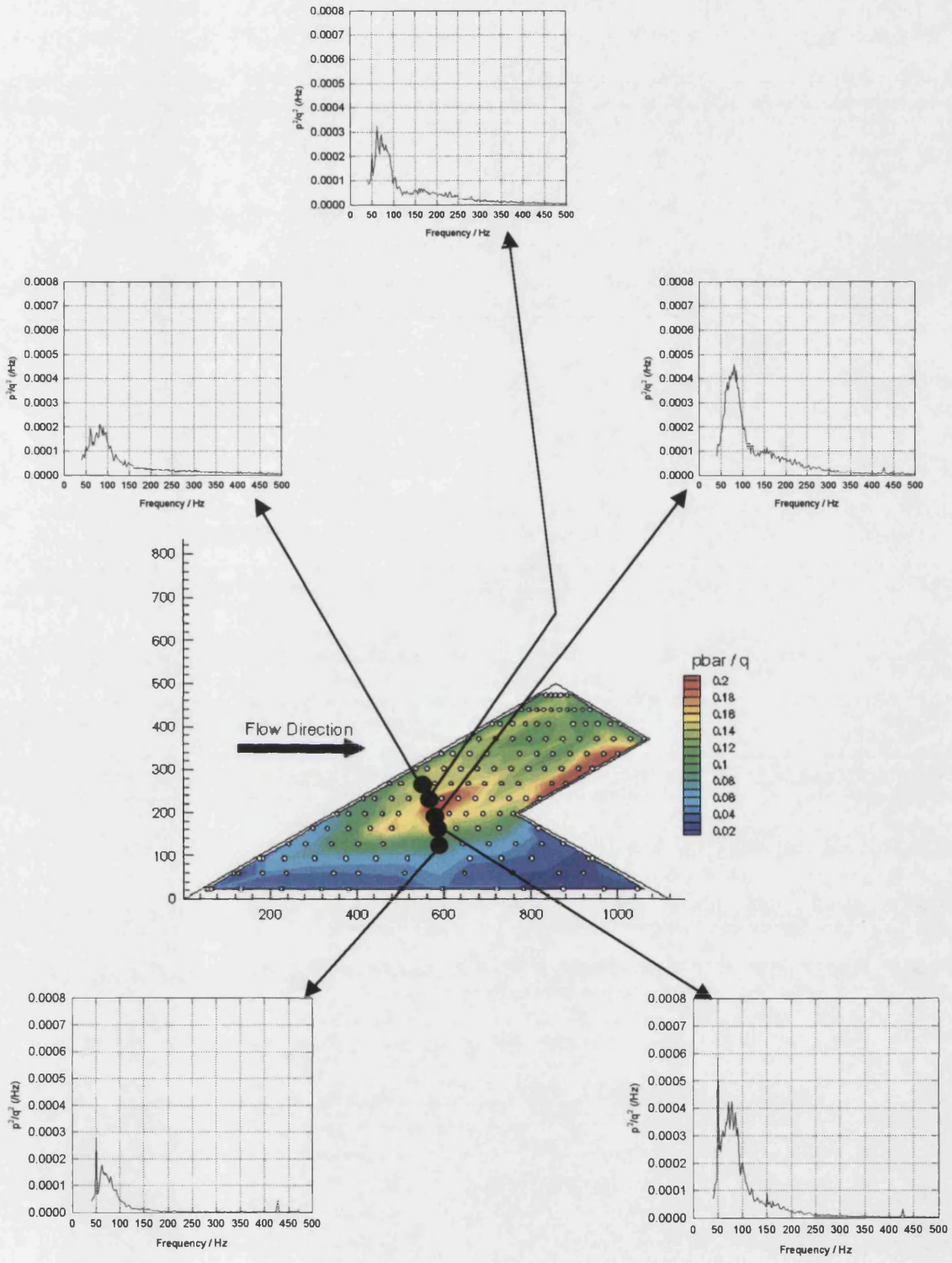

Figure 4.78: Spanwise Variation of Power Spectra, Model 4, α=25°

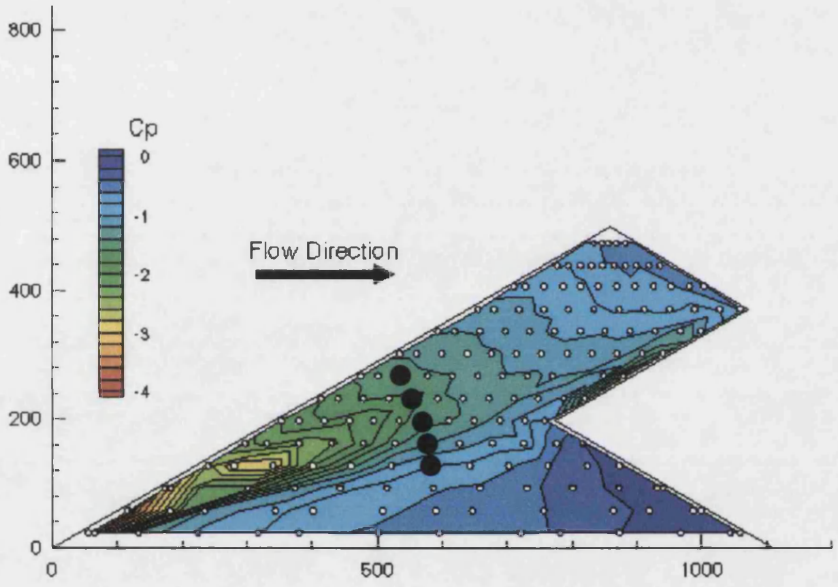

Figure 4.79: Model 4 Mean Pressures, $\alpha = 25°$

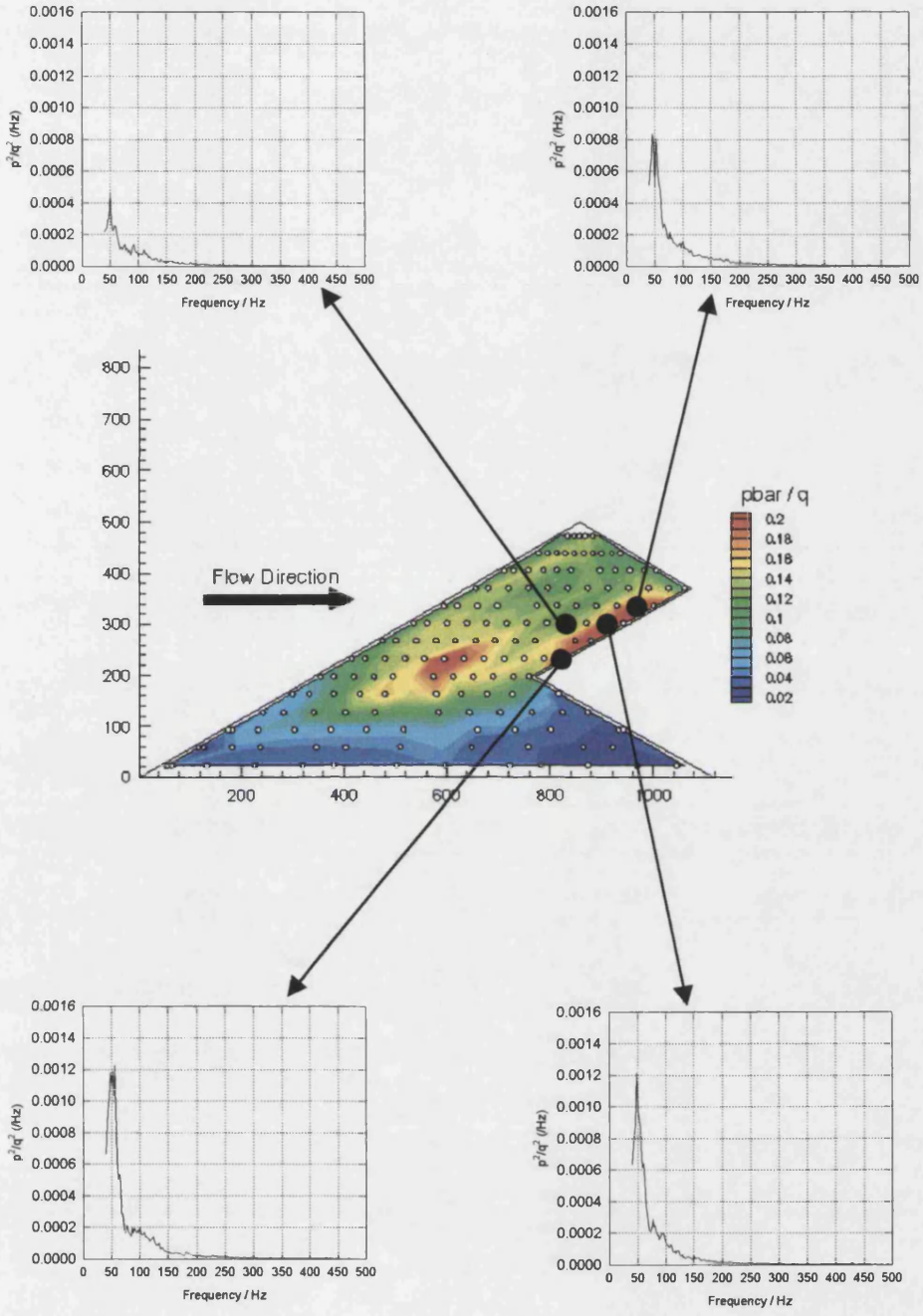

Figure 4.80: Variation of Power Spectra Near Mid-Trailing Edge, Model 4, $\alpha = 25°$

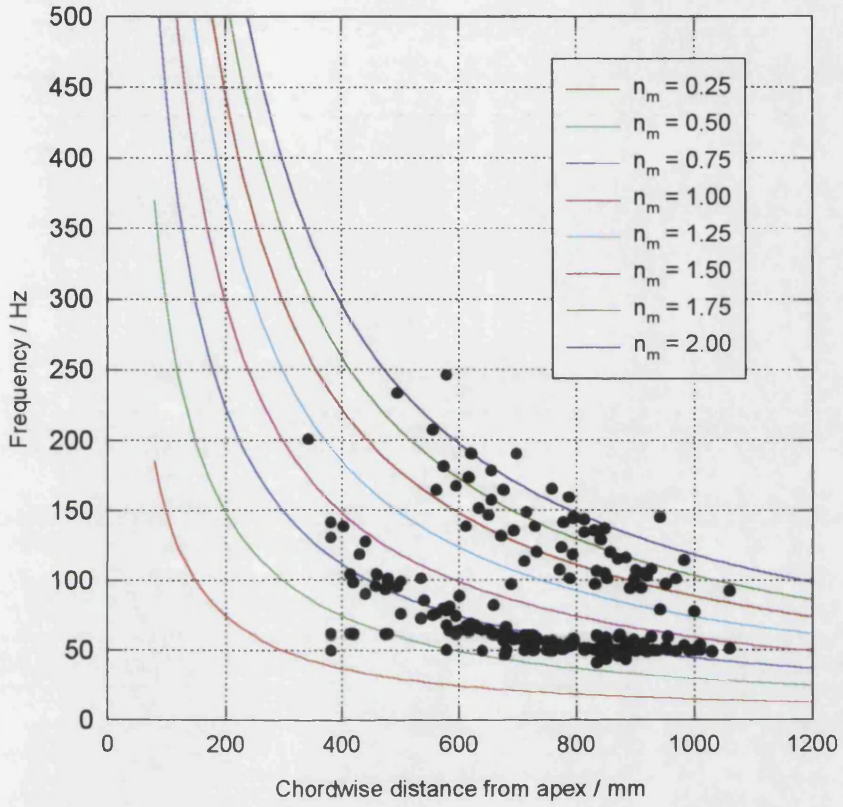

Figure 4.81: Variation of Centre Frequencies with Chordwise Location, Model 4, $\alpha = 25°$

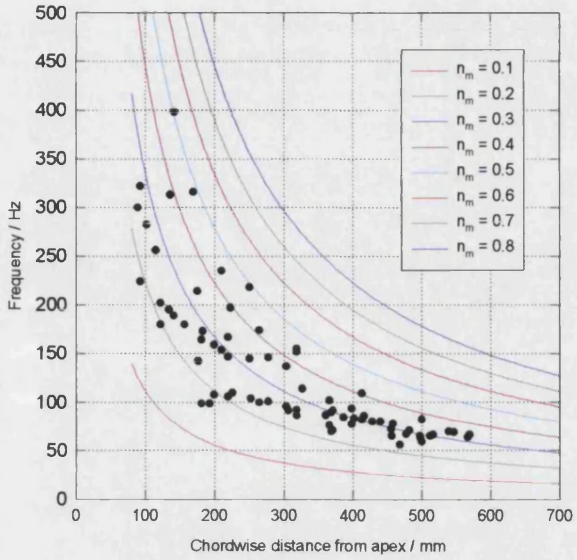

Figure 4.82: Variation of Centre Frequencies with Chordwise Distance from Apex, Model 3*, $\alpha = 13°$

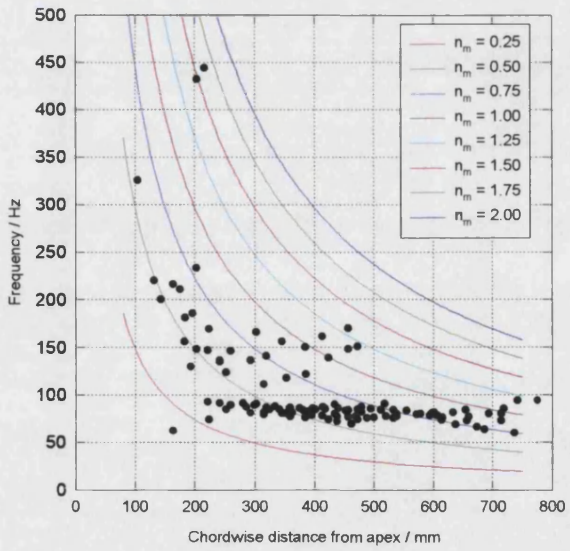

Figure 4.83: Variation of Centre Frequencies with Chordwise Distance from Apex, Model 4*, $\alpha = 25°$

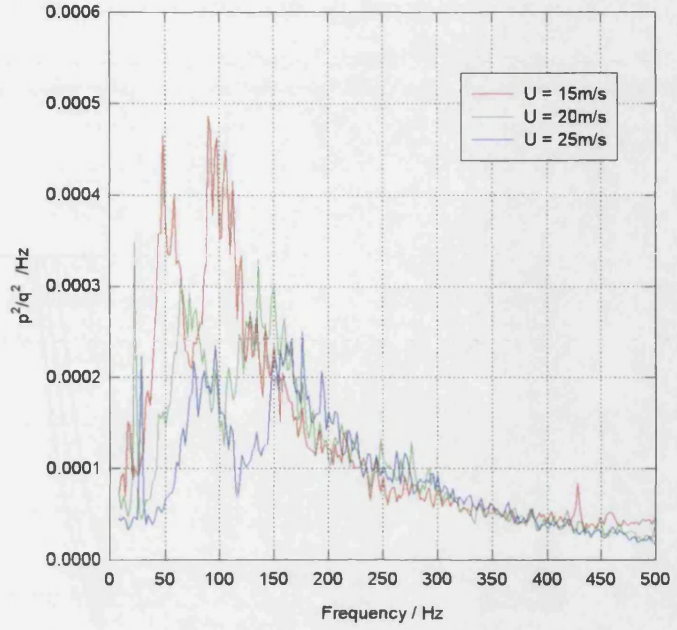

Figure 4.84: Variation of Power Spectra with Free Stream Velocity

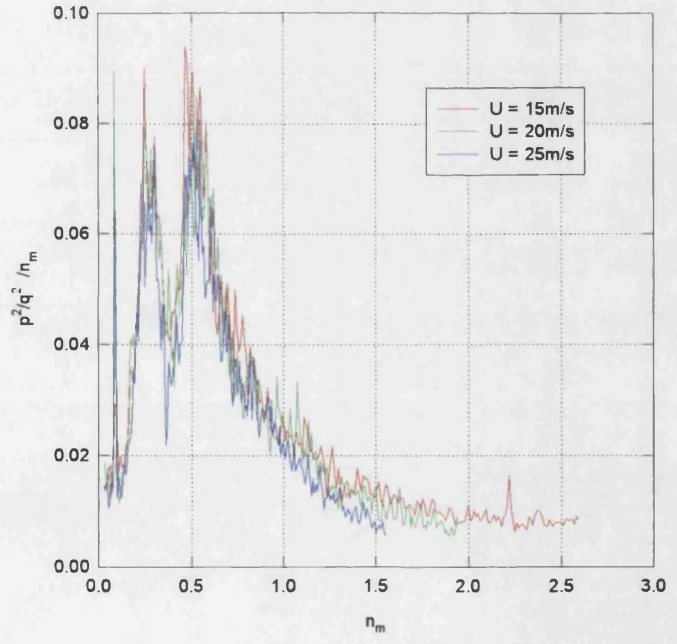

Figure 4.85: Variation of Non-Dimensionalised Power Spectra with Free Stream Velocity

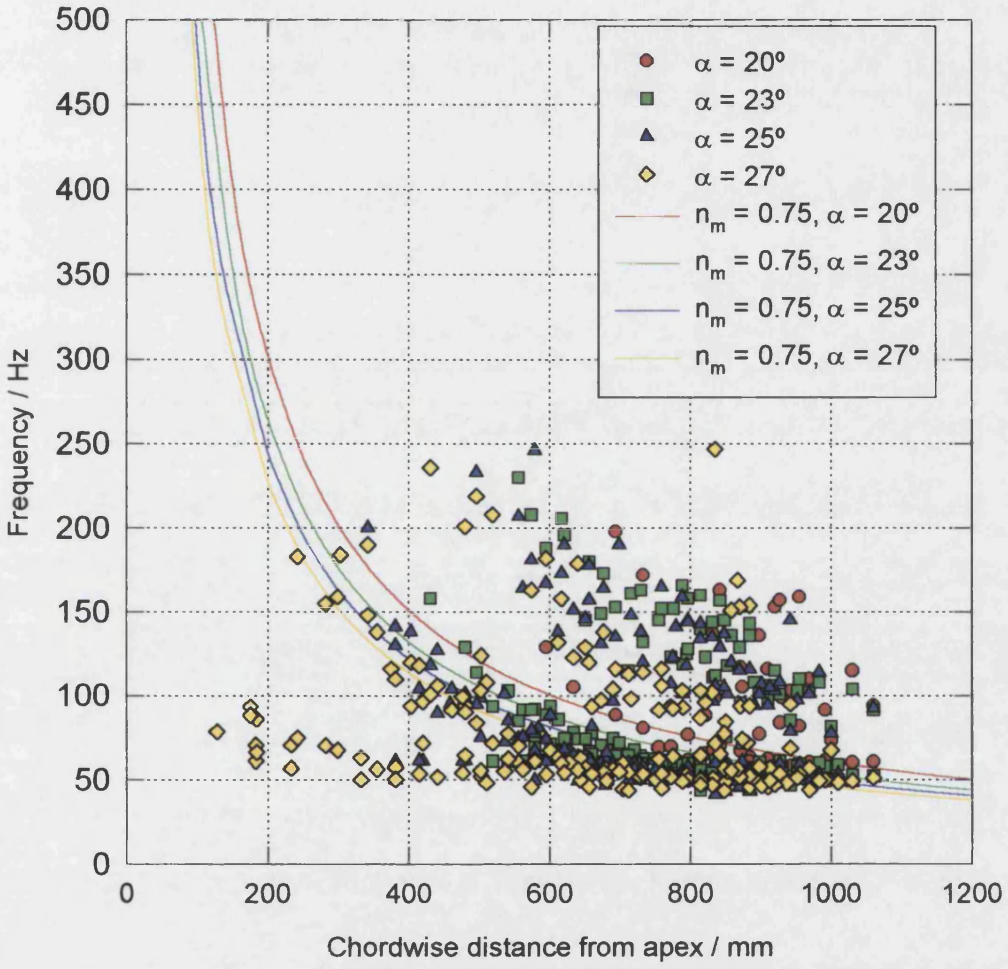

Figure 4.86: Variation of Centre Frequencies with Incidence

CHAPTER 5. PRELIMINARY DEVELOPMENT OF BUFFET PREDICTION TOOL

5.1 Overview

The aim of a wing buffet prediction tool is to be able to predict the power spectra acting over the entire surface of the wing. This would comprise a complete description of the spectra, including the frequencies at which peaks occur, the magnitude of the peaks and the shape of the peaks. The importance of this last criterion, the *shape* of the peaks in the buffet spectra, should not be underestimated since it will be of critical importance when the response of the structure due to buffet (buffeting) is calculated. A spectrum with a sharp peak at a frequency will cause little buffeting until a flight condition is reached that causes interaction between the buffet and the narrow resonance peak, due to low structural damping, of the structure. Conversely, a broad peak will cause a response throughout the speed/incidence range of the aircraft.

A complete description of the buffet spectra would lead to a simple derivation of the RMS buffet acting over the wing, since the RMS buffet can be calculated by simply considering the area under the power spectra. Therefore, prediction of the buffet spectra presents

the broadest prediction method necessary. However, this approach requires the following parameters to be calculated at all points over the wing:

- The frequency/frequencies at which buffet is a maximum
- The magnitude of the buffet at each of these frequencies
- A measure of the breadth of the peaks

It was with these criteria in mind that the curve-fitting program detailed in Chapter 3 was written. This results in up to seven parameters to describe each power spectra, which is described as the superposition of base excited mass/spring/damper systems:

- The natural frequency/frequencies of each system
- A forcing amplitude for each system
- The damping of each system

In addition to these parameters, an additional constant amplitude function was added such that noise in the system could be accounted for. Comparison of the requirements and the output of the program indicate that the parameters output by the system were ideal for the development of a prediction methodology.

However, despite the large number of tappings built into each wing, there were still relatively few areas over the wing at which phenomena such as double peaks in the spectra were apparent. For example, over Model 3 at an incidence of 13° there were

eight tappings where double peaks were apparent and only three where the 'intermediate frequency' peak was apparent. Also, as was evident from the scatter plots of the centre frequencies shown in Chapter 4 (see, for example, Figures 4.75 and 4.79), there was a large spread of centre frequencies with no obvious trend in the variation of the *spread* as the incidence or planform was changed. Therefore, it is difficult to speculate as to the cause of the variation. However, any buffet data acquired is susceptible to the natural statistical variation present in any such stochastic process, and it seems possible that this is the cause of much of the spread in the data.

Hence, since such variation in the RMS pressures was known, (it was tested at the start of each wind-tunnel test) it was decided to pursue an alternative route to predicting the buffet spectra. This would involve the prediction of the RMS pressures as the first step in the process. The next step would be to predict the number and frequencies of the peaks in the power spectra. The shape of the peaks would then be estimated and the relationship between the RMS pressures and the power spectra would then be utilised to derive the power spectra.

A first step toward this approach is demonstrated in the subsequent section. The reconstruction of the RMS pressures and PSDs over Model 3 is undertaken. This reconstruction could then be applied to the other Models and, if successful, a step toward a prediction methodology would have been made.

It should be noted that this is intended as a demonstration that such a concept is feasible, and that this approach has the potential to be extended such that separation induced pressure fluctuations can be predicted over aircraft at an early design stage. It is proposed as a first step to such a methodology, and significant development of this technique is required to enable its use in a design environment.

5.2 Reconstruction of RMS Buffet

A schematic diagram of a typical spanwise RMS pressure distribution is depicted in Figure 5.1. A low level of excitation is found at the centreline of the model. The level of RMS buffet then stays approximately constant until the outer edge of the shear layer is reached, where it begins to rise rapidly. The RMS level of pressure fluctuations reaches a peak slightly inboard of the core of the vortex before decaying outboard of the vortex core. It was proposed in Chapter 4 that, at points on the wing between the primary attachment line and the vortex core, there were two competing effects present. These effects were the rate of addition of fluctuations from the shear layer and the rate of dissipation of any unsteadiness present in the flow. Therefore, if the rates of addition and dissipation can be predicted together with the level of excitation at the centreline of the model, the level of RMS excitation over the planform can be calculated.

If this model of conflicting addition and dissipation is applied to the spanwise distribution of RMS pressures over Model 3, where propagation is only noticeable downstream, a simple exponential fit can be made to represent the decay of the pressure fluctuation *outboard* of the shear layer where:

$$\frac{\overline{p}}{q} = \left(\frac{\overline{p}}{q}\right)_{\max} e^{-k\left(\frac{y}{s} - \frac{y}{s_{\max}}\right)}$$

This assumes that at points outboard of the vortex core there is no addition term, but that the dissipation process continues. Spanwise slices were taken through the steady and RMS pressure distributions over Model 3. A simple Visual Basic program within Microsoft Excel was then utilised to locate the points of maximum suction and perform a least squares fit to estimate the constant, k. The variation of k, the rate of dissipation, is plotted against incidence at a number of chordwise stations in Figure 5.2. Two observations can be made from this graph, upon which lines of best fit have been superposed. Firstly, at a given incidence the dissipation, k, which is based on non-dimensional spanwise location y/s, is larger toward the trailing edge of the model. Secondly, the dissipation changes more rapidly as the incidence is increased at the trailing edge of the model.

The gradients and intercepts of the lines of best fit are plotted in Figures 5.3 and 5.4. As is clear from these, a simple linear relationship between chordwise location,

incidence and damping parameter can be derived such that:

$$k = (3.384x - 0.738)\alpha + (12.27 - 63.17x)$$

where x is the chordwise distance from the apex and α is the incidence of the model measured in degrees. The damping parameter can therefore be calculated for an arbitrary chordwise location and incidence.

Once the damping parameter had been calculated by examining the decay of the pressure fluctuations outboard of the suction peak the other required parameter, the rate of additions from the shear layer, could be calculated. If the rate of the addition from the shear layer is assumed to be proportional to the pressure gradient, it follows that:

$$\frac{d(RMS)}{d\left(y/s\right)} = a\frac{dC_p}{d\left(y/s\right)} + k(RMS)$$

where a is the addition constant. This can be manipulated to give the expression:

$$RMS\left(y/s\right) = ae^{k y/s}\int e^{-k y/s}\frac{dC_p}{d\left(y/s\right)}d\left(y/s\right)$$

Hence, if the dissipation constant, k, is known together with the spanwise RMS distribution, $RMS\left(y/s\right)$, the addition constant a can be calculated. The Microsoft Excel macro was enlarged to numerically calculate the integral. Use was also made use of Excel's ability to iterate to calculate a least squares fit between the predicted and experimental values of RMS pressures, thus estimating a value for a.

The calculated vales of a are plotted for a range of incidences and chordwise locations in Figure 5.5. The values of the addition parameter increase as the incidence increases, and grow toward the trailing edge of the model.

The circulation contained within a leading edge vortex increases approximately linearly with chordwise location (Visser and Nelson – 1993), and it seems plausible to assume that the addition parameter might be related to the local circulation. Figure 5.6 depicts the addition parameter divided by chordwise distance from the apex, thus showing an approximate relationship between the addition parameter per unit of circulation, chordwise location and incidence. A linear relationship between addition parameter divided by chordwise location and incidence can now be determined, and this is superposed on Figure 5.6. Although there are deviations of approximately ±10% between the experimental results and the linear relationship there does appear to be a strong correlation between this scaled parameter and incidence which is largely independent of the chordwise location of the points. Indeed, the largest deviations are found at the maximum incidence at which significant buffet was experienced. Visser and Nelson's work indicated that the increase in circulation

contained within the leading edge vortex as the incidence was increased was reduced as stall was approached. It can be hypothesised that the observed deviation from a linear relationship at higher incidences is due to this effect.

Nevertheless, this relationship between incidence, chordwise location and addition parameter can be utilised to estimate the addition parameter a using the relationship:

$$\frac{a}{x} = 0.1855 - 0.0382\alpha$$

where α is measured in degrees.

The final parameter required to enable prediction of RMS buffet over the planform is the level of buffet at the centre of the model. This is plotted against the steady pressure coefficient at the centre of the model in Figure 5.7. There is a correlation between these two parameters which can be expressed as:

$$RMS = 0.0267C_p + 0.0539$$

All of the required parameters for reconstruction of the RMS pressures over the model can now been calculated at any point on the wing. There is a limitation to the scheme, however, in that it requires an uninterrupted spanwise slice to be available to calculate the RMS pressure distribution. It is therefore not possible to calculate the RMS pressure distribution at locations downstream of the reverse apex on the model.

The relationships that have been derived during this analysis were utilised, together with another Visual Basic program, to calculate the RMS pressure distribution over the model at an incidence of 14°. The inputs to the program were spanwise steady pressure distributions at defined chordwise locations. The suction peaks were then identified, and the addition parameter a, the dissipation parameter k and the centreline level of RMS buffet were then calculated. These values then enabled the spanwise RMS pressure distributions to be calculated. A contour plot of the resulting RMS pressure distribution over the model at an incidence of 14° is depicted in Figure 5.8. This can be compared with the experimentally measured RMS buffet, which is displayed in Figure 5.9.

The spanwise locations of peak RMS buffet are well replicated by the calculations. This is largely controlled by the value of the 'dissipation parameter'. However, the peak values of the RMS pressure are not as well represented, especially toward the rear of the calculated area. Maximum experimental values of RMS pressure were approximately 0.17 in this area, but predictions indicated that the maximum RMS pressure would be 0.15. This 11% error can be largely explained by the variation in the addition parameter indicated in the discussion of Figure 5.6.

The first necessity of a buffet prediction method, the reconstruction of levels of RMS buffet, has now been achieved. This will enable the magnitudes of the peaks of the PSDs to be estimated once the number, frequency and shape of the peaks has been estimated.

5.3 Forecast of Centre Frequencies

The concept of modified reduced frequency parameter, n_m, was introduced in Section 4.5.2, and it was shown that there were peaks corresponding to three distinct values of n_m over the wings with 40° of leading edge sweep. The lowest frequency of these peaks was present at the largest number of locations, and corresponded to modified reduced frequency parameter of 0.30. Deviations of ±10% from this value of n_m were found over the wing.

The highest frequency peak was apparent at values of n_m between 0.57 and 0.60. These peaks were found in the regions of highest RMS and were rare, with only 8 tappings out of the 165 present over the wing experiencing two peaks in their pressure spectra. Toward the trailing edge of the model the frequency of these peaks appeared to reduce, although this was possibly due to the difficulty of discriminating between two peaks with similar frequencies. This high frequency peak was always accompanied by the low frequency peak described in the previous paragraph.

The rarest of the peaks in the spectra were encountered in the region directly under the primary attachment line. The frequency of these peaks was approximately midway between the other two that were detected and corresponded to a reduced frequency parameter of 0.45.

It was decided to use the spanwise RMS pressure distribution to determine the number and frequency of the peaks that were present. Areas outboard of the high RMS region where two peaks were present experience only a single, low frequency, peak and areas inboard experience a peak of intermediate frequency. The frequencies of these peaks were defined by their modified reduced frequency parameter, as described previously.

5.4 Estimation of Damping of Peaks

To enable the reconstruction of the power spectra, the shape of the peaks and the relative magnitudes of any peaks must be known in addition to their frequencies and RMS pressures. The damping of the peaks, as derived by the curve fitting program (see Chapter 3 and Appendix A) over Model 3 at an incidence of 14° are depicted in Figure 5.10. The sizes of the symbols in this plot are proportional to the amplitude of the peaks that were detected. As is clear from this figure, there was no clear trend to enable the damping to be estimated accurately. Plotting the damping against modified reduced frequency parameter, as well as a number of other variables, was also undertaken. It was felt that a correlation between n_m and damping was most likely. This might have, for example, shown that the mid-frequency peak with n_m=0.45 was a broader peak than the low frequency n_m=0.30 peak. However, no correlation was found. It may be that if more points in this 'broadband peak' area had been identified that such a correlation would be forthcoming.

The only 'relationship' that was noted is depicted on Figure 5.10. It was found that the damping was somewhat affected by chordwise location. Plotting the damping against any other parameter or combination of parameters resulted in an even worse correlation, with points located entirely randomly over the plot. Although there is little in the way of a correlation between damping and chordwise location, it can be seen from Figure 5.10 that points upstream of the reverse apex generally correspond to dampings of between 0.10 and 0.30. Downstream of the reverse apex higher dampings are more commonplace.

To enable some estimate of the PSDs to be made, a weighted average of the damping of the peaks was made for locations upstream of the reverse apex. The weighting variable utilised was the amplitude of the peaks. This resulted in a weighted average damping of 0.216.

5.5 Reconstruction of Power Spectra

The final remaining task to enable the reconstruction of the power spectra over the wing planform was to estimate the relative heights of the peaks at frequencies relating to reduced modified frequency parameters of 0.30, 0.45 and 0.58. As was stated in Section 5.3, it was decided to use the region of maximum RMS pressure as a reference point to determine the frequency content of the PSDs.

This can be expanded upon to enable both the amplitude and frequency of the peaks to be estimated. This approach is depicted in Figure 5.11. The figure shows the relative amplitude of peaks at the three frequencies at a spanwise slice. The spanwise dimension, w, is the distance from the primary attachment line to the point of maximum RMS pressure. The distances indicated on the diagram have been derived by inspection of the PSDs over the surface of the models. The relative amplitudes of the $n_m = 0.30$ and $n_m = 0.58$ peaks result from the observation that PSDs have been measured where the amplitude of the high frequency peaks have been double that of the low frequency peaks. The scheme depicted allows for this event, although it will only be apparent in a very narrow region within the shear layer. The high frequency peak has not been noted outboard of the suction peak, so outboard of this location only the $n_m = 0.30$ peak is present.

The full PSD reconstruction scheme can now be described:

1) Estimate the spanwise RMS distribution as detailed in Section 5.2.
2) Locate the spanwise location of the point of interest on Figure 5.11.
3) Subtract the centreline RMS from the calculated RMS. This is then placed as a white noise signal on the PSD.
4) The relative amplitudes of the frequency peaks, together with their damping (ζ=0.216) are now known. Iterate the amplitudes of these peaks to achieve the required RMS, calculated in Step 1).

Comparisons between estimated and measured PSDs over the surface of the Model are shown in Figures 5.12 and 5.13.The PSDs have been calculated using the above technique, including the estimation of the RMS pressures.

Figure 5.12 shows the predicted and experimentally measured PSDs at tappings in an approximately spanwise slice through the high RMS region. The predicted frequencies match those measured experimentally extremely well. The magnitude of the peaks is not as well replicated. This is largely due to errors in the RMS estimate at tappings. An error of 10% in the predicted RMS pressure results in a difference of 21% in the area under the PSDs, thus making the comparison look less satisfactory. To evaluate whether this is the cause of the differences between the predicted and actual PSDs, an advantage of the two-stage process could be utilised. The experimental values of RMS pressure could be utilised in Step 1) of the process, and the PSDs could then be calculated using Steps 2) to 4) using these values.

The shape of the predicted peaks is generally good, particularly for the PSD at the centre of the three tappings (in the high RMS area). This can be noted by examining the reduction in amplitude of the pressure fluctuations at higher frequencies, the predicted curve follows the experimental data closely.

Figure 5.13 shows a comparison of the predicted and estimated PSDs at three tappings in the high RMS region. As for the spanwise slice, the frequencies at which there are peaks in the spectra are very well replicated. As before, the errors in

amplitude are largely due to deviations between the experimental and predicted RMS pressures. This observation indicates the importance of improved estimation of the addition parameter, possibly by examining any possible relationship between the circulation of the leading edge vortex and the parameter.

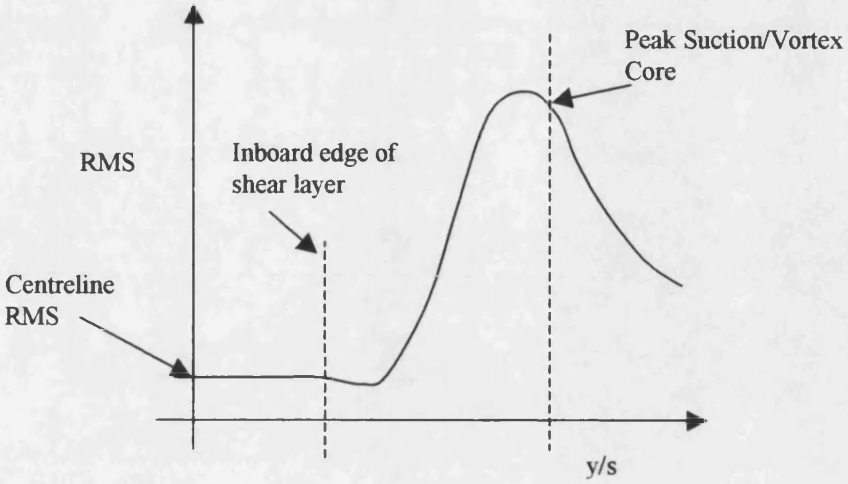

Figure 5.1: Schematic of Spanwise RMS Pressure Distribution

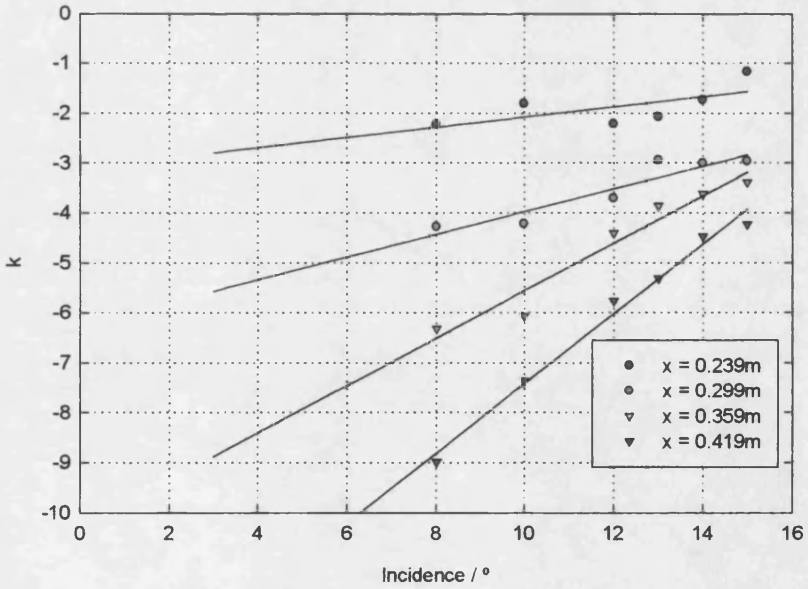

Figure 5.2: Variation in Dissipation Parameter with Incidence and Chordwise Location

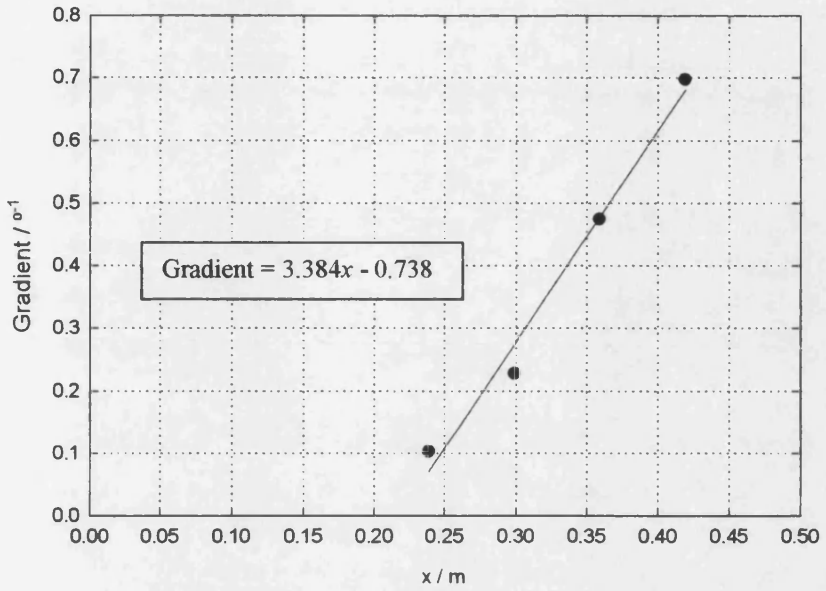

Figure 5.3: Variation of Gradient of Dissipation Parameter with Chordwise Location

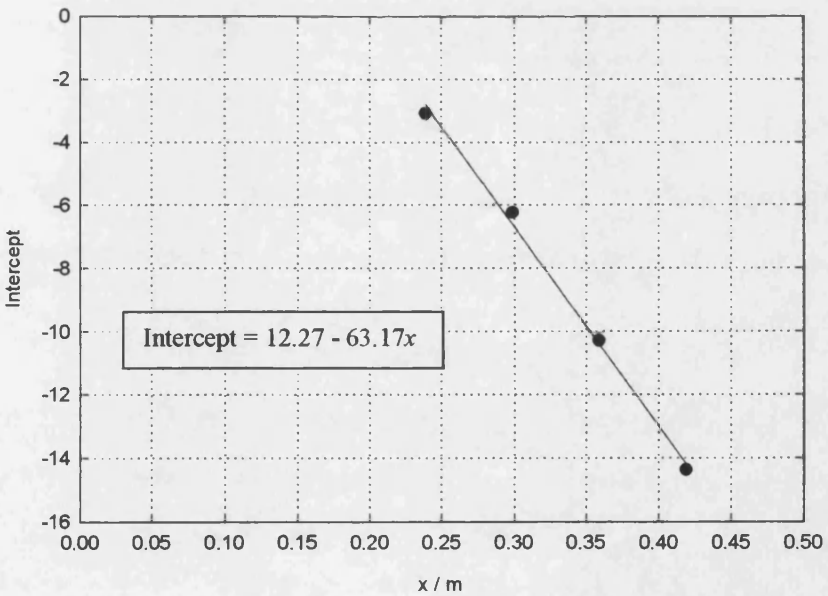

Figure 5.4: Variation of Intercept of Dissipation Parameter with Chordwise Location

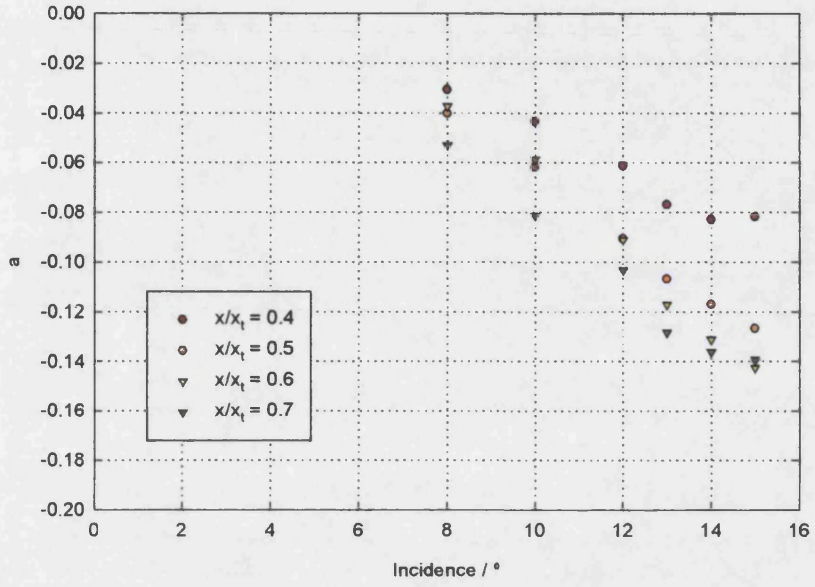

Figure 5.5: Variation of Addition Parameter with Chordwise Location and Incidence

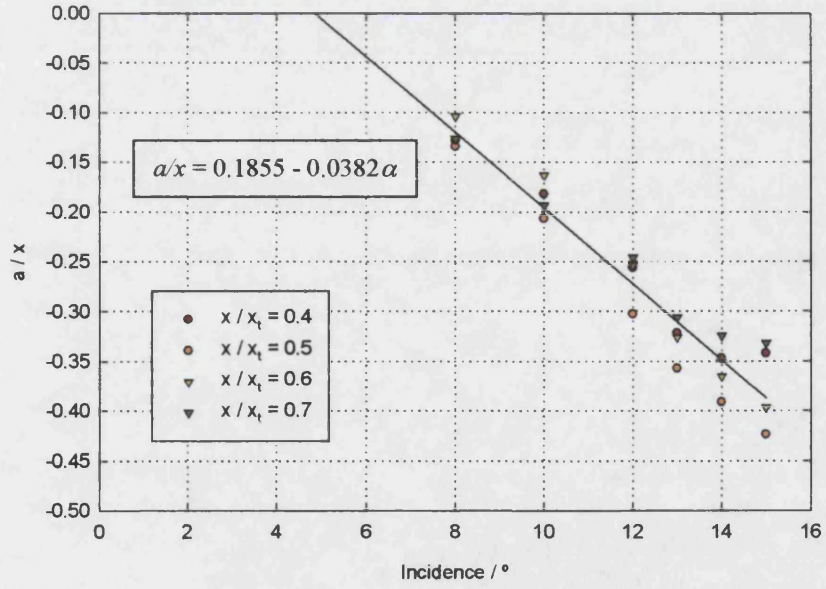

Figure 5.6: Variation of Addition Parameter Divided by Chordwise Location

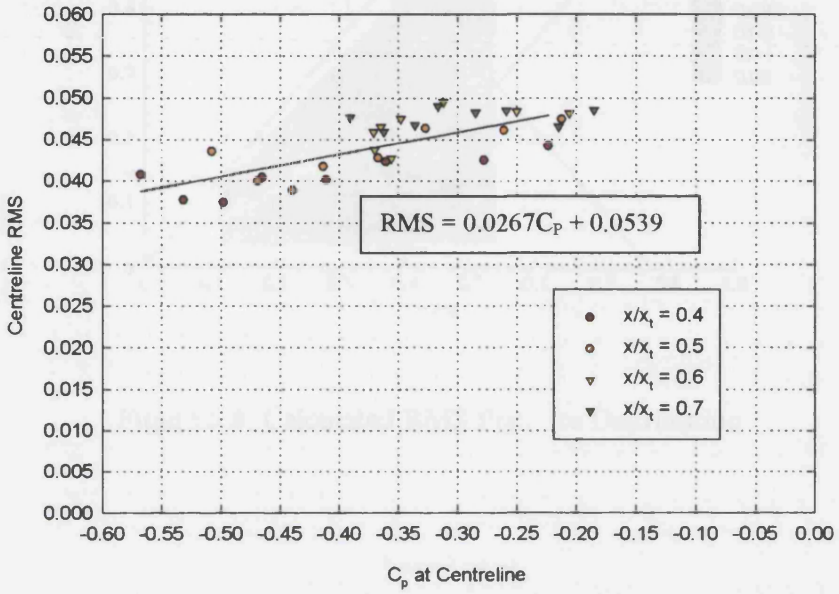

Figure 5.7: Variation of Centreline RMS with Centreline Pressure Coefficient

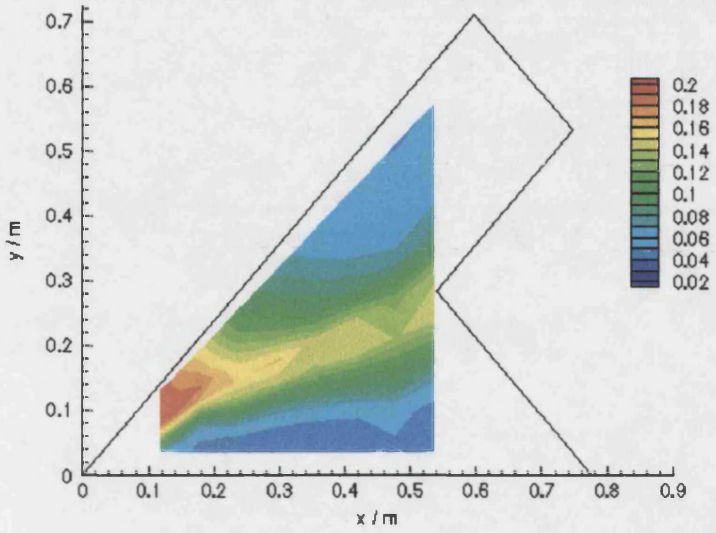

Figure 5.8: Calculated RMS Pressure Distribution

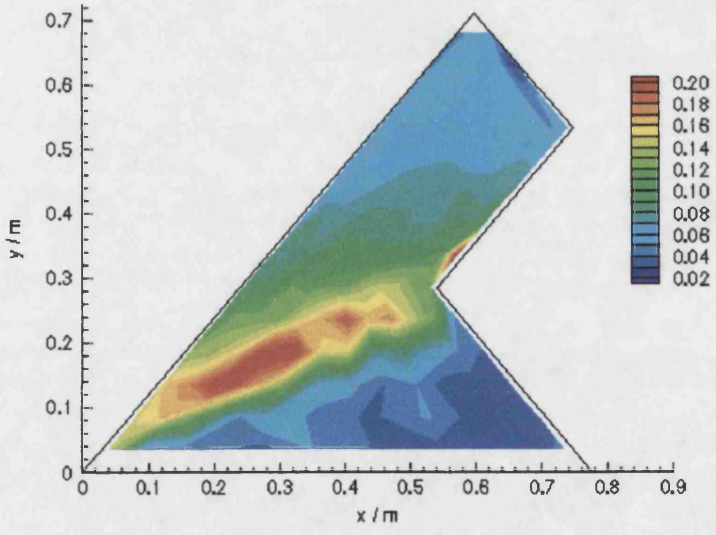

Figure 5.9: Experimental RMS Pressure Distribution

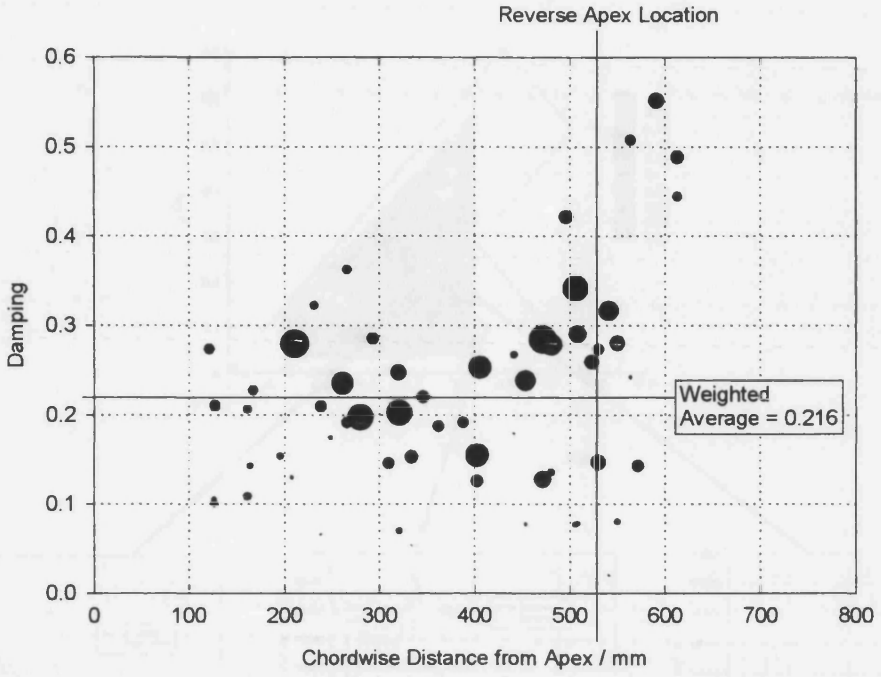

Figure 5.10: Damping of Peaks

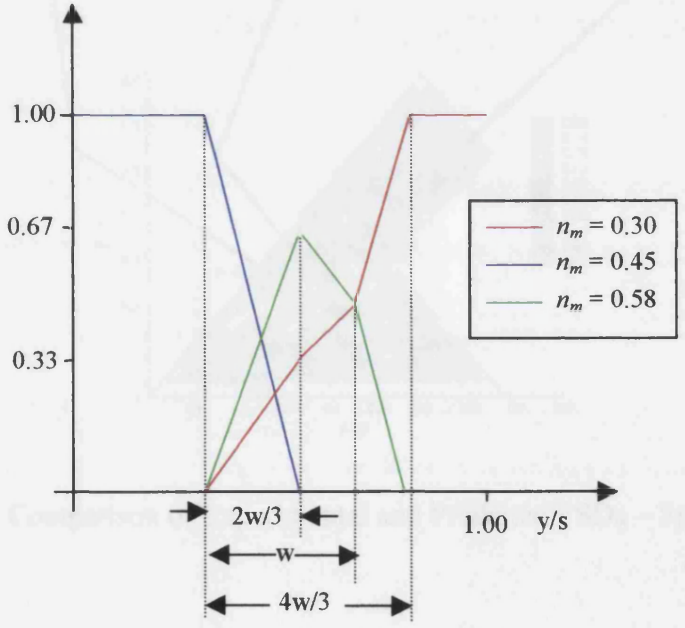

Figure 5.11: Relative Amplitude of Frequency Peaks

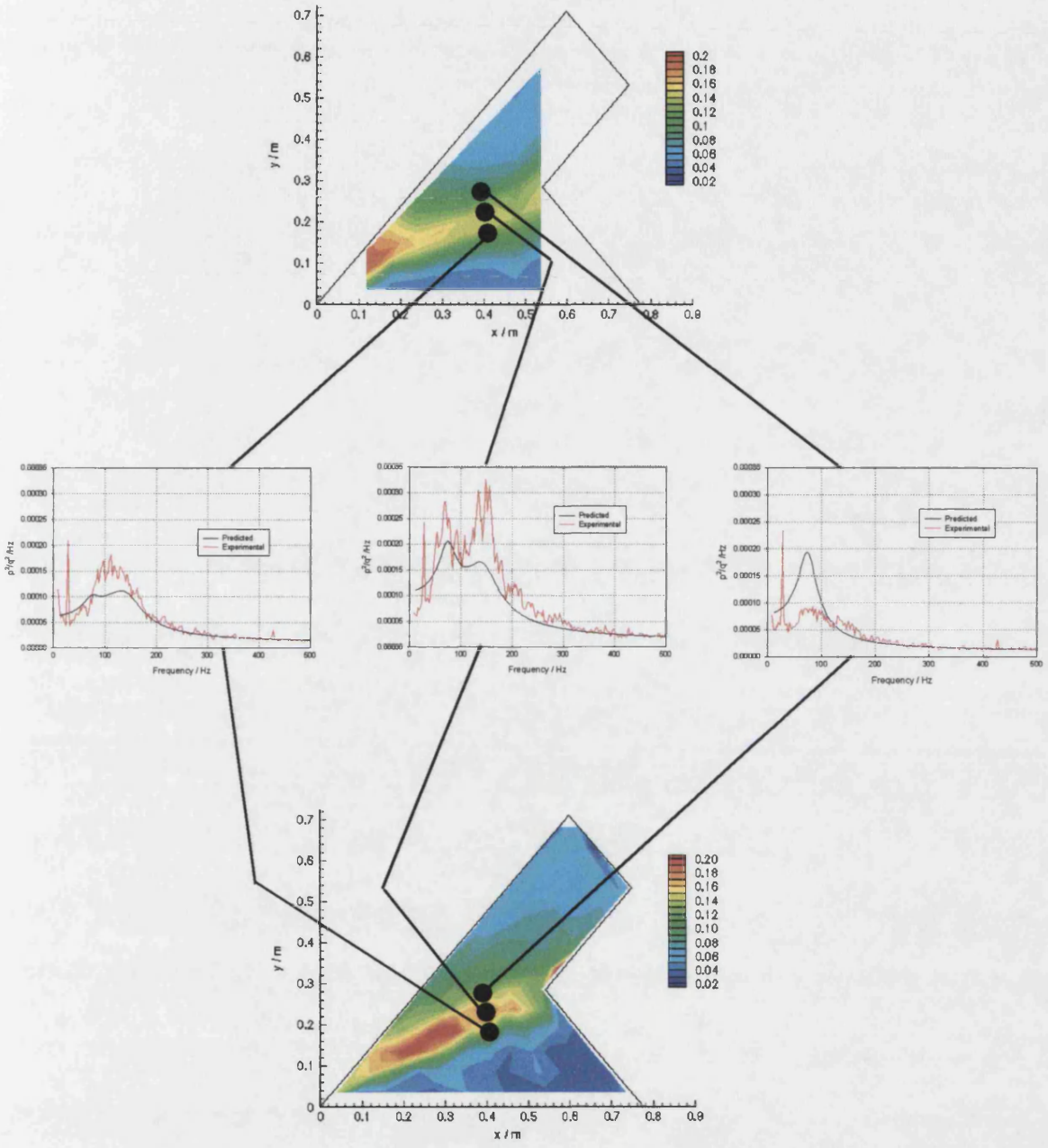

Figure 5.12: Comparison of Experimental and Predicted PSDs – Spanwise Slice

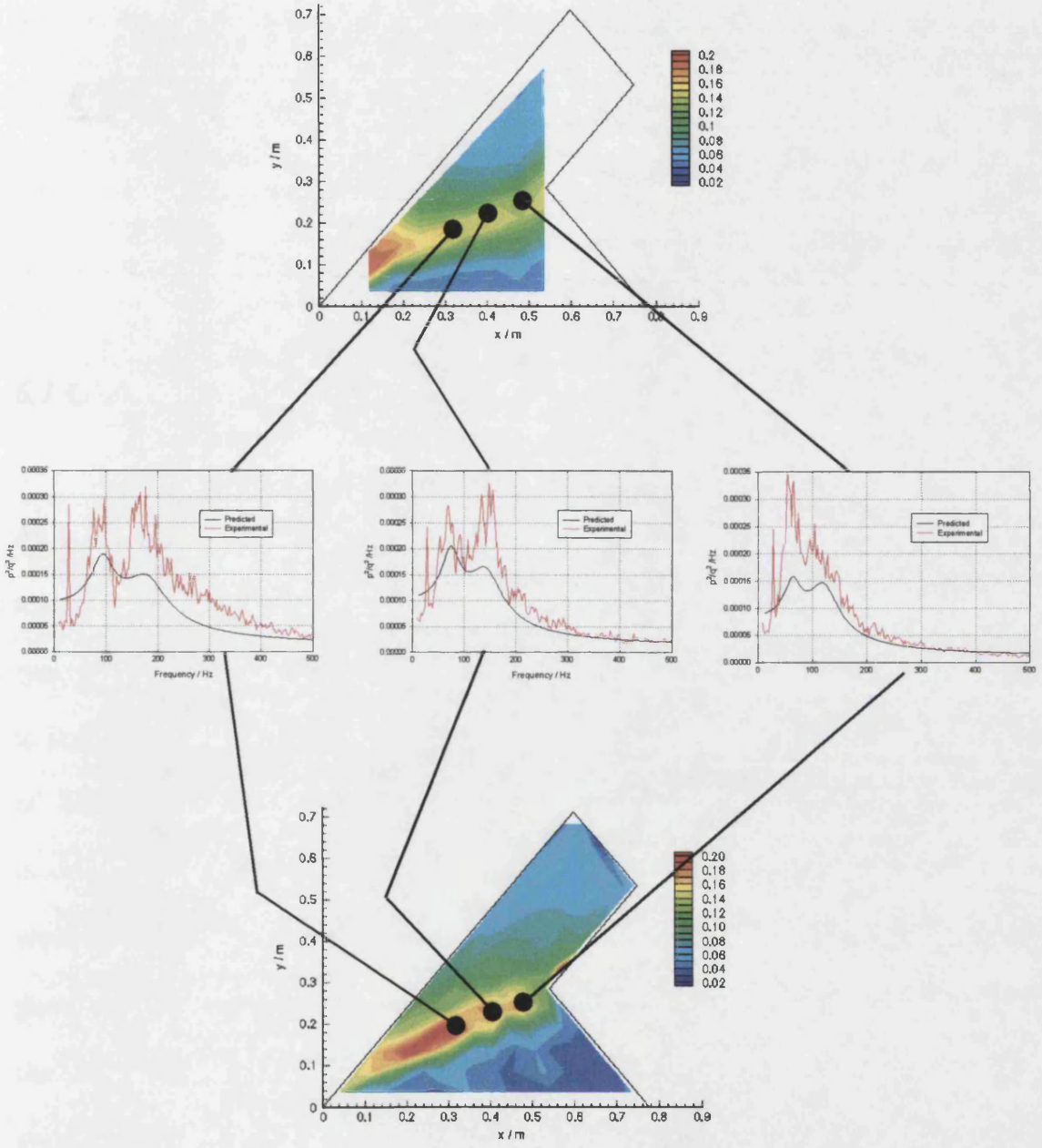

Figure 5.13: Comparison of Experimental and Predicted PSDs – High RMS Region

CHAPTER 6. CONCLUSIONS AND FUTURE WORK

6.1 Conclusions

An investigation has been made of the pressure fluctuations over the upper surface of a generic series of 'low-observable' planforms. Aircraft of this type are particularly susceptible to shortcomings in performance due to unsteady loads, since problems due to buffet are generally discovered late in the design process when the external shape of the aircraft has been fixed. Stealthy aircraft cannot have their external lines modified to rectify such problems since this will adversely affect their radar cross-section. They therefore have to have the structural strength of the affected panel/component increased to increase the separation between the centre frequency of the buffet and the structural mode. This process adds more weight to the aircraft than would be the case on an aircraft with a more usual radar cross-section. This is due to the internal structure of stealthy aircraft being partially defined by cross-section targets. It is therefore necessary to be able to predict such loads in the early phases of the aircraft design process.

To achieve this ambitious target within the time available a new model construction technique had to be developed. The technique utilised built on previous expertise within the University of Bath to produce four fully instrumented models, complete with accelerometers and unsteady pressure transducers as well as up to 165 Scanivalve tappings. The models were constructed of styrofoam, glass fibre and carbon fibre bonded together with cold cure epoxy resin.

To enable a prediction methodology to be contemplated, a large amount of data over the entire upper surface of the models would be required. It would not have been possible to achieve this without developing a new technique for the measurement of unsteady pressure data, since the pressure transducers available at the time cost approximately £500. A new technique was developed which utilised a simple Scanivalve apparatus. Each Scanivalve tapping was dynamically calibrated to enable the pressure fluctuations at the tappings to be derived from those measured at the Scanivalve transducer. This enabled unsteady pressure data to be acquired at each of the Scanivalve tappings for a cost of approximately 50p/tapping, a reduction in the cost of unsteady data acquisition by a factor of 1000. The technique has subsequently been adopted by British Aerospace and DERA for certain types of unsteady data acquisition.

Both steady and unsteady pressure data was acquired over a range of incidences for a total of six configurations. Oilflow visualisation data was acquired in addition to the pressure data. Data was acquired at a range of incidences for each model and later in

the test programme, when suitable data storage was available, tests at a variety of speeds were performed. This data was processed to allow the PSDs at each point over the surface to be calculated, and to enable the computation of the RMS pressure fluctuations.

Examination of the pressure data demonstrated that the peak RMS pressure fluctuations were not found under the vortex core (Woods and Wood – 1996) as had previously been accepted. Maximum pressure fluctuations were found inboard of the core. This revelation was made possible by the enhanced spatial resolution available using the calibrated Scanivalve technique. It was found that there were frequencies other than those previously measured by other researchers within the region of high RMS pressures. Specifically, there were points on the surface where two distinct peaks were apparent in the pressure spectra. In addition a third peak was detected directly underneath the primary attachment line of the leading edge vortex. The frequencies of all of these peaks has been shown to vary inversely with the chordwise distance from the leading edge apex. This had been reported previously (Gursul – 1994) but only one peak had been identified and only six tappings examined. The frequencies were also found to scale linearly with free stream velocity, as expected.

It was found that changes in the free stream speed gave an apparent variation in the calculated RMS pressure fluctuations. However, it was discovered that this was due to the variation in non-dimensional frequency that the readings were taken at for differing velocities. Doubling the free stream velocity halves the maximum non-

dimensional frequency at which data is acquired if a fixed limit is imposed on the maximum frequency that can be discerned, as was the case for the calibrated Scanivalve technique.

Distinct differences were found between models with 40° and 60° of leading edge sweep. The location of the vortex burst had a large influence on the RMS pressure fluctuations over the wing with 60° of sweep. Upstream of the burst there was very little buffet. Conversely, buffet was of similar magnitudes both up and downstream of the vortex burst over the wings with 40° of sweep.

A simple model of conflicting addition and dissipation of pressure fluctuations was proposed to explain the shape of the spanwise RMS pressure distribution. Addition of fluctuations from the shear layer is counteracted by dissipation, with the resulting pressure fluctuations swept outboard. This causes the RMS pressure fluctuations to rise from the primary attachment toward the suction peak. However, the dissipation causes the maximum RMS pressure to move inboard of the core. Cross correlation calculations of the pressure fluctuations at points under the shear layer could demonstrate or disprove this hypothesis, but the calibrated Scanivalve technique is limited in this respect. Since data is not acquired simultaneously at adjacent points, it is not possible to undertake such measurements.

This model was applied to a planform under investigation, and a series of programs was written to derive the variation of the rates of addition from the shear layer and

dissipation at the surface of the model by considering the steady and RMS pressure distributions. These parameters have been plotted and can be reconstructed using simple relationships involving the chordwise location and model incidence. This has enabled the RMS pressure to be reconstructed if the steady pressure distribution is known.

Comparisons between the reconstructed and experimental RMS pressure distributions show good agreement in the spanwise location of maximum RMS pressure. However, the amplitude of the RMS pressure was less well reconstructed, with errors of up to 11% apparent.

The relationships between the chordwise location and frequencies at which excitation was a maximum has enabled these frequencies to be estimated over the surface of the model. This, together with a very simple model of the distribution of the relative amplitudes of the three peaks in the spectra and estimates of the breadth of the peaks, has enabled the power spectra over the surface of the model to be predicted. The estiimation of the centre frequencies of the peaks is very good, and the shape of the individual peaks is well replicated. However, the magnitude of the peaks is less well represented. This is largely due to the errors in the RMS pressure prediction, since an 11% error in RMS pressure fluctuations corresponds to a 21% error in the area under a PSD.

6.2 Recommendations for Future Work

There are a large number of areas where further work is required to result in a technique for the prediction of buffet which is of use to industry as a design tool:

1) The tests that have been undertaken are at low speeds of the order of M=0.1. Despite the relative insensitivity of vortical flows to Reynolds number, compressibility effects at a typical manoeuvring speed of M=0.6 cannot be discounted. Therefore, further testing should be undertaken at higher Mach numbers.
2) Insufficient spatial resolution has been achieved within the region of high RMS pressures to map the evolution of the pressure spectra in a spanwise direction. Typically, only one point at a given chordwise location is within this region. This makes it very difficult to estimate the relative amplitude of the three peaks, thus forming a major source of error in the PSD prediction. Tests could be undertaken to resolve this by clustering tappings within this region for future tests.
3) It is not clear whether disturbances present within the shear layer are being convected outboard, and whether the reverse is true when there is a source of excitation downstream. Tests could be undertaken with a small number of surface mounted transducers to examine cross-correlations between adjacent tappings.

4) The reconstruction of the RMS and PSDs should be applied to the other planforms. This will demonstrate whether it is of use for the *prediction* of these parameters.

5) The major source of error in the reconstruction of the parameters appears to be the non-linearity of the variation of the addition parameter, especially as stall is approached. A combination of LDA or PIV with surface pressure measurements would resolve whether there is a relationship between circulation and addition parameter.

CHAPTER 7: REFERENCES

1) Bean D.E. (1990), The Analysis and Suppression of Vortex Induced Unsteady Loads at High Angles of Attack, PhD Thesis, University of Bath

2) Bendat J.S., Piersol A.G. (1971), Random Data: Analysis and Measurement Procedures, John Wiley and Sons, New York, ISBN 0-471-06470-X

3) Benjamin T.B. (1962), Theory of the Vortex Breakdown Phenomenon, J. Fluid Mech., **14** (4), pp.593-629

4) Benjamin T.B. (1967), Some Developments in the Theory of Vortex Breakdown, J. Fluid Mech., **28** (1), pp. 65-84

5) Brown G.L., Roshko A. (1974), On Density Effects and Large Structure in Turbulent Mixing Layers, J. Fluid Mech., **64**, pp.775-816

6) Cassidy J.J., Falvey H.T., (1970), Observations of Unsteady Flow Arising After Vortex Breakdown, J. Fluid Mech., **41** (4), pp. 727-736

7) Chesneau T.R., (1996), Configuration Dependent Buffeting of a Generic Single Fin Combat Aircraft, PhD Thesis, University of Bath

8) Chesneau T.R., Wood N.J. (1994), Effect of Forebody Shape on Fin Buffeting Response-Annual Progress Report, 077/1994, School of Mechanical Engineering, University of Bath

9) Danks M. (1995), Issues Relating to Laminar Flow Control on the Leading Edge of Swept Wings, Ph.D. Thesis, School of Mechanical Engineering, University of Manchester

10) Del Frate J.H., Fisher D.F., Zuniga F.A., (1990) In-Flight Flow Visualisation and Pressure Measurements at Low Speeds on the NASA F-18 High Alpha Research Vehicle, AGARD-CP-494, Symposium of the Fluid Dynamics Panel, Scheveningen, Netherlands, 1st to 4th October 1990

11) Erickson G.E., Scheiner J.A., Rogers L.W. (1989), On the Structure, Interaction, and Breakdown Characteristics of Slender Wing Vortices at Subsonic, Transonic, and Supersonic Speeds, AIAA Atmospheric Flight Mechanics Conference, Boston, MA, August 1989

12) Escudier M. (1984), Observations of Flow Produced in a Cylindrical Container by a Rotating Endwall, Experiments in Fluids, **2**, pp.189-196

13) Escudier M. (1988), Vortex Breakdown: Observations and Explanations, Prog. Aero. Sci., **25**, pp.189-229

14) Faler J.H., Leibovich S. (1977), Disrupted States of Vortex Flow and Vortex Breakdown, Phys. Fluids, **20**, pp.1385-1400

15) Fraenkel L.E. (1967), On Benjamin's Theory of Conjugate Flows, J. Fluid Mech., **28** (1), pp. 85-96

16) Gad-el-Hak M., Blackwelder R.F. (1985), The Discrete Vortices from a Delta Wing, AIAA Journal, **23** (6), pp.961-962

17) Garg A.K., Leibovich S. (1979) Spectral Characteristics of Vortex Breakdown Flowfields, Phys. Fluids, **22** (11), pp. 2053-2064

18) Greenwell D.I. (1993), Control of Asymmetric Vortical Flow Over a Delta Wing at High Angles of Attack, Ph.D. Thesis, School of Mechanical Engineering, University of Bath

19) Greenwell D.I., Wood N.J. (1992), Determination of Vortex Burst Location on Delta Wings from Surface Pressure Measurements, AIAA Journal, **30** (11), pp. 2736-2739

20) Gursul I. (1994), Unsteady Flow Phenomena Over Delta Wings at High Angles of Attack, AIAA Journal, **32** (2), pp.225-231

21) Gursul I. (1995), Criteria for the Location of Vortex Breakdown Over Delta Wings, Aeronautical Journal, pp. 194-196

22) Hall M.G. (1961), A Theory for the Core of a Leading Edge Vortex, J. Fluid Mech., **11**, pp. 209-228

23) Hall M.G. (1966), The Structure of Concentrated Vortex Cores, Prog. Aero. Sci., **7**, pp. 53-110

24) Hall M.G. (1972), Vortex Breakdown, Ann. Rev. Fluid Mech., **4**, pp. 195-?

25) Harvey J.K.(1962), Some Observations of the Vortex Breakdown Phenomenon, J. Fluid Mech., **14** (4), pp. 585-592

26) Herbst W.B. (1983), Dynamics of Air Combat. J. Aircraft, **20**, (7), pp. 594-598

27) Hodgkin F., Woods M.I. (1994), Buffet Characteristics of Novel Wing planforms, Final Year Project Report AE8/94, School of Mechanical Engineering, University of Bath

28) Hoeijmakers H.W.M. (1990), Modelling and Numerical Simulation of Vortex Flow in Aerodynamics, AGARD-CP-494, Symposium of the Fluid Dynamics Panel, Scheveningen, Netherlands, 1st to 4th October 1990

29) Honkan A., Andreopoulos A. (1997), Instantaneous Three-Dimensional Vorticity Measurements in Vortical Flow over a Delta Wing, AIAA Journal, **35**, (10), pp. 1612-1620

30) Houghton E.L., Carpenter P.W. (1993), Aerodynamics for Engineering Students, Edward Arnold, London, ISBN 0-340-54847-9

31) Hubner J.P., Komerath N.M. (1995), Spectral Mapping of Quasi-Periodic Structures in a Vortex Flow, J. Aircraft, **32** (3), pp. 493-500

32) Jumper E.J., Nelson R.C., Cheung K. (1993), A Simple Criterion for Vortex Breakdown, AIAA-93-0866

33) Jupp, M. L., Coton, F. N., Green, R. B., Galbraith, R. A. McD. (1998), An Analysis of a Pitching Delta Wing Using High Resolution Pressure Measurements, 16th AIAA Applied Aerodynamics Conference, Albuquerque, NM, June 15-18

34) Khorrami M.R. (1991), On the Viscous Modes of Instability of a Trailing Line Vortex, J. Fluid Mech., **225**, pp. 197-212

35) Kribus A., Leibovich S. (1994), Instability of Strongly Non-Linear Waves in Vortex Flows, J. Fluid Mech., **269**, pp. 247-264

36) Lambert M. (1994), Jane's All the World's Aircraft 1994-95, Jane's Information Group Ltd., ISBN 0 7106 1160 9

37) Lambourne N.C., Bryer D.W. (1962) The Bursting of Leading-Edge Vortices - Some Observations and Discussion of the Phenomenon, ARC, R.& M. 3282 (22,775)

38) Lee B.H.K, Valerio N.R., Tang F.C. (1994), Steady and Unsteady Pressure Distributions on an F/A-18 Wing at $\alpha = 30°$, J. Aircraft, **31**, 4, pp. 862-867

39) Lee M., Ho C.M. (1990), Lift Force of Delta Wings, Applied Mechanic Reviews, 43 (9), pp. 209-221

40) Leibovich S. (1984), Vortex Stability and Breakdown: Survey and Extension, AIAA Journal, **22** (9), pp. 1192-1206

41) Leibovich S. (1985), Attempts to Assess the Effects of Azimuthal Asymmetries in Vortex Breakdown, Colloquim of Vortex Breakdown, February 11th-12th, 1985,Aachen

42) Leibovich S., Stewartson K. (1983), A Sufficient Condition for the Instability of Columnar Vortice, J. Fluid Mech., **126**, pp. 335-356

43) Lessen M., Singh P.J., Paillet F. (1974), The Stability of a Trailing Line Vortex. Part 1. Inviscid Theory, J. Fluid Mech., **63** (4), pp. 753-763

44) Lessen M., Paillet F. (1974b), The Stability of a Trailing Line Vortex. Part 2. Viscous Theory, J. Fluid Mech., **65** (4), pp. 769-779

45) Lowson M.V. and Riley A.J., (1995), Vortex Breakdown Control by Delta Wing Geometry, J. Aircraft, **32**, (4), pp.832-838

46) Lynn R. (1997), Dynamic Calibration of Tube-Transducer Systems for Unsteady Pressure Measurement, DERA/AS/HWA/WP97008

47) Mabey D.G. (1991), Measurements of Fin Buffeting on an 'F-18' Model and Derived Interpretive Hypothesis, DRA Bedford, Technical Memorandum Aero 2224

48) Mager A. (1972), Dissipation and Breakdown of a Wing-Tip Vortex, J. Fluid Mech., **55**, pp.609-628

49) Nelson R.C., Visser K.D. (1990), Breaking Down the Delta Wing Vortex. The Role of Vorticity in the Breakdown Process, AGARD-CP-494, Symposium of the Fluid Dynamics Panel, Scheveningen, Netherlands, 1st to 4th October 1990

50) Peckham D.H. (1961), Low Speed Wind Tunnel Tests on a Series of Uncambered Slendar Pointed Wings with Sharp Edges, ARC, R.&M. No. 508 (19632)

51) Pilkington D.J, Wood N.J., (1994), Unsteady Aerodynamic Effects of Trailing Edge Controls on Delta Wings, ICAS-94-10.1.1, 19th Conference of the International Council of the Aeronautical Sciences, Anaheim, 18th-23rd September 1994

52) Press W.H, Flannery B.P., Teukolsky S.A., Vetterling W.T. (1986), Numerical Recipes - The Art of Scientific Computing, Cambridge University Press, ISBN 0-521-30811-9

53) Randall J.D., Leibovich S. (1973), The Critical State: A Trapped Wave Model of Vortex Breakdown, J. Fluid Mech., **58** (3), pp. 495-515

54) Rao D.M. (1990),Vortex Control - Further Encounters, AGARD-CP-494, Symposium of the Fluid Dynamics Panel, Scheveningen, Netherlands, 1st to 4th October 1990

55) Rediniotis O.K., Stapountzis H., Telionis D.P. (1993), Periodic Vortex Shedding Over Delta Wings, AIAA Journal, **31** (9), pp. 1555-1562

56) Reynolds G.A., Abtahi A.A. (1989), Three Dimensional Vortex Development, Breakdown and Control, AIAA-89-0998

57) Sarpkaya T. (1971a), On Stationary and Travelling Vortex Breakdowns, J. Fluid Mech., **45** (3), pp.545-559

58) Sarpkaya T. (1971b), Vortex Breakdown in Swirling Conical Flows, AIAA Journal, **9** (9), pp.1972-1979

59) Sarpkaya T. (1974), Effect of the Adverse Pressure Gradient on Vortex Breakdown, AIAA Journal, **12** (5), pp. 602-607

APPENDIX A: Curve Fit Program Listing

This Appendix contains a program listing for fitting seven parameters to a PSD. The program fits parameters for buffet data alpha sweep of Model 3. PSDs are read from an ASCII text file generated from a Microsoft Excel spreadsheet containing all Model 3 PSDs.

```
      PROGRAM CFIT
************************************************************************
*
* PROGRAM CFIT takes input(text) files defining tapping locations
* and PSDs and models the PSDs as the summation of two base excited
* second order systems and a white noise signal. A white noise input
* to the second order systems is assumed.
* The Levenberg-Marquardt method non-linear least squares routine is
* utilised to optimise 7 parameters.
* These are:
*       A(1) -       White noise amplitude
*       A(2) -       First System undamped natural frequency
*       A(3) -       Second System undamped natural frequency
*       A(4) -       First System zeta
*       A(5) -       Second System zeta
*       A(6) -       First System input
*       A(7) -       Second System input
************************************************************************
*
      PARAMETER (NPTS=231,NVARS=7,NFIT1=7,NTAPS=165)
      INTEGER O,INC,FIT(NTAPS),LISTA(NVARS)

      REAL
FREQ(NPTS),X(NTAPS),Y(NTAPS),TOTAL,PSQQSQ(NPTS),DYDA(NVARS),
     +   SIGMA(NPTS),COVAR(NVARS,NVARS),CHISQ,A(NVARS),TEST(NPTS),
     +
BETA(NVARS),ALPHA(NVARS,NVARS),WD(2),NMN(2),NMD(2),DIST(NTAPS)

      CHARACTER C1*1, C2*2, FILNAM*16
```

```
* Open files to read frequencies and tapping locations
      OPEN(9,FILE='D:\M3TAP.TXT',STATUS='OLD')
      OPEN(10,FILE='D:\FREQ.TXT',STATUS='OLD')
      OPEN(11,FILE='D:\M3FIT.TXT',STATUS='OLD')

* Read in frequencies of data points
      DO 10 I=1,NPTS
       READ(10,509) FREQ(I)
 10   CONTINUE

* Read in locations of tappings and numbers of 'bad' tappings (Model
3)
      DO 12 I=1,NTAPS
       READ(9,519) X(I), Y(I)
       READ(11,549) FIT(I)
       DIST(I)=X(I)
 12   CONTINUE

* Open a file to write parameters/standard errors to
      OPEN(21, FILE='M325P2OR.TXT', STATUS='UNKNOWN')
      OPEN(22, FILE='M325C2OR.TXT', STATUS='UNKNOWN')
      OPEN(23, FILE='M325CURV.TXT', STATUS='UNKNOWN')

* Loop through all incidences
      DO 22 K=1,12

* Work out what the incidence is...
       IF (K.LE.2) THEN
          INC=(2*K)+1
       ELSE IF (K.LE.5) THEN
          INC=(2*K)+2
       ELSE IF (K.LE.8) THEN
          INC=K+7
       ELSE IF (K.LE.10) THEN
          INC=(3*K)-10
       ELSE
          INC =(4*K)-23
       ENDIF

* ...and incorporate it in the filename to read PSD data from.
       IF(INC.LT.10) THEN
          WRITE (C1,'(I1)') INC
          FILNAM='D:\M325'//C1//'.TXT'
       ELSE
          WRITE (C2,'(I2)') INC
          FILNAM='D:\M325'//C2//'.TXT'
       ENDIF
       PRINT*,' Opening file: ',FILNAM
       OPEN(12, FILE=FILNAM, STATUS='OLD')

* Loop through each tapping...
       DO 20 L=1,NTAPS

* Read in the data...
          READ(12,529)PSQQSQ

* ... estimating variance etc. of points...
          PRINT*,' PSD ',L,' read... '
          TOTAL=0.0
          DO 14 M=1,NPTS
```

```
              TOTAL = TOTAL+PSQQSQ(M)
 14          CONTINUE

* ... checking if a fit is required...
           IF ((TOTAL.GT.0.0064).AND.(FIT(L).EQ.1))THEN
              CALL FIRST(NPTS,INC,A,PSQQSQ,FREQ,NVARS,NFIT1,CHISQ,
     +             BETA,LISTA,SIGMA,TOTAL,L,DIST(L),ALPHA,COVAR,NFIT)

* Write standard errors to file
              WRITE(22,579)INC,L
              DO 16 O=1,7
               WRITE (22,569) COVAR(O,1), COVAR(O,2), COVAR(O,3),
     +               COVAR(O,4), COVAR(O,5),COVAR(O,6),COVAR(O,7)
 16             CONTINUE

* Output curves to file
              DO 18 I=1,NPTS
               CALL FUNCS1(FREQ(I),A,TEST(I),DYDA,NVARS)
 18             CONTINUE
              WRITE(23,579)INC,L
              WRITE(23,559)PSQQSQ
              WRITE(23,559)TEST
              WRITE(23,509)CHISQ

* Calculate the damped natural frequencies
              RINC=FLOAT(INC)*3.141592654/180.0
              DO 19 I=1,2
               IF (A(I+3).LT.0.0) A(I+3)=-1.0*A(I+3)
               IF (A(I+5).LT.0.0) A(I+5)=-1.0*A(I+5)
               IF (ABS(A(I+3)).LT.1.0) THEN
                  WD(I)=A(I+1)*SQRT(1.0-A(I+3)**2)
                  NMN(I)=A(I+1)*SIN(RINC)*DIST(L)/25000.0
                  NMD(I)=WD(I)*SIN(RINC)*DIST(L)/25000.0
               ELSE
                  WD(I)=0.0
                  NMN(I)=0.0
                  NMD(I)=0.0
               ENDIF
 19             CONTINUE

* If a curve hasn't been fitted, set the noise to the mean and zero
* the other parameters
           ELSE
              DO 24 M=2,7
               A(M)=0.0
 24             CONTINUE
              RNPTS=FLOAT(NPTS)
              A(1)=TOTAL/RNPTS
              CHISQ=0.0
              DO 26 M=1,2
               WD(M)=0.0
               NMN(M)=0.0
               NMD(M)=0.0
 26             CONTINUE
           ENDIF




* Output parameters to file
```

```
          PRINT*,'Writing parameters and errors to file '
          WRITE (21,539) INC,L, X(L),Y(L),CHISQ,A(1),A(2),A(3),
     +          A(4),A(5),A(6),A(7),WD(1),WD(2),NMN(1),NMN(2),NMD(1),
     +          NMD(2),DIST(L)
 20       CONTINUE
 22    CONTINUE

 509   FORMAT (F7.2)
 519   FORMAT (2F8.2)
 529   FORMAT (231E16.2)
 539   FORMAT (2(I3,1X),17(E10.4,1X))
 549   FORMAT (I3)
 559   FORMAT (231(E10.5,1X))
 569   FORMAT (5(E10.4,1X))
 579   FORMAT (2(I3,1X))


       END


*****************************************************************
      SUBROUTINE FUNCS1(X,A,Y,DYDA,NA)
*****************************************************************
* SUBROUTINE FUNCS1 calculates the function and all derivatives
* at all the required data points for  2 second order systems
* plus a white noise signal.
*****************************************************************

      DIMENSION A(NA), DYDA(NA)

* Calculate terms
      Y=0.0
      DYDA(1)=0.0
      DO 11 I=1,2
       IF (A(I+3).EQ.0.0) GOTO 12
       RES=(X*X)/(A(I+1)*A(I+1))
       ZET=4.0*A(I+3)*A(I+3)
       BOT=(1.0-RES)*(1.0-RES)+ZET*RES
* Calculate value of response...
       Y=Y+A(I+5)*SQRT((1.0+ZET*RES)/BOT)
* ...and calculate the derivatives
       DYDA(I+5)=SQRT((1.0+ZET*RES)/BOT)
       DYDA(I+1)=0.5*A(I+5)*SQRT(BOT/(1.0+ZET*RES))*
     +             ((-1.0*BOT*2.0*ZET*RES/A(I+1))-
     +             (1.0+ZET*RES)*(-4.0*RES*RES+4.0*RES-2.0*ZET*RES))
     +             /(A(I+1)*BOT*BOT)
       DYDA(I+3)=0.5*A(I+5)*SQRT(BOT/(1.0+ZET*RES))*
     +             (BOT*8.0*RES*A(I+3)-(1.0+ZET*RES)*8.0*RES*A(I+3))
     +             /(BOT*BOT)
 12       CONTINUE
 11    CONTINUE


* Calculate value and derivative of noise
      Y=Y+A(1)
      DYDA(1)=1.0

      RETURN
      END
*****************************************************************
*
```

```
      SUBROUTINE
FIRST(NPTS,INC,A,PSQQSQ,FREQ,NVARS,NFIT1,CHISQ,BETA,
     +   LISTA,SIGMA,TOTAL,L,X,ALPHA,COVAR,NFIT)
************************************************************************
*
* SUBROUTINE FIRST makes initial guesses of parameters and iterates
* to minimise chi-squared.
************************************************************************
*

      REAL A(NVARS),PSQQSQ(NPTS),FREQ(NPTS),BETA(NVARS),SIGMA(NPTS),
     +   COVAR(NVARS,NVARS),ALPHA(NVARS,NVARS),OCHISQ

      INTEGER LISTA(NVARS)

* Guess parameters from PSDs
      IBIG=1
      DO 102 I=1,NPTS
       IF (PSQQSQ(I).GT.PSQQSQ(IBIG)) IBIG=I
 102  CONTINUE
      RNPTS=FLOAT(NPTS)
      RINC=FLOAT(INC)
      A(1)=TOTAL/(RNPTS*1.0)
      A(2)=FREQ(IBIG)
      IHIGH=((4*IBIG+76)-38)/2
      ILOW=(IBIG-19)/2
      IF (ILOW.LE.1) THEN
       A(3)=2.0*A(2)
      ELSE IF (IHIGH.GT.NPTS) THEN
       A(3)=0.5*A(2)
      ELSE IF (PSQQSQ(IHIGH).GT.PSQQSQ(ILOW)) THEN
       A(3)=2.0*A(2)
      ELSE
       A(3)=0.5*A(2)
      ENDIF
      A(4)=0.1
      A(5)=0.1
      A(6)=A(1)
      A(7)=A(1)
      DO 10 M=1,NPTS
       SIGMA(M)=0.02*TOTAL/SQRT(RNPTS)
 10   CONTINUE

* Initialise LISTA for fitting of parameters
      NFIT=NFIT1
      DO 12 I=1,NVARS
       LISTA(I)=I
 12   CONTINUE

* Initialise the subroutine MRQMIN
 100  CONTINUE
      ALAMDA=-1.0
      CALL MRQMIN(FREQ,PSQQSQ,SIGMA,NPTS,A,NVARS,LISTA,NFIT,
     +   COVAR,ALPHA,NVARS,CHISQ,FUN,ALAMDA,BETA,OCHISQ,1)
      PRINT*,' Matrix Initialised '

* Loop until chi-squared is minimised
      PRINT*,' Minimising chi-squared... '
      DO 16 N=1,30000
       PRINT*,' Incidence = ',INC,' Tapping = ',L
       PRINT*,' Search loop ',N
```

```
      OCHISQ=CHISQ
      CALL MRQMIN(FREQ,PSQQSQ,SIGMA,NPTS,A,NVARS,LISTA,
     +     NFIT,COVAR,ALPHA,NVARS,CHISQ,FUN,ALAMDA,BETA,
     +     OCHISQ,1)
      PRINT*,A(6),A(2),A(4)
      PRINT*,A(7),A(3),A(5),A(1)

* Check if a damping has grown too large, zero and restart...
      DO 14 I=4,5
         IF ((A(I+2).LT.0.0).OR.(ABS(A(I)).GT.100.0)) THEN
            DO 11 K=2,-2,-2
             A(I+K)=0.0
             IF (NFIT.NE.6) THEN
                DO 13 J=(I+K),(NVARS-1)
                 LISTA(J)=LISTA(J+1)
13                  CONTINUE
                LISTA(NVARS)=I+K
             ELSE
                DO 24 J=(I+K-1),(NVARS-2)
                 LISTA(J)=LISTA(J+1)
24                  CONTINUE
                LISTA(NVARS-1)=I+K
             ENDIF
11            CONTINUE
            NFIT=NFIT-3
            PRINT*,' Large Damping... Zero and re-initialise '
            GOTO 100
         ENDIF
14      CONTINUE


      IF((CHISQ.LT.0.1).OR.(((CHISQ/OCHISQ).GT.0.999995)
     +     .AND.((CHISQ/OCHISQ).LT.1.0)))GOTO 17
16    CONTINUE
17    CONTINUE

* Check if white noise is negative, zero and restart
      IF (A(1).LT.0.0) THEN
       A(1)=0.0
       DO 15 J=(1),(NVARS-1)
          LISTA(J)=LISTA(J+1)
15      CONTINUE
       LISTA(NVARS)=1
       NFIT=NFIT-1
       PRINT*,' Negative noise... Zero and re-initialise '
       GOTO 100
      ENDIF

* Check if all amplitudes zero, restart with noise only
      IF ((A(1).EQ.0.0).AND.(A(6).EQ.0.0).AND.(A(7).EQ.0.0)) THEN
       A(1)=TOTAL/RNPTS
       LISTA(1)=1
       NFIT=1
       GOTO 100
      ENDIF

* Check if peak amplitude less than noise, zero and restart
      DO 18 I=6,7
       IF (A(I-2).NE.0.0) THEN
          RPEAK=A(I)/(2.0*ABS(A(I-2)))
       ELSE
```

```
            RPEAK=0.0
          ENDIF
          IF ((RPEAK.LT.A(1)).AND.(A(I).NE.0.0)) THEN
             DO 20 K=0,-4,-2
                A(I+K)=0.0
                DO 22 J=(I+K),(NVARS-1)
                 LISTA(J)=LISTA(J+1)
 22               CONTINUE
                LISTA(NVARS)=I+K
 20           CONTINUE
             NFIT=NFIT-3
             PRINT*,' Small Amplitude... Zero and re-initialise '
             GOTO 100
          ENDIF
 18     CONTINUE


       PRINT*,' Search complete '

* Set lambda to zero and calculate covariance matrix
       ALAMDA=0.0
       CALL MRQMIN(FREQ,PSQQSQ,SIGMA,NPTS,A,NVARS,LISTA,
      +    NFIT,COVAR,ALPHA,NVARS,CHISQ,FUN,ALAMDA,BETA,
      +    OCHISQ,1)


       RETURN
       END

*****************************************************************
       SUBROUTINE MRQMIN(X,Y,SIG,NDATA,A,MA,LISTA,MFIT,COVAR,ALPHA,
      +    NCA,CHISQ,FUN,ALAMDA,BETA,OCHISQ,MODEL)
*****************************************************************
* SUBROUTINE MRQMIN attempts to minimize the value of chi-
* squared of a fit between NDATA points X,Y and the function
* defined in SUBROUTINE FUNCS. This routine is taken from
* 'Numerical Recipes', 1986 (ISBN 0 521 30811 9), pp. 526-527.
*****************************************************************
       PARAMETER (MMAX=20)
       DIMENSION X(NDATA),Y(NDATA),SIG(NDATA),A(MA),LISTA(MA),
      +    COVAR(NCA,NCA),ALPHA(NCA,NCA),ATRY(MMAX),BETA(MA),
      +    DA(MMAX)

* Initialisation loop
       IF(ALAMDA.LT.0.0) THEN
        KK=MFIT+1
        DO 12 J=1,MA
           IHIT=0
           DO 11 K=1,MFIT
              IF(LISTA(K).EQ.J) IHIT=IHIT+1
 11         CONTINUE
           IF (IHIT.EQ.0) THEN
              LISTA(KK)=J
              KK=KK+1
           ELSE IF (IHIT.GT.1) THEN
              PRINT*, 'Improper permutaion in LISTA (Type 1) '
              STOP
           ENDIF
 12      CONTINUE
        IF (KK.NE.(MA+1)) THEN
           PRINT*, 'Improper permutaion in LISTA (Type 2) '
```

```
          STOP
        ENDIF
        ALAMDA=1.0
        CALL MRQCOF(X,Y,SIG,NDATA,A,MA,LISTA,MFIT,ALPHA,BETA,NCA,
     +       CHISQ,FUN,MODEL)
        DO 13 J=1,MA
          ATRY(J)=A(J)
 13     CONTINUE
      ENDIF

* Set old value of chi-squared for later comparison and reset DA
      OCHISQ=CHISQ
      DO 99 I=1,MA
       DA(I)=0.0
 99   CONTINUE

* Alter linearised fitting matrix by augmenting diagonal elements
* ie. Multiply diagonal elements by 1+ALAMDA
      DO 15 J=1,MFIT
       DO 14 K=1,MFIT
          COVAR(J,K)=ALPHA(J,K)
 14     CONTINUE
       COVAR(J,J)=ALPHA(J,J)*(1.0+ALAMDA)
          DA(J)=BETA(J)
 15   CONTINUE

* Call subroutine to solve matrix
      CALL GAUSSJ(COVAR,MFIT,NCA,DA,1,1)

* If converged (ie. ALAMDA has been set to 0.0) then calculate the
* covariance matrix
      IF (ALAMDA.EQ.0.0) THEN
       CALL COVSRT(COVAR,NCA,MA,LISTA,MFIT)
       RETURN
      ENDIF

* Check if solution is converging...
      DO 16 J=1,MA
       ATRY(LISTA(J))=A(LISTA(J))+DA(J)
 16   CONTINUE
      CALL MRQCOF(X,Y,SIG,NDATA,ATRY,MA,LISTA,MFIT,COVAR,DA,
     +   NCA,CHISQ,FUN,MODEL)

* Print old and new chisquared on screen
      PRINT*,' Chi-squared = ',CHISQ
      PRINT*,' Old chi-squared = ',OCHISQ

* ...If it is then accept the solution...
      IF((CHISQ.LT.OCHISQ).AND.(ALAMDA.GT.0.1E-30)) THEN
       ALAMDA=0.1*ALAMDA
       DO 18 J=1,MFIT
          DO 17 K=1,MFIT
             ALPHA(J,K)=COVAR(J,K)
 17        CONTINUE
          BETA(J)=DA(J)
          A(LISTA(J))=ATRY(LISTA(J))
 18     CONTINUE


* ...If not increase ALAMDA and return
      ELSEIF (ALAMDA.LT.0.1E+15) THEN
```

```
       ALAMDA=10.0*ALAMDA
       CHISQ=OCHISQ
      ELSE
       CHISQ=0.999999*OCHISQ
      ENDIF

      RETURN
      END

*****************************************************************
      SUBROUTINE MRQCOF(X,Y,SIG,NDATA,A,MA,LISTA,MFIT,ALPHA,
     +   BETA,NALP,CHISQ,FUN,MODEL)
*****************************************************************
* SUBROUTINE MRQCOF calculates the linearised fitting matrix
* ALPHA and vector BETA. This routine is taken from
* 'Numerical Recipes', 1986 (ISBN 0 521 30811 9), pp. 527-528.
*****************************************************************

      PARAMETER (MMAX=20)
      DIMENSION X(NDATA),Y(NDATA),SIG(NDATA),ALPHA(NALP,NALP),
     +   BETA(MA),DYDA(MMAX),LISTA(MFIT),A(MA)

* Initialise ALPHA and BETA
      DO 12 J=1,MFIT
       DO 11, K=1,J
          ALPHA(J,K)=0.0
 11      CONTINUE
       BETA(J)=0.0
 12   CONTINUE

      CHISQ=0.0

* Summation loop over all data
      DO 15 I=1,NDATA
       IF (MODEL.EQ.1) THEN
          CALL FUNCS1(X(I),A,YMOD,DYDA,MA)
       ELSE
          CALL FUNCS2(X(I),A,YMOD,DYDA,MA)
       ENDIF
       SIG2I=1.0/(SIG(I)*SIG(I))
       DY=Y(I)-YMOD
       DO 14 J=1,MFIT
          WT=DYDA(LISTA(J))*SIG2I
          DO 13 K=1,J
             ALPHA(J,K)=ALPHA(J,K)+WT*DYDA(LISTA(K))
 13        CONTINUE
          BETA(J)=BETA(J)+DY*WT
 14      CONTINUE

* Calculate chi-squared
       CHISQ=CHISQ+DY*DY*SIG2I
 15   CONTINUE

* Fill in the symmetric side
      DO 17 J=2,MFIT
       DO 16 K=1,J-1
          ALPHA(K,J)=ALPHA(J,K)
 16      CONTINUE
 17   CONTINUE

      RETURN
```

```
      END

*********************************************************************
      SUBROUTINE GAUSSJ(A,N,NP,B,M,MP)
*********************************************************************
* SUBROUTINE GAUSSJ solves the matrix A by Gauss-Jordan elimination.
* This basis of this subroutine is taken from 'Numerical Recipes',
* 1986 (ISBN 0 521 30811 9), pp28-29, although it has been modified.
*********************************************************************

      PARAMETER(NMAX=50)
      DIMENSION A(NP,NP),B(NP,MP),IPIV(NMAX),INDXR(NMAX),
     +   INDXC(NMAX)

      DO 11 J=1,N
       IPIV(J)=0
 11   CONTINUE

* Loop over columns to be reduced
      DO 22 I=1,N
       BIG=0.0
*Search for a pivot element
       DO 13 J=1,N
          IF(IPIV(J).NE.1) THEN
             DO 12 K=1,N
              IF (IPIV(K).EQ.0) THEN
                 IF(ABS(A(J,K)).GE.BIG) THEN
                  BIG=ABS(A(J,K))
                  IROW=J
                  ICOL=K
                 ENDIF
              ELSE IF (IPIV(K).GT.1)THEN
                 PRINT*, 'Singular Matrix 1'
                 STOP
              ENDIF
 12            CONTINUE
          ENDIF
 13      CONTINUE
       IPIV(ICOL)=IPIV(ICOL)+1

* Interchange rows, if needed to put the pivot on the diagonal
       IF (IROW.NE.ICOL) THEN
          DO 14 L=1,N
             DUM=A(IROW,L)
             A(IROW,L)=A(ICOL,L)
             A(ICOL,L)=DUM
 14        CONTINUE
          DO 15 L=1,M
             DUM=B(IROW,L)
             B(IROW,L)=B(ICOL,L)
             B(ICOL,L)=DUM
 15        CONTINUE
       ENDIF

* Divide the pivot row by the pivot element
       INDXR(I)=IROW
       INDXC(I)=ICOL
       IF(A(ICOL,ICOL).EQ.0.0) THEN
          PRINT*, 'Singular Matrix 2'
          DO 101 IN=1,5
             WRITE(*,999) (A(IN,JN), JN=1,5)
```

```
 101        CONTINUE
 999      FORMAT (7E10.2)
          STOP
       ENDIF
       PIVINV=1.0/A(ICOL,ICOL)
       DO 16 L=1,N
          A(ICOL,L)=A(ICOL,L)*PIVINV
 16      CONTINUE
       A(ICOL,ICOL)=1.0
       DO 17 L=1,M
          B(ICOL,L)=B(ICOL,L)*PIVINV
 17      CONTINUE

* Reduce the rows
       DO 21 LL=1,N
          IF(LL.NE.ICOL)THEN
             DUM=A(LL,ICOL)
             DO 18 L=1,N
              A(LL,L)=A(LL,L)-A(ICOL,L)*DUM
 18            CONTINUE
             A(LL,ICOL)=0.0
             DO 19 L=1,M
              B(LL,L)=B(LL,L)-B(ICOL,L)*DUM
 19            CONTINUE
          ENDIF
 21      CONTINUE
 22    CONTINUE


       RETURN
       END

*********************************************************************
*
       SUBROUTINE COVSRT(COVAR,NCVM,MA,LISTA,MFIT)
*********************************************************************
**
* SUBROUTINE COVSRT repacks the covariance matrix COVAR to the
* true order of the parameters. This routine is taken from
* 'Numerical Recipes', 1986 (ISBN 0 521 30811 9), p515.
*********************************************************************
*

       DIMENSION COVAR(NCVM,NCVM),LISTA(MFIT)

* Zero all elements below the diagonal
       DO 12 J=1,MA-1
        DO 11 I=J+1,MA
          COVAR(I,J)=0.0
 11       CONTINUE
 12    CONTINUE

* Repack off diagonal elements to fit into correct locations below
* diagonal
       DO 14 I=1,MFIT-1
        DO 13 J=I+1,MFIT
          IF (LISTA(J).GT.LISTA(I)) THEN
             COVAR(LISTA(J),LISTA(I))=COVAR(I,J)
          ELSE
             COVAR(LISTA(I),LISTA(J))=COVAR(I,J)
          ENDIF
```

```
 13       CONTINUE
 14    CONTINUE

* Temporarily store original elements in top row and zero diagonal
       SWAP=COVAR(1,1)
       DO 15 J=1,MA
        COVAR(1,J)=COVAR(J,J)
        COVAR(J,J)=0.0
 15    CONTINUE
       COVAR(LISTA(1),LISTA(1))=SWAP

* Sort elements into proper order on diagonal
       DO 16 J=2,MFIT
        COVAR(LISTA(J),LISTA(J))=COVAR(1,J)
 16    CONTINUE

* Fill in above diagonal by symmetry
       DO 18 J=2,MA
        DO 17 I=1,J-1
           COVAR(I,J)=COVAR(J,I)
 17       CONTINUE
 18    CONTINUE

       RETURN
       END
```